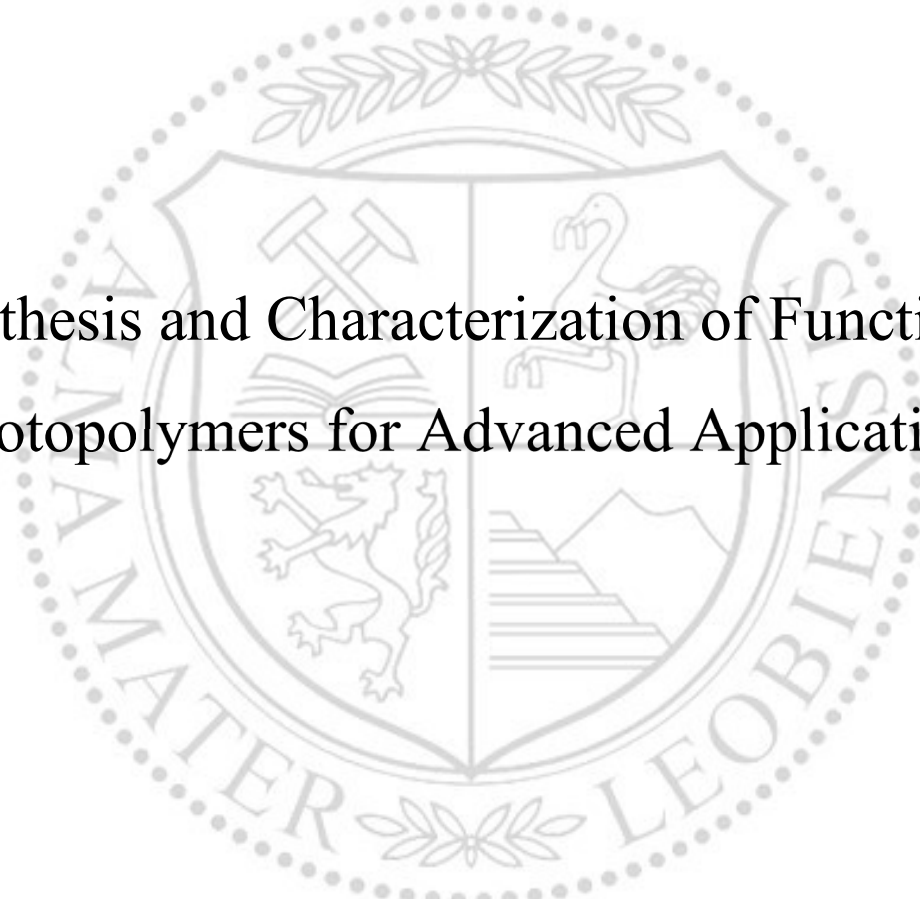




Chair of Chemistry of Polymeric Materials

Doctoral Thesis



Synthesis and Characterization of Functional  
Photopolymers for Advanced Applications

Dipl.-Ing. Elisabeth Rossegger, BSc

March 2021



**MONTANUNIVERSITÄT LEOBEN**

www.unileoben.ac.at

**AFFIDAVIT**

I declare on oath that I wrote this thesis independently, did not use other than the specified sources and aids, and did not otherwise use any unauthorized aids.

I declare that I have read, understood, and complied with the guidelines of the senate of the Montanuniversität Leoben for "Good Scientific Practice".

Furthermore, I declare that the electronic and printed version of the submitted thesis are identical, both, formally and with regard to content.

Date 01.03.2021

---

Signature Author  
Elisabeth Rossegger

# ACKNOWLEDGMENT

The research work was performed within the COMET-Module “Chemitecture”(project-no.: 21647048) and the COMET- K1 projects “Characterization and Tailoring of Copper-Polymer Interfaces in Multilayer Composites used for Microelectronic Applications” (project-no.: 1061010a) and “3D Printing of Functional Metamaterials” (project-no.: 1061920) at the Polymer Competence Center Leoben GmbH (PCCL, Austria) within the framework of the COMET-program of the Federal Ministry for Transport, Innovation and Technology and the Federal Ministry for Digital and Economic Affairs with contributions by Montanuniversitaet Leoben (Institute of Chemistry of Polymeric Materials and Institute of Material Science and Testing of Polymers). The PCCL is funded by the Austrian Government and the State Governments of Styria, Upper and Lower Austria.

First, I would like to thank Priv.-Doz. DI Dr. Sandra Schlögl for the excellent supervision, professional support and especially for her patience and the educational time in her group. Sincere thanks are given to Univ.-Prof. Mag. Dr. Wolfgang Kern for enabling this work as well as Assoc.Prof. Dipl.-Ing. Dr. Thomas Grießer for the scientific support.

Special thanks go to:

- Rita Höller for always helping me and her dedicated work during her bachelor project
- Jakob Strasser for all the DSC measurements and his big effort during his master project, as well as, David Reisinger for all the rheometer measurements
- Evelyn Sattler for always supporting me and Viktoria Wieser for her great assistance
- all the people of the polymer chemistry institute and the PCCL for having such a good working atmosphere, the great support and all the interesting discussions
- the administration team of the PCCL, in particular Elke Holzer, Brunner Doris, Kerstin Fischer and Petra Köck
- Claudia Wieser and Heike Noll for their administrative support at the university
- the PCCL GmbH for the financing

- all my friends for their friendship and their support in difficult times – in particular: Josef, Sophie, Franzi, Maria, Isabella, Theresa, Janine, Lara, Hojabr, Michi and Paul
- my sister Johanna for her great graphical work

Finally, I want to thank my family for always believing in me, being there for me, the good advices in every situation and their endless support. Thanks to my parents Thomas and Renate, my sisters Johanna and Marlene, my brothers Michael and Daniel, my grandmothers Christine and Ingrid and my boyfriend Florian for always cheering me up.

# PUBLICATIONS

The results of this thesis were published in five peer-reviewed scientific papers.

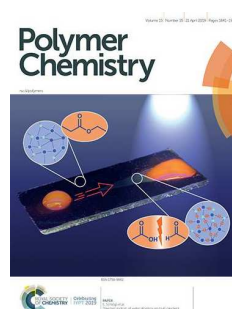
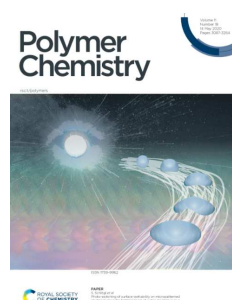
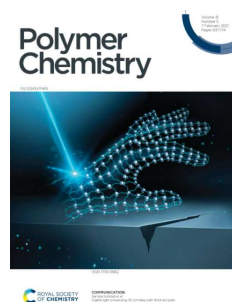
**Rossegger, E.;** Moazzen, K.; Fleisch, M.; Schlögl, S. Locally controlling dynamic exchange reactions in 3D printed thiol-acrylate vitrimers using dual-wavelength digital light processing. *Nature communications*, **2021 under revision**

**Rossegger, E.;** Höller, R.; Reisinger, D.; Fleisch, M.; Strasser, J.; Wieser, V.; Griesser, T.; Schlögl, S. High resolution additive manufacturing with acrylate based vitrimers using organic phosphates as transesterification catalyst. *Polymer*, **2021**, *221*, 123631. <https://doi.org/10.1016/j.polymer.2021.123631>

**Rossegger, E.;** Höller, R.; Reisinger, D.; Strasser, J.; Fleisch, M.; Griesser, T.; Schlögl, S. Digital light processing 3D printing with thiol-acrylate vitrimers. *Polym. Chem.*, **2021**, *12*, 639-644. <https://doi.org/10.1039/D0PY01520B>.

**Rossegger, E.;** Nees, D.; Turisser, S.; Radl, S.; Griesser, T.; Schlögl, S. Photo-switching of surface wettability on micropatterned photopolymers for fast transport of water droplets over a long-distance. *Polym. Chem.*, **2020**, *11*, 3125-3135. <https://doi.org/10.1039/D0PY00263A>.

**Rossegger, E.;** Hennen, D.; Griesser, T.; Roppolo, I.; Schlögl, S. Directed motion of water droplets on multi-gradient photopolymer surfaces. *Polym. Chem.*, **2019**, *10*, 1882-1893. <https://doi.org/10.1039/C9PY00123A>.



## ABSTRACT

Aim of the present thesis was the development of new stimuli-responsive photopolymers for advanced applications. By introducing photoreactive moieties or dynamic covalent bonds into the photopolymer network, smart materials with switchable properties were obtained. In a first step, bi-functional alkynes bearing ortho-nitrobenzyl ester linkages were synthesized and crosslinked with multifunctional thiols by visible light exposure. Via asymmetrical irradiation of the polymer surface with UV-light, polar groups were generated, due to photocleavage reactions of the chromophores and photooxidation upon prolonged UV exposure under air. The wettability increased with increasing exposure dose and a gradient surface with static water contact angles ranging from 97 to 19 ° was obtained. By introducing the wettability gradient in wedge-shaped patterns, an additional Laplace pressure gradient was inscribed and directional motion of water droplets over a reasonable distance (10 mm) was feasible. Based on the high adhesion to the polymeric surface, the droplet could be moved in a controlled way, even on an inclined surface (20 °) or on an upside down turned surface. In another approach, the directional movement of a water droplet was further increased (20 mm) by applying nanoimprint lithography for additional surface texture changes. To generate highly hydrophobic surfaces (static water contact angle approximately 140 °), photo-reactive thiol-acrylate resins consisting of *o*-nitrobenzyl alcohol moieties with terminal acrylate groups, multi-functional thiols and a fluorinated methacrylate monomer were patterned via visible light assisted nanoimprint lithography. Subsequent irradiation of the microstructures with UV-light under air resulted in the localized formation of polar groups and erosion of the needle-like microstructures until fully wettable surfaces (static water contact angle of 7 °) were obtained. Along with photocleavable chromophores, thermally triggered dynamic covalent bonds were introduced into 3D printable photopolymers. They enable numerous advanced functionalities such as self-healing, recyclability, malleability and shape memory. One of the most attractive dynamic networks are vitrimers that rely on thermoresponsive exchange reactions such as the transesterification of hydroxyl ester species. Commonly used catalysts suffer from poor solubility and compromise on the curing rate and pot life of photopolymers. Thus, a mono-functional methacrylate

phosphate was introduced as new transesterification catalyst to overcome these limitations. First, thiol-acrylate vitrimer systems were developed for prototyping of soft-robotic 3D objects via digital light processing 3D printing. After photocuring, the dynamic networks were able to rapidly undergo thermal induced rearrangement reactions. Triple-shape memory and thermal mendability of the 3D printed objects were successfully demonstrated. In a second step, the toolbox of acrylate monomers for 3D printing of vitrimers was further extended. A series of acrylic dynamic networks was prepared and their mechanical performance was conveniently adjusted by the chemical functionality and structure of the monomers. Rheometer studies demonstrated that the stress relaxation rate decreases with increasing crosslink density and glass transition temperature of the photopolymeric networks. By increasing the amount of catalyst, the relaxation rate was significantly increased again. Via digital light processing 3D objects with feature sizes around 50  $\mu\text{m}$  were prepared and the dynamic nature of the network enabled thermally triggered shape-memory and mendability, even of highly crosslinked networks. In a subsequent approach, light and temperature were combined as an external stimulus to locally control the dynamic exchange reactions in 3D printed parts by using a photoacid generator as latent transesterification catalyst. Triphenylsulfonium salts form strong Brønsted acids upon UV exposure (365 nm) and enable fast transesterification reactions at elevated temperatures. The photoacid generator was introduced into visible light (405 nm) curable thiol-acrylate resins. Based on the orthogonality between the curing reaction and the activation of the catalyst, dynamic exchange reactions were selectively triggered in the 3D printed objects by using a dual wavelength 3D printer (operating at 405 nm and 365 nm) and soft active devices with locally controllable topology arrangements above the  $T_v$  could be fabricated.

# KURZFASSUNG

Ziel der vorliegenden Arbeit war die Entwicklung neuer Photopolymere, die auf externe Stimuli reagieren können. Durch die Einführung photoreaktiver Gruppen bzw. dynamisch-kovalenter Bindungen in das Photopolymer-Netzwerk wurden intelligente Materialien mit schaltbaren Eigenschaften hergestellt. Zunächst wurden hierfür bifunktionelle Alkine mit ortho-Nitrobenzylesterbindungen synthetisiert und mit multifunktionellen Thiolen durch Belichtung mit sichtbarem Licht vernetzt. Asymmetrische Bestrahlung mittels UV-Licht führte zu Spaltungsreaktionen der Chromophore und Photooxidation, wodurch polare Gruppen auf der Polymeroberfläche entstanden. Die Benetzbarkeit nahm mit steigender Belichtungs-dosis zu und eine Gradientenoberfläche mit statischen Wasserkontaktwinkeln von  $97^\circ$  bis  $19^\circ$  wurde hergestellt. Durch das Einschreiben des Benetzbarkeitsgradienten in Keilform wurde ein zusätzlicher Laplace-Druckgradient generiert und ein gezielter Transport von Wassertropfen über eine Distanz von 10 mm ermöglicht. Aufgrund der hohen Adhäsion zur Polymeroberfläche konnte der Tropfen auch auf einer geneigten ( $20^\circ$ ) und auf einer auf den Kopf gestellten Oberfläche transportiert werden. Darauf aufbauend wurde die gerichtete Bewegung eines Wassertropfens durch Mikrostrukturierung der Oberfläche mittels Nanoimprint-Lithographie weiter erhöht (20 mm). Zur Erzeugung hochgradig hydrophober Oberflächen (statischer Wasserkontaktwinkel um  $140^\circ$ ) wurden photoreaktive Thiol-Acrylat-Harze, bestehend aus *o*-Nitrobenzylalkoholderivaten mit terminalen Acrylatgruppen, multifunktionellen Thiolen und einem fluorierten Methacrylat-Monomer, durch sichtbares Licht assistierter Nanoimprint-Lithographie strukturiert. Die anschließende Bestrahlung der Mikrostrukturen mit UV-Licht unter atmosphärischen Bedingungen führte wiederum zur lokalen Bildung polarer Gruppen und zur Erosion der nadelförmigen Mikrostrukturen, bis vollständig benetzbare Oberflächen (statischer Wasserkontaktwinkel von  $7^\circ$ ) erhalten wurden. In Kombination mit der Einschreibung eines Laplace-Druckgradienten konnte ein Wassertropfen über 22 mm transportiert werden. Des Weiteren wurde die Einführung von dynamisch-kovalenter Bindungen in 3D-druckbare Photopolymere untersucht, da diese zahlreiche fortschrittliche Funktionalitäten wie Selbstheilung, Recyclingfähigkeit, Verformbarkeit



und Formgedächtnis ermöglichen. Ein in diesem Kontext besonders vielversprechendes Polymer-Netzwerk ist jenes der Vitrimere, das auf thermoresponsive Austauschreaktionen, wie der Umesterung, beruht. Gängige Katalysatoren für solche Umesterungsreaktionen weisen eine schlechte Löslichkeit in Photopolymeren auf und beeinträchtigen die Aushärtungsgeschwindigkeit und Lagerstabilität von Photopolymeren. Um dies zu umgehen, wurde ein monofunktionelles Methacrylatphosphat als neuer Umesterungskatalysator eingeführt. Dafür wurden zunächst Thiol-Acrylat-Vitrimer-Systeme für das Prototyping von Soft-Robotic 3D-Objekten mittels digitaler Lichtverarbeitung („digital light processing“ 3D Druck) entwickelt. Nach der Lichthärtung waren die dynamischen Netzwerke in der Lage, schnell thermisch induzierte Umlagerungsreaktionen zu durchlaufen, welche dreifaches Formgedächtnis sowie thermische Selbstheilung der gedruckten Bauteile ermöglichten. Anschließend wurde eine Reihe dynamischer Acrylatnetzwerke hergestellt, deren mechanische Eigenschaften durch die chemische Funktionalität und Struktur der Monomere eingestellt werden konnte. Rheologische Untersuchungen zeigten, dass die Spannungsrelaxationsrate mit zunehmender Vernetzungsdichte und Glasübergangstemperatur der photopolymeren Netzwerke abnimmt. Durch Erhöhung der Katalysatormenge konnte die Relaxationsrate jedoch wieder deutlich gesteigert werden. Mittels digitaler Lichtverarbeitung wurden 3D-Objekte mit Strukturgrößen um 50  $\mu\text{m}$  hergestellt und die dynamische Natur der Netzwerke ermöglichte ein thermisch ausgelöstes Formgedächtnis und eine Verformbarkeit auch bei hohen Netzwerkdichten. In einem weiteren Ansatz wurden Licht und Temperatur als externe Reize kombiniert, um die dynamischen Austauschreaktionen in 3D-gedruckten Bauteilen lokal zu steuern. Photosäuregeneratoren wie Triphenylsulfoniumsalze bilden unter UV-Belichtung (365 nm) starke Brønsted-Säuren. Es konnte gezeigt werden, dass diese Brønsted-Säuren in der Lage sind Umesterungsreaktionen bei erhöhten Temperaturen zu katalysieren. Der photolatente Katalysator wurde in ein mit sichtbarem Licht (405 nm) härtbares Thiol-Acrylat-Harz eingebracht. Mit Hilfe eines 2-Wellenlängen 3D-Druckers (405 nm und 365 nm) und auf Grund der Orthogonalität zwischen der Aushärtungsreaktion und der Aktivierung des Katalysators konnten die dynamischen Austauschreaktionen in den 3D-

gedruckten Objekten selektiv gestartet werden und aktive Bauelemente mit lokal steuerbaren Topologieanordnungen (bei Temperaturen über dem  $T_v$ ) hergestellt werden.

# CONTENT

<b>INTRODUCTION</b>	<b>16</b>
<b>MAIN GOALS OF THE THESIS</b>	<b>19</b>
<b>STATE – OF – THE – ART</b>	<b>20</b>
<b>1. PHOTO-TRIGGERED REACTIONS</b>	<b>20</b>
1.1. PHOTO-INDUCED BOND FORMATION	23
1.1.1. Chain-growth mechanism	29
1.1.2. Step-growth mechanism	33
1.1.2.1. Thiol-ene/-yne click reaction: radical mediated step-growth mechanism	35
1.1.3. Mixed step-chain growth mechanism	40
1.2. PHOTO-INDUCED CLEAVAGE REACTIONS OF COVALENT BONDS	42
1.2.1. Cleavage of o-nitrobenzyl alcohol groups	43
1.2.2. Photooxidation	46
<b>2. PROCESSING OF PHOTO-REACTIVE RESINS</b>	<b>48</b>
2.1. 2D STRUCTURES: PHOTOLITHOGRAPHY	48
2.2. 2.5D STRUCTURES: NANOIMPRINT LITHOGRAPHY	52
2.3. 3D STRUCTURES: DIGITAL LIGHT PROCESSING (DLP) 3D PRINTING	54
2.4. 4D PRINTING	58
2.4.1. Vitrimers	62
<b>METHODOLOGY</b>	<b>69</b>
<b>CHEMICAL CHARACTERIZATION</b>	<b>69</b>
<b>THERMAL CHARACTERIZATION</b>	<b>69</b>
<b>OPTICAL CHARACTERIZATION</b>	<b>69</b>
<b>MECHANICAL CHARACTERIZATION</b>	<b>69</b>
<b>SUMMARY</b>	<b>70</b>
<b>OUTLOOK</b>	<b>73</b>
<b>REFERENCES</b>	<b>74</b>

---

**INCLUDED PUBLICATIONS** **102**

---

**PUBLICATION I:** **104**

<b>DIRECTED MOTION OF WATER DROPLETS ON MULTI-GRADIENT PHOTOPOLYMER SURFACES</b>	<b>104</b>
ABSTRACT	106
INTRODUCTION	106
RESULTS AND DISCUSSION	109
Synthesis and curing of photo-responsive thiol–yne networks	109
Photo-switching the properties of photo-responsive thiol–yne networks	114
Directed movement of water droplets on the surface of photo-responsive thiol–yne networks	118
EXPERIMENTAL	121
Materials and chemicals	121
Synthesis	121
Physico-chemical characterization of the photo-responsive alkyne monomers	123
Preparation of thiol–alkyne formulations	124
Characterization of the curing and cleavage kinetics	124
Characterization of surface polarity and wettability	125
Preparation and characterization of polymer surfaces with wettability gradient and Laplace pressure gradient	126
CONCLUSIONS	126
ACKNOWLEDGEMENTS	128
REFERENCES	128
SUPPORTING INFORMATION	131

---

**PUBLICATION II:** **138**

<b>PHOTO-SWITCHING OF SURFACE WETTABILITY ON MICROPATTERNED PHOTOPOLYMERS FOR FAST TRANSPORT OF WATER DROPLETS OVER A LONG DISTANCE</b>	<b>138</b>
ABSTRACT	140
INTRODUCTION	140
RESULTS AND DISCUSSION	144
Synthesis and characterization of photocleavable acrylate and thiol–acrylate networks for visible light assisted NIL	144
Surface properties of photocleavable acrylate and thiol– acrylate networks as a function of surface patterns	148

Directed movement of water droplets on patterned acrylate and thiol–acrylate networks	152
CONCLUSIONS	156
EXPERIMENTAL	157
Materials and chemicals	157
Synthesis	157
Characterization of the photo-responsive acrylate monomer	158
Preparation of acrylate/thiol-acrylate formulations	158
Characterization of the curing and cleavage kinetics	159
Preparation and characterization of needle-like polymer surfaces	159
Preparation of non-patterned polymer samples	160
Characterization of surface polarity and wettability	160
Preparation and characterization of polymer surfaces with wettability gradient and Laplace pressure gradient	161
ACKNOWLEDGEMENTS	161
REFERENCES	162
SUPPORTING INFORMATION	165
<b>PUBLICATION III:</b>	<b>170</b>
<b>DIGITAL LIGHT PROCESSING 3D PRINTING WITH THIOL-ACRYLATE VITRIMERS</b>	<b>170</b>
ABSTRACT	172
INTRODUCTION	172
RESULTS AND DISCUSSION	175
CONCLUSIONS	180
EXPERIMENTAL SECTION	180
Materials	180
Preparation of resin-ER-1	180
Characterization	180
DLP 3D printing	181
Self-healing and shape memory experiments	181
ACKNOWLEDGEMENTS	182
REFERENCES	182
SUPPORTING INFORMATION	185

**PUBLICATION IV:** **189**

---

**HIGH RESOLUTION ADDITIVE MANUFACTURING WITH ACRYLATE BASED VITRIMERS USING ORGANIC PHOSPHATES AS**

<b>TRANSESTERIFICATION CATALYST</b>	<b>189</b>
ABSTRACT	190
INTRODUCTION	190
RESULTS AND DISCUSSION	193
EXPERIMENTAL	201
Materials	201
Preparation of Resin Formulations	201
Characterization Methods	202
3D Printing Experiments	203
Self-healing and Re-Shaping Experiments	203
CONCLUSIONS	204
FUNDING SOURCES	204
ABBREVIATIONS	205
REFERENCES	205

**PUBLICATION V:** **209**

---

**LOCALLY CONTROLLING DYNAMIC EXCHANGE REACTIONS IN 3D PRINTED THIOL-ACRYLATE VITRIMERS USING DUAL-**

<b>WAVELENGTH DIGITAL LIGHT PROCESSING</b>	<b>209</b>
ABSTRACTS	210
INTRODUCTION	210
RESULTS AND DISCUSSION	212
CONCLUSIONS	218
EXPERIMENTAL SECTION	218
Materials	218
Preparation of resin-ER-1-lat	218
Characterization	219
DLP 3D printing	219
Re-shaping experiments	220
ACKNOWLEDGEMENTS	220
REFERENCES	220
SUPPORTING INFORMATION	223

**APPENDIX** **225**

---

**CURRICULUM VITAE** **225**

**LIST OF PUBLICATIONS** **227**

## INTRODUCTION

Photopolymers already have a long history in polymer science. The photoresponsive nature of Judean asphalt (also called Syrian bitumen) was known since antiquity and used for mummification and caulking of wooden ships based on its hardening and insolubilization upon sun light exposure.[1] First of all, Niépce developed similar materials to record photographic images.[2] These primitive photopolymers lead to the development of advanced materials and processes, enabling today's microelectronic photoresists. The total microelectronic revolution relies on such photoreactive resins, since there would be no computers, microprocessors or data storage systems without photolithography. In combination with new processing techniques, such as nanoimprint lithography or 3D printing, and increasing environmental awareness or rather the pressure from various regulations, it is justified to expect an even greater application field of photopolymer technology, ranging from automotive, aircraft, interior/exterior architectural coatings, biomedical applications, over tissue engineering to high density data storage systems. Many of these applications require highly tailored polymers which fulfill exactly the requirements of the individual applications.[2] Combined with materials whose structure, architecture, properties, and characteristics can be influenced and changed by another internal and/or external stimulus, new smart materials with switchable properties can be developed. Apart from light, stimuli-sensitive materials can respond to external, as well as internal stimuli such as temperature [3–5], pH-value [6] or water [7,8]. The stimulus response within a polymer is significantly influenced by the propagation capacity of the stimulus in the respective polymer and can be defined in different ways. Due to cross-linking or cleavage reactions, changes in the polymer chain dimension, secondary structure, solubility, stiffness, wettability and degree of intermolecular interconnections can occur. This opens up an even broader application field, such as shape memory polymers, triggered sensors, biological polymers for drug delivery in medicine or self-healing materials.[9–13]

The present work, addresses the development of new stimuli-responsive photopolymers for advanced applications. By introducing photoreactive moieties or dynamic covalent



## INTRODUCTION

bonds into photopolymer networks, smart materials with switchable properties based on external triggers such as light and temperature, are prepared.

The introduction of chromophores such as *o*-nitrobenzyl alcohol derivatives enable the light induced switching of wettability due to light induced cleavage reactions. Synthesizing bi-functional photosensitive monomers bearing *o*-nitro benzyl linkages and terminal alkyne or acrylate functionalities, enables the network formation via visible light irradiation without inducing the photocleavage reaction. Upon prolonged UV-light exposure in air, polar groups are formed based on the cleavage reaction and additional oxidation reactions, which enhance the surface wettability. By introducing the wettability gradient in wedge-shaped patterns, an additional Laplace pressure gradient can be inscribed and directional motion of water droplets is feasible. The directional movement of a water droplet can be further increased by applying additional surface texture changes, since the wettability of a surface depends on the chemical structure, as well as on the roughness of the surface.[14] One possible approach represents visible light assisted nanoimprint lithography combined with fluorinated monomers to generate highly hydrophobic, micro-patterned surfaces. Subsequent irradiation of the microstructures with UV-light in air again leads to the localized formation of polar groups (due to the photocleavage and photooxidation reaction). Moreover by erosion of the microstructures fully wettable surfaces are obtained. However, the photocleavable chromophores only allow a one-time switching of the photopolymers' properties.

In order to repeatedly switch properties of photopolymer networks, dynamic covalent bonds can be introduced into 3D printable photopolymers. One of the most attractive dynamic networks are vitrimers that rely on thermoresponsive exchange reactions such as transesterification of hydroxyl ester species. Commonly used catalysts for transesterification reactions suffer from poor solubility and compromise on curing rate and pot life of photopolymers. For example, triazabicyclodecene (TBD), a common highly efficient transesterification catalyst, acts as radical scavenger and retards radically induced photopolymerization reactions.[15] To overcome these limitations, an oligomeric mono-functional methacrylate phosphate is introduced as new transesterification catalyst. The catalyst is liquid, easily soluble in a broad range of acrylic monomers and covalently

## INTRODUCTION

incorporated into the network due to its methacrylate group. Furthermore, phosphates are used in thiol-click formulations to increase their pot life[16], which enables the development of thiol-acrylate vitrimers that have not been reported yet. In the biofuel research field, the usage of mineral phosphates as heterogeneous catalysts for transesterification in solution is already well established.[17] The monofunctional methacrylate phosphate contains free –OH groups and is a strong Brønsted acid, which should be capable of catalyzing both esterifications and transesterifications.[18,19] After 3D printing by digital light processing, the stress relaxation performance of the newly developed vitrimers is determined by rheometer measurements. Subsequently, shape-memory, self-healing and mendability experiments are carried out to demonstrate the efficiency of the thiol-acrylate vitrimer. In a next step, a series of acrylic dynamic networks is prepared with adjustable mechanical properties based on the chemical functionality and structure of the monomers, to underline the versatile applicability of the new catalyst. Finally, light and temperature should be combined as external stimuli to locally control the transesterification reactions in 3D printed parts by using a photoacid generator as latent transesterification catalyst. It is well known that photoacid generators such as triphenylsulfonium salts form strong Brønsted acids upon UV exposure [20] which could enable fast transesterification reactions at elevated temperatures. The photosensitive salt is introduced into visible light (405 nm) curable resins and based on the orthogonality between the curing reaction and the activation of the catalyst, dynamic exchange reactions can be selectively triggered in the 3D printed objects by using a dual wavelength 3D printer (operating at 405 nm and 365 nm).

The new approaches have succeeded in paving new ways towards the development of switchable photopolymers, and have also been applied for the fabrication of patterned and 3D printed polymers with additional functionalities.

## MAIN GOALS OF THE THESIS

Goal of the present thesis was the development of new stimuli-responsive photopolymers for advanced/functional applications. By introducing photoreactive moieties or dynamic covalent bonds into photopolymeric networks, smart materials with switchable properties and an increased application range should be fabricated.

The developed photopolymers should have the following points in common:

- the synthesis of potential monomers should be easily realizable and occur in high yield to allow further processing
- the resins should be curable upon visible light to enable orthogonality with additional light induced reactions, such as the UV-light induced cleavage of ortho-nitrobenzyl esters or the generation of photoacids
- the curing should follow the radical induced thiol-ene/-yne reaction and/or acrylic homopolymerization to obtain fast curing rates and high conversions for facilitating different photo-induced processing techniques
- the networks should be thermally and mechanically stable for the desired application and possess sufficiently high glass transitions temperatures
- the resins are applicable in photopatterning, nanoimprinting and/or 3D-printing techniques to enable the fabrication of complex structures
- the fabricated objects should keep their stimuli-responsive nature even after the processing step to allow post-modifications such as inscribing a wettability gradient or shape-memory and self-healing behavior

By fulfilling all these points, the preparation of smart materials with switchable properties and complex structures will be feasible. An increased application field due to customized manufacturing techniques, recyclability, re-shape ability, self-healing behavior and/or tailoring/switching wettability of these materials will be aimed at.

## STATE – OF – THE – ART

### 1. *Photo-triggered reactions*

Using light to control structural and mechanical properties and the formation of polymers is one of the most powerful tools in polymer science. It enables the production of specific, adaptable and high-quality polymers and can be used for the formation, degradation, functionalization and crosslinking of polymers. At the beginning, photochemical reactions in polymers were utilized in ship sealants, mummification and photography. In the 1940s, the first patent on UV-curable inks was published.[21] Nowadays, photoreactions are used in microelectronics, stereolithography, biotechnology, biomedicine, energy harvesting, optics, coating industry, inks, 4D – printing, and many more.

Photochemistry features a lot of advantages over conventional reaction methods in polymer chemistry. Energetically unfavorable reactions which normally would need high temperatures to overcome the activation barrier, occur at room temperature or mild conditions by photoinitiation. The activation energy of the reaction can be decreased by applying light due to high energy input of the irradiation.[22,23] Radiation of the full electromagnetic spectrum can be used to start a reaction. The energy of the radiation increases with decreasing wavelength (see Figure 1), however, with increasing energy the penetration depth of light decreases.[21] By choosing the right light source, irradiation with the required energy for a specific reaction can be performed. Figure 1: Electromagnetic spectrum of light

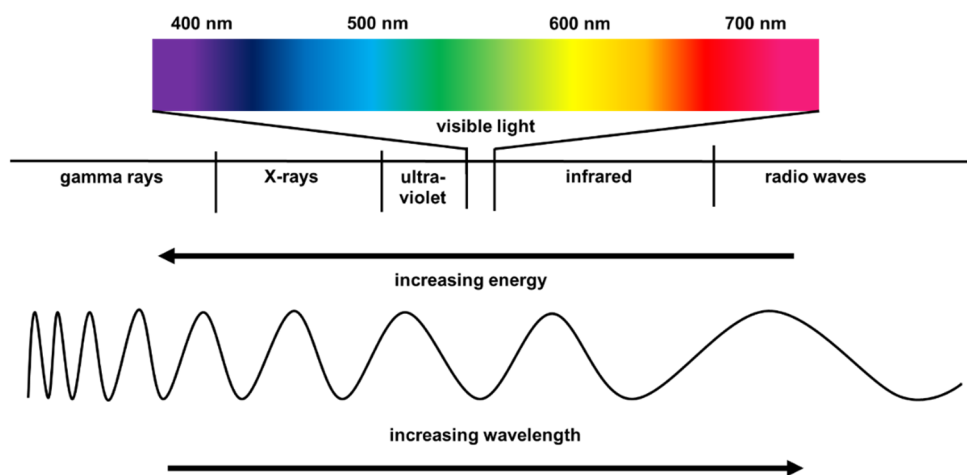


Figure 1: Electromagnetic spectrum of light. Figure adapted from [24].

## STATE-OF-THE-ART

Another advantage is the temporal control of photo-induced reactions. By turning a light source on, reactions are activated and there is no additional need in extreme environmental conditions (solvents, toxic components etc.) to start a reaction. Light facilitates “greener” processes and some processes (e.g. radical polymerization, photoisomerization and photocyclization) can be easily stopped by switching off the light.[22]

Apart from temporal control also spatial control is feasible in photochemistry. Two dimensional control of photoreactions can be achieved by masking or patterning of the illumination. By using optical fibers, light can be focused within a volume and three-dimensional control can be accomplished. Many different polymer processing techniques such as photolithography or stereolithography rely on the spatiotemporal control of photoreactions that enables mechanical and structural changes of the polymeric material in the exposed area in contrast to the unexposed area.[22,23]

Generally, photoreactions in polymeric materials follow two basic laws:[25]

- The *Grotthus-Draper Law* states that only the light absorbed by a molecule can initiate a photoreaction.
- The *Stark-Einstein Law* (also called photochemical equivalence law) states that every absorbed quantum of radiation initiates the reaction of one molecule.

Photoreactions rely on the electronic excitation of a molecule. Via the absorbance of a photon, an electron advances from the HOMO (highest occupied molecular orbital) to the LUMO (lowest un-occupied molecular orbital), if the incident light has adequate energy for the HOMO-LUMO transition (see Figure 2). Furthermore, the spectral emission of the light source has to be overlapping with the absorption spectrum of the molecule.[25]

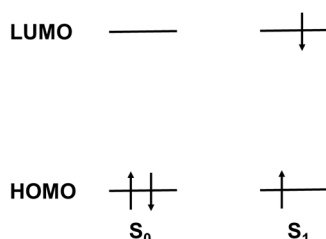


Figure 2: Schematic HOMO - LUMO transition

## STATE-OF-THE-ART

The *Beer-Lambert law* describes the absorption of a single absorbing molecule: [26]

$$A = \epsilon cd = -\log\left(\frac{I}{I_0}\right)$$

$A$  describes the absorbance of irradiation within a film and depends on  $c$ , the concentration of the absorbant,  $d$ , the optical path length,  $\epsilon$ , the molar extinction coefficient,  $I_0$ , the incident intensity of light and  $I$ , the intensity exiting the film. If more than one absorbing species is present, the absorbance is replaced by the sum of the absorbances of each species at a given wavelength. The sum of absorbed intensity,  $I_A$ , is calculated by differing incident and exiting intensity:

$$I_A = (I_0 - I)$$

The quantum yield,  $\varphi$ , represents the part of absorbed photons which result in the required molecular process. Together with the total absorbed intensity,  $I_A$ , the rate of the required molecular process,  $R_i$ , can be calculated for a single absorbing molecule from:

$$R_i = \varphi I_A = \varphi(I_0 - I)$$

Since all these parameters (molar absorption, quantum yield...) are strongly dependent on the wavelength, the total absorption of photons and the reactivity can be determined from the integration over the absorption spectrum of the molecule in respect to the emission spectrum of the irradiation source.[22] For fast reaction rates, a high absorption is necessary, which displays one of the major drawbacks of photo-induced reactions. Photoreactions only take place where light can be absorbed or intermediates can diffuse. Therefore, highly absorptive, colored, opaque or/and thick films result in light intensity/rate gradients and thus gradients in material properties.

The energy of an absorbed photon is described by the *Plank-Law*:

$$E = h\nu = hc\lambda$$

The absorbed Energy  $E$  depends directly on the Plank's constant  $h$  and the frequency of the photon  $\nu$ , which is a function of the speed of light in vacuum,  $c$ , and the wavelength  $\lambda$ .

By absorption of the photon's energy, an electron promotes from the ground state ( $S_0$ ) to an excited singlet state ( $S_n$ ) and has different possibilities of subsequent deactivation, which are described in the Jablonski diagram (see Figure 3).

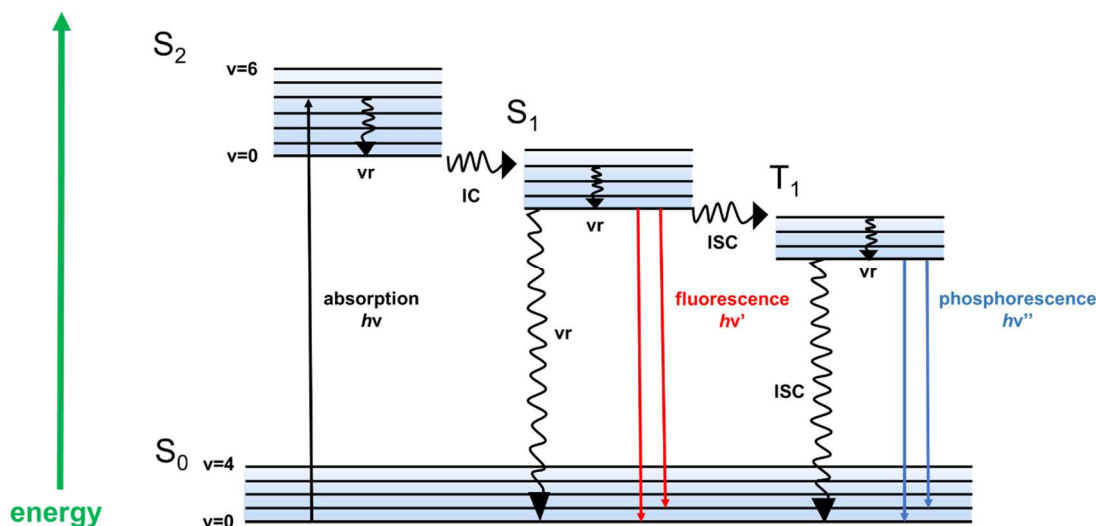


Figure 3: Schematic Jablonski diagram; adapted from reference [25]. ISC = intersystem crossing; IC=internal conversion; vr = vibration-relaxation.

Via internal conversion and vibration relaxation (= radiationless processes), the molecule reaches the lowest excited singlet state ( $S_1$ ). From  $S_1$  the molecule deactivates back to the ground state ( $S_0$ ) within  $10^{-12} - 10^{-6}$  s via vibration-relaxation, fluorescence or a photochemical reaction. If the energy difference between  $S_1$  and  $S_0$  is smaller than the absorbed energy, the emitted wavelength is shifted to higher wavelengths (Stoke's shift). Another possible transition is intersystem crossing (ISC) to the triplet state, which is quantum-mechanical forbidden, since the electron's spin has to be inverted. From  $T_1$  the molecule deactivates back to  $S_0$  within  $10^{-7} - 10$  s via vibration-relaxation, phosphorescence or chemical reaction. The energy difference between  $T_1$  and  $S_0$  is smaller than the difference between  $S_1$  and  $S_0$ , therefore the emitted wavelength of phosphorescence is further shifted to higher wavelengths.[25,27–29]

### 1.1. Photo-induced bond formation

Photopolymerization can proceed in many different ways. On the one hand, a photo-initiator can be used to start a reaction between mono- and/or oligomers to build up a

## STATE-OF-THE-ART

network, or, on the other hand, monomers and/or polymers which are bearing chromophores in their side- or main chain can directly react with each other. The chromophores are absorbing light and form new bonds via photodimerization/photocycloaddition reactions, for instance. Anthracene[30], coumarin[31], cinnamic ester/acid[32] and thymine[33] are characteristic examples (see Figure 4).

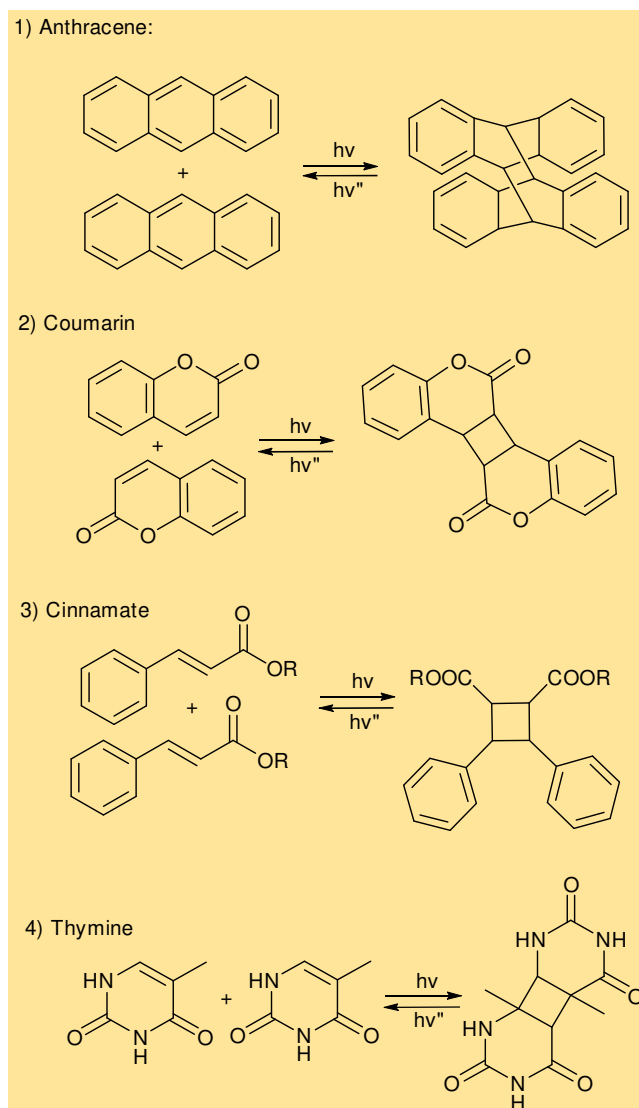


**Figure 4: Photodimerization reactions of 1) anthracene, 2) coumarin, 3) cinnamate and 4) thymine**

Whilst anthracene undergoes a [4+4] cycloaddition reaction, coumarin, cinnamate and thymine follow a [2+2] cycloaddition mechanism. The usage of these chromophores allows for the light induced formation and cleavage of covalent bonds. Thereby, they already have a long history in polymer science. In 1955, the first negative toned photoresist was produced based on the photodimerization reaction of poly(vinyl cinnamate).[22]



Beside numerous other strategies, the usage of photoinitiators represents a widely-used method to form covalent bonds. Generally, two different initiation systems have to be distinguished: the ionic (anionic/cationic) and the radical initiated mechanism. [34] The cationic photopolymerization already has a long history. In the late 1970s Crivello published the usage of onium salts, also called photo acid generators (PAGs), to initiate a cationic polymerization. [20,35] Due to several advantages, such as insensitivity to oxygen, low shrinkage and shrinkage induced stress based on ring opening curing, good adhesion to inorganic substrates, less toxic monomers than many (meth)acrylates, high thermal stability and good solubility of the PAGs and a subsequent post curing effect, these photo acid generators are used in the production of chemically amplified photoresists. [36] The cationic initiation of a photopolymerization or any other acid-catalyzed reaction is based on the formation of a Brønsted acid,  $H^+$ , which is formed via the photoinduced decomposition of the onium salt and subsequent reaction with solvents or monomers of the formulation (see Figure 5). [37] The acidic strength of the formed acid depends on the nature of the counteranion – the bigger the anion, the lower is its nucleophilicity and, thereby, the stronger is the generated acid. [37,38]

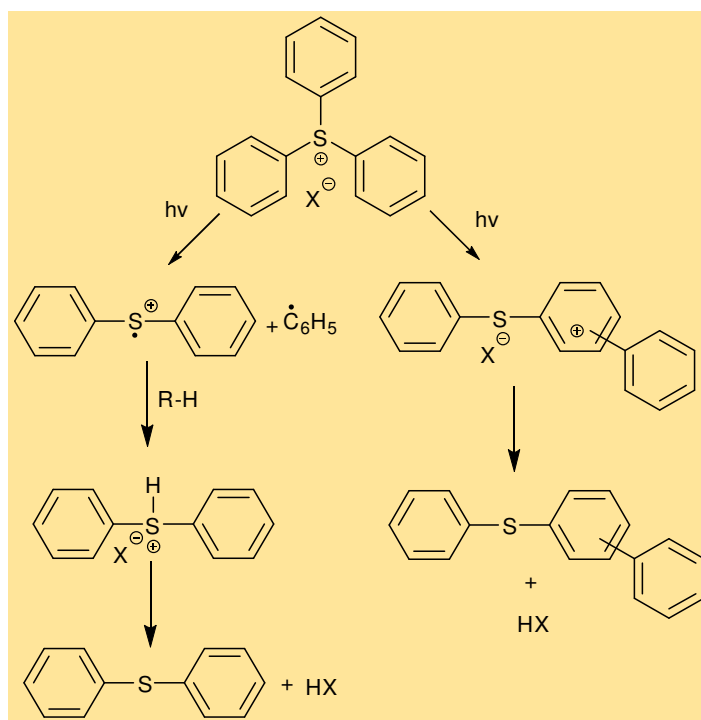


Figure 5: Photoinduced decomposition of a triarylsulfonium salt and subsequent formation of a Brønsted acid

Many of the typical onium salts have their absorption maximum between 200 – 300 nm. Thus, the development of cationic photoinitiators that generate an acid upon longer wavelength exposure, is of great interest. One approach to shift the initiation to higher wavelengths is the so called radical-induced cationic polymerization. [39] The initiation system uses camphorquinone combined with a benzyl alcohol, for instance, to form free radicals by visible light irradiation. The formed radicals subsequently induce the decomposition of the aryliodonium salt and protons are formed to start cationic reactions. Other approaches involve dye-sensitized photoinitiated cationic polymerizations [40] where an electron transfer occurs between the excited molecule and the onium salt and excitation of charge transfer complexes of onium salts. [34,41]

Although, photoinitiated cationic reactions are already well developed, their anionic counterpart is still under investigation. [42] Reactions such as urethane formation, ring opening reactions of epoxides and Michael additions reactions can be catalyzed by a photobase and are inert to oxygen and moisture, which is an advantage for coating technologies. Similar to the cationic reactions, also anionic reactions have a living character, and dark curing can be exploited to reach higher conversions. The major drawbacks of the published photobases are either their low catalytic activity, long-term stability or solubility. Nevertheless, in the last decade researchers have developed new systems for photolabile bases to make them applicable. Catalysts such as tertiary amines, 1,5-diazobicyclo-[4.3.0]non-5-ene (DBN), tetramethylguanidine or 1,8-diazabicyclo-[5.4.0]undec-5-ene (DBU) can be released upon illumination and start an anionic reaction. [43,44] Other auspicious types of photobases are based on thioxanthone acetic acid or quaternary ammonium salts of phenylglyoxylic acid. [45,46] Recently, Romano *et al.* reported the use of 4-(hexahydro-pyrrolo[1,2-a] pyrimidin-1-ylmethyl)-benzoic acid methyl ester as photolabile base in thiol-epoxy resins for the production of dual-responsive photoresists. [47]

Radically induced photopolymerization has already been implemented in many different application fields, such as lithography, UV-curable inks, coatings, dental materials, tissue engineering, adhesives and so on. [22] In general, there are two types of radical initiation: Norrish type I ( $\alpha$ -cleavage), where unimolecular bond cleavage occurs to generate

radicals, and Norrish type II (H-abstraction type), where a bimolecular reaction generates radicals by interaction between the excited states of the absorbing molecule and the second one (Figure 6). [48]

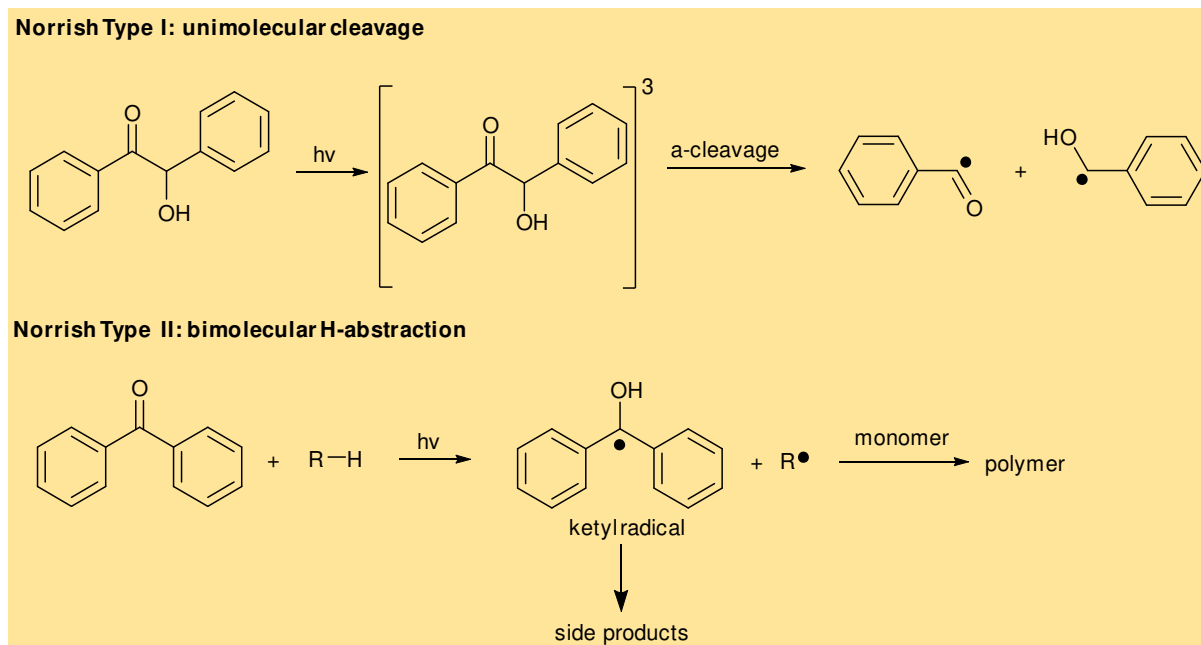


Figure 6: Norrish Type I and II photoinitiation mechanism

For a typical radical photoinitiator system, which forms two identical radicals, the rate of initiation can be described as:

$$R_i = 2f\phi I_0[I]\varepsilon$$

$I_0$  describes the light intensity,  $\varepsilon$ ,  $f$ ,  $\phi$  and  $[I]$  are variables that characterize the initiator: molar absorptivity, the radical efficiency, quantum yield and concentration of the initiator, respectively. Assumption for validity of the equation is a low light attenuation through the film or rather an optically thin film. [22]

Norrish type I photoinitiators are often aromatic carbonyl compounds, such as benzoin and its derivatives, benzyl ketals, acetophenones, aminoalkyl phenones, O-acyl- $\alpha$ -oximino ketones,  $\alpha$ -hydroxylalkyl ketones and acylphosphine oxides, which generate free radicals by  $\alpha$ -cleavage upon radiation (see Figure 6 with benzoin as example). Benzoin is one of the most common photoinitiators due to its high quantum efficiency and reactivity. However, it is thermally instable due to the benzylic hydrogen which can be abstracted and thus, its storage life is limited at room temperature. [34] In contrast, acylphosphine

oxides feature good thermal stability and high reactivity of the photo generated phosphonyl radicals. This relies on the high electron density at the phosphorus atom and the pyramidal structures of the radicals, which provide more advantageous steric conditions for the unpaired radical site to start the polymerization. [49]

The initiation rate of Norrish type II photoinitiators and their curing rate is generally lower due to the bimolecular reaction mechanism. Irradiation of aromatic ketones, such as benzophenone (see Figure 6), thioxanthenes, benzyl and quionones in the presence of hydrogen donors results in the generation of ketyl radicals and another radical deduced from the hydrogen donor. [50] For polymerization usually the hydrogen donor radical is used, since ketyl radicals are quite stable and not reactive towards vinyl monomers regarding steric hindrance and delocalization of unpaired electrons. Ketyl radicals can terminate the polymerization yielding ketyl species within the (relatively short) polymer chains. [51] To prevent chain termination, onium salts or bromo compounds can be added to react with the ketyl radical by oxidation or bromination, respectively. [34] The onium salt can generate additional phenyl radicals by interaction with the ketyl radicals for initiating the polymerization and increases the overall initiation rate. [52] The appropriate co-initiator (H-donor) is crucial for a fast photoinitiation. Tertiary amines increase the reactivity of the bimolecular system more than alcohols or ethers, for example. In combination with thioxanthone moieties, which act as a sensitizer, absorption characteristics comparable to type II benzophenones can be observed. One limitation of alkylamines is their highly volatile and odorous nature. [34] Therefore, the group of Y. Yagci has done a lot of research on thioxanthone species which do not need a co-initiator, because the hydrogen donor is integrated into the thioxanthone structure. Thioxanthone-anthracene is able to initiate the photopolymerizations of acrylates and styrene monomers in oxygen atmosphere due to the formation of endoperoxides, that are generated by the addition of photochemically produced singlet oxygen to the anthracene molecule. The cleavage of those endoperoxides results in the formation of initiating radicals. [53]

Most of the already mentioned photoinitiators are absorbing in the UV-range, but there are also uni- and bimolecular initiator types, that start a reaction in the visible light range. Titanocene and camphorquinone in combination with an amine are common examples for

the respective mechanism. [54] A new class of  $\alpha$ -cleavable initiators for radical photopolymerization upon visible light exposure was developed by Moszner *et al.*. They investigated organic ketones comprising germanium which follow a type I mechanism to generate radicals for photopolymerization of methacrylates. [55] The introduction of dyes as light absorbing chromophores represents another possibility to shift the initiation into the visible light region. By photoinduced electron transfer between the dye and a co-initiator, the initiating radicals are generated. Due to thermodynamic reasons and the low excitation energies of dyes, an energy transfer to the monomers is not favored. By using a photoreducible dye, the electron transfer occurs from the co-initiator to the excited dye and by using a photooxidizable dye, the electron is transferred from the excited dye to the co-initiator. [54]

All the above mentioned initiators are capable of starting a photopolymerization if the right light source is used and all the other rules are fulfilled. In general, it can be differentiated between chain-growth and step-growth polymerization mechanism. The differences, properties, advantages and disadvantages of each mechanism will be described in the next chapters.

### 1.1.1. Chain-growth mechanism

Chain growth polymerizations have to be initiated by an ionic or radical initiator. Subsequently, the formed radicals/ions of the initiator react with the monomers and the chain starts growing. By combination of two active chain ends or chain transfer reactions, the growing of the main chain is terminated (see Figure 7). [56,57] The polymerization of (meth)acrylic resins is a very popular example for free radical photopolymerization.

## STATE-OF-THE-ART

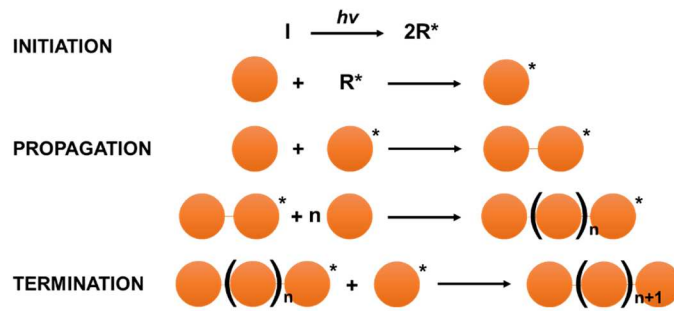


Figure 7: Schematic illustration of the reaction steps in chain growth photopolymerizations

Since chain growth reactions occur rapidly, the material properties change drastically. Initially low viscous liquids become glassy and highly crosslinked within a few seconds. This has significant impact on the polymeric behavior and causes diffusion controlled reactions, delays in obtaining equilibrium properties [58], gradients in concentration, light intensity and temperature [59] and heterogeneous crosslink density. [60] In case of linear polymerization, the molecular structure and weight distribution is fixed after polymerization, but other polymer properties, such as the shape, can be modified in different processing steps, whereas in case of in-situ formed networks no post-modification is feasible. [61] Therefore, a good comprehension of the reaction mechanism is essential for choosing the right curing conditions.

For initiating a chain growth photopolymerization, the afore mentioned initiators can be used. Upon light exposure, the initiator decomposes and forms primary radicals which can react with the unsaturated C=C bonds to start the network formation. This step involves the direct interaction of light with the material. Thus, strongly absorbing photoinitiators or thick, pigmented and/or dyed films induce gradients in light intensity and initiation rate. [62] Throughout the reaction mass transfer becomes more difficult and the efficiency of the initiator decreases, as primary radicals are more caged and tend to recombine. [58]

During the propagation step, monomer/oligomer radicals are added to a C=C double bond and a new radical at the end of the chain is generated. The crosslink density increases with increasing reaction time and results in vitrification of the polymer and diffusion limitation. In general, it's assumed that this bimolecular step is not dependent on the chain-length of the polymer [63], however polymerization degrees below 10-50 are influenced by the

oligomer/polymer chain length. [64] The overall propagation reaction rate can be obtained from:

$$R_p = k_p[M][M_n.]$$

The propagation rate constant is represented by  $k_p$ , the double bond concentration by  $[M]$  and the total radical concentration by  $[M_n.]$ . However, also reactions of pendant and monomeric double bonds, initiation of radicals generated by chain transfer and reactions of the different radicals within the system affect the reaction rate. [58,61]

If two radicals react with each other, termination of the polymerization occurs. The ideal kinetics exclude chain length dependency, heterogeneity within the network and radical trapping and can be described as:

$$R_T = 2k_T[M_n.]^2$$

$k_T$  describes the termination rate constant and  $[M_n.]$  the total radical concentration. The termination step is often limited by diffusion control, which causes the so called *Trommsdorff effect* or *gel effect*. [65] As mass transfer is hindered, termination due to chain combination reactions is difficult and the concentration of primary radicals increases significantly, which results in increasing polymerization rates and temperatures (since curing is an exothermic reaction). The increasing temperature also causes faster radical generation and is difficult to divert due to the increasing viscosity of the system. [65,66] Additional termination occurs by radical trapping – radicals are trapped in highly crosslinked polymer regions and cannot react with unreacted species within a sufficient time frame but stay in the polymer from month to years. [58,61]

One current drawback of free radical photopolymerization is related to oxygen inhibition. On the one hand, excited states of the photoinitiator can be quenched by oxygen and result in an inefficient primary radical generation. On the other hand, initiating and propagating radicals can react with oxygen in a diffusion-controlled way [67] and highly stable peroxy radicals are formed, which are not participating in any subsequent polymerization initiation reaction (see Figure 8). Hence, only after full consumption of the dissolved oxygen, the polymerization can proceed. [68] This is used in the polymerization of deeper regions in thick films, since the dissolved oxygen is already consumed and cannot further

diffuse. Dental applications, such as the restoration of increments with light curing resin composites, use this phenomenon. [69]

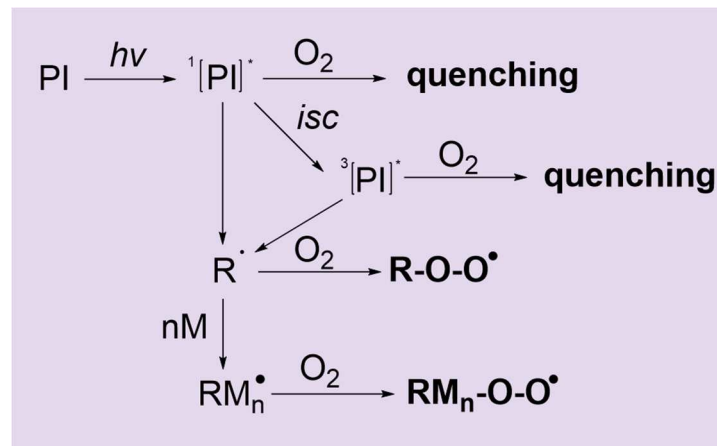


**Figure 8: Schematic representation of oxygen inhibition in photo induced free radical polymerization**

Various approaches have been studied to overcome oxygen inhibition, such as the usage of high-intensity lamps, inert atmosphere or the addition of amines or thiols [34], since the formed peroxy radical is able to withdraw hydrogen atoms from amine and thiol moieties, although it is unreactive towards propagation reactions.[61] Numerous cyclic and acyclic *N*-vinylamides and *N*-alkylamides also have a positive impact on oxygen inhibition and lead to rapid polymerization rates under air and at low exposure doses. [70] Another possibility is represented by the usage of thioxanthone-anthracene species as photoinitiator, since the initiation process is based on the presence of oxygen as already mentioned in chapter 1.1. [34,53]

Furthermore, chain-transfer reactions to the polymer backbone complicate the free radical polymerizations, particularly those of acrylic monomers.[71] All these complexities result in very heterogeneous networks with varying crosslink densities and thereby, differences in glass transition temperatures [72] and relaxation times [73] within the polymeric network. Another disadvantage of free radical polymerization is the curing induced shrinkage stress, which can reach 1-3 MPa[61] and has a significant effect on the performance of films, coatings, additive manufacturing and biomaterials. [74,75] Based on the reduction of free volume during polymerization, shrinkage and shrinkage stress are developed and cause crack formation and/or delamination at interfaces. Numerous methods have been published to reduce the shrinkage stress without declining the



mechanical properties of the polymeric network, such as the addition of low shrinkage additives (prepolymers), phase-separating systems, reactive nanogels, hyperbranched polymers and/or dendrimers. Aside from that, stresses can be reduced by photo-induced addition fragmentation reactions or cationic ring opening polymerization of oxarines, siloranes or epoxides, relying on their comparably low shrinkage per mole of reacting group.[76] By using a soft-start- (reduced light intensity) or pulse-photocuring system, decreased shrinkage stress comes along with a reduced overall conversion.[77]

Nevertheless, radically induced photopolymerization is one of the most facile and powerful polymerization techniques. Rapid polymerization in a spatially and temporally controlled way of different monomers into highly crosslinked, functional materials represents only one big advantage.[61] Depending on the used monomers, variation of the curing performance (rate and overall conversion)[78,79] and the coherent mechanical properties such as flexibility and hardness[79], is feasible.

### *1.1.2. Step-growth mechanism*

Generally, step-growth polymerization does not need an initiator to start the reaction, since it proceeds via the reaction of difunctional monomers or two different monomers with contrary functions in equimolar concentration. In contrast to chain growth polymerization, the molecular weight increases very slowly at the beginning of the reaction and only one type of reaction occurs repeatedly to form the polymer (see Figure 9) (initiation, propagation and termination steps are negligible).[80]

## STATE-OF-THE-ART

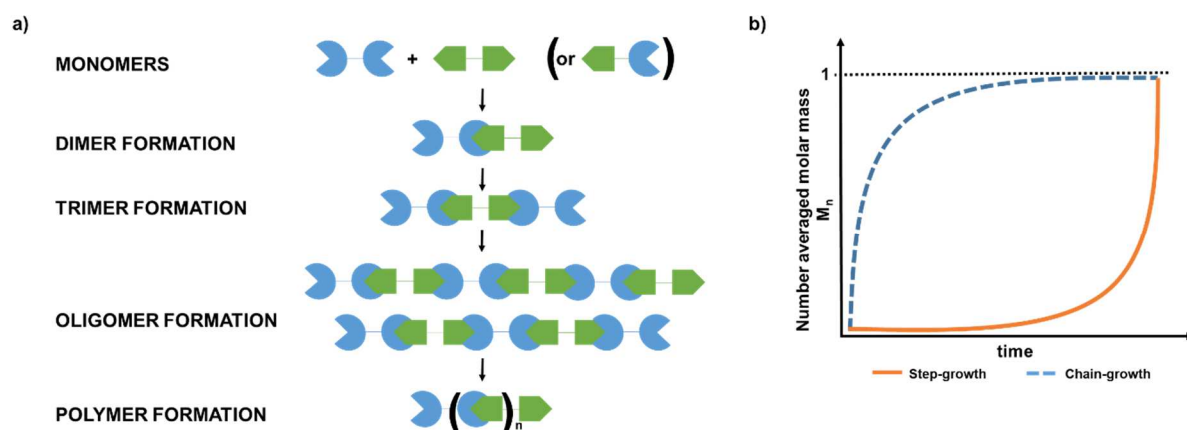


Figure 9: a) Schematic representation of a step-growth polymerization mechanism and b) polymerization kinetic profiles for common chain-growth and step-growth mechanisms. Figure adapted from [81].

The polymerization results from the reaction of the functional groups of the monomers. At the beginning, a dimer is formed by the reaction of two monomers and subsequently, the dimer reacts with another monomer to generate a trimer or with another dimer to generate a tetramer. This reaction is repeated at the same reaction rate over a quite long period of time until full conversion is obtained (see Figure 9b).[81] In general, the reactivity of the functional group on the end of the polymer stays the same as the reactivity of a monomer. However, the reaction slows down if the mobility of the polymer decreases, such as in bulk polymerization or network formation, where the viscosity increases with increasing conversion. At a certain stage of the polymerization, the gel-point is reached and the material becomes insoluble (but swellable).

In general, the polymerization degree  $DP$  in step-growth polymerizations can be described with the Carothers equation for a given conversion  $p$ : [82]

$$DP = \frac{2}{2 - pf}$$

The variable  $f$  represents the average number of functional groups for all kinds of used monomers.

Bakelite was one of the first synthetic polymers, which is formed by a step-growth polymerization mechanism. Via the condensation of phenol (tri-functional) with formaldehyde (di-functional), a network is formed with thermosetting material properties.[83] The first real photo-induced step-growth polymerization was only

published in 2006 by V. Kumbaraci *et al.*. They reported the synthesis of polyester out of benzodioxinones by photo triggered decomposition of this hetero-bifunctional monomers bearing chromophoric and aliphatic hydroxyl moieties.[84]

Step-growth polymerizations are usually categorized after their reaction type, including polyamidation, polyesterification, polyaddition or polycondensation. However, they can also occur by cycloaddition reactions, Passerini reaction, electron transfer and radical coupling reactions and atom transfer radical addition or coupling reactions, for example. One special kind of step-growth polymerization proceeds via click-reactions.[80,85]

In 2001, Sharpless *et al.* established the term “click reaction” to outline a set of reactions that fulfill several criteria, such as: (i) performance at ambient/mild conditions, (ii) modular, high yields, (iii) insensitivity to oxygen or water, (iv) regio-specificity, stereo-specificity and orthogonality with other reactions, (v) missing or harmless side products which can be easily isolated and (vi) favored by many different functional groups to facilitate the usage of numerous common educts.[86] Copper catalyzed azide-alkyne cycloaddition (CuAAC), Diels-Alder reactions, nucleophilic ring opening reactions and thiol-ene/-yne reactions are just a few examples for established click reactions.[87,88] In the next chapter, step-growth polymerizations relying on thiol-ene/-yne click-reactions will be described.

#### 1.1.2.1. Thiol-ene/-yne click reaction: radical mediated step-growth mechanism

Since the early 1900s, the general concept of reactions between unsaturated carbon-carbon bonds and thiols has been well known.[89] Nowadays, two thiol reactions are of particular interest – the radical mediated addition of thiols to electron-rich and/or –poor alkenes/alkynes and the anionic catalyzed thiol-Michael addition to electron-poor carbon-carbon double bonds.[87] The former one follows a radical mediated step growth mechanism, which involves the addition of a thiyl radical to a vinyl function, which afterwards abstracts a hydrogen atom from another thiol group by chain transfer to generate a thioether species (with anti-Markovnikov orientation) and a thiyl radical (see Figure 10a).[90–92] Termination can occur by radical-radical coupling reactions.[90]

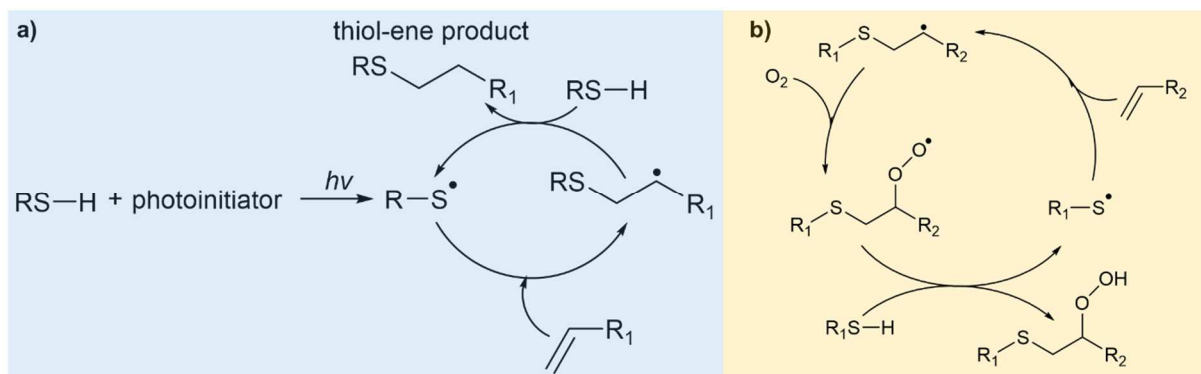


Figure 10: a) Representation of the photoinitiated thiol-ene reaction mechanism and b) influence of oxygen on radical mediated thiol-ene reaction

This kind of click reaction combines motifs of a chain-growth mechanism with those of a step-growth mechanism. Due to the chain-growth character, rapid reaction rates, high degrees of amplification, high conversion and the possible division of the reaction in initiation, propagation and termination step can be obtained. Step-growth polymerization characteristics can be observed by the molecular weight evolution, the lower shrinkage stress, homogeneous networks with narrow glass transition temperature distribution, the low amount of unreacted, leachable moieties and the resistance to oxygen inhibition.[16,87,90,91] By alteration between propagation and chain transfer reactions, the molecular weight increases linearly, which results in a delayed gel-point conversion. Until the gel point is reached, the resin has a low viscosity, since especially low molecular weight species are formed. After reaching the gel-point, the viscosity increases and diffusion rates are reduced.[93] The resistance to oxygen inhibition can be attributed to the ability of the peroxy radical to abstract a hydrogen atom from a thiol to generate a thiyl radical for further polymerization (see Figure 10b).[16]

The overall conversion rate in thiol-ene reactions directly depends on the electron density of the ene-moiety. Electron-rich enes react more quickly than electron-poor ones, except highly conjugated unsaturated bonds, methacrylates and styrene, where the formed carbon-centered radical is stabilized and thus, the hydrogen-abstraction rate constant is lowered. Another exception are norbornenes, which undergo free radical addition of thiols very rapidly, due to a combination of the relieved ring strain by the addition of a thiyl radical to the double bond and the rapid hydrogen-abstraction rate of a thiol hydrogen by

the carbon radical. The order of reactivity of ene-species can slightly change with the thiol structure, however, in general it can be written as:[16,82]

norbonene > vinyl ether > propenyl > alkene  $\approx$  vinyl ester > *N*-vinyl amides >  
allyl ether  $\sim$  allyltriazine  $\sim$  allylisocyanurate > acrylate  $\sim$  unsaturated ester  $\sim$   
*N*-substituted maleimide > acrylonitrile  $\sim$  methacrylate > styrene > conjugated dienes

Apart from the electron density of the ene, also the substitution has an influence on the reactivity.[94] Highly substituted moieties are less reactive than unsubstituted ones and also the position of the ene groups has an impact on the polymerization rate. The addition of a thiyl radical to a *cis*-ene bond is reversible and the *cis*-structure can be efficiently isomerized, which results in the less reactive *trans*-structure. The *trans*-ene bond reacts efficiently with thiyl radicals but still reversibly and slower than with terminal ene-groups. For rapid reaction rates, moieties with terminal ene-groups have to be chosen.[95]

Regarding the thiol structure, thiols comprising propionate and glycolate esters yield higher reaction rates than alkyl thiols, due to hydrogen bonding between thiol functionalities and carbonyl groups, which leads to the weakening of the sulfur-hydrogen bond. If the chain-transfer step is not the rate-limiting step, there is no dependency between rate and thiol structure expected.[16] Thiol-ene click reactions can be initiated in many ways – e.g. thermally, oxidative and photo-triggered.[16,87] Photo-triggered initiation efficiently occurs by either hydrogen-abstraction or an  $\alpha$ -cleavage process, but can also proceed without any initiator. Via direct excitation of the thiol, the cleavage of the labile sulfur-hydrogen bond is induced and hydrogen and thiyl radicals are formed.[96,97]

Generally, thiol-ene reactions have many advantages over classical photopolymerization techniques, such as (i) higher conversion of multifunctional monomers (common multifunctional (meth)acrylates reach gelation already at low conversions), (ii) lower shrinkage stress due to high conversions in the low viscous state before gelation occurs, (iii) lower shrinkage due to the monofunctional nature of vinyl groups in thiol-ene reactions what in turn results in less contraction of the van der Waals distances, (iv) good adhesion to many different substrates relying on the thioether linkages, which are quite flexible, and (v) network homogeneity in respect to crosslink density and narrow glass-

transition region.[16,87,91,98] The major drawbacks of thiol-ene systems are (i) unpleasant odors, (ii) limited shelf stability regarding thermal activation and (iii) softness (networks with low glass transition temperatures and low moduli).[98,99] By improving synthetic procedures, eliminating residual thioglycolic acid or mercaptopropionic acid from the multifunctional thiols and using high molecular weight thiols, the odor can be reduced.[16] The limited shelf-life stability can have many reasons: (i) polymerization due to a base-catalyzed addition reaction, [87,99] (ii) decomposition of peroxide impurities which initiate the radical polymerization, (iii) reaction of hydroperoxide impurities to generate thiyl radicals or (iv) spontaneous initiation via radical formation by a ground-state charge transfer complex formed between the components in the mixture.[16,100] Depending on the chemical structure of the ene and the synthesis route, the stability can range from hours to months – vinyl ether containing formulations seem to be the most unstable ones. To increase the shelf-life several strategies have already been published, such as (i) the addition of triallyl phosphates, which act as vinyl radical scavengers, (ii) phosphorous acids that are used as acid co-stabilizers for buffering the system, (iii) phenolic antioxidants acting as radical inhibitors or (iv) thermal stabilizers such as pyrogallol, which stabilizes radicals to enhance the pot-life and avoid gelation under dark conditions.[16,101] Due to the flexible thioether bonds and a lower crosslink density, common thiol-ene networks are limited in their applications by their low glass transition temperatures. The lower crosslink density relies also on the monofunctional nature of vinyl bonds in a step growth mechanism. In a chain-growth polymerization each vinyl bond is replaced by two single bonds (difunctional nature), which yields high crosslink densities, while in thiol-ene reactions each vinyl unit is converted into only one thioether linkage (monofunctional nature), what limits the crosslink density.[102] To produce tough networks with higher  $T_g$ , monomers with norbornene moieties[103] are applied, which lead to networks with a  $T_g$  around 80 °C due to mobility restrictions. In addition, multifunctional thiocarbamate oligomers[104] are employed resulting in networks with a  $T_g$  over 90 °C due to hydrogen bonding. Other approaches are represented by the usage of dual-cure processes relying on thermal amine catalyzed thiol-epoxy reaction and

subsequent light triggered thiol-ene reaction[105] or the thiol-yne click reaction.[102,106–109]

The thiol-yne reaction mechanism proceeds analogously to the thiol-ene polymerization with the advantage that each alkyne group can react with two thiol moieties.[102,108,110] A vinyl-sulfide radical is formed by the addition of a thiyl radical (formed by initiation of the reaction) to the C-C triple bond. By chain transfer reaction, the vinyl-sulfide radical abstracts a hydrogen atom from another thiol and a new thiyl radical and vinyl sulfide are formed. This radical can be added to the vinyl sulfide to generate a dithioether radical, which again abstracts a hydrogen atom from a new thiol for the formation of a dithioether and a new thiyl radical (see Figure 11).[99] Due to the difunctional nature of the alkyne group, networks with higher crosslink density and therefore higher moduli and glass transition temperatures can be obtained while all the other benefits of a radical mediated step growth mechanism can be retained.[108]

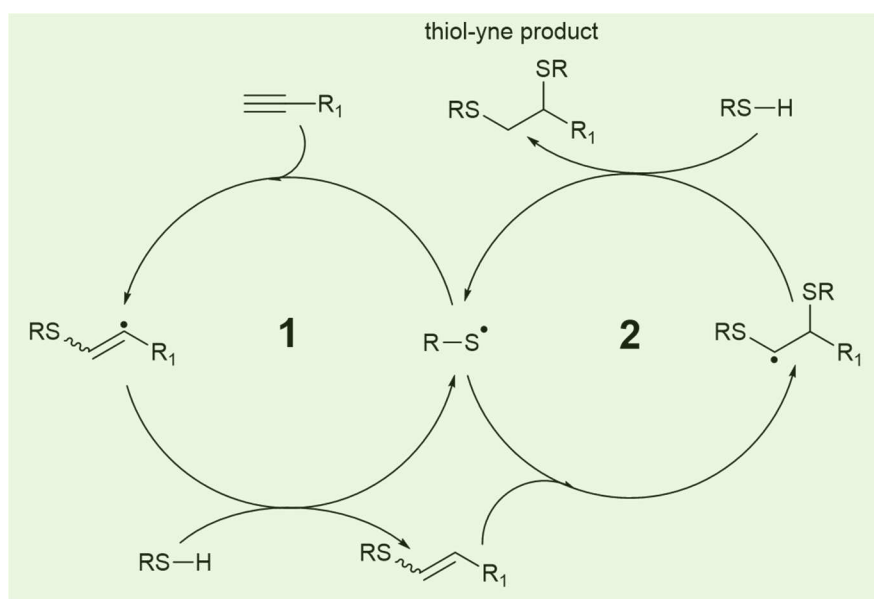


Figure 11: Prospected reaction mechanism of thiol-yne click reactions

Generally, the reaction between alkyne and thiol proceeds slower than the second reaction of thiol with vinyl sulfide. S. Fairbanks *et al.* studied the relative reactivity of different alkyne moieties with alkyl thiols and reported the following order of reactivity:[98,102,108]



Regarding cyclooctyne, methyl propargylamine and ethyl propiolate only a reaction between the alkynes and thiols (fast in case of cyclooctyne, but slowly in case of the other two) could be observed and no subsequent reaction of the formed vinyl sulfides.[108] If the thiols are added in a stoichiometric excess, no vinyl sulfide moieties are present in the resin and if the alkyne is added in excess, -yne and vinyl sulfide species can undergo homopolymerization. This indicates initial polymerization kinetics of nearly first order relying on the thiol concentration and nearly zero order relying on the alkyne concentration, which represents the chain transfer step as rate limiting one.[108,109]

Although, the radical addition of thiols to alkynes has already been published in the 1930s [111], the usage of this reaction to synthesize highly crosslinked photopolymer networks has gained more interest only 11 years ago.[102,108] Nowadays, big effort has been put into the usage of thiol-yne resins in advanced applications. For example, the group of T. Griesser showed the applicability of thiol-yne based photopolymers in 3D-printing of biomedical materials, due to the higher biocompatibility of alkynes in comparison to common (meth)acrylates.[106,107] Roppolo *et al.* represented 3D-printing of thiol-yne resins via an off-stoichiometric route to enable selective post-functionalization of the additive [112], which also gives new perspectives in the biomedical field.

### 1.1.3. *Mixed step-chain growth mechanism*

By using electron poor -ene moieties, such as acrylates, in combination with thiols, a mixed step-chain growth mechanism can be observed with rapid polymerization rates. On the one hand, the acrylate copolymerizes with the thiol following the thiol-ene reaction mechanism and on the other hand, it homopolymerizes according to a chain-growth mechanism (see Figure 12).[16]



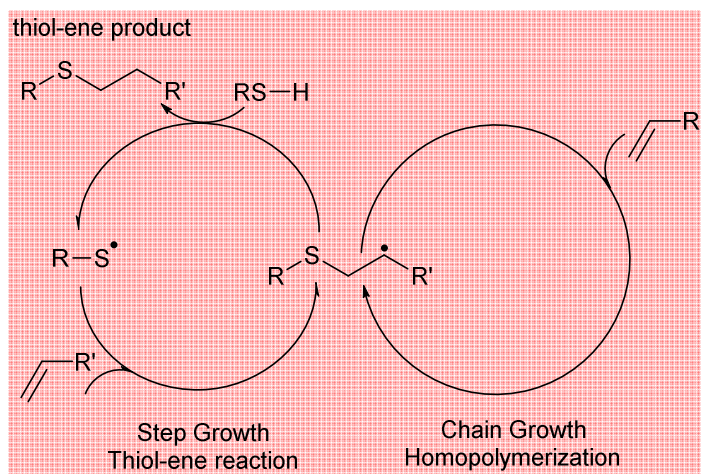


Figure 12: Mixed step-chain growth polymerization mechanism

Two different approaches are feasible – a binary system consisting of (meth)acrylates and thiols and ternary systems involving thiols, vinyls and (meth)acrylates. Both approaches result in complex polymerization processes, network structures and thereby material properties, as two different reaction cycles are comprised. The relative rates of these cycles depend on the chemical properties of the components and their concentrations. M. Sahin *et al.* have shown that in thiol-acrylate systems the reaction kinetics is strongly influenced by the chain growth of the acrylic moieties and that homopolymerization increases if thiols with low functionality or reactivity are added. By increasing homopolymerization, heterogeneity of the network increases again and thereby, the thermo-mechanical properties change (broader glass transition temperature region, higher stiffness).[113] In contrast to common pure (meth)acrylic systems, already 1-10 wt% thiol can significantly reduce oxygen inhibition[114] and enables the curing without nitrogen atmosphere, expensive initiator combinations or high intensity light sources. Moreover, the usage of thiols leads to reduced shrinkage and delayed gel point conversion, which continually results improved resolution in photolithography.[115] By only adding small amounts of thiol (5 – 20 %), no significant reductions in glass transition temperature and modulus can be observed compared to pure (meth)acrylic systems, while the overall polymerization rate increases depending on the oxygen amount.[114] For applications where polymerization under oxygen atmosphere is crucial, such as tissue engineering and hydrogels for biomedical devices, thiol-(meth)acrylate photopolymers are interesting candidates due to their tunable network structure.[116] Furthermore, the addition of

multifunctional thiols also enables a rapid photopolymerization of pigmented diacrylates (rate acceleration of a factor around 10) under air with reduced photoinitiator concentration.[117] Usually, extremely high concentrations of photoinitiator are used to achieve rapid curing rates of pigmented systems.

In spite of many advantages, binary thiol-(meth)acrylate photopolymerization suffers from some limits. While acrylates are polymerized rapidly with minimum affection by the thiol, the polymerization of methacrylates is slowed down by the addition of a thiol, which leads to limited final conversion and reduced benefits of the combination thiol-ene with homopolymerization. Moreover, the relative kinetics of the chain-transfer and homopolymerization for thiol-acrylate resins are nearly fixed and only small changes can be achieved by varying the thiol or acrylate. By increasing the thiol content to an off-stoichiometric ratio, glass transition temperature and rubbery storage modulus decrease.[118] This situation leads to residual thiol-groups at termination of the reaction in specific thiol-methacrylate systems. To overcome these drawbacks, ternary thiol-ene-methacrylate systems are applied.[119] The ternary system is less sensitive to the functional group stoichiometric ratio, and achieves nearly equivalent glass transition temperatures with reduced half-width of the  $T_g$  - region, compared to pure methacrylic systems.

### 1.2. *Photo-induced cleavage reactions of covalent bonds*

To cleave a covalent bond by light exposure, the molecule has to absorb the light (as already mentioned) and the light requires adequately high energy to overcome the binding energy of covalent bonds.[29] Many different types of bond breaking reactions can be induced by light exposure, such as retro-cyclization reactions (reverse reaction to the already mentioned cyclization), the formation of active metal catalysts and radical, acid/cationic or base/anionic intermediates and deprotection reactions. Many of them are used to form reactive intermediates or catalysts for subsequent reactions, such as radical polymerization, thiol-ene/yne reactions, cationic polymerization, chemically amplified photoresist production or copper-catalyzed azide-alkyne cycloaddition reactions. By

implementation of photo triggered cleavage reactions, controlling of polymer structures, biological and chemical functionalization and controlled degradation of polymers has been enabled.[22] Due to cleavage reactions within a polymer, spatiotemporally selective degradation (molecular weight loss) or deprotection of specific functional groups can occur. One prevalent application for photo-induced cleavage reactions represents the production of positive toned photoresists in the sub-micrometer region.[120]

### 1.2.1. Cleavage of *o*-nitrobenzyl alcohol groups

*Ortho*-nitro benzyl alcohol groups are one of the most investigated photo-labile groups in polymer science due to their versatile applicability.[121] In 1966, *ortho*-nitro benzyl ester groups (*o*-NBE) were already used as photo protecting groups for carboxylic acids in organic synthesis[122] and since 1901, it is known that 2-nitro benzaldehyde undergoes an intramolecular rearrangement upon light exposure.[123] The photo-cleavage proceeds via a radical mechanism based on a *Norrish Type II reaction* upon UV-light irradiation (see Figure 13). By UV-light irradiation, an  $n-\pi^*$  transition arises and the molecule passes from a singlet excitation state to a triplet state. Subsequently, the nitro group abstracts a hydrogen atom from the methylene or methine C-atom in  $\gamma$ -position via the formation of aci-nitro tautomers. By intramolecular rearrangement, a benzoisoxazoline derivative is formed, which cleaves in the following step to yield a carboxylic acid and *o*-nitrosobenzaldehyde as primary photoproducts. In a secondary photoreaction, azobenzene groups are generated by dimerization of the *o*-nitrosobenzaldehyde.[124]

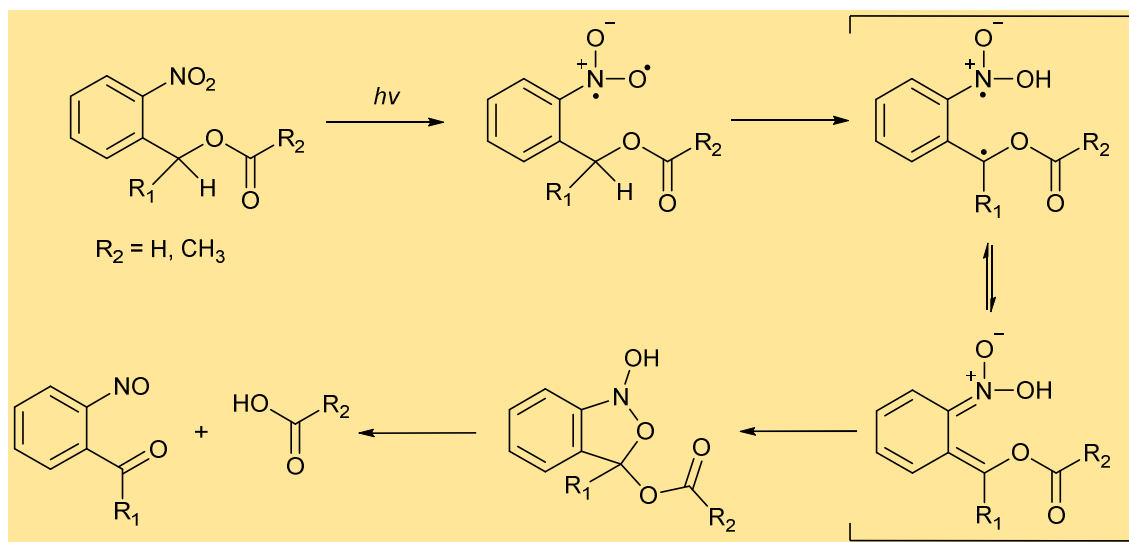


Figure 13: Light triggered cleavage reaction of *o*-nitrobenzyl ester moieties

The highest efficiency of photocleavage can be achieved with light irradiation between 300 – 365 nm, where *o*-nitrobenzyl ester moieties have their absorption maximum.[125] Special substituents at the aromatic ring or at the benzyl position of the link and photo-sensitizing mechanism can shift the absorption maximum to longer wavelengths to increase the efficiency and reduce the amount of side products due to photodimerization reactions.[126–130] By inducing the deprotection reaction under near infrared light via two photon absorption mechanism, new advanced biomedical applications are feasible.[131,132]

In 1977, *o*-nitrobenzyl alcohol moieties were applied in polymer chemistry for the first time.[133] Nowadays, they are already well-established in polymer based drug delivery systems such as hydrogels[134–137], micelles[138,139] and other nanocarrier systems[140–145], which all use the photocleavage reaction for spatially and temporally controlled release of substances. The usage of *o*-NB alcohol species in photoresist technologies[47,146–153] represents another widespread application. Giebler et al. synthesized polydimethylsiloxane (PDMS) networks with *o*-NBE junctions to produce negative and positive toned photoresists and demonstrated their controlled degradation by either hydrolytical or photo-triggered reaction. By photo-induced cleavage reactions of the *o*-NBE junctions, a positive toned photoresist with a resolution of 50  $\mu\text{m}$  was obtained. At higher exposure doses, re-crosslinking due to the photodimerization of the nitroso-moiety could be observed and was used to produce negative toned photoresist, since the

dimerization product was not sensitive to hydrolytic degradation.[154] More recently, the same group demonstrated the preparation of photopatternable and rewritable epoxy-anhydride vitrimers based on *o*-NBE species. By thermal curing of epoxy-terminated *o*-nitrobenzyl esters with anhydrides and a transesterification catalyst, a network with dynamic covalent bonds (will be described in chapter 2.4.1) was obtained. Upon UV exposure, the photolysis of *o*-NBE moieties was triggered and the solubility was locally changed. Positive toned microstructures with a feature size of 20  $\mu\text{m}$  were produced. Due to macroscopic reflow, which is based on the thermo-activated exchange reactions between hydroxyl ester linkages, the patterns could be fully erased at temperatures above the topological freezing transition of the vitrimeric networks. The smooth surface of the regenerated film can be reused for photopatterning.[155] The group of C. Barner-Kowollik used bi-functional acrylates with *o*-NBE moieties for the 3D printing of microstructures via two-photon absorption of 900 nm laser-light. In a subsequent step, they selectively erased some parts of the microstructures (using two-photon absorption of 700 nm laser light) by photolysis of the *o*-NBE species, followed by a final developing step. They introduced a new high-resolution photoresist via 3D laser lithography.[156]

Apart from the already mentioned bulk applications, the photo-responsive nature of *o*-NB alcohol chromophores is also used for switches in surface chemistry.[47,157,158] In 2009, Brown *et al.* demonstrated the preparation of polymer brushes bearing *o*-NBE moieties for hydrophilic patterning. By photolysis of the *o*-NBE junctions in the brushes, the wettability of the surface was changed due to the formation of more polar photodegradation products. On a planar surface, the water contact angle was around 70 ° before UV-exposure – after exposure, the angle decreased to 65 ° indicating an increasing hydrophilicity by the formation of polar cleavage products. By increasing the roughness of the surface, this effect could be increased to a starting angle of 142 °, which decreased to 51 ° upon UV irradiation.[157] It is well known, that the surface wettability depends on both –chemical composition and roughness.[159] The group of Picraux showed that a rough surface increases the photo induced water contact angle switch of a photo-sensitive surface by a factor of 2 compared to the smooth surface and decreases the contact angle hysteresis.[160] A small hysteresis is necessary for the directed movement of a water

droplet.[161–163] Romano and co-workers were able to further enhance this hydrophilicity switch by carrying out the UV- exposure of an *o*-NBE containing network under air. They demonstrated that photolysis of *o*-NBE derivatives in combination with photooxidation reactions under air results in fully wettable surfaces, whereas illumination in nitrogen atmosphere results in a plateau of wettability.[47] More recently, the same group exploited bifunctional vinyl monomers bearing *o*-NBE chromophores, for inscribing microscale 2.5D patterns into thiol-ene networks via direct laser writing. Positive toned micropatterns were directly inscribed with a laser-beam source (375 nm) based on the photocleavage reaction of *o*-NBE species, without an additional development step. The amount of carboxylic acid groups on the surface (formed by the photodegradation reaction) could be simply adjusted by varying the laser energy dose. The generated groups were used in a subsequent modification step for attaching model proteins, which represents an interesting method for biosensing applications.[164] L. Xue *et al.* combined the photolysis of *o*-NBE derivatives with photopolymerization and transesterification to develop a photo-induced strategy for regulating the stationary growth of microstructures from a swollen and dynamic surface. They used the photocleavage reaction to form dissociable ionic groups for enhanced swelling behavior which moves nutrient solutions comprising polymerizable monomers into the illuminated area. Via transesterification, the newly formed polymers were incorporated into the original network structure. Such a procedure enables the spatially and temporally controlled production of microstructures on a surface and the healing of large-scale surface damages.[158]

### 1.2.2. Photooxidation

In general, photooxidation reactions are mostly related to weathering and life-time reduction of polymers.[165–167] J. –F. Larché and co-workers studied the photo-oxidation of polymeric materials in detail to get an understanding for the degradation mechanism. They used a well-characterized phenoxy resin and an acrylate-melamine thermoset as model substances and showed that chain scission processes are not the predominant cleavage reactions as widely known. The mechanical property changes owing to photo-

oxidation can be attributed to the degradation of the ether functionality in phenolic resins or the melamine ethers in the acrylic one.[168]

There are only a few studies in literature on the targeted use of photooxidation reactions in preparing functional polymers. Beside the already mentioned applicability in changing the hydrophilicity of a polymeric surface via photooxidation in combination with photolysis of *o*-NBE linkages[47], Y. Ito *et al.* prepared a gradient photopolymeric surface via photooxidation for the directed transport of a water droplet. Upon irradiation with vacuum ultraviolet light (172 nm), they degraded an alkylsilane self-assembled monolayer (Figure 14) and the droplet moved from the hydrophobic to the hydrophilic area by spreading out with a velocity between 0.5 to 6 mm/s. The velocity of the movement could be directly related to the sharpness of the gradient – the sharper the gradient, the faster the movement.[169][169]

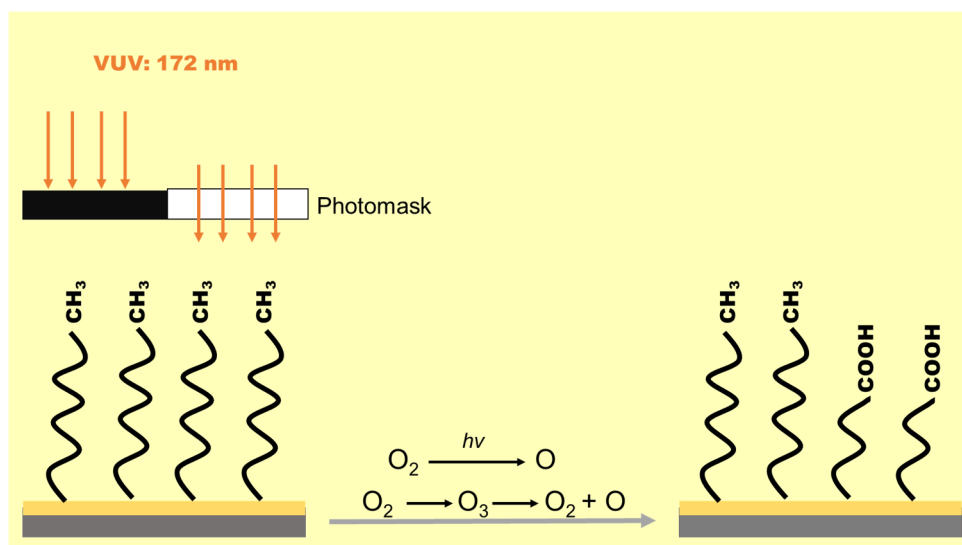


Figure 14: Preparation of gradient surfaces via photooxidation of alkylsilane self-assembled monolayers. Figure adapted from reference [169].

The group of T. Griesser demonstrated the use of photooxidation for the preparation of complex protein bifunctional nanopatterns. Via the UV-induced oxidation of the thiols, sulfonate groups were formed and used to selectively immobilize amino-functionalized molecules after activation with triphenylphosphine triflate. Furthermore, protein-resistant poly(oligoethyleneglycolmethacrylate) brushes were grafted from the non-illuminated thiol groups. The protein-resistant character of the brushes was maintained in the masked areas, whereas site-specific binding of a green fluorescent protein was enabled in the

lithographically defined regions.[170] Under ambient conditions, surface bound thiol groups can be easily oxidized to disulfides. The subsequent oxidation to sulfinate and sulfonate moieties proceeds at very slow rates[171], although direct oxidation by electrochemical or wet chemical treatment is possible.[172,173] However, UV irradiation enables spatially defined conversion of thiols to sulfonates. [174,175]

Other groups demonstrated the use of triazine-based covalent organic polymers as catalyst for the oxidative degradation of acidic and basic dyes upon visible light exposure[176] and methods to generate hydrophilic nanoporous materials with conserved nanostructures by photooxidation of hydrophobic nanoporous polymers under air. Carboxylic acid and hydroxyl groups were formed by the light induced oxidation to generate hydrophilic micro-patterns. Relying on the physiochemical properties of the nanoporous material, such as refractive index contrast, self-confinement and flow of water, procurable reactive functional groups and large surface areas, many new applications were feasible.[177]

## ***2. Processing of photo-reactive resins***

In the last years, numerous strategies have been introduced to process photopolymers owing to the already discussed chemistry. Lithography is one of the standard methods to prepare high-resolution two dimensional patterns. By nanoimprint lithography (NIL) it is feasible to produce 2.5D structures and digital light processing enables the manufacturing of 3D structures. With the help of an additional external stimulus (light, temperature, pH-value...) 4D printing can be accomplished. In the next chapters, these methods will be discussed in detail.

### ***2.1. 2D Structures: Photolithography***

Photolithography represents the most traditional process for photopolymers due to its importance and long history in microelectronic industry. The process relies on the transfer of the image on a mask, having transparent and opaque regions, to the photoresponsive



material. The mask can be in direct contact with the resin or in close proximity to it. As an alternative, the image can be projected on the photoresist by appropriate projection systems. Upon irradiation, the solubility of the exposed film changes and parts of the polymeric film can be selectively removed in a suitable solvent. For negative toned resists, irradiation results in polymerization and/or crosslinking reactions, which decrease the solubility. Thus, non-exposed areas of the resist can be removed with an appropriate solvent and patterns, corresponding to the transparent parts of the mask, with raised features can be obtained. In the case of positive toned resists, illumination results in cleavage reactions and thereby, in decreasing molecular weight and/or changing polarity and thus, increasing solubility. Hence, the irradiated regions will be removed with a suitable solvent and patterns, corresponding to the opaque regions of the mask, can be obtained (Figure 15).[178]

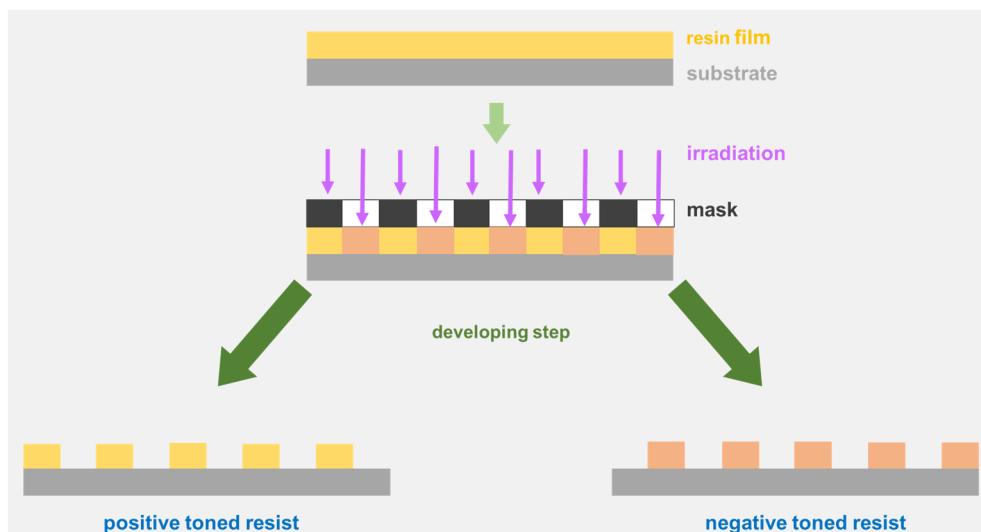


Figure 15: Schematic illustration of the preparation of positive/negative toned resists

The resolution  $R$  of the resists is defined as the width of the patterns and is given by the following equation:

$$R = \frac{k_1 \lambda}{NA}$$

$\lambda$  represents the wavelength of the used irradiation source,  $k_1$  an empiric coefficient with a lower limit of 0.25[179] and  $NA$  the numerical aperture of the optical system, which correlates with  $n \cdot \sin(\theta)$  with  $n$  as the refractive index of the medium above the photoresist and  $\theta$  the largest incident angle formed by the light beam with the normal of the

photopolymeric film. The coefficient  $k_1$  depends on the photoresist, the illumination system and the mask pattern. In general, the resolution is limited by the diffraction of light.[180] The second main limitation in photolithography is the depth of focus (DoF), which can be described as the amount of focus change along an optical axis, in which the imaging occurs with appropriate quality:

$$DoF = \frac{k_2 \lambda}{NA^2}$$

In this equation,  $k_2$  displays a process dependent empirical coefficient. Generally, the depth of focus restricts the maximum thickness of the photoresist and the position of the thin film in relation to the image formation plane. To achieve a better resolution, the optical system (light source), the photoresist materials and the processing can be improved.

Regarding the optical system, the resolution can be simply approved by reducing the wavelength. Shorter wavelengths lead to higher resolution – from visible light at 436 nm and UV-light at 365 nm (mercury lamp) to deep UV-light at 248 nm (KrF excimer laser), 193 nm (ArF excimer laser) and even shorter wavelength at 157 nm (F<sub>2</sub> laser) or extreme UV-light at 13.5 nm, the resolution increases. Furthermore, the numerical aperture can be increased by using objectives with higher working angles or by applying immersion liquids, which increase the refractive index of the medium between lens and photoresist. Whereas, air and nitrogen have a refractive index around 1, high-purity water has one around 1.44 without decreasing the absorption at 193 nm.[180] In addition, a significant increase in resolution can also be observed by using multiple structuring techniques, which consist of successive exposures with laterally offset mask images[181] and which exceed the resolution limits due to optical diffraction.[182]

In respect to the materials and their processing, photoresists have to fulfill numerous criteria, such as (i) the ability to form thin films with uniform thickness, (ii) suitable sensitivity to the used wavelengths, (iii) high-resolution efficiency, (iv) capability to produce high aspect ratio (height to width) patterns, (v) resistance to extreme processing conditions, such as the implementation of plasma, ion, acid or temperature treatments and (vi) having a certain viscosity.[180,183] The sensitivity  $S$  of a photoresist can be obtained from the characteristic curves of the resists (Figure 16). The curves are calculated at

different exposure doses and plotted against the remaining film thickness after the developing step. The logarithmic representation of the dose results in curves from which the sensitivity and the contrast of the respective resist can be observed. To assess the sensitivity, the values of the dose are specified. Regarding positive toned resists,  $D^{0,0}$ , the necessary dose to remove the resist completely, is indicated. In respect to negative toned resists, different dose values are specified. A high sensitivity in combination with a low dose value suggest a sufficient reactivity and hence, a faster production.[27] Chemical amplification [184] leads to an increased sensitivity, since one photon can trigger a series of reactions.

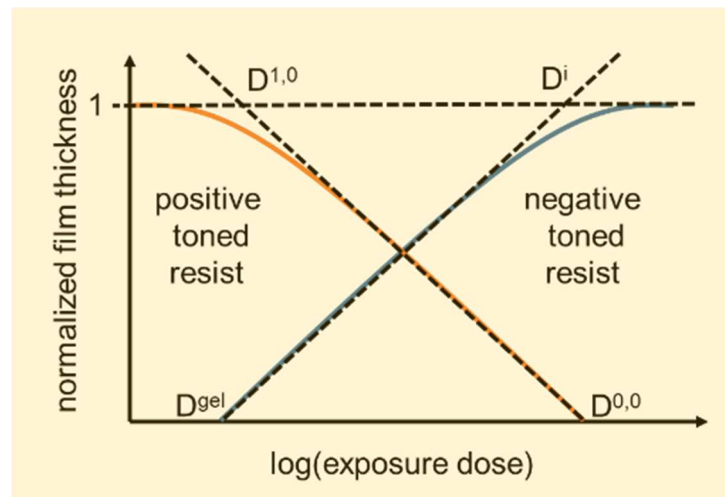


Figure 16: Characteristic devolution of the sensitivity and the contrast in positive and negative toned resists. Adapted from [27].

The contrast of a resist can be determined via the following equation:

$$\gamma = \frac{1}{\log \frac{D_1}{D_0}}$$

A resist with high contrast reduces the empirical coefficient  $k_1$  and improves the resolution. Generally, resist material have contrast values between 2 and 3.[27] Furthermore, positive photoresists enable a higher resolution, since during the developing step the solvent does not permeate the whole resist and it can maintain its size and pattern. In negative resist, the solvent permeates unexposed and exposed areas and leads to swelling and distortions of the patterns. Fast curing speed, wide process latitude, better adhesion to many

substrates and lower operating costs are the advantages of negative toned photoresists.[185]

Apart from microelectronic industry, photolithography is also applied in protein patterning [47,147,170,186], tissue engineering, liquid crystalline surfaces with responsive topographies, to modulate mechanical properties of hydrogels and to program shape morphing in stimuli responsive systems. [180]

## 2.2. 2.5D Structures: Nanoimprint Lithography

Nanoimprint lithography (NIL) is a suitable low-cost method with high throughput to generate well-defined nanostructures with high aspect ratio over a large area with resolutions below 10 nm. By mechanical deformation via a mold of a low viscosity resin, which polymerizes upon light exposure, binary patterns can be produced. After curing, the mold is detached from the cured resin and an inverse patterning of it is obtained (Figure 17).[187] As NIL enables the replication of various stamp topographies by 3D displacement of the material and can utilize bending stamps to fill the mold cavities, it is essentially a 3D process. However, the design freedom is strongly restricted due to lithographical boundary conditions, such as the binding to a substrate. Thus, nanoimprinting is often termed as a 2.5D process, as binary or hierarchical structures with ultra-high aspect ratios (higher than 100:1 width to height ratios) can be generated, which are locally 2D (based on the attachment to the substrate) but globally 3D.[188]

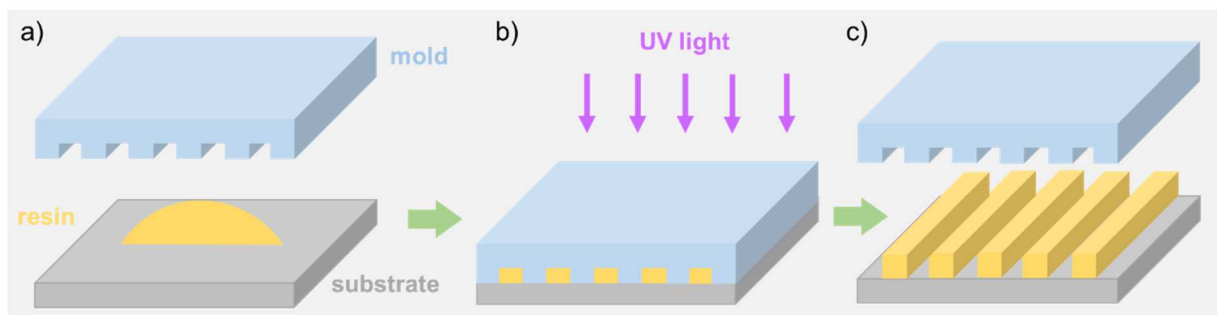


**Figure 17: Schematic illustration of UV-light assisted nanoimprint lithography: a) representation of the mold and the resin which are placed on a substrate; b) photo-curing of the resin while pressed against the mold; c) resin with inverse patterning of the mold. Adapted from [99]**

## STATE-OF-THE-ART

To nanoimprint non-flat or flexible substrates [189], a roll-to-roll (R2R) continuous process has been investigated, connecting basic research with real applications in the market of flexible electronics. [190,191] R2R UV-light induced NIL facilitates the nanostructuring of large areas, is cost-effective and mechanically flexible, which is required in adhesive, drag reducing, anti-reflective or special wetting surfaces of films, paper or textiles.[190] For industrial processes, resins with low viscosity, to achieve material flow into the mold features without high pressure, and rapid curing performance at room temperature to be suitable for R2R techniques, are crucial.

In general, acrylic resins are a common material for light-induced NIL, since their properties are tunable over a wide range. However, their applicability is limited by oxygen inhibition and curing induced shrinkage, which leads to defects.[192] Although, epoxy monomers are not sensitive to oxygen and less shrinkage occurs, they are rarely used in NIL processes, as solvents are necessary to decrease the viscosity of epoxy based resins to enable a successful molding process.[193] To overcome all these issues, thiol-ene resins have been applied to prepare high resolution patterns. Carter *et al.* published for the first time the utilization of a thiol-ene resin for nanoimprinting. [194] To adjust the mechanical properties of the material, they investigated stoichiometric mixtures out of pentaerythritol tetrakis(3-mercaptopropionate) and different alkenes. After coating the photoresists on substrates, which had been functionalized with acrylic silanes for better adhesion, they were compressed via a mold and photopolymerized at 365 nm. By incorporating 2, 2, 2-trifluoroethyl methacrylate the composition of the mold was improved and an enhanced release could be achieved. They observed, that thiol-ene resins with higher modulus lead to a much better resolution and fidelity in the nanoimprinted patterns.

Via advanced deposition methods of the photoresin, including the micro-deposition technique in jet-and-flash imprint lithography (J-FIL), defects are reduced. Resolutions up to 5 nm can be observed.[195] Resolutions in the sub-10 nm region are especially interesting for the semiconductor industry. To reduce defects and enhance the applicability in industry, the particles in the air have to be controlled, the throughput of wafers is improved and the durability of the molds is extended. [196] Besides the semiconductor industry, nanoimprinting is also an interesting method to add

nanostructures to the back reflector of a photovoltaic device, in order to improve the light absorption without increasing the thickness of the active material. [197] Furthermore, NIL is used for the preparation of patterned surfaces for cell-substrate interaction studies, biomimetic surfaces, which reduce anisotropic friction and with specific wettability. The production of periodic structures is used for the generation of sensitive substrates for Raman scattering detection or to prepare optical elements, such as wire-grid polarizers, antireflective surfaces or foils for optoelectronic devices.[180]

### 2.3. 3D Structures: Digital Light Processing (DLP) 3D printing

The principles of 3D printing, also known as additive manufacturing (AM), rapid prototyping (RP) or solid-freeform technology (SFT), were investigated by Charles Hull. In the early 1980s, Hull started his work on producing photopolymeric devices at Ultra Violet Products in California.[198] In 1986, he was granted the patent for stereolithography [199] and introduced the .STL file format, which transfers the structural information from a computer aided design (CAD) software to the printer. A .STL file saves the information for each layer of the 3D model in the profile of triangulated section, where the coordinates of the corner points are described in a text file.[200] The first 3D printer was named “Stereolithography Apparatus” and the SLA-250 was the first commercially available 3D-printer. [198] Together with the work of Scott Crump, who developed the concept of 3D-printing via fused deposition modeling (FDM) [201], 3D printing started to change manufacturing and research. Nowadays, 3D printing is already used in automotive and aerospace industries for the production of prototypes of car and airplane parts, in architecture to prepare structural models, in consumer goods industries, in private and government defense for gun prototyping [198], in the medical field for printing of implants [202], prosthetics and organs [203], in food industry [204] and fashion. [205]

Stereolithography represents the oldest rapid prototyping method and can be divided in different approaches, including direct/laser writing (Figure 18a) and mask-based writing (digital light processing; Figure 18b).[206] In addition, it can be differed between a bath configuration (free surface; Figure 18a) and layer configuration (constrained surface;

Figure 18b), depending on the position of the light source. Both systems contain a movable platform, a resin vat and a light source. In digital light printing systems an additional digital mirror device (DMD) is integrated, which represents the “mask” and allows the curing of a single layer at once. [198]

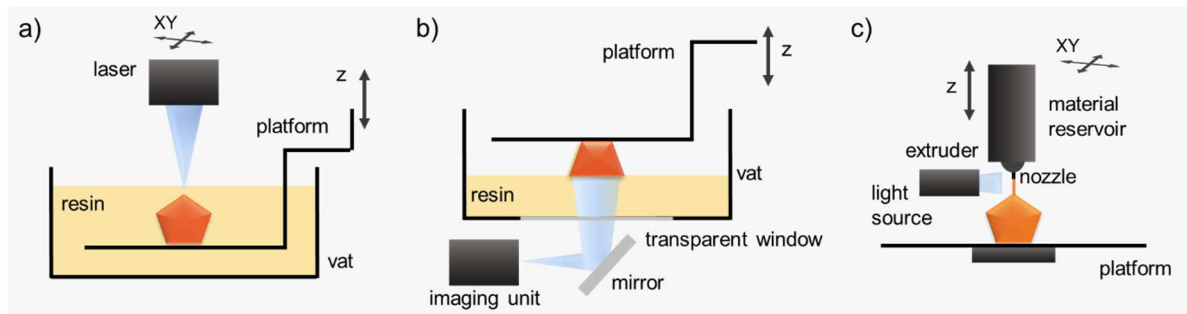


**Figure 18: Schematic illustration of a) SLA printer with direct laser writing as curing mechanism; b) DLP printer with mask-based writing as curing mechanism and c) FDM-printer in combination with a light source - curing can occur in-situ (within the nozzle), as a post-processing step when the material is already deposited or the resin is already pre-crosslinked within the extruder. Figure adapted from reference [180]**

In SLA printers with vat configuration, a light beam traces 2D cross-sections onto a platform which is submerged in the resin vat. The curing thickness depends on exposure time, scan speed, light intensity, energy of the light source and amount of photoinitiator and absorber. By using a photoabsorber, the thickness can be reduced and the resolution enhanced. [180,198,207] After finishing one 2D cross-section, the platform is subsequently lowered into the resin by a defined distance and the curing of the next cross-section starts on the top of the previous layer. By repeating these steps, layer-by-layer, a 3D object is built. This process is the oldest SLA method and suffers from various drawbacks, such as restrictions in maximum height based on the size of the vat, high amount of resin waste, extensive cleaning and long writing times. [206] Moreover, many common resins rely on free-radical polymerization and are sensitive to oxygen inhibition, which occurs when the curing layer is in contact with the atmosphere, as in SLA printing.[207]

DLP printers consist of the same parts as an SLA printer, however the platform is placed above the vat and not submerged in it and the light source is beneath the vat, which has a clear bottom with an anti-stick layer. This layer reduces the adhesion of the photocured resin to the vat and minimizes undesired deformation or damage of the created object. Via a spatial light modulator, the image of a complete layer is created at once, which reduces

the writing time compared to SLA-systems. The DMD (digital micromirror device) is usually integrated in an overhead projection system and consists of an array of over 2 million aluminum micromirrors (10  $\mu\text{m}$  side), which can be simultaneously controlled and allow the curing of an entire layer.[208] First, a thin bottom layer of resin is cured in direct contact with the platform and subsequently, the platform raises and uncured resin fills the gaps, which are left from the cured layer. This process is repeated until the printing of the object is finished. If the resin is highly viscous, the filling slows the printing process down. [198] Compared to SLA, DLP is not affected by oxygen inhibition, since the polymerization occurs on the bottom of the vat and there is no direct contact with air. The lateral resolution of DLP systems depends on the number of pixel/mirror provided by the DMD and the used optics, but is usually in the range of 10-50  $\mu\text{m}$ . The vertical resolution (smallest layer thickness) depends on the penetration depth of light and therefore on the intensity and energy of the light source and the reactivity of the resin. By using absorbing dyes, the vertical resolution can be adjusted and unwanted effects caused by scattered light can be reduced. [207] The following equation expresses the thickness of the cured layer ( $C_D$ ):

$$C_D = D_P \ln\left(\frac{E}{E_C}\right)$$

The cured layer is defined by the penetration depth ( $D_P$ ), the intensity of the light source ( $E$ ) and the critical energy to cure the resin ( $E_C$ ). [209]

Generally, high resolutions can be achieved, but in respect to the surface tension of the residual liquid resin, various small defects can occur.[210] To increase the resolution of stereolithography based 3D printing, two photon polymerization can be used.[211] A method to overcome the time limitation, caused by the renewal of the liquid resin after photocuring of each layer in SLA and DLP printing, has been introduced by DeSimone *et al.*. Continuous liquid interface production (CLIP) reduces the production time by using an oxygen-permeable amorphous fluoropolymer instead of the transparent window in DLP. Free radical polymerization is strongly inhibited by the permeation of oxygen in the so called "death-zone" (only a few tens of microns) and thus, the processing is performed in a continuously fast fashion, since the generated 3D object does not stick to the bottom layer. [212] Computer axial lithography (CAL) enables the use of highly viscous resins and



the production of objects with overhanging features or disconnected parts without additional support structures, which are necessary in common DLP and SLA techniques. CAL relies on irradiation of a rotating volume of a photo-reactive resin via dynamically evolving light pattern. [213]

In addition to the already mentioned methods, 3D printing can also be performed via fused deposition modeling (FDM). Usually, thermoplastic materials are extruded at high temperatures and deposited on a stage layer-by-layer, where solidification takes place while cooling below the glass transition temperature (Figure 18c). [214] Viscoelastic inks, which have filament formation characteristics and can keep their structure after deposition and yield-stress inks, which only flow when a specific pressure limit is exceeded in the ink reservoir generating an excess of shear stress in the needle and a dramatic decrease of viscosity, can be also printed via FDM processes at room temperature. After deposition, the shear stress disappears in the yield-ink and a gel is formed, which enables the formation of 3D objects. [215] If photocurable yield-stress inks are used, the deposited structure is fixed by light irradiation, which is usually done layer-by-layer (post-crosslinking). Another possibility is the usage of light-transmissive capillaries, which enable the light induced curing of any photopolymerizable ink without limitation on the viscosity. In this case, the ink is partially cured while passing through the capillary (in-situ crosslinking). As a third possibility, the photocuring can take place before the extrusion starts (pre-crosslinking). [216] Compared to DLP based printing, FDM takes longer and suffers from a lower throughput and lower resolution. The quality of the surface is reduced (Figure 19) in respect to staircase and chordal effects, owing to the constitution of the slicing software and the .STL file format. Internal defects are based on heterogeneities in the filament feed diameter and density. [198,207]

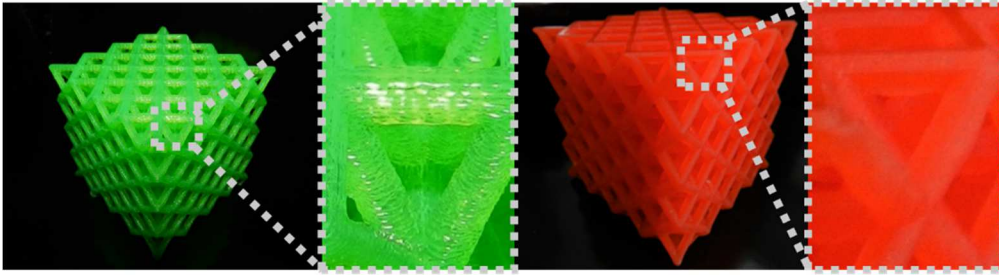


Figure 19: Images of 3D printed cubes via FDM (green) and DLP (red), which display the differences in surface quality.

Overall, SLA and DLP printing enable on-demand, fast, flexible and cost effective preparation of complex 3D structures, with customized size and shape, minimal post-processing and via sequential printing the usage of multiple materials is also possible. Therefore, these technologies are an essential tool for rapid prototyping and are already well established in academia, engineering industries, healthcare sections, optics, biomedicine, automotive and robotics, to name a few examples. Nowadays, new challenges arise in incorporating additional functions into the 3D printed object. New materials are necessary to go beyond structural and aesthetic functionalities. [180]

#### 2.4. 4D Printing

In contrast to static 3D printed structures, 4D printing enables configurational or functional changes of 3D printed objects in response to external stimuli such as temperature [3–5], light [217–219], pH-value [6], water [7,8] etc., with time. The term “4D printing” was introduced by Tibbits in 2013, at a TED Talk about 3D printed subjects that shift their shape over time.[220] Shortly after, the first paper about 4D printing was published: Printed active composites were used to transform the printed sheet into complex structures via shape memory.[221] First, 4D printing was defined as 3D printing with time as a fourth dimension. However, the concept has been further enhanced to shape, property and functionality changes of 3D printed objects by predetermined stimuli over time. [220,222] Although, it is still a young research field, it is already established as a powerful technology for advanced applications such as tissue engineering[223,224] , electronic devices[225,226] and high performance metamaterials[227–229] .

## STATE-OF-THE-ART

Due to the fourth dimension, 4D printing has some advantages over common 3D printing. The fabrication of smart objects enables the evolution of different shapes and functions of the materials. Furthermore, via 4D printing of thin-walled objects or lattices, printing time and material consumption can be saved (around 60-87 %) owing to self-folding properties.[4,230] Based on stimulus responsive shape-changing features, storage and transportation space can also be saved. 4D printing of shape memory polymers, which are programmed into flat surfaces, facilitates easier post-treatment on the surface, transportation and storage, for example.[220] In comparison to smart metals or smart ceramics, smart polymers provide larger deformability and various stimulus responsivities.[231]

So far, 4D printing has been focused on polymeric materials - in particular, on shape shifting materials and structures. The simplest method to change a shape relies on creating localized eigenstrain (or mismatch strain) within a printed structure during or after the prototyping process.[232] Moreover, stimuli responsive liquid crystalline elastomers (LCE), (composite) hydrogels, shape memory polymer (SMP) composites or multimaterials can be used to achieve 4D printing, whereas single shape memory polymers represent the simplest and widest-spread material in addition to LCEs. [220,233,234]

Shape memory polymers (SMPs) are capable of maintaining a temporary shape and recover their permanent shape via an external stimulus such as light or heat.[235] For reshaping, a programming and a recovery step is necessary. During the programming step, the SMP is heated above the transition temperature ( $T_t$ ), subsequently deformed, cooled down below  $T_t$  and finally, unloaded. For semicrystalline polymers the transition temperature is related to the melting temperature ( $T_m$ ) and for amorphous polymers  $T_t$  is consistent with the glass transition temperature ( $T_g$ ). In the recovery step, the SMP is heated again above the  $T_t$  and it recovers its permanent shape owing to entropic elasticity.[236]



Figure 20: Schematic illustration of a shape changing process in SMPs

For larger shape changes, a large stretchability at temperatures above  $T_t$  is crucial. Photopolymers are usually characterized by poor elongation at break, based on their high crosslinking densities via covalent links with multifunctional, commercially available acrylates for DLP 3D printing. Ge and co-workers increased the ductility of a methacrylic resin by using benzyl methacrylate as a chain extender and various difunctional acrylic oligomers as crosslinkers. They demonstrated the 3D printing of mechanically and thermally tailorable SMPs with high resolution, rubbery moduli from 1 to 100 MPa, glass transition temperatures from  $-50$  to  $180$  °C and failure strains up to 300 %, which has represented a significant improvement in contrast to conventional photo-reactive resins. Hence, 4D printing with controlled shape shifts and large deformation of robotic devices such as active self-expandable stents or grippers for the medical field, has been performed.[5] Via SLA 3D printing, commercially available methacrylic polycaprolactone (PCL) photo-reactive resins have been used to produce shape-shifting structures. The semicrystalline macromers were molten in a heated vat and 3D structures could be printed via light induced crosslinking. Above  $55$  °C (melting point of PCL macromeres), the obtained rigid networks become more flexible and deformation could be applied. By cooling down the objects below the melting point, while keeping the applied deformation, different shapes could be generated. To regain the permanent shape, the object has to be heated above  $55$  °C. Zarek *et al.* used this biocompatible and biodegradable SMP to produce complex architectures for biomedical devices[237] and flexible electronics.[234] Furthermore, multiple shape changes can be accomplished by multi-shape memory effects and automated shape changes without a programming step by materials with heat-shrinkable properties. To obtain multiple shape changes, the material (material with broad glass transition temperature region, for example) has to be programmed into different shapes at different temperatures. By passing these transition temperatures during reheating, sequential shape recovery can be observed.[238] Shape changes without a

programming step rely on the release of internal strain energy, which is introduced in the polymer during the printing process, via heating the polymer above its glass transition temperature. Zhang *et al.* printed a 2D lattice out of polylactide acid (PLA) via fusion filament fabrication and demonstrated folding/unfolding in a controllable way without any programming steps.[239,240] Liu and co-workers patterned inks with different absorption maxima as hinges on pre-strained polystyrene sheets to demonstrate controlled folding by relief of the strain in dependency on the used light and color of the ink. The printed inks absorbed light, which resulted in heating of the underlying polymer across its thickness and folding was induced due to the easing strain. Sequential sheet folding concerning time and space could be observed.[241]

Lately, the concept of 4D printing expanded from only shape changing processes to function and property switching ones. Time-dependent functional properties such as tissue maturation[242], degradability[243], self-healing[244], color shifting[6] or wettability changes[245–247] of 3D printed objects can be denoted as 4D printing. SMPs can be used to control the surface microstructure texture and thus, the wettability. As already mentioned, the surface wettability depends on surface chemistry and structuring of the surface - surface chemistry determines the intrinsic hydrophilicity/-phobicity, whilst microstructures enhance this effect. By combining chemistry and microstructures of the surface, superwetting behavior can be observed. To control the surface chemistry, responsive molecules (e.g. *o*-NBE linkages or photo-oxidation reactions) can be used to switch between hydrophilicity and -phobicity or high and low adhesion via an external stimulus. By using microstructures in addition to surface chemistry, new functions are feasible, such as self-cleaning properties, anisotropic wetting behavior or directional liquid-solid adhesion. Various surface microstructure shapes can be prepared via an external stimulus and recovered, based on the shape recovery behavior of SMPs. The reversible control of wettability enables switchable isotropic/anisotropic wetting, gradient wetting, droplet transportation and storage.[248]

### 2.4.1. Vitrimers

Another interesting material, which facilitates not only shape-memory properties, but also self-healing, recycling and remolding properties, is represented by so called vitrimers. In 2011, Leibler et al. introduced this new class of polymeric material and opened a completely new research field with high potential for future applications.[249] In this next chapter, the general properties of vitrimeric materials will be described and their application in 4D printing explained.

In general, thermosets are intractable, insoluble, largely inert, permanently and covalently crosslinked polymeric networks. Hence, their application ranges from wind turbine blades over aerospace applications to adhesives, but their performance and utilization are constrained by their permanent nature.[250] By combining properties of conventional thermosets with reversible bond exchange reactions, covalent adaptable networks (CANs) can be obtained[251] and self-healing, controllable shape changes, welding and reprocessing of thermosets are applicable. Self-healing facilitates the repair of defects, whilst recyclability enables a more sustainable and efficient management of resources. Additionally, due to weldability, the preparation of new complex geometries and flexible assembly of numerous structural parts is feasible.[252] In 2011, Leibler and co-workers termed CANs with silica-like fluidity as vitrimers and demonstrated their flow behavior above their topology freezing transition temperature ( $T_v$ ), while featuring rigid thermoset-like characteristics below it.[249]

Dynamic Covalent Networks (DCNs), also called Covalent Adaptable Networks (CANs), are characterized by dynamic bonds which break and reform either autonomously or upon an external stimulus. The bond exchange relies on interactions between repeating units, following an associative (bond forming/breaking mechanism) or dissociative (bond breaking/forming mechanism) pathway.[253] The energy profile in Figure 21a describes the theoretically ideal bond exchange mechanism for vitrimers and is also termed concerted molecular network rearrangement. The transition between reactants and products does not involve reactive intermediates, since the transition state comprises only a temporary more crosslinked species which is not thermodynamically stable. Therefore, the kinetics only depend on the overlapping of the free Gibbs energy curves, which

displays the ideal case with constant crosslink density and no side-reactions. In reality, a molecular network rearrangement (MNR) occurs in a complex multi-step pathway, depending on the chemistry of the interacting species and the usage of catalysts or external reagents. To simplify the process, Figure 21b and c describe the MNRs following an associative and dissociative pathway, respectively, with only one reactive intermediate formed. In associative CANs, bond exchange reactions occur by forming an intermediate reactant with temporarily increased crosslink density. This effect can be neglected since soon after the new crosslink is formed, the former bond is cleaved, which leads to a nearly constant crosslink density.[254] However, in dissociative CANs a bond scission is followed by bond formation, resulting in a temporary decrease in crosslink density and viscosity and subsequently the topology rearranges.[255]

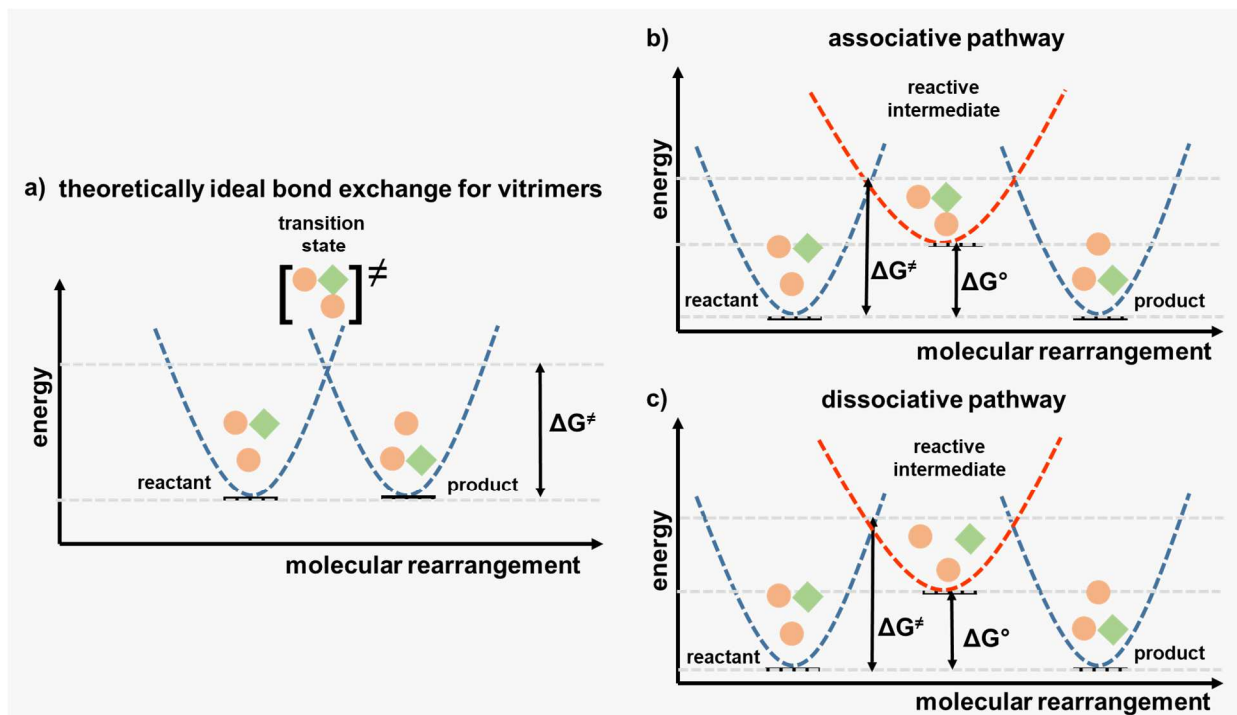


Figure 21: Schematic representation of the energy profiles of a) ideal b) associative and c) dissociative bond exchange mechanisms. Adapted from reference [254].

The reversibility of the reaction and the loss of mechanical integrity provoke softening processes, comparable to thermoplastic reprocessing. The favored state (crosslinked vs. de-crosslinked) in such systems, is the net result of two reverse driving forces: entropy prefers de-crosslinking and enthalpy crosslinking. Hence, an appropriate high temperature can shift the equilibrium towards de-crosslinking.[254] If the required

temperature exceeds the degradation temperature of the network (for example when  $\Delta H$  is high), the dissociated state cannot be observed.[256]

The topology freezing transition temperature ( $T_v$ ) characterizes the flow behavior of vitrimers – above this temperature, vitrimers flow according to an Arrhenius trend, comparable to silica-based glasses.[249] Below the  $T_v$ , vitrimers behave like thermosets, however, above the  $T_v$ , they are similar to viscoelastic re-shapeable, malleable and re-processable fluids.[252–255] By tuning the crosslink density, exchange reaction kinetics (based on catalyst loading, favored chemical affinity between reactants and thermodynamic factors), monomer mobility and stiffness of the network, the  $T_v$  of the network changes.[255] Thermoplastic materials also demonstrate decreasing viscosity with increasing temperatures. However, this phenomenon is based on a glass transition between two amorphous (or semicrystalline) regions and follows the Williams-Landel-Ferry theory.[257] It could be assumed that topology freezing represents another kind of “glass transition”, since it is influenced by the cooling rate and a third amorphous domain originates above the  $T_v$ . Though, while the  $T_g$  is referred to the thermal onset of long range chain motion between repeating units, the  $T_v$  is based on dynamic molecular rearrangements via exchange reactions of cross-links.[252] Moreover, thermoplastics dissolve in an appropriate solvent at elevated temperatures to shift the equilibrium to the solution state.[252]

Summing up, vitrimers should be characterized as associative dynamic networks[254] and according to Denissen *et al.* they should feature the following properties: [255]

1. Organic network with covalent crosslinks
2. Thermally induced rearrangement reactions following an associative pathway
3. Viscosity follows the Arrhenius law above the  $T_v$  and decreases due to chemical exchange reactions
4. Constant crosslink density and insolubility at all temperatures until degradation

Though, some dissociative networks also feature all these properties[254], there are also vitrimers, which can be fully dissolved in a sufficient solvent after an adequate time. The group of Breuillac prepared a polybutadiene vitrimer based on spontaneous metathesis of



boron-heterocyclic crosslinks. Owing to the high dynamics and low activation energy of the dioxaborolane units, the network could be fully dissolved in tetrahydrofuran after 120 h.[258] Since vitrimers are a quite new material class there are still some open points to debate and the lines become a little blurred.

Diels-Alder chemistry (DA) represents the most important dissociative CAN chemistry and relies on a [4+2] cycloaddition between electron-rich dienes and electron-poor dienophiles.[259] At elevated temperatures, the equilibrium is shifted towards the de-crosslinked state (retro-Diels Alder reaction). Although this type of reaction is already well established in chemistry, Wudl *et al.* introduced it into polymer science first in 2002. The obtained networks, consisting of tetrafunctional furan and trifunctional maleimide monomers, enabled shape memory processes, recyclability and self-healing.[253,259]

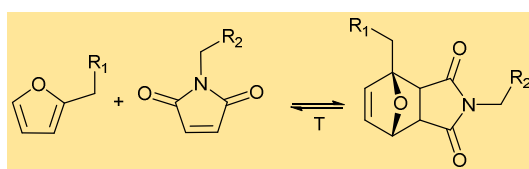


Figure 22: Diels-Alder reaction between maleimide and a furan species

Associative CANs are mostly based on reactions where organic groups are exchanged, such as transamination of vinylogous acyls, transalkylation of triazolium salts, transcarbamoylation, imine-amine exchange, disulfide exchange, transesterification, olefin metathesis and siloxane-silanol exchange.[252] In a transesterification (TE) reaction, the organic rest of an ester is exchanged with an alcoholic one, for example (Figure 23). Typical catalysts are Brønsted acids[19], organo-metallic complexes or organic bases.[260]

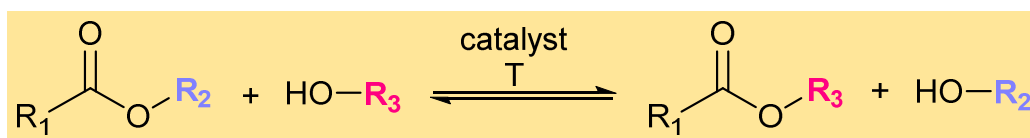


Figure 23: Schematic transesterification reaction

The first published vitrimer of Leibler and co-workers was based on transesterification chemistry, in 2011. They mixed diglycidyl ether of bisphenol A (DGEBA) with fatty tricarboxylic and dicarboxylic acids (epoxy/COOH ratio 1:1), together with  $Zn(Ac)_2$  as catalyst, to prepare an insoluble network with the ability of stress-relaxation and flowing

at high temperatures. By grinding the material into small pieces and using those in an injection molding process, the reprocessability of the network was proven. Subsequent material testing demonstrated that the original mechanical properties can be fully restored. Furthermore, they tested an epoxy-anhydride system consisting of glutaric anhydride (GA) and DGEBA (1:1 epoxy/acyl ratio), in presence of 5-10 mol%  $\text{Zn}(\text{acac})_2$  as a catalyst. Similar activation energies compared to the epoxy/acid system and reprocessing via compression moulding could be achieved.[249] From that time on, scientists all over the world worked on the development of new ideas and applications of transesterification reactions. Due to the high amount of commercially available and straight-forward chemicals, vitrimers based on transesterification chemistry are easy to implement in different applications fields.[252,261] Chen *et al.* reported the usage of TE reactions to produce aligned, healable and recyclable graphene/epoxy composites.[262] Lee and co-workers used vitrimers based on TE for hot embossing patterning of biocompatible and reconfigurable microgrooves for tissue engineering applications.[263] The group of Zhang demonstrated the synthesis of bioepoxy vitrimers with high  $T_g$  and self-healing ability[264] and Lyon *et al.* performed photopatterning and nanoimprint lithography with remoldable thiol-ene vitrimers based on TE chemistry[15] – just to mention a few examples.

To enhance the bond exchange rate and therewith fasten the stress relaxation and tuning the topology freezing transition, a suitable catalyst has to be added to the resin.[257] There are only a few examples of vitrimers that show sufficient stress-relaxation without a catalyst.[265–268] Zinc acetylacetonate ( $\text{Zn}(\text{acac})_2$ ) and similar zinc-based organometallic salts are already widespread catalysts for transesterification reactions due to their high thermal stability. The role of the Zn-catalyst relies on (i) bringing the reactive species together via directional coordination, (ii) increasing the electrophilicity of the carbonyl group via polarization and (iii) shifting the alcohol/alkoxide equilibrium towards the more nucleophile alkoxide.[268] By increasing the amount of Zn, the exchange rate increases linearly, whereas the activation energy is maintained in the same range.[18] Recently, Niu *et al.* prepared a catalyst for DGEBA and sebacic acid by randomly copolymerizing zinc methacrylate and acrylonitrile. The catalyst performed with higher efficiency than

common  $\text{Zn}(\text{acac})_2$  and TBD under the same loading conditions.[269] Another interesting catalyst is triazabicyclodecene (TBD) – a strong guanidine base which increases the nucleophilicity of alcoholic groups by H-bonding and enhances the rate of transesterification efficiently.[270] On the contrary, triphenylphosphine (TPP) catalyzes transesterification reactions owing to the lone pair on its phosphorous atom.[271] Compared to  $\text{Zn}(\text{acac})_2$  and TBD, the addition of TPP results in lower activation energy and lower  $T_v$  what in turn leads to slower exchange reaction rates.[257] Moreover, stannous octoate ( $\text{Sn}(\text{oct})_2$ ) was used as a catalyst in a vitrimeric network out of polylactide and diisocyanate. It demonstrated sufficient catalytic activity in transesterification, indeed in presence of a low amount of free hydroxyl- groups, high stability and low toxicity.[272] Lastly, dibutyltin dilaurate (DBTDL) was reported as a suitable catalyst for TE reactions in epoxy-anhydride systems.[273] More recently, the transesterification reaction in polyester vitrimers was activated by the addition of Brønsted acids to clarify the dependency of pKa values on the stress relaxation behavior of the material. Apart from the general acceleration of the Fischer-transesterification reaction, stronger acids also increased the mechanical activation energy, although the exchange reaction rate itself occurred faster. Stress relaxation times in order of hours could be already monitored at room temperature due to the high catalytic efficiency of Brønsted acids. Furthermore, Bates *et al.* noticed a significant difference in efficiency between Brønsted acids and Lewis acids, with the last one being less effective based on a different manifested exchange mechanism.[19] Du Prez and co-workers studied the influence of small amounts of TBD, *p*-toluenesulfonic acid (pTsOH) or dibutyltinlaurate (DBTL) on the exchange reactions in normally catalyst-free vinylogous urethane vitrimers. By adding these catalysts, the viscoelastic properties could be adjusted over multiple orders of magnitude. Each catalyst lead to a different activation energy due to various exchange mechanism. In case of a catalyst-free system or the addition of a Brønsted acid, the transamination proceeded via a protic pathway, whereas the addition of strong bases result in inhibition of the protic pathway and the manifestation of a new exchange mechanism with a higher energy barrier.[274] Moreover, neighboring groups and supramolecular interactions can influence the exchange reactions in vitrimers.[18]

## STATE-OF-THE-ART

In respect to 4D printing of vitrimeric materials, there have been only a few studies published yet. Shi et al. printed thermosetting epoxy inks via direct ink writing (DIW) at elevated temperatures to obtain complex 3D structures. By dissolving the printed part in ethylene glycol in a sealed container at high temperatures, the ink was recycled and used for further printing processes. They were able to print the same material for four times without losing printability and demonstrated pressure-free self-healing of printed parts.[275] The group of C. Bowman investigated a thiol-ene photopolymer for photolithographic applications which can be recycled and repolymerized owing to its thiol-thioester exchange reactions.[276] Furthermore, they synthesized another thiol-ene photopolymer with higher glass transition temperature for nanoimprinting experiments. The photopolymer featured vitrimeric behavior based on transesterification reactions and remolding or rather multiple patterning of the same material was enabled.[15] The same group also developed a bistable switchable material by the addition of a photobase/photoacid to the photocurable resin. They coupled thiol-thioester exchange with photolabile reagents as catalysts to achieve permanent on demand phase transitions (fluid to solid and vice versa) with nearly perfect spatiotemporal control. Complex, multi-step molding processes and on-demand recycling could be observed with this material.[277] Yang *et al.* performed light induced transesterification in liquid crystalline vitrimers with dispersed carbon nanotubes to enable the generation of dynamic 3D structures out of a flat film upon light exposure. The formed 3D objects could be modified on demand, restored from distortion, repaired, in situ self-healed, assembled to more sophisticated structures, reconfigured and recycled, even at extremely low temperatures (-130 °C).[278] Lastly, Zhang and co-workers fabricated reprocessable thermosets for 3D printing via DLP. They synthesized an acrylic resin in the presence of  $Zn(acac)_2$ , which featured high mechanical and thermal resistance and can be printed with high resolution. Based on the transesterification reaction, reprocessing, recycling and self-healing of the material was feasible.[279]

## METHODOLOGY

On the one hand, parts of this thesis were done by theoretical literature research, but on the other hand, most of the results were accomplished by experimental work. The experimental work comprises organic synthesis, followed by purification methods, such as liquid-liquid extraction, filtration and column chromatography, photo-induced network formation and chemical, thermal, optical and mechanical characterization. The developed resins were used for different manufacturing techniques such as photo-patterning, nanoimprint lithography and digital-light processing 3D printing.

### *Chemical Characterization*

The synthesized monomers/polymers were characterized by using NMR- (nuclear magnetic resonance-), IR- (infrared-) and UV/Vis-spectroscopy to determine their chemical structures, curing performance and absorbance behavior. To characterize the wettability behavior of the prepared photo-curable surfaces, static and dynamic contact angle measurements with water droplets were carried out.

### *Thermal Characterization*

The thermal characteristics such as glass transition temperature and decomposition temperature of the prepared networks were determined by using DSC (differential scanning calorimetry) and TGA (thermogravimetric analysis) measurements, respectively.

### *Optical Characterization*

To observe the surface structures of 3D-printed objects optical microscopy was used, while the nanoimprinted surfaces were characterized by AFM (atomic force microscopy) and SEM (scanning electron microscopy) measurements.

### *Mechanical Characterization*

The mechanical parameters, such as maximum strain/stress, were determined by tensile tests. To obtain the stress-relaxation behavior of the networks and the viscosity of the resins, various rheometer measurements were performed.

## SUMMARY

The present work highlights various strategies to enhance the functionality of photopolymers. By introducing photo-reactive moieties or dynamic covalent bonds into the photopolymer network, smart materials with switchable properties were obtained. In combination with innovative processing techniques such as 3D printing and nanoimprint lithography, advanced polymer devices and functional 3D structures were realized.

Bi-functional alkynes bearing ortho-nitrobenzyl ester linkages were successfully synthesized and crosslinked with multifunctional thiols by visible light exposure. Via asymmetrical irradiation of the polymer surface with UV-light, polar groups were generated, due to photocleavage reactions of the chromophores and photooxidation upon prolonged UV exposure in air. The wettability increased with the exposure dose, and a gradient surface with static water contact angles ranging from 97 to 19 ° was prepared. By introducing the wettability gradient in wedge-shaped patterns, an additional Laplace pressure gradient was inscribed, and the high starting hysteresis was overcome to transport a water droplet over a reasonable distance (10 mm). Based on the high adhesion of the polymeric surface, the droplet could be moved in a controlled way, even on an inclined surface (20 °) or on an upside down turned surface, which hasn't been reported before (Rossegger *et al.*, *Polym. Chem.*, **2019**, *10*, 1882-1893).

The directional movement of a water droplet was further enhanced (over 20 mm) by applying nanoimprint lithography for additional surface texture changes. To generate highly hydrophobic surfaces (static water contact angle around 140 °), photo-reactive thiol-acrylate resins consisting of *o*-nitrobenzyl alcohol moieties with terminal acrylate groups, multi-functional thiols and a fluorinated methacrylate monomer were patterned via visible light assisted nanoimprint lithography. Subsequent irradiation of the microstructures with UV-light under air resulted again in the localized formation of polar groups and erosion of the needle-like microstructures until fully wettable surfaces (static water contact angle of 7 °) were obtained. On linear shaped gradients the directed transport over 14 mm was feasible, whereas an additional Laplace-pressure gradient lead

## SUMMARY

to an increased transport over 22 mm. This is the largest distance reported to date (Rossegger *et al. Polym. Chem.*, **2020**, *11*, 3125-3135)

Along with the introduction of photocleavable chromophores, the present work also demonstrates the introduction of thermally triggered dynamic covalent bonds into 3D printable photopolymers to enable reversible property changes in contrast to the irreversible nature of *ortho*-nitrobenzylesters. One of the most attractive dynamic networks are vitrimers that rely on thermo-responsive exchange reactions such as the transesterification of hydroxyl ester species. Commonly used catalysts suffer from poor solubility and compromise on the curing rate and pot life of photopolymers. In a completely new approach, a mono-functional methacrylate phosphate was introduced as new transesterification catalyst to overcome these limitations. The oligomeric monofunctional methacrylate phosphate features free –OH groups and is a Brønsted acid, which is able to catalyze esterification and transesterification reactions. For the first time, thiol-acrylate vitrimer systems were developed for prototyping of soft-robotic 3D objects via digital light processing. After photocuring, the dynamic networks rapidly underwent thermally induced rearrangement reactions. The dynamic exchange reactions endowed the photopolymer with triple-shape memory and thermal mendability, which was demonstrated by reshaping and self-healing experiments, respectively (Rossegger *et al., Polym. Chem.*, **2021**, *12*, 639-644).

Furthermore, the excellent solubility of the new catalyst in numerous photo-reactive resins was exploited to extend the toolbox of acrylate monomers for 3D printing of vitrimers, since up to now the variety is limited due to solubility and stability issues. A series of acrylate based dynamic networks was prepared and their mechanical performance was conveniently adjusted by the chemical functionality and structure of the monomers. Rheometer studies demonstrated that the stress relaxation rate decreases with increasing crosslink density and glass transition temperature of the photopolymer networks. By increasing the amount of catalyst, the relaxation rate was significantly increased. Via digital light processing 3D objects with feature sizes around 50  $\mu\text{m}$  were prepared and the dynamic nature of the network enabled thermally triggered shape-memory and

## SUMMARY

mendability, even of highly crosslinked networks (Rossegger *et al.*, *Polymers*, **2021**, 221, 123631).

In a last step, light as well as temperature were both used as external stimuli to locally control the dynamic exchange reactions in 3D printed parts by using a photoacid generator as latent transesterification catalyst. Triphenylsulfonium salts form strong Brønsted acids upon UV exposure (365 nm), which are able to catalyze transesterification reactions at elevated temperatures. The photolabile catalyst was introduced into visible light (405 nm) curable thiol-acrylate resins, and by increasing the UV-A exposure dose or the photoacid generator content, the stress relaxation reactions were accelerated. Based on the orthogonality between the curing reaction and the activation of the catalyst, dynamic exchange reactions were selectively started in the 3D printed objects by using a dual wavelength 3D printer (operating at 405 nm and 365 nm). Soft active devices with locally controllable topology arrangements above the  $T_v$  were fabricated for the first time (Rossegger *et al.*, *nature communications*, **2021** under revision).



### OUTLOOK

Advancing from 2.5D patterning, the developed concept of photo-induced polarity changes has the potential to be transferred to additively manufactured structures. This enables a controlled movement of water or other droplets on surfaces with extensive topology and adjusted surface polarity. Based on this work, further studies in respect to directed water droplet movements on 3D printed shape memory structures are envisaged, which could be promising functional materials for future microfluidics or lab on a chip applications, and facilitate reversible polarity switching.

Additional work in the field of 3D printable vitrimers should deal with determining the exact reaction mechanism behind the phosphate catalyzed exchange reactions. It would be interesting to tailor network properties and structure of the catalyst to prepare photopolymer networks, which are healable, re-shapeable and reprocessbale at lower temperatures. In respect to industrialization of these concepts, limitations such as the adjustment between self-healing efficiency and mechanical properties, and the usually long relaxation times of vitrimers in contrast to the fast processing of commercially available thermoplastics, have to be addressed.

## References

1. Seymour, R.B.; Deanin, R.D. History of Polymer Composites. *VNU Science Press* **1987**, 319–320.
2. Crivello, J.V.; Reichmanis, E. Photopolymer Materials and Processes for Advanced Technologies. *Chem. Mater.* **2014**, *26*, 533–548, doi:10.1021/cm402262g.
3. Kotikian, A.; Truby, R.L.; Boley, J.W.; White, T.J.; Lewis, J.A. 3D Printing of Liquid Crystal Elastomeric Actuators with Spatially Programed Nematic Order. *Adv. Mater.* **2018**, *30*, doi:10.1002/adma.201706164.
4. Ge, Q.; Dunn, C.K.; Qi, H.J.; Dunn, M.L. Active origami by 4D printing. *Smart Mater. Struct.* **2014**, *23*, 94007, doi:10.1088/0964-1726/23/9/094007.
5. Ge, Q.; Sakhaei, A.H.; Lee, H.; Dunn, C.K.; Fang, N.X.; Dunn, M.L. Multimaterial 4D Printing with Tailorable Shape Memory Polymers. *Sci. Rep.* **2016**, *6*, 31110, doi:10.1038/srep31110.
6. Nadgorny, M.; Xiao, Z.; Chen, C.; Connal, L.A. Three-Dimensional Printing of pH-Responsive and Functional Polymers on an Affordable Desktop Printer. *ACS Appl. Mater. Interfaces* **2016**, *8*, 28946–28954, doi:10.1021/acsami.6b07388.
7. Gladman, A.S.; Matsumoto, E.A.; Nuzzo, R.G.; Mahadevan, L.; Lewis, J.A. Biomimetic 4D printing. *Nat. Mater.* **2016**, *15*, 413–418, doi:10.1038/nmat4544.
8. Raviv, D.; Zhao, W.; McKnelly, C.; Papadopoulou, A.; Kadambi, A.; Shi, B.; Hirsch, S.; Dikovsky, D.; Zyracki, M.; Olguin, C.; et al. Active printed materials for complex self-evolving deformations. *Sci. Rep.* **2014**, *4*, 7422, doi:10.1038/srep07422.
9. Gao, S.; Tang, G.; Hua, D.; Xiong, R.; Han, J.; Jiang, S.; Zhang, Q.; Huang, C. Stimuli-responsive bio-based polymeric systems and their applications. *J. Mater. Chem. B* **2019**, *7*, 709–729, doi:10.1039/c8tb02491j.
10. Jochum, F.D.; Theato, P. Temperature- and light-responsive smart polymer materials. *Chem. Soc. Rev.* **2013**, *42*, 7468–7483, doi:10.1039/c2cs35191a.
11. Roth, P.J.; Lowe, A.B. Stimulus-responsive polymers. *Polym. Chem.* **2017**, *8*, 10–11, doi:10.1039/C6PY90169G.

## REFERENCES

12. Roy, D.; Cambre, J.N.; Sumerlin, B.S. Future perspectives and recent advances in stimuli-responsive materials. *Progress in Polymer Science* **2010**, *35*, 278–301, doi:10.1016/j.progpolymsci.2009.10.008.
13. Theato, P.; Sumerlin, B.S.; O'Reilly, R.K.; Epps, T.H. Stimuli responsive materials. *Chem. Soc. Rev.* **2013**, *42*, 7055–7056, doi:10.1039/c3cs90057f.
14. Wenzel, R.N. Resistance of solid surfaces to wetting by water. *Industrial and engineering chemistry* **1936**, *28*, 8, 988–994.
15. Lyon, G.B.; Cox, L.M.; Goodrich, J.T.; Baranek, A.D.; Ding, Y.; Bowman, C.N. Remoldable Thiol–Ene Vitrimers for Photopatterning and Nanoimprint Lithography. *Macromolecules* **2016**, *49*, 8905–8913, doi:10.1021/acs.macromol.6b01281.
16. Hoyle, C.E.; Lee, T.Y.; Roper, T. Thiol-enes: Chemistry of the past with promise for the future. *J. Polym. Sci. A Polym. Chem.* **2004**, *42*, 5301–5338, doi:10.1002/pola.20366.
17. Bazi, F.; El Badaoui, H.; Sokori, S.; Tamani, S.; Hamza, M.; Boulaajaj, S.; Sebti, S. Transesterification of Methylbenzoate with Alcohols Catalyzed by Natural Phosphate. *Synthetic Communications* **2006**, *36*, 1585–1592, doi:10.1080/00397910600591508.
18. Guerre, M.; Taplan, C.; Winne, J.M.; Du Prez, F.E. Vitrimers: directing chemical reactivity to control material properties. *Chem. Sci.* **2020**, *11*, 4855–4870, doi:10.1039/D0SC01069C.
19. Self, J.L.; Dolinski, N.D.; Zayas, M.S.; Read de Alaniz, J.; Bates, C.M. Brønsted-Acid-Catalyzed Exchange in Polyester Dynamic Covalent Networks. *ACS Macro Lett.* **2018**, *7*, 817–821, doi:10.1021/acsmacrolett.8b00370.
20. Crivello, J.V. The discovery and development of onium salt cationic photoinitiators. *Journal of Polymer Science: Part A: Polymer Chemistry* **1999**, *37*, 4241–4254.
21. J.-P. Fouassier. *Radiation Curing in Polymer Science and Technology: Vol 1: Fundamentals and Methods*, 1st ed.; Springer, 1993.
22. Chatani, S.; Kloxin, C.J.; Bowman, C.N. The power of light in polymer science: photochemical processes to manipulate polymer formation, structure, and properties. *Polym. Chem.* **2014**, *5*, 2187–2201, doi:10.1039/C3PY01334K.

## REFERENCES

23. Cabane, E.; Zhang, X.; Langowska, K.; Palivan, C.G.; Meier, W. Stimuli-responsive polymers and their applications in nanomedicine. *Biointerphases* **2012**, *7*, 9, doi:10.1007/s13758-011-0009-3.
24. Chan, B.P. Biomedical applications of photochemistry. *Tissue Eng. Part B Rev.* **2010**, *16*, 509–522, doi:10.1089/ten.TEB.2009.0797.
25. Wardle, B. *Principles and Applications of Photochemistry*; Wiley, 2009.
26. Mäntele, W.; Deniz, E. UV-VIS absorption spectroscopy: Lambert-Beer reloaded. *Spectrochim. Acta A Mol. Biomol. Spectrosc.* **2017**, *173*, 965–968, doi:10.1016/j.saa.2016.09.037.
27. Schnabel W. *Polymers and light: Fundamentals and technical applications*; Wiley-VCH: Weinheim, 2007.
28. Montalti, M.; Credi, A.; Prodi, L.; Gandolfi, M.T. *Handbook of photochemistry*, 3rd ed.; CRC Press, 2006.
29. Kagan J. *Organic Photochemistry: Principles and Applications*; London, Academic Press, 1993.
30. Kaiser, S.; Radl, S.V.; Manhart, J.; Ayalur-Karunakaran, S.; Griesser, T.; Moser, A.; Ganser, C.; Teichert, C.; Kern, W.; Schlögl, S. Switching "on" and "off" the adhesion in stimuli-responsive elastomers. *Soft Matter* **2018**, *14*, 2547–2559, doi:10.1039/c8sm00284c.
31. Cazin, I.; Rossegger, E.; La Guedes de Cruz, G.; Griesser, T.; Schlögl, S. Recent Advances in Functional Polymers Containing Coumarin Chromophores. *Polymers (Basel)* **2020**, *13*, doi:10.3390/polym13010056.
32. Koch, H.; Laschewsky, A.; Ringsdorf, H.; Teng, K. Photodimerization and photopolymerization of amphiphilic cinnamic acid derivatives in oriented monolayers, vesicles and solution. *Makromol. Chem.* **1986**, *187*, 1843 - 1853.
33. Ishikawa, N.; Furutani, M.; Arimitsu, K. Adhesive Materials Utilizing a Thymine–Adenine Interaction and Thymine Photodimerization. *ACS Macro Lett.* **2015**, *4*, 741–744, doi:10.1021/acsmacrolett.5b00359.

## REFERENCES

34. Yagci, Y.; Jockusch, S.; Turro, N.J. Photoinitiated Polymerization: Advances, Challenges, and Opportunities. *Macromolecules* **2010**, *43*, 6245–6260, doi:10.1021/ma1007545.
35. Crivello, J.V. Cationic polymerization; Iodonium and sulfonium salt photoinitiators. *Advances in Polymer Science* **1984**, *62*, 3–48.
36. Ito, H. Chemical Amplification Resists for Microlithography. *Adv. Polym. Sci* **2005**, *172*, 37–245, doi:10.1007/b97574.
37. Crivello, J.V.; Lam, J.H.W. Photoinitiated cationic polymerization with triarylsulfonium salts. *Journal of Polymer Science: Polymer Chemistry Edition* **1979**, *17*, 977–999.
38. Sangermano, M.; Roppolo, I.; Chiappone, A. New Horizons in Cationic Photopolymerization. *Polymers (Basel)* **2018**, *10*, 1–8, doi:10.3390/polym10020136.
39. Crivello, J.V. Redox initiated cationic polymerization. *J. Polym. Sci. A Polym. Chem.* **2009**, *47*, 1825–1835, doi:10.1002/pola.23284.
40. Crivello, J.V.; Lam, J.H.W. Dye-sensitized photoinitiated cationic polymerization. *Journal of Polymer Science: Polymer Chemistry Edition* **1978**, *16*, 2441–2451.
41. Sangermano, M.; Razza, N.; Crivello, J.V. Cationic UV-Curing: Technology and Applications. *Macromol. Mater. Eng.* **2014**, *299*, 775–793, doi:10.1002/mame.201300349.
42. Suyama, K.; Shirai, M. Photobase generators: Recent progress and application trend in polymer systems. *Progress in Polymer Science* **2009**, *34*, 194–209, doi:10.1016/j.progpolymsci.2008.08.005.
43. Arimitsu, K.; Endo, R. Application to Photoreactive Materials of Photochemical Generation of Superbases with High Efficiency Based on Photodecarboxylation Reactions. *Chem. Mater.* **2013**, *25*, 4461–4463, doi:10.1021/cm4022485.
44. Dietliker, K.; Jung, T.; Studer, K.; Benkhoff, J. Photolabile Tertiary Amines – A New Technology Platform for Radiation Curing. *CHIMIA* **2007**, *61*, 655–660, doi:10.2533/chimia.2007.655.
45. Dong, X.; Hu, P.; Zhu, G.; Li, Z.; Liu, R.; Liu, X. Thioxanthone acetic acid ammonium salts: highly efficient photobase generators based on photodecarboxylation. *RSC Adv.* **2015**, *5*, 53342–53348, doi:10.1039/C5RA09314G.

## REFERENCES

46. Salmi, H.; Allonas, X.; Ley, C.; Defoin, A.; Ak, A. Quaternary ammonium salts of phenylglyoxylic acid as photobase generators for thiol-promoted epoxide photopolymerization. *Polym. Chem.* **2014**, *5*, 6577–6583, doi:10.1039/C4PY00927D.
47. Romano, A.; Roppolo, I.; Giebler, M.; Dietliker, K.; Možina, Š.; Šket, P.; Mühlbacher, I.; Schlögl, S.; Sangermano, M. Stimuli-responsive thiol-epoxy networks with photo-switchable bulk and surface properties. *RSC Adv.* **2018**, *8*, 41904–41914, doi:10.1039/C8RA08937J.
48. Hageman, H.J. Photoinitiators for free radical polymerization. *Progress in Organic Coatings* **1985**, *13*, 123–150.
49. Sumiyoshi, T.; Schnabel, W. On the reactivity of phosphonyl radicals towards olefinic compounds. *Makromol. Chem.* **1985**, *186*, 1811–1823.
50. Davidson, R.S. The Chemistry of Excited Complexes: a Survey of Reactions. *Advances in Physical Organic Chemistry Volume 19*; Elsevier, 1983; pp 1–130, ISBN 9780120335190.
51. Hutchison, J.; Lambert, M.C.; Ledwith, A. Role of semi-pinacol radicals in the benzophenone-photoinitiated polymerization of methyl methacrylate. *Polymer* **1973**, *14*, 250–254.
52. Yağci, Y.; Aydoğan, A.C.; Sizgek, A.E. Influence of the Cationic Salt on Free Radical Polymerization Initiated by Phenylazotriphenylmethane. *Journal of Polymer Science: Polymer Letters Edition* **1984**, *22*, 2, 103–106.
53. Dadashi-Silab, S.; Aydogan, C.; Yagci, Y. Shining a light on an adaptable photoinitiator: advances in photopolymerizations initiated by thioxanthenes. *Polym. Chem.* **2015**, *6*, 6595–6615, doi:10.1039/C5PY01004G.
54. Allen, N.S. Photoinitiators for UV and visible curing of coatings" mechanisms and properties. *Journal of Photochemistry and Photobiology A: Chemistry* **1996**, *100*, 101–107.
55. Moszner, N.; Fischer, U.K.; Ganster, B.; Liska, R.; Rheinberger, V. Benzoyl germanium derivatives as novel visible light photoinitiators for dental materials. *Dent. Mater.* **2008**, *24*, 901–907, doi:10.1016/j.dental.2007.11.004.
56. Braun, D. Origins and Development of Initiation of Free Radical Polymerization Processes. *International Journal of Polymer Science* **2009**, *2009*, 1–10, doi:10.1155/2009/893234.

## REFERENCES

57. Wu, J.; Zhao, Z.; Hamel, C.M.; Mu, X.; Kuang, X.; Guo, Z.; Qi, H.J. Evolution of material properties during free radical photopolymerization. *Journal of the Mechanics and Physics of Solids* **2018**, *112*, 25–49, doi:10.1016/j.jmps.2017.11.018.
58. Kloosterboer, J.G. Network formation by chain crosslinking photopolymerization and its applications in electronics. *Electronic Applications. Advances in Polymer Science* **1988**, *84*, 1–61, doi:10.1007/BFb0025902.
59. Goodner, M.D.; Bowman, C.N. Modeling Primary Radical Termination and Its Effects on Autoacceleration in Photopolymerization Kinetics. *Macromolecules* **1999**, *32*, 20, 6552–6559, doi:10.1021/ma9901947.
60. Dusek, K.; Spevacek, J. Cyclization in vinyl-divinyl copolymerization. *Polymer* **1980**, *21*, 750–756.
61. Bowman, C.N.; Kloxin, C.J. Toward an enhanced understanding and implementation of photopolymerization reactions. *AIChE J.* **2008**, *54*, 2775–2795, doi:10.1002/aic.11678.
62. Miller, G.A.; Gou, L.; Narayanan, V.; Scranton, A.B. Modeling of photobleaching for the photoinitiation of thick polymerization systems. *Journal of Polymer Science: Part A: Polymer Chemistry* **2002**, *40*, 793–808.
63. Russell, G.T.; Gilbert, R.G.; Napper, D.H. Chain-Length-Dependent Termination Rate Processes in Free-Radical Polymerizations. 1. Theory. *Macromolecules* **1992**, *25*, 2459–2469.
64. O'Neil, G.A.; Torkelson, J.M. Modeling Insight into the Diffusion-Limited Cause of the Gel Effect in Free Radical Polymerization. *Macromolecules* **1999**, *32*, 411–422, doi:10.1021/ma9811324.
65. Russell, G.T.; Napper, D.H.; Gilbert, R.G. Termination in Free-Radical Polymerizing Systems at High Conversion. *Macromolecules* **1988**, *21*, 2133–2140.
66. Trommsdorff, E.; Kohle, H.; Lagally, P. Zur Polymerisation des Methacrylsäuremethylesters. *Makromol. Chem.* **1948**, *1*, 169–199.
67. Maillard, B.; Ingold, K.U.; Scaiano, J.C. Rate Constants for the Reactions of Free Radicals with Oxygen in Solution. *J. Am. Chem. Soc.* **1983**, *105*, 15, 5099–5105.
68. O'Brien, A.K.; Bowman, C.N. Impact of Oxygen on Photopolymerization Kinetics and Polymer Structure. *Macromolecules* **2006**, *39*, 2501–2506, doi:10.1021/ma051863l.

## REFERENCES

69. Shawkat, E.S.; Shortall, A.C.; Addison, O.; Palin, W.M. Oxygen inhibition and incremental layer bond strengths of resin composites. *Dental Materials* **2009**, *25*, 1338–1346.
70. Miller, C.W.; Hoyle, C.E.; Jönsson, S.; Nason, C.; Lee, T.Y.; Kuang, W.F.; Viswanathan, K. N -Vinylamides and Reduction of Oxygen Inhibition in Photopolymerization of Simple Acrylate Formulations. In *Photoinitiated Polymerization*; Belfield, K.D., Crivello, J.V., Eds.; American Chemical Society: Washington, DC, 2003; pp 2–14, ISBN 0-8412-3813-8.
71. Berchtold, K.A.; Hacıoğlu, B.; Lovell, L.; Nie, J.; Bowman, C.N. Using Changes in Initiation and Chain Transfer Rates To Probe the Kinetics of Cross-Linking Photopolymerizations: Effects of Chain Length Dependent Termination. *Macromolecules* **2001**, *34*, 5103–5111, doi:10.1021/ma0019095.
72. Lu, H.; Lovell, L.G.; Bowman, C.N. Exploiting the Heterogeneity of Cross-Linked Photopolymers To Create High- Tg Polymers from Polymerizations Performed at Ambient Conditions. *Macromolecules* **2001**, *34*, 8021–8025, doi:10.1021/ma010542g.
73. Kannurpatti, A.R.; Bowman, C.N. Structural Evolution of Dimethacrylate Networks Studied by Dielectric Spectroscopy. *Macromolecules* **1998**, *31*, 3311–3316.
74. Shah, P.K.; Stansbury, J.W.; Bowman, C.N. Application of an Addition-Fragmentation-Chain Transfer Monomer in Di(meth)acrylate Network Formation to Reduce Polymerization Shrinkage Stress. *Polym. Chem.* **2017**, *8*, 4339–4351, doi:10.1039/C7PY00702G.
75. Karalekas, D.; Aggelopoulos, A. Study of shrinkage strains in a stereolithography cured acrylic photopolymer resin. *Journal of Materials Processing Technology* **2003**, *136*, 146–150, doi:10.1016/S0924-0136(03)00028-1.
76. Ye, S.; Cramer, N.B.; Smith, I.R.; Voigt, K.R.; Bowman, C.N. Reaction Kinetics and Reduced Shrinkage Stress of Thiol-Yne-Methacrylate and Thiol-Yne-Acrylate Ternary Systems. *Macromolecules* **2011**, *44*, 9084–9090, doi:10.1021/ma2018809.
77. Lu, H.; Stansbury, J.W.; Bowman, C.N. Impact of curing protocol on conversion and shrinkage stress. *J. Dent. Res.* **2005**, *84*, 822–826, doi:10.1177/154405910508400908.



## REFERENCES

78. Khudyakov, I.V.; Legg, J.C.; Purvis, M.B.; Overton, B.J. Kinetics of Photopolymerization of Acrylates with Functionality of 1–6. *Ind. Eng. Chem. Res.* **1999**, *38*, 3353–3359, doi:10.1021/ie990306i.
79. Moussa, K.; Decker, C. Light-induced polymerization of new highly reactive acrylic monomers. *Journal of Polymer Science: Part A: Polymer Chemistry* **1993**, *31*, 2197–2203.
80. Yilmaz, G.; Yagci, Y. Light-induced step-growth polymerization. *Progress in Polymer Science* **2020**, *100*, 101178, doi:10.1016/j.progpolymsci.2019.101178.
81. Colebatch, A.L.; Weller, A.S. Amine-Borane Dehydropolymerization: Challenges and Opportunities. *Chemistry* **2019**, *25*, 1379–1390, doi:10.1002/chem.201804592.
82. Morgan, C.R.; Magnotta, F.; Ketley, D. Thiol/ene photocurable polymers. *Journal of Polymer Science: Polymer Chemistry Edition* **1977**, *15*, 627–645.
83. Crespy, D.; Bozonnet, M.; Meier, M. 100 years of bakelite, the material of a 1000 uses. *Angew. Chem. Int. Ed Engl.* **2008**, *47*, 3322–3328, doi:10.1002/anie.200704281.
84. Kumbaraci, V.; Talinli, N.; Yagci, Y. Photoinduced Synthesis of Oligoesters. *Macromolecules* **2006**, *39*, 6031–6035, doi:10.1021/ma0607721.
85. Hurrle, S.; Goldmann, A.S.; Gliemann, H.; Mutlu, H.; Barner-Kowollik, C. Light-Induced Step-Growth Polymerization of AB-Type Photo-Monomers at Ambient Temperature. *ACS Macro Lett.* **2018**, *7*, 201–207, doi:10.1021/acsmacrolett.7b01001.
86. Kolb, H.C.; Finn, M.G.; Sharpless, K.B. Click Chemistry: Diverse Chemical Function from a Few Good Reactions. *Angew. Chem. Int. Ed.* **2001**, *40*, 2004–2021.
87. Hoyle, C.E.; Bowman, C.N. Thiol-ene click chemistry. *Angew. Chem. Int. Ed Engl.* **2010**, *49*, 1540–1573, doi:10.1002/anie.200903924.
88. Fournier, D.; Hoogenboom, R.; Schubert, U.S. Clicking polymers: a straightforward approach to novel macromolecular architectures. *Chem. Soc. Rev.* **2007**, *36*, 1369–1380, doi:10.1039/b700809k.
89. Posner, T. Beiträge zur Kenntniss der ungesättigten Verbindungen. II. Ueber die Addition von Mercaptanen an ungesättigte Kohlenwasserstoffe. *EurJIC* **1905**, *38*, 1, 646–657.
90. Lowe, A.B. Thiol-ene “click” reactions and recent applications in polymer and materials synthesis. *Polym. Chem.* **2010**, *1*, 17–36, doi:10.1039/B9PY00216B.

## REFERENCES

91. Hoyle, C.E.; Lowe, A.B.; Bowman, C.N. Thiol-click chemistry: a multifaceted toolbox for small molecule and polymer synthesis. *Chem. Soc. Rev.* **2010**, *39*, 1355–1387, doi:10.1039/b901979k.
92. Lu, H.; Carioscia, J.A.; Stansbury, J.W.; Bowman, C.N. Investigations of step-growth thiol-ene polymerizations for novel dental restoratives. *Dent. Mater.* **2005**, *21*, 1129–1136, doi:10.1016/j.dental.2005.04.001.
93. Cramer, N.B.; Davies, T.; O'Brien, A.K.; Bowman, C.N. Mechanism and Modeling of a Thiol–Ene Photopolymerization. *Macromolecules* **2003**, *36*, 4631–4636, doi:10.1021/ma034072x.
94. Roper, T.M.; Lee, T.Y.; Guymon, C.A.; Hoyle, C.E. In Situ Characterization of Photopolymerizable Systems Using a Thin-Film Calorimeter. *Macromolecules* **2005**, *38*, 10109–10116, doi:10.1021/ma051586i.
95. Claudino, M.; Johansson, M.; Jonsson, M. Thiol–ene coupling of 1,2-disubstituted alkene monomers: The kinetic effect of cis/trans-isomer structures. *European Polymer Journal* **2010**, *46*, 2321–2332, doi:10.1016/j.eurpolymj.2010.10.001.
96. Meissner, M.; Thompson, H.W. The photolysis of mercaptans. *Trans. Faraday Soc.* **1938**, *34*, 1238–1239.
97. Cramer, N.B.; Scott, J.P.; Bowman, C.N. Photopolymerizations of Thiol–Ene Polymers without Photoinitiators. *Macromolecules* **2002**, *35*, 5361–5365, doi:10.1021/ma0200672.
98. Cramer, N.B.; Bowman, C.N. CHAPTER 1. Thiol-ene and Thiol-yne Chemistry in Ideal Network Synthesis. In *Thiol-X Chemistries in Polymer and Materials Science*; Lowe, A., Bowman, C., Eds.; Royal Society of Chemistry: Cambridge, 2013; pp 1–27, ISBN 978-1-84973-660-2.
99. Blasco, E.; Wegener, M.; Barner-Kowollik, C. Photochemically Driven Polymeric Network Formation: Synthesis and Applications. *Adv. Mater.* **2017**, *29*, doi:10.1002/adma.201604005.
100. Klemm, E.; Gorski, U. Untersuchungen zur thioladdition an polybutadiene. *Die Angewandte Makromolekulare Chemie* **1993**, *201*, 187–193.

## REFERENCES

101. Esfandiari, P.; Ligon, S.C.; Lagref, J.J.; Frantz, R.; Cherkaoui, Z.; Liska, R. Efficient stabilization of thiol-ene formulations in radical photopolymerization. *J. Polym. Sci. Part A: Polym. Chem.* **2013**, *51*, 4261–4266, doi:10.1002/pola.26848.
102. Fairbanks, B.D.; Scott, T.F.; Kloxin, C.J.; Anseth, K.S.; Bowman, C.N. Thiol-Yne Photopolymerizations: Novel Mechanism, Kinetics, and Step-Growth Formation of Highly Cross-Linked Networks. *Macromolecules* **2009**, *42*, 211–217, doi:10.1021/ma801903w.
103. Carioscia, J.A.; Schneidewind, L.; O'Brien, C.; Ely, R.; Feeser, C.; Cramer, N.; Bowman, C.N. Thiol–norbornene materials: Approaches to develop highTg thiol–ene polymers. *J. Polym. Sci. A Polym. Chem.* **2007**, *45*, 5686–5696, doi:10.1002/pola.22318.
104. Li, Q.; Zhou, H.; Wicks, D.A.; Hoyle, C.E. Thiourethane-based thiol-ene highTg networks: Preparation, thermal, mechanical, and physical properties. *J. Polym. Sci. A Polym. Chem.* **2007**, *45*, 5103–5111, doi:10.1002/pola.22252.
105. Carioscia, J.A.; Stansbury, J.W.; Bowman, C.N. Evaluation and Control of Thiol-ene/Thiol-epoxy Hybrid Networks. *Polymer* **2007**, *48*, 1526–1532, doi:10.1016/j.polymer.2007.01.044.
106. Oesterreicher, A.; Gorsche, C.; Ayalur-Karunakaran, S.; Moser, A.; Edler, M.; Pinter, G.; Schlögl, S.; Liska, R.; Griesser, T. Exploring Network Formation of Tough and Biocompatible Thiol-yne Based Photopolymers. *Macromol. Rapid Commun.* **2016**, *37*, 1701–1706, doi:10.1002/marc.201600369.
107. Oesterreicher, A.; Wiener, J.; Roth, M.; Moser, A.; Gmeiner, R.; Edler, M.; Pinter, G.; Griesser, T. Tough and degradable photopolymers derived from alkyne monomers for 3D printing of biomedical materials. *Polym. Chem.* **2016**, *7*, 5169–5180, doi:10.1039/C6PY01132B.
108. Fairbanks, B.D.; Sims, E.A.; Anseth, K.S.; Bowman, C.N. Reaction Rates and Mechanisms for Radical, Photoinitiated Addition of Thiols to Alkynes, and Implications for Thiol–Yne Photopolymerizations and Click Reactions. *Macromolecules* **2010**, *43*, 4113–4119, doi:10.1021/ma1002968.

## REFERENCES

109. Lowe, A.B.; Hoyle, C.E.; Bowman, C.N. Thiol-yne click chemistry: A powerful and versatile methodology for materials synthesis. *J. Mater. Chem.* **2010**, *20*, 4745, doi:10.1039/b917102a.
110. Hoogenboom, R. Thiol-yne chemistry: a powerful tool for creating highly functional materials. *Angew. Chem. Int. Ed Engl.* **2010**, *49*, 3415–3417, doi:10.1002/anie.201000401.
111. Bader, H.; Cross, L.C.; Helbron, I.; Jones, E.R.H. Researches on Acetylenic Compounds. Part XVIII. The Addition of Thiolacetic Acid to Acetylenic Hydrocarbons. The Conversion of Monosubstituted Acetylenes into Aldehydes and 1:2-Dithiols. *J. Chem. Soc.* **1949**, *132*, 619–623.
112. Roppolo, I.; Frascella, F.; Gastaldi, M.; Castellino, M.; Ciubini, B.; Barolo, C.; Scaltrito, L.; Nicosia, C.; Zanetti, M.; Chiappone, A. Thiol-yne chemistry for 3D printing: exploiting an off-stoichiometric route for selective functionalization of 3D objects. *Polym. Chem.* **2019**, *10*, 5950–5958, doi:10.1039/C9PY00962K.
113. Sahin, M.; Ayalur-Karunakaran, S.; Manhart, J.; Wolfahrt, M.; Kern, W.; Schlögl, S. Thiol-Ene versus Binary Thiol-Acrylate Chemistry: Material Properties and Network Characteristics of Photopolymers. *Adv. Eng. Mater.* **2017**, *19*, 1600620, doi:10.1002/adem.201600620.
114. O'Brien, A.K.; Cramer, N.B.; Bowman, C.N. Oxygen inhibition in thiol-acrylate photopolymerizations. *J. Polym. Sci. A Polym. Chem.* **2006**, *44*, 2007–2014, doi:10.1002/pola.21304.
115. Dickey, M.D.; Collister, E.; Raines, A.; Tsiartas, P.; Holcombe, T.; Sreenivasan, S.V.; Bonnacaze, R.T.; Willson, C.G. Photocurable Pillar Arrays Formed via Electrohydrodynamic Instabilities. *Chem. Mater.* **2006**, *18*, 2043–2049, doi:10.1021/cm052592w.
116. Rydholm, A.E.; Bowman, C.N.; Anseth, K.S. Degradable thiol-acrylate photopolymers: polymerization and degradation behavior of an in situ forming biomaterial. *Biomaterials* **2005**, *26*, 4495–4506, doi:10.1016/j.biomaterials.2004.11.046.
117. Roper, T.M.; Kwee, T.; Lee, T.Y.; Guymon, C.A.; Hoyle, C.E. Photopolymerization of pigmented thiol-ene systems. *Polymer* **2004**, *45*, 2921–2929, doi:10.1016/j.polymer.2004.02.038.

## REFERENCES

118. Cramer, N.B.; Bowman, C.N. Kinetics of thiol–ene and thiol–acrylate photopolymerizations with real-time fourier transform infrared. *Journal of Polymer Science: Part A: Polymer Chemistry* **2001**, *39*, 3311–3319.
119. Reddy, S.K.; Cramer, N.B.; Bowman, C.N. Thiol–Vinyl Mechanisms. 2. Kinetic Modeling of Ternary Thiol–Vinyl Photopolymerizations. *Macromolecules* **2006**, *39*, 3681–3687, doi:10.1021/ma0600097.
120. Stepanova, M.; Dew, S. *Nanofabrication: Techniques and principles*; Springer Wien New York: Vienna, 2012.
121. Romano, A.; Roppolo, I.; Rossegger, E.; Schlögl, S.; Sangermano, M. Recent Trends in Applying Ortho-Nitrobenzyl Esters for the Design of Photo-Responsive Polymer Networks. *Materials (Basel)* **2020**, *13*, doi:10.3390/ma13122777.
122. Barltrop, J.A.; Plant, P.J.; Schofield, P. Photosensitive Protective Groups. *Chemical Communications* **1966**, 22.
123. George, M.V.; Scalano, J.C. Photochemistry of o-Nitrobenzaldehyde and Related Studies. *The Journal of Physical Chemistry* **1980**, *84*, 492–495.
124. Bochet, C.G. Photolabile protecting groups and linkers. *J. Chem. Soc., Perkin Trans. 1* **2002**, *2*, 125–142, doi:10.1039/b009522m.
125. Il'ichev, Y.V.; Schwörer, M.A.; Wirz, J. Photochemical reaction mechanisms of 2-nitrobenzyl compounds: methyl ethers and caged ATP. *J. Am. Chem. Soc.* **2004**, *126*, 4581–4595, doi:10.1021/ja039071z.
126. Zhao, H.; Sterner, E.S.; Coughlin, E.B.; Theato, P. o -Nitrobenzyl Alcohol Derivatives: Opportunities in Polymer and Materials Science. *Macromolecules* **2012**, *45*, 1723–1736, doi:10.1021/ma201924h.
127. Zhang, X.; Xi, W.; Gao, G.; Wang, X.; Stansbury, J.W.; Bowman, C.N. o -Nitrobenzyl-Based Photobase Generators: Efficient Photoinitiators for Visible-Light Induced Thiol-Michael Addition Photopolymerization. *ACS Macro Lett.* **2018**, *7*, 852–857, doi:10.1021/acsmacrolett.8b00435.
128. Kretschy, N.; Holik, A.-K.; Somoza, V.; Stengele, K.-P.; Somoza, M.M. Next-Generation o-Nitrobenzyl Photolabile Groups for Light-Directed Chemistry and

## REFERENCES

- Microarray Synthesis. *Angew. Chem. Int. Ed Engl.* **2015**, *54*, 8555–8559, doi:10.1002/anie.201502125.
129. Wöll, D.; Laimgruber, S.; Galetskaya, M.; Smirnova, J.; Pfeleiderer, W.; Heinz, B.; Gilch, P.; Steiner, U.E. On the mechanism of intramolecular sensitization of photocleavage of the 2-(2-nitrophenyl)propoxycarbonyl (NPPOC) protecting group. *J. Am. Chem. Soc.* **2007**, *129*, 12148–12158, doi:10.1021/ja072355p.
130. Wöll, D.; Smirnova, J.; Galetskaya, M.; Prykota, T.; Bühler, J.; Stengele, K.-P.; Pfeleiderer, W.; Steiner, U.E. Intramolecular sensitization of photocleavage of the photolabile 2-(2-nitrophenyl)propoxycarbonyl (NPPOC) protecting group: photoproducts and photokinetics of the release of nucleosides. *Chemistry* **2008**, *14*, 6490–6497, doi:10.1002/chem.200800613.
131. Zeng, X.; Zhou, X.; Wu, S. Red and Near-Infrared Light-Cleavable Polymers. *Macromol. Rapid Commun.* **2018**, *39*, 180034–180049, doi:10.1002/marc.201800034.
132. Lee, G.; Park, Y.I. Lanthanide-Doped Upconversion Nanocarriers for Drug and Gene Delivery. *Nanomaterials (Basel)* **2018**, *8*, doi:10.3390/nano8070511.
133. Petropoulos, C. Synthesis of novel photodegradable poly(o-nitrobenzaldehyde acetal) polymers. *Journal of Polymer Science: Polymer Chemistry Edition* **1977**, *15*, 1637–1644.
134. Klinger, D.; Landfester, K. Dual Stimuli-Responsive Poly(2-hydroxyethyl methacrylate- co -methacrylic acid) Microgels Based on Photo-Cleavable Cross-Linkers: pH-Dependent Swelling and Light-Induced Degradation. *Macromolecules* **2011**, *44*, 9758–9772, doi:10.1021/ma201706r.
135. Kloxin, A.M.; Kasko, A.M.; Salinas, C.N.; Anseth, K.S. Photodegradable hydrogels for dynamic tuning of physical and chemical properties. *Science* **2009**, *324*, 59–63, doi:10.1126/science.1169494.
136. Kloxin, A.M.; Tibbitt, M.W.; Kasko, A.M.; Fairbairn, J.A.; Anseth, K.S. Tunable hydrogels for external manipulation of cellular microenvironments through controlled photodegradation. *Adv. Mater.* **2010**, *22*, 61–66, doi:10.1002/adma.200900917.

## REFERENCES

137. Lunzer, M.; Shi, L.; Andriotis, O.G.; Gruber, P.; Markovic, M.; Thurner, P.J.; Ossipov, D.; Liska, R.; Ovsianikov, A. A Modular Approach to Sensitized Two-Photon Patterning of Photodegradable Hydrogels. *Angew. Chem. Int. Ed Engl.* **2018**, *57*, 15122–15127, doi:10.1002/anie.201808908.
138. Yang, F.; Cao, Z.; Wang, G. Micellar assembly of a photo- and temperature-responsive amphiphilic block copolymer for controlled release. *Polym. Chem.* **2015**, *6*, 7995–8002, doi:10.1039/C5PY01435B.
139. Han, D.; Tong, X.; Zhao, Y. Block copolymer micelles with a dual-stimuli-responsive core for fast or slow degradation. *Langmuir* **2012**, *28*, 2327–2331, doi:10.1021/la204930n.
140. Cao, Z.; Li, Q.; Wang, G. Photodegradable polymer nanocapsules fabricated from dimethyldiethoxysilane emulsion templates for controlled release. *Polym. Chem.* **2017**, *8*, 6817–6823, doi:10.1039/C7PY01153A.
141. Hegazy, M.; Zhou, P.; Rahoui, N.; Wu, G.; Taloub, N.; Lin, Y.; Huang, X.; Huang, Y. A facile design of smart silica nanocarriers via surface-initiated RAFT polymerization as a dual-stimuli drug release platform. *Colloids and Surfaces A: Physicochemical and Engineering Aspects* **2019**, *581*, 123797, doi:10.1016/j.colsurfa.2019.123797.
142. Liu, C.; Ewert, K.K.; Yao, W.; Wang, N.; Li, Y.; Safinya, C.R.; Qiao, W. A Multifunctional Lipid Incorporating Active Targeting and Dual-Control Release Capabilities for Precision Drug Delivery. *ACS Appl. Mater. Interfaces* **2020**, *12*, 70–85, doi:10.1021/acsmi.9b14470.
143. Liu, G.; Liu, W.; Dong, C.-M. UV- and NIR-responsive polymeric nanomedicines for on-demand drug delivery. *Polym. Chem.* **2013**, *4*, 3431, doi:10.1039/c3py21121e.
144. Mo, B.; Liu, H.; Zhou, X.; Zhao, Y. Facile synthesis of photolabile dendritic-unit-bridged hyperbranched graft copolymers for stimuli-triggered topological transition and controlled release of Nile red. *Polym. Chem.* **2015**, *6*, 3489–3501, doi:10.1039/C5PY00132C.
145. Schumers, J.-M.; Bertrand, O.; Fustin, C.-A.; Gohy, J.-F. Synthesis and self-assembly of diblock copolymers bearing 2-nitrobenzyl photocleavable side groups. *J. Polym. Sci. A Polym. Chem.* **2012**, *50*, 599–608, doi:10.1002/pola.25069.

## REFERENCES

146. Wilkins, C.W., JR.; Reichmonis, E.; Chondross, E.A. Lithographic Evaluation of an o-Nitrobenzyl Ester Based Deep U.V. Resist System. *J. Electrochem. Soc.: SOLID-STATE SCIENCE AND TECHNOLOGY* **1982**, *129*, *11*, 2552–2555.
147. Doh, J.; Irvine, D.J. Photogenerated polyelectrolyte bilayers from an aqueous-processible photoresist for multicomponent protein patterning. *J. Am. Chem. Soc.* **2004**, *126*, 9170–9171, doi:10.1021/ja048261m.
148. Ionov, L.; Diez, S. Environment-friendly photolithography using poly(N-isopropylacrylamide)-based thermoresponsive photoresists. *J. Am. Chem. Soc.* **2009**, *131*, 13315–13319, doi:10.1021/ja902660s.
149. Radl, S.V.; Schipfer, C.; Kaiser, S.; Moser, A.; Kaynak, B.; Kern, W.; Schlögl, S. Photo-responsive thiol–ene networks for the design of switchable polymer patterns. *Polym. Chem.* **2017**, *8*, 1562–1572, doi:10.1039/C7PY00055C.
150. Giebler, M.; Radl, S.; Ules, T.; Griesser, T.; Schlögl, S. Photopatternable Epoxy-Based Thermosets. *Materials (Basel)* **2019**, *12*, doi:10.3390/ma12152350.
151. Radl, S.; Roppolo, I.; Pölzl, K.; Ast, M.; Spreitz, J.; Griesser, T.; Kern, W.; Schlögl, S.; Sangermano, M. Light triggered formation of photo-responsive epoxy based networks. *Polymer* **2017**, *109*, 349–357, doi:10.1016/j.polymer.2016.12.070.
152. Radl, S.; Kreimer, M.; Manhart, J.; Griesser, T.; Moser, A.; Pinter, G.; Kalinka, G.; Kern, W.; Schlögl, S. Photocleavable epoxy based materials. *Polymer* **2015**, *69*, 159–168, doi:10.1016/j.polymer.2015.05.055.
153. Reichmanis, E.; Wilkins, C.W.; Chandross, E.A. A novel approach to o -nitrobenzyl photochemistry for resists. *Journal of Vacuum Science and Technology* **1981**, *19*, 1338–1342, doi:10.1116/1.571272.
154. Giebler, M.; Radl, S.V.; Ast, M.; Kaiser, S.; Griesser, T.; Kern, W.; Schlögl, S. Dual-Responsive Polydimethylsiloxane Networks. *J. Polym. Sci. Part A: Polym. Chem.* **2018**, *56*, 2319–2329, doi:10.1002/pola.29206.
155. Giebler, M.; Alabiso, W.; Wieser, V.; Radl, S.; Schlögl, S. Photopatternable and Rewritable Epoxy-Anhydride Vitrimers. *Macromol. Rapid Commun.* **2020**, e2000466, doi:10.1002/marc.202000466.



## REFERENCES

156. Batchelor, R.; Messer, T.; Hippler, M.; Wegener, M.; Barner-Kowollik, C.; Blasco, E. Two in One: Light as a Tool for 3D Printing and Erasing at the Microscale. *Adv. Mater.* **2019**, *31*, e1904085, doi:10.1002/adma.201904085.
157. Brown, A.A.; Azzaroni, O.; Huck, W.T.S. Photoresponsive polymer brushes for hydrophilic patterning. *Langmuir* **2009**, *25*, 1744–1749, doi:10.1021/la8032308.
158. Xue, L.; Xiong, X.; Krishnan, B.P.; Puza, F.; Wang, S.; Zheng, Y.; Cui, J. Light-regulated growth from dynamic swollen substrates for making rough surfaces. *Nat. Commun.* **2020**, *11*, 963, doi:10.1038/s41467-020-14807-x.
159. Wenzel, R.N. Resistance of solid surfaces to wetting by water. *Industrial and engineering chemistry* **1936**, *28*, 8, 988–994.
160. Rosario, R.; Gust, D.; Garcia, A.A.; Hayes, M.; Taraci, J.L.; Clement, T.; Dailey, J.W.; Picraux, S.T. Lotus Effect Amplifies Light-Induced Contact Angle Switching. *J. Phys. Chem. B* **2004**, *108*, 12640–12642, doi:10.1021/jp0473568.
161. Zheng, Y.; Bai, H.; Huang, Z.; Tian, X.; Nie, F.-Q.; Zhao, Y.; Zhai, J.; Jiang, L. Directional water collection on wetted spider silk. *Nature* **2010**, *463*, 640–643, doi:10.1038/nature08729.
162. Zhang, J.; Han, Y. Shape-gradient composite surfaces: water droplets move uphill. *Langmuir* **2007**, *23*, 6136–6141, doi:10.1021/la063376k.
163. Deng, S.; Shang, W.; Feng, S.; Zhu, S.; Xing, Y.; Li, D.; Hou, Y.; Zheng, Y. Controlled droplet transport to target on a high adhesion surface with multi-gradients. *Sci. Rep.* **2017**, *7*, 45687, doi:10.1038/srep45687.
164. Romano, A.; Angelini, A.; Rossegger, E.; Palmara, G.; Castellino, M.; Frascella, F.; Chiappone, A.; Chiadò, A.; Sangermano, M.; Schlögl, S.; et al. Laser-Triggered Writing and Biofunctionalization of Thiol-Ene Networks. *Macromol. Rapid Commun.* **2020**, *41*, 2000084–2000090, doi:10.1002/marc.202000084.
165. Celina, M.C. Review of polymer oxidation and its relationship with materials performance and lifetime prediction. *Polymer Degradation and Stability* **2013**, *98*, 2419–2429, doi:10.1016/j.polymdegradstab.2013.06.024.

## REFERENCES

166. La Mantia, F.P.; Morreale, M.; Botta, L.; Mistretta, M.C.; Ceraulo, M.; Scaffaro, R. Degradation of polymer blends: A brief review. *Polymer Degradation and Stability* **2017**, *145*, 79–92, doi:10.1016/j.polymdegradstab.2017.07.011.
167. Mailhot, B.; Morlat, S.; Gardette, J.-L.; Boucard, S.; Duchet, J.; Gérard, J.-F. Photodegradation of polypropylene nanocomposites. *Polymer Degradation and Stability* **2003**, *82*, 163–167, doi:10.1016/S0141-3910(03)00179-4.
168. Larché, J.-F.; Bussière, P.-O.; Thérias, S.; Gardette, J.-L. Photooxidation of polymers: Relating material properties to chemical changes. *Polymer Degradation and Stability* **2012**, *97*, 25–34, doi:10.1016/j.polymdegradstab.2011.10.020.
169. Ito, Y.; Heydari, M.; Hashimoto, A.; Konno, T.; Hirasawa, A.; Hori, S.; Kurita, K.; Nakajima, A. The movement of a water droplet on a gradient surface prepared by photodegradation. *Langmuir* **2007**, *23*, 1845–1850, doi:10.1021/la0624992.
170. Mostegel, F.H.; Ducker, R.E.; Rieger, P.H.; El Zubir, O.; Xia, S.; Radl, S.V.; Edler, M.; Cartron, M.L.; Hunter, C.N.; Leggett, G.J.; et al. Versatile thiol-based reactions for micrometer- and nanometer-scale photopatterning of polymers and biomolecules. *J. Mater. Chem. B* **2015**, *3*, 4431–4438, doi:10.1039/c5tb00345h.
171. Pavlovic, E.; Quist, A.P.; Gelius, U.; Nyholm, L.; Oscarsson, S. Generation of Thiolsulfonates/Thiolsulfonates by Electrooxidation of Thiols on Silicon Surfaces for Reversible Immobilization of Molecules. *Langmuir* **2003**, *19*, 4217–4221, doi:10.1021/la026846t.
172. Balachander, N.; Sukenik, C.N. Monolayer Transformation by Nucleophilic Substitution: Applications to the Creation of New Monolayer Assemblies. *Langmuir* **1990**, *6*, 11, 1621–1627.
173. van Bergen, L.A.H.; Roos, G.; Proft, F. de. From thiol to sulfonic acid: modeling the oxidation pathway of protein thiols by hydrogen peroxide. *J. Phys. Chem. A* **2014**, *118*, 6078–6084, doi:10.1021/jp5018339.
174. Bhatia, S.K.; Hickman, J.J.; Ligler, F.S. New Approach To Producing Patterned Biomolecular Assemblies. *J. Am. Chem. Soc.* **1992**, *114*, 4432–4433.

## REFERENCES

175. Ding, Y.-X.; Streitmatter, S.; Wright, B.E.; Hlady, V. Spatial variation of the charge and sulfur oxidation state in a surface gradient affects plasma protein adsorption. *Langmuir* **2010**, *26*, 12140–12146, doi:10.1021/la101674b.
176. Xu, N.; Wang, R.-L.; Li, D.-P.; Meng, X.; Mu, J.-L.; Zhou, Z.-Y.; Su, Z.-M. A new triazine-based covalent organic polymer for efficient photodegradation of both acidic and basic dyes under visible light. *Dalton Trans.* **2018**, *47*, 4191–4197, doi:10.1039/c8dt00148k.
177. Ndoni, S.; Li, L.; Schulte, L.; Szewczykowski, P.P.; Hansen, T.W.; Guo, F.; Berg, R.H.; Vigild, M.E. Controlled Photooxidation of Nanoporous Polymers. *Macromolecules* **2009**, *42*, 3877–3880, doi:10.1021/ma900485q.
178. Levinson, H.J. *Principles of Lithography*; SPIE: Bellingham, 2011.
179. Lin, B.J. *Optical Lithography: Here Is Why*; SPIE: Bellingham, 2011.
180. del Barrio, J.; Sánchez-Somolinos, C. Light to Shape the Future: From Photolithography to 4D Printing. *Adv. Optical Mater.* **2019**, *7*, 1900598, doi:10.1002/adom.201900598.
181. Dusa, M.; Arnold, B.; Fumar-Pici, A. in *Proc. IEEE Int. Symp. Semiconductor Manufacturing*; San Jose, CA, USA, 2005.
182. Levenson, M.D.; Viswanathan, N.S.; Simpson, R.A. Improving Resolution in Photolithography with a Phase-Shifting Mask. *IEEE Transactiond on electron devices* **1982**, *29*,12, 1828–1836.
183. del Campo, A.; Arzt, E. Fabrication approaches for generating complex micro- and nanopatterns on polymeric surfaces. *Chem. Rev.* **2008**, *108*, 911–945, doi:10.1021/cr050018y.
184. Reichmanis, E.; Houlihan, F.M.; Nalamasu, O.; Neenan, T.X. Chemically amplified resists: Chemistry and processes. *Advanced Materials for Optics and Electronics* **1994**, *4*, 83–93.
185. Yeh, W.-M.; Noga, D.E.; Lawson, R.A. Comparison of positive tone versus negative tone resist pattern collapse behavior. *Journal of Vacuum Science & Technology B* **2010**, *28*,6, 2166–2746.

## REFERENCES

186. Kim, M.; Choi, J.-C.; Jung, H.-R.; Katz, J.S.; Kim, M.-G.; Doh, J. Addressable micropatterning of multiple proteins and cells by microscope projection photolithography based on a protein friendly photoresist. *Langmuir* **2010**, *26*, 12112–12118, doi:10.1021/la1014253.
187. Haisma, J. Mold-assisted nanolithography: A process for reliable pattern replication. *J. Vac. Sci. Technol. B* **1996**, *14*, 4124, doi:10.1116/1.588604.
188. Schiff, H. Nanoimprint lithography: 2D or not 2D? A review. *Appl. Phys. A* **2015**, *121*, 415–435, doi:10.1007/s00339-015-9106-3.
189. Ruchhoeft, P.; Colburn, M.; Choi, B.; Nounu, H.; Johnson, S.; Bailey, T.; Damle, S.; Stewart, M.; Ekerdt, J.; Sreenivasan, S.V.; et al. Patterning curved surfaces: Template generation by ion beam proximity lithography and relief transfer by step and flash imprint lithography. *J. Vac. Sci. Technol. B* **1999**, *17*, 2965, doi:10.1116/1.590935.
190. Leitgeb, M.; Nees, D.; Ruttloff, S.; Palfinger, U.; Götz, J.; Liska, R.; Belegatis, M.R.; Stadlober, B. Multi-Length Scale Patterning of Functional Layers by Roll-to-Roll Ultraviolet-Light Assisted Nanoimprint Lithography. *ACS Nano* **2016**, *10*, 5, 4926–4941.
191. Thesen, M.W.; Nees, D.; Ruttloff, S.; Rumler, M.; Rommel, M.; Schlachter, F.; Grützner, S.; Vogler, M.; Schleunitz, A.; Grützner, G. Inkjettable and photo-curable resists for large-area and high-throughput roll-to-roll nanoimprint lithography. *J. Micro/Nanolith. MEMS MOEMS* **2014**, *13*, 43003, doi:10.1117/1.JMM.13.4.043003.
192. Ligon, S.C.; Husár, B.; Wutzel, H.; Holman, R.; Liska, R. Strategies to reduce oxygen inhibition in photoinduced polymerization. *Chem. Rev.* **2014**, *114*, 557–589, doi:10.1021/cr3005197.
193. Mihi, A.; Beck, F.J.; Lasanta, T.; Rath, A.K.; Konstantatos, G. Imprinted electrodes for enhanced light trapping in solution processed solar cells. *Adv. Mater.* **2014**, *26*, 443–448, doi:10.1002/adma.201303674.
194. Hagberg, E.C.; Malkoch, M.; Ling, Y.; Hawker, C.J.; Carter, K.R. Effects of modulus and surface chemistry of thiol-ene photopolymers in nanoimprinting. *Nano Lett.* **2007**, *7*, 233–237, doi:10.1021/nl061217f.

## REFERENCES

195. Austin, M.D.; Ge, H.; Wu, W.; Li, M.; Yu, Z.; Wasserman, D.; Lyon, S.A.; Chou, S.Y. Fabrication of 5nm linewidth and 14nm pitch features by nanoimprint lithography. *Appl. Phys. Lett.* **2004**, *84*, 5299–5301, doi:10.1063/1.1766071.
196. Takabayashi, Y.; Hiura, M.; Morohoshi, H.; Kodachi, N.; Hayashi, T.; Kimura, A.; Yoshida, T.; Mishima, K.; Suzaki, Y.; Choi, J. Nanoimprint system development for high-volume semiconductor manufacturing the and status of overlay performance. *Proc of SPIE*, *10144*, 1014405-1-10, doi:10.1117/12.2258385.
197. González Lazo, M.A.; Teuscher, R.; Leterrier, Y.; Månson, J.-A.E.; Calderone, C.; Hessler-Wyser, A.; Couty, P.; Ziegler, Y.; Fischer, D. UV-nanoimprint lithography and large area roll-to-roll texturization with hyperbranched polymer nanocomposites for light-trapping applications. *Solar Energy Materials and Solar Cells* **2012**, *103*, 147–156, doi:10.1016/j.solmat.2012.04.034.
198. Gross, B.C.; Erkal, J.L.; Lockwood, S.Y.; Chen, C.; Spence, D.M. Evaluation of 3D printing and its potential impact on biotechnology and the chemical sciences. *Anal. Chem.* **2014**, *86*, 3240–3253, doi:10.1021/ac403397r.
199. Hull, C.W. Apparatus for production ofthree-dimensional objects by stereolithography. *U.S. Patent 4,575,330* **1986**.
200. Dolenc, A.; Mäkelä, I. Slicing procedures for layered manufacturing techniques. *Computer-Aided Design* **1994**, *26*, 2, 119–126.
201. Crump, S.S. Apparatus and method for creating three-dimensional objects. *U.S. Patent 5,121,329* **1992**.
202. Leukers, B.; Gülkan, H.; Irsen, S.H.; Milz, S.; Tille, C.; Schieker, M.; Seitz H. Hydroxyapatite scaffolds for bone tissue engineering made by 3D printing. *Journal of Material Science: Materials in Medicine* **2005**, *16*, 1121–1124.
203. Mironov, V.; Boland, T.; Trusk, T.; Forgacs, G.; Markwald, R.R. Organ printing: computer-aided jet-based 3D tissue engineering. *Trends in Biotechnology* **2003**, *21*, 157–161, doi:10.1016/S0167-7799(03)00033-7.
204. Lipton, J.; Arnold, D.; Nigl, F.; Lopez, N.; Cohen, D.; Norén, N.; Lipson, H. Multi-material food printing with complex internal structure suitable for conventional post-processing. *Solid Freeform Fabrication Symposium*, **2010**.

## REFERENCES

205. Daanen, H.; Hong, S.-A. Made-to-measure pattern development based on 3D whole body scans. *J. J. Text. Apparel, Technol. Manage.* **2008**, *20*, 1, 15–25, doi:10.1108/09556220810843502.
206. Hribar, K.C.; Soman, P.; Warner, J.; Chung, P.; Chen, S. Light-assisted direct-write of 3D functional biomaterials. *Lab Chip* **2014**, *14*, 268–275, doi:10.1039/c3lc50634g.
207. Ligon, S.C.; Liska, R.; Stampfl, J.; Gurr, M.; Mühlaupt, R. Polymers for 3D Printing and Customized Additive Manufacturing. *Chem. Rev.* **2017**, *117*, 10212–10290, doi:10.1021/acs.chemrev.7b00074.
208. Bártolo, P.J. Stereolithographic Processes. In *Stereolithography*; Bártolo, P.J., Ed.; Springer US: Boston, MA, 2011; pp 1–36, ISBN 978-0-387-92903-3.
209. Jacobs, P.F. *Rapid Prototyping and Manufacturing: Fundamentals of Stereolithography*; Society of Manufacturing Engineers: Dearborn, MI, 1992.
210. Kowsari, K.; Zhang, B.; Panjwani, S.; Chen, Z.; Hingorani, H.; Akbari, S.; Fang, N.X.; Ge, Q. Photopolymer formulation to minimize feature size, surface roughness, and stair-stepping in digital light processing-based three-dimensional printing. *Additive Manufacturing* **2018**, *24*, 627–638, doi:10.1016/j.addma.2018.10.037.
211. Xing, J.-F.; Zheng, M.-L.; Duan, X.-M. Two-photon polymerization microfabrication of hydrogels: an advanced 3D printing technology for tissue engineering and drug delivery. *Chem. Soc. Rev.* **2015**, *44*, 5031–5039, doi:10.1039/c5cs00278h.
212. Asvany, O.; Yamada, K.M.T.; Brünken, S.; Potapov, A.; Schlemmer, S. Vibrational dynamics. Experimental ground-state combination differences of CH<sub>5</sub><sup>+</sup>. *Science* **2015**, *347*, 1346–1349, doi:10.1126/science.aaa3304.
213. Kelly, B.E.; Bhattacharya, I.; Heidari, H.; Shusteff, M.; Spadaccini, C.M.; Taylor, H.K. Volumetric additive manufacturing via tomographic reconstruction. *Science* **2019**, *363*, 1075–1079, doi:10.1126/science.aau7114.
214. Tofail, S.A.M.; Koumoulos, E.P.; Bandyopadhyay, A.; Bose, S.; O'Donoghue, L.; Charitidis, C. Additive manufacturing: scientific and technological challenges, market uptake and opportunities. *Materials Today* **2018**, *21*, 22–37, doi:10.1016/j.mattod.2017.07.001.

## REFERENCES

215. Compton, B.G.; Lewis, J.A. 3D-printing of lightweight cellular composites. *Adv. Mater.* **2014**, *26*, 5930–5935, doi:10.1002/adma.201401804.
216. Ouyang, L.; Highley, C.B.; Rodell, C.B.; Sun, W.; Burdick, J.A. 3D Printing of Shear-Thinning Hyaluronic Acid Hydrogels with Secondary Cross-Linking. *ACS Biomater. Sci. Eng.* **2016**, *2*, 1743–1751, doi:10.1021/acsbiomaterials.6b00158.
217. Habault, D.; Zhang, H.; Zhao, Y. Light-triggered self-healing and shape-memory polymers. *Chem. Soc. Rev.* **2013**, *42*, 7244–7256, doi:10.1039/c3cs35489j.
218. Yang, H.; Leow, W.R.; Wang, T.; Wang, J.; Yu, J.; He, K.; Qi, D.; Wan, C.; Chen, X. 3D Printed Photoresponsive Devices Based on Shape Memory Composites. *Adv. Mater.* **2017**, *29*, doi:10.1002/adma.201701627.
219. Kuksenok, O.; Balazs, A.C. Stimuli-responsive behavior of composites integrating thermo-responsive gels with photo-responsive fibers. *Mater. Horiz.* **2016**, *3*, 53–62, doi:10.1039/C5MH00212E.
220. Kuang, X.; Roach, D.J.; Wu, J.; Hamel, C.M.; Ding, Z.; Wang, T.; Dunn, M.L.; Qi, H.J. Advances in 4D Printing: Materials and Applications. *Adv. Funct. Mater.* **2019**, *29*, 2, 1–23.
221. Ge, Q.; Qi, H.J.; Dunn, M.L. Active materials by four-dimension printing. *Appl. Phys. Lett.* **2013**, *103*, 131901, doi:10.1063/1.4819837.
222. Li, Y.-C.; Zhang, Y.S.; Akpek, A.; Shin, S.R.; Khademhosseini, A. 4D bioprinting: the next-generation technology for biofabrication enabled by stimuli-responsive materials. *Biofabrication* **2016**, *9*, 12001, doi:10.1088/1758-5090/9/1/012001.
223. Murphy, S.V.; Atala, A. 3D bioprinting of tissues and organs. *Nat. Biotechnol.* **2014**, *32*, 773–785, doi:10.1038/nbt.2958.
224. Derby, B. Printing and prototyping of tissues and scaffolds. *Science* **2012**, *338*, 921–926, doi:10.1126/science.1226340.
225. Cho, J.H.; Lee, J.; Xia, Y.; Kim, B.; He, Y.; Renn, M.J.; Lodge, T.P.; Frisbie, C.D. Printable ion-gel gate dielectrics for low-voltage polymer thin-film transistors on plastic. *Nat. Mater.* **2008**, *7*, 900–906, doi:10.1038/nmat2291.

## REFERENCES

226. Wei, T.-S.; Ahn, B.Y.; Grotto, J.; Lewis, J.A. 3D Printing of Customized Li-Ion Batteries with Thick Electrodes. *Adv. Mater.* **2018**, *30*, e1703027, doi:10.1002/adma.201703027.
227. Bodaghi, M.; Damanpack, A.R.; Liao, W.H. Adaptive metamaterials by functionally graded 4D printing. *Materials & Design* **2017**, *135*, 26–36, doi:10.1016/j.matdes.2017.08.069.
228. Zheng, X.; Lee, H.; Weisgraber, T.H.; Shusteff, M.; DeOtte, J.; Duoss, E.B.; Kuntz, J.D.; Biener, M.M.; Ge, Q.; Jackson, J.A.; et al. Ultralight, ultrastiff mechanical metamaterials. *Science* **2014**, *344*, 1373–1377, doi:10.1126/science.1252291.
229. Eckel, Z.C.; Zhou, C.; Martin, J.H.; Jacobsen, A.J.; Carter, W.B.; Schaedler, T.A. Additive manufacturing of polymer-derived ceramics. *Science* **2016**, *351*, 6268, 58–62.
230. Ding, Z.; Weeger, O.; Qi, H.J.; Dunn, M.L. 4D rods: 3D structures via programmable 1D composite rods. *Materials & Design* **2018**, *137*, 256–265, doi:10.1016/j.matdes.2017.10.004.
231. Ma, J.; Franco, B.; Tapia, G.; Karayagiz, K.; Johnson, L.; Liu, J.; Arroyave, R.; Karaman, I.; Elwany, A. Spatial Control of Functional Response in 4D-Printed Active Metallic Structures. *Sci. Rep.* **2017**, *7*, 46707, doi:10.1038/srep46707.
232. Lee, J.; Kim, H.C.; Choi, J.-W.; Lee, I.H. A Review on 3D Printed Smart Devices for 4D Printing. *International Journal of Precision Engineering and Manufacturing- Green Technology* **2017**, *4*, 3, 373–383.
233. Li, H.; Gao, X.; Luo, Y. Multi-shape memory polymers achieved by the spatio-assembly of 3D printable thermoplastic building blocks. *Soft Matter* **2016**, *12*, 3226–3233, doi:10.1039/c6sm00185h.
234. Zarek, M.; Layani, M.; Cooperstein, I.; Sachyani, E.; Cohn, D.; Magdassi, S. 3D Printing of Shape Memory Polymers for Flexible Electronic Devices. *Adv. Mater.* **2016**, *28*, 4449–4454, doi:10.1002/adma.201503132.
235. Roy, D.; Cambre, J.N.; Sumerlin, B.S. Future perspectives and recent advances in stimuli-responsive materials. *Progress in Polymer Science* **2010**, *35*, 278–301, doi:10.1016/j.progpolymsci.2009.10.008.



## REFERENCES

236. Yu, K.; Ge, Q.; Qi, H.J. Reduced time as a unified parameter determining fixity and free recovery of shape memory polymers. *Nat. Commun.* **2014**, *5*, 3066, doi:10.1038/ncomms4066.
237. Zarek, M.; Mansour, N.; Shapira, S.; Cohn, D. 4D Printing of Shape Memory-Based Personalized Endoluminal Medical Devices. *Macromol. Rapid Commun.* **2017**, *38*, doi:10.1002/marc.201600628.
238. Xie, T. Tunable polymer multi-shape memory effect. *Nature* **2010**, *464*, 267–270, doi:10.1038/nature08863.
239. Zhang, Y.; Zhang, F.; Yan, Z.; Ma, Q.; Li, X.; Huang, Y.; Rogers, J.A. Printing, folding and assembly methods for forming 3D mesostructures in advanced materials. *Nat Rev Mater* **2017**, *2*, doi:10.1038/natrevmats.2017.19.
240. Zhang, Q.; Yan, D.; Zhang, K.; Hu, G. Pattern transformation of heat-shrinkable polymer by three-dimensional (3D) printing technique. *Sci. Rep.* **2015**, *5*, 8936, doi:10.1038/srep08936.
241. Liu, Y.; Shaw, B.; Dickey, M.D.; Genzer, J. Sequential self-folding of polymer sheets. *Science Advances* **2017**, *3*, 1–7.
242. Gao, B.; Yang, Q.; Zhao, X.; Jin, G.; Ma, Y.; Xu, F. 4D Bioprinting for Biomedical Applications. *Trends in Biotechnology* **2016**, *34*, 746–756, doi:10.1016/j.tibtech.2016.03.004.
243. Choi, J.; Kwon, O.-C.; Jo, W.; Lee, H.J.; Moon, M.-W. 4D Printing Technology: A Review. *3D Printing and Additive Manufacturing* **2015**, *2*, 159–167, doi:10.1089/3dp.2015.0039.
244. Kuang, X.; Chen, K.; Dunn, C.K.; Wu, J.; Li, V.C.F.; Qi, H.J. 3D Printing of Highly Stretchable, Shape-Memory, and Self-Healing Elastomer toward Novel 4D Printing. *ACS Appl. Mater. Interfaces* **2018**, *10*, 7381–7388, doi:10.1021/acsami.7b18265.
245. Graeber, G.; Martin Kieliger, O.B.; Schutzius, T.M.; Poulikakos, D. 3D-Printed Surface Architecture Enhancing Superhydrophobicity and Viscous Droplet Repellency. *ACS Appl. Mater. Interfaces* **2018**, *10*, 43275–43281, doi:10.1021/acsami.8b16893.

## REFERENCES

246. Waheed, S.; Cabot, J.M.; Macdonald, N.P.; Lewis, T.; Guijt, R.M.; Paull, B.; Breadmore, M.C. 3D printed microfluidic devices: enablers and barriers. *Lab Chip* **2016**, *16*, 1993–2013, doi:10.1039/c6lc00284f.
247. Yang, Y.; Li, X.; Zheng, X.; Chen, Z.; Zhou, Q.; Chen, Y. 3D-Printed Biomimetic Super-Hydrophobic Structure for Microdroplet Manipulation and Oil/Water Separation. *Adv. Mater.* **2018**, *30*, doi:10.1002/adma.201704912.
248. Zhang, D.; Cheng, Z.; Liu, Y. Smart Wetting Control on Shape Memory Polymer Surfaces. *Chemistry* **2019**, *25*, 3979–3992, doi:10.1002/chem.201804192.
249. Damien Montarnal, Mathieu Capelot, François Tournilhac, Ludwik Leibler. Silica-Like Malleable Materials from Permanent Organic Networks. *Science* **2011**, *334*, 965–968, doi:10.1126/science.1211649.
250. Bowman, C.N.; Kloxin, C.J. Covalent adaptable networks: reversible bond structures incorporated in polymer networks. *Angew. Chem. Int. Ed Engl.* **2012**, *51*, 4272–4274, doi:10.1002/anie.201200708.
251. Kloxin, C.J.; Scott, T.F.; Adzima, B.J.; Bowman, C.N. Covalent Adaptable Networks (CANs): A Unique Paradigm in Crosslinked Polymers. *Macromolecules* **2010**, *43*, 2643–2653, doi:10.1021/ma902596s.
252. Alabiso, W.; Schlögl, S. The Impact of Vitrimers on the Industry of the Future: Chemistry, Properties and Sustainable Forward-Looking Applications. *Polymers (Basel)* **2020**, *12*, doi:10.3390/polym12081660.
253. Zou, W.; Dong, J.; Luo, Y.; Zhao, Q.; Xie, T. Dynamic Covalent Polymer Networks: from Old Chemistry to Modern Day Innovations. *Adv. Mater.* **2017**, *29*, doi:10.1002/adma.201606100.
254. Winne, J.M.; Leibler, L.; Du Prez, F.E. Dynamic covalent chemistry in polymer networks: a mechanistic perspective. *Polym. Chem.* **2019**, *10*, 6091–6108, doi:10.1039/C9PY01260E.
255. Denissen, W.; Winne, J.M.; Du Prez, F.E. Vitrimers: permanent organic networks with glass-like fluidity. *Chem. Sci.* **2016**, *7*, 30–38, doi:10.1039/c5sc02223a.
256. Jourdain, A.; Asbai, R.; Anaya, O.; Chehimi, M.M.; Drockenmuller, E.; Montarnal, D. Rheological Properties of Covalent Adaptable Networks with 1,2,3-Triazolium Cross-

## REFERENCES

- Links: The Missing Link between Vitrimers and Dissociative Networks. *Macromolecules* **2020**, *53*, 1884–1900, doi:10.1021/acs.macromol.9b02204.
257. Capelot, M.; Unterlass, M.M.; Tournilhac, F.; Leibler, L. Catalytic Control of the Vitriimer Glass Transition. *ACS Macro Lett.* **2012**, *1*, 789–792, doi:10.1021/mz300239f.
258. Breuillac, A.; Kassalias, A.; Nicolaÿ, R. Polybutadiene Vitrimers Based on Dioxaborolane Chemistry and Dual Networks with Static and Dynamic Cross-links. *Macromolecules* **2019**, *52*, 7102–7113, doi:10.1021/acs.macromol.9b01288.
259. Chakma, P.; Konkolewicz, D. Dynamic Covalent Bonds in Polymeric Materials. *Angew. Chem. Int. Ed Engl.* **2019**, *58*, 9682–9695, doi:10.1002/anie.201813525.
260. Liu, T.; Zhao, B.; Zhang, J. Recent development of repairable, malleable and recyclable thermosetting polymers through dynamic transesterification. *Polymer* **2020**, *194*, 122392, doi:10.1016/j.polymer.2020.122392.
261. Capelot, M.; Montarnal, D.; Tournilhac, F.; Leibler, L. Metal-catalyzed transesterification for healing and assembling of thermosets. *J. Am. Chem. Soc.* **2012**, *134*, 7664–7667, doi:10.1021/ja302894k.
262. Chen, J.; Huang, H.; Fan, J.; Wang, Y.; Yu, J.; Zhu, J.; Hu, Z. Vitriimer Chemistry Assisted Fabrication of Aligned, Healable, and Recyclable Graphene/Epoxy Composites. *Front. Chem.* **2019**, *7*, 632, doi:10.3389/fchem.2019.00632.
263. Kim, N.K.; Cha, E.J.; Jung, M.; Kim, J.; Jeong, G.-J.; Kim, Y.S.; Choi, W.J.; Kim, B.-S.; Kim, D.-G.; Lee, J.-C. 3D hierarchical scaffolds enabled by a post-patternable, reconfigurable, and biocompatible 2D vitriimer film for tissue engineering applications. *J. Mater. Chem. B* **2019**, *7*, 3341–3345, doi:10.1039/C9TB00221A.
264. Liu, T.; Hao, C.; Zhang, S.; Yang, X.; Wang, L.; Han, J.; Li, Y.; Xin, J.; Zhang, J. A Self-Healable High Glass Transition Temperature Bioepoxy Material Based on Vitriimer Chemistry. *Macromolecules* **2018**, *51*, 5577–5585, doi:10.1021/acs.macromol.8b01010.
265. Debnath, S.; Kaushal, S.; Ojha, U. Catalyst-Free Partially Bio-Based Polyester Vitrimers. *ACS Appl. Polym. Mater.* **2020**, *2*, 1006–1013, doi:10.1021/acsapm.0c00016.
266. Guerre, M.; Taplan, C.; Nicolaÿ, R.; Winne, J.M.; Du Prez, F.E. Fluorinated Vitriimer Elastomers with a Dual Temperature Response. *J. Am. Chem. Soc.* **2018**, *140*, 13272–13284, doi:10.1021/jacs.8b07094.

## REFERENCES

267. Han, J.; Liu, T.; Hao, C.; Zhang, S.; Guo, B.; Zhang, J. A Catalyst-Free Epoxy Vitrimer System Based on Multifunctional Hyperbranched Polymer. *Macromolecules* **2018**, *51*, 6789–6799, doi:10.1021/acs.macromol.8b01424.
268. Zheng, N.; Hou, J.; Xu, Y.; Fang, Z.; Zou, W.; Zhao, Q.; Xie, T. Catalyst-Free Thermoset Polyurethane with Permanent Shape Reconfigurability and Highly Tunable Triple-Shape Memory Performance. *ACS Macro Lett.* **2017**, *6*, 326–330, doi:10.1021/acsmacrolett.7b00037.
269. Niu, X.; Wang, F.; Li, X.; Zhang, R.; Wu, Q.; Sun, P. Using Zn<sup>2+</sup> Ionomer To Catalyze Transesterification Reaction in Epoxy Vitrimer. *Ind. Eng. Chem. Res.* **2019**, *58*, 5698–5706, doi:10.1021/acs.iecr.9b00090.
270. Kiesewetter, M.K.; Scholten, M.D.; Kirn, N.; Weber, R.L.; Hedrick, J.L.; Waymouth, R.M. Cyclic guanidine organic catalysts: what is magic about triazabicyclodecene? *J. Org. Chem.* **2009**, *74*, 9490–9496, doi:10.1021/jo902369g.
271. Yadav, J.S.; Reddy, B.V.S.; Krishna, A.D.; Reddy, C.S.; Narsaiah, A.V. Triphenylphosphine: An efficient catalyst for transesterification of  $\beta$ -ketoesters. *Journal of Molecular Catalysis A: Chemical* **2007**, *261*, 93–97, doi:10.1016/j.molcata.2006.07.060.
272. Brutman, J.P.; Delgado, P.A.; Hillmyer, M.A. Polylactide Vitrimers. *ACS Macro Lett.* **2014**, *3*, 607–610, doi:10.1021/mz500269w.
273. Liu, W.; Schmidt, D.F.; Reynaud, E. Catalyst Selection, Creep, and Stress Relaxation in High-Performance Epoxy Vitrimers. *Ind. Eng. Chem. Res.* **2017**, *56*, 2667–2672, doi:10.1021/acs.iecr.6b03829.
274. Denissen, W.; Droesbeke, M.; Nicolaÿ, R.; Leibler, L.; Winne, J.M.; Du Prez, F.E. Chemical control of the viscoelastic properties of vinylogous urethane vitrimers. *Nat. Commun.* **2017**, *8*, 14857, doi:10.1038/ncomms14857.
275. Shi, Q.; Yu, K.; Kuang, X.; Mu, X.; Dunn, C.K.; Dunn, M.L.; Wang, T.; Jerry Qi, H. Recyclable 3D printing of vitrimer epoxy. *Mater. Horiz.* **2017**, *4*, 598–607, doi:10.1039/C7MH00043J.

## REFERENCES

276. Wang, C.; Goldman, T.M.; Worrell, B.T.; McBride, M.K.; Alim, M.D.; Bowman, C.N. Recyclable and repolymerizable thiol–X photopolymers. *Mater. Horiz.* **2018**, *5*, 1042–1046, doi:10.1039/C8MH00724A.
277. Worrell, B.T.; McBride, M.K.; Lyon, G.B.; Cox, L.M.; Wang, C.; Mavila, S.; Lim, C.-H.; Coley, H.M.; Musgrave, C.B.; Ding, Y.; et al. Bistable and photoswitchable states of matter. *Nat. Commun.* **2018**, *9*, 2804, doi:10.1038/s41467-018-05300-7.
278. Yang, Y.; Pei, Z.; Li, Z.; Wei, Y.; Ji, Y. Making and Remaking Dynamic 3D Structures by Shining Light on Flat Liquid Crystalline Vitriimer Films without a Mold. *J. Am. Chem. Soc.* **2016**, *138*, 2118–2121, doi:10.1021/jacs.5b12531.
279. Zhang, B.; Kowsari, K.; Serjouei, A.; Dunn, M.L.; Ge, Q. Reprocessable thermosets for sustainable three-dimensional printing. *Nat. Commun.* **2018**, *9*, 1831, doi:10.1038/s41467-018-04292-8.

## INCLUDED PUBLICATIONS

### **I. Directed motion of water droplets on multi-gradient photopolymer surfaces**

Rossegger, Elisabeth; Hennen, Daniel; Griesser, Thomas; Roppolo, Ignazio; Schlögl, Sandra: *Polymer Chemistry*, **2019**, *10*, 1882-1894, <https://doi.org/10.1039/C9PY00123A>

### **II. Photo-switching of surface wettability on micropatterned photopolymers for fast transport of water droplets over a long distance**

Rossegger, Elisabeth; Nees, Dieter; Turisser, Simon; Radl, Simone; Griesser, Thomas; Schlögl, Sandra: *Polymer Chemistry*, **2020**, *11*, 3125-3135, <https://doi.org/10.1039/D0PY00263A>

### **III. Digital light processing 3D printing with thiol-acrylate vitrimers**

Rossegger, Elisabeth; Höller, Rita; Reisinger, David; Strasser, Jakob; Fleisch, Mathias; Griesser, Thomas; Schlögl, Sandra: *Polymer Chemistry*, **2021**, *12*, 639-644, <https://doi.org/10.1039/D0PY01520B>

### **IV. High resolution additive manufacturing with acrylate based vitrimers using organic phosphates as transesterification catalyst**

Rossegger, Elisabeth; Höller, Rita; Reisinger, David; Fleisch, Mathias; Strasser, Jakob; Wieser, Viktoria; Griesser, Thomas; Schlögl, Sandra: *Polymer*, **2021**, *221*, 123631, <https://doi.org/10.1016/j.polymer.2021.123631>

### **V. Locally controlling dynamic exchange reactions in 3D printed thiol-acrylate vitrimers using dual-wavelength digital light processing**

Rossegger, Elisabeth; Moazzen, Khadijeh; Fleisch, Mathias; Schlögl, Sandra: *Nature communications*, **2021 under revision**

**Table 1: Summarized contribution to the included publications**

	Conception and planning	Experiments	Analysis and interpretation	Manuscript preparation
Publication I	80%	80%	80%	50%
Publication II	90%	80%	90%	50%
Publication III	90%	70%	80%	50%
Publication IV	90%	60%	80%	50%
Publication V	90%	80%	90%	50%

**PUBLICATION I:**

*Directed motion of water droplets on multi-gradient photopolymer  
surfaces*

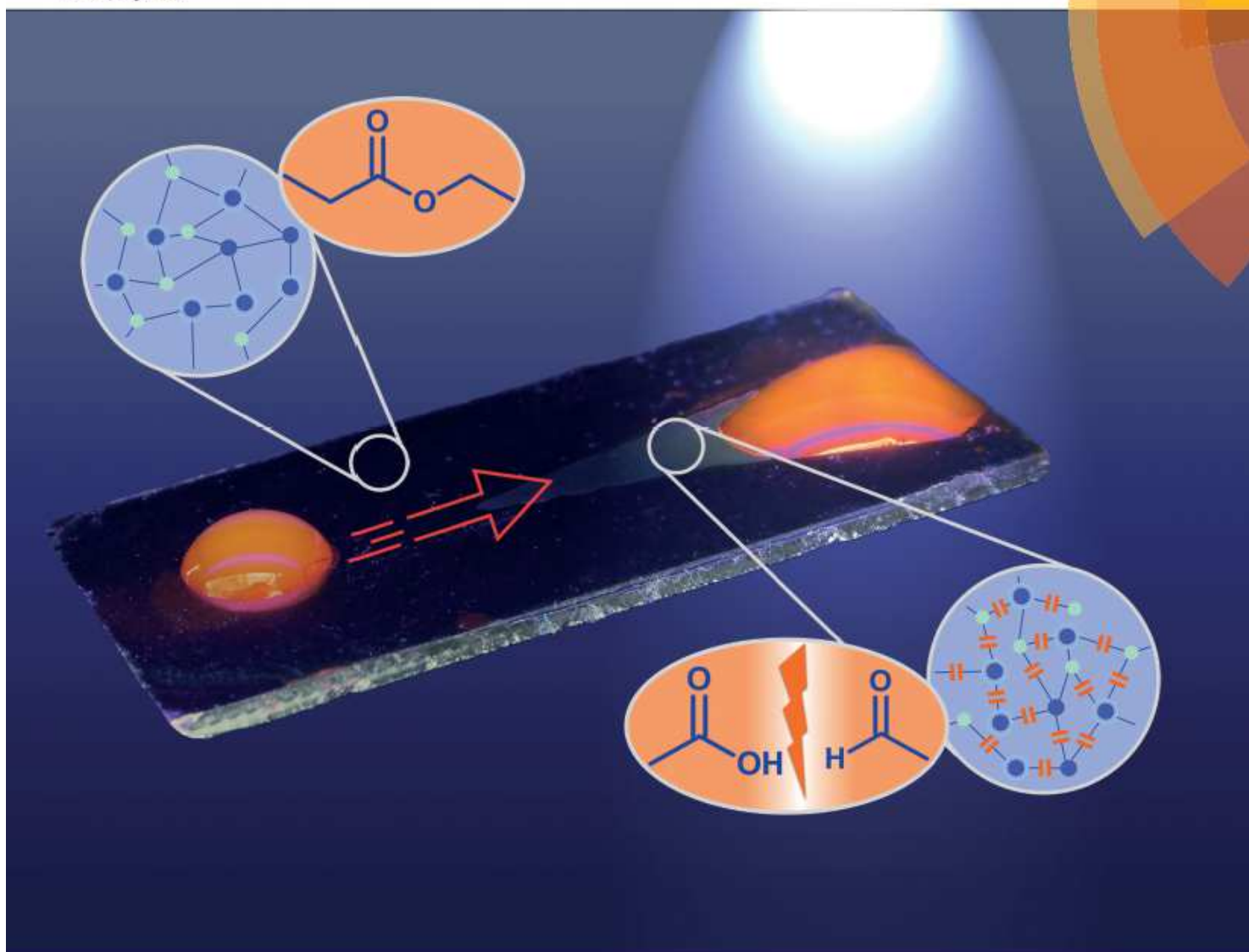
Rossegger, Elisabeth; Hennen, Daniel; Griesser, Thomas; Roppolo, Ignazio;  
Schlögl, Sandra

*Polymer Chemistry*, 2019, 10, 1882-1894



# Polymer Chemistry

rsc.li/polymers



ISSN 1759-9962



ROYAL SOCIETY  
OF CHEMISTRY

Celebrating  
IYPT 2019

PAPER

S. Schlögl *et al.*

Directed motion of water droplets on multi-gradient photopolymer surfaces

### *Abstract*

The present work highlights the controlled directional movement of water droplets across a photopolymer surface. The movement is propelled by multi-gradients including a wettability gradient and a Laplace pressure gradient. Both gradients are conveniently adjusted by light employing a photoresponsive thiol-yne photopolymer. *o*-Nitrobenzyl alcohol derivatives with terminal alkyne groups are synthesized and cured across di- and tri-functional thiols upon visible light exposure. The wettability gradient is generated in a subsequent step involving an asymmetrical irradiation of the polymer surface with light in the UV-A spectral region. Polar groups are formed in the exposed areas due to the photocleavage of the chromophore and photo-oxidation reactions (upon prolonged UV exposure in air). The wettability rises with increasing exposure dose and gradient surfaces are prepared with static water contact angles ranging from 97 to 19°. By simultaneously inscribing the wettability gradient in wedge-shaped patterns, a Laplace pressure gradient is realized on the photopolymer surface, which can be easily tailored by the size and the angle of the wedge. The combination of both gradients enables a rapid and directed movement of water droplets (2  $\mu$ L droplet) over a reasonable distance (up to 10 mm). Due to the high adhesion of the photopolymer surface, the droplet can be driven in a controlled way, even if the surface is inclined (20°) or turned upside down.

### *Introduction*

Inspired by nature, the directed motility of droplets on polymer surfaces has gained increased attention over the past years.<sup>1</sup> Benefiting from a controlled liquid transport without the requirement of pumps or other external devices,<sup>2</sup> directed movement is of great interest for numerous future applications such as microfluidic devices,<sup>3</sup> fog-harvesting<sup>4</sup> and functional coatings (e.g. self-cleaning, anti-fog, anti-corrosion).<sup>5</sup>

Directed motility is realized by various surface designs that are characterized by thermal (e.g. Marangoni-driven spreading of liquids),<sup>6</sup> chemical (e.g. wettability gradient)<sup>7</sup> or shape gradients (e.g. asymmetrically structured surfaces, surfaces with a curvature gradient).<sup>8</sup> For microscale systems it was demonstrated that directed motility is strongly

governed by surface tension since it is able to overpower the inertial force.<sup>9</sup> In the late 1970s, Greenspan has provided the theoretical basis for the movement of a water droplet on a surface with a gradient in wettability.<sup>10</sup> This work has become the starting point towards experimental realization of this unique behavior on various material surfaces.<sup>7,11</sup> In particular, Chaudhury and Whitesides reported that the contact-angle hysteresis on a surface has to be below  $10^\circ$  to drive a droplet along the wettability gradient, even if the surface is inclined.<sup>7</sup> In further studies, Daniel and co-workers showed that directed motility is influenced by unbalanced contact angles at the droplet edges in the direction of the gradient.<sup>12</sup> They also demonstrated that directed movement can be realized on surfaces with higher contact-angle hysteresis if vibration is applied.<sup>13</sup>

Regarding polymer-based surfaces, mainly two different strategies have been pursued to create a wettability gradient. The first approach involves the gradual surface modification of a polymer surface by irradiation, chemical etching, corona discharge or radio frequency plasma discharge.<sup>14</sup> Alternatively, self-assembled monolayers, polymer brushes, thin polymer films or coatings are gradually applied on a substrate.<sup>15</sup>

Among the various techniques, preparation routes based on a light triggered change in wettability have gained increased attention since photo-induced reactions have several advantages such as a temporal and spatial control, are not invasive and can be carried out at room temperature.<sup>16</sup>

Ito and co-workers reported the switching between hydrophobic and hydrophilic surface properties by following a photodegradation of an alkylsilane self-assembled monolayer.<sup>17</sup> The wettability gradient on the surface was adjusted by the irradiation dose. In addition, they showed that the gradient significantly influences the speed of the moving droplet, which increases at higher gradients.

Ichimura et al. modified a surface with a calix[4]resorcinarene derivative containing photoreversible azobenzene units at the terminal positions.<sup>18</sup> They were able to force a droplet in a directional motion over the surface by asymmetrical photoisomerization of the azobenzenes groups. In the cis-state the azobenzene units increased the hydrophilicity of the surface whilst in the trans-state the surface was hydrophobic. Thus, a gradient in surface free energy was obtained by an asymmetrical irradiation and the velocity of the

droplet was easily adjusted by the intensity and gradient of the light exposure. Another interesting approach is reported by Leigh and coworkers, who transported a liquid droplet by using rotaxanebased photoresponsive molecular shuttles.<sup>19</sup>

The ability to induce and manipulate liquid motion simply by light exposure has gained increased attention in the design of microfluidic devices, where the fluids flow enclosed in micrometer sized channels.<sup>20</sup> Another approach in the design of micro-reactors and in laboratory-on-a-chip settings relies on the light-induced movement of discrete droplets with a volume in the range of pL to mL. By using photo-reversible chemical reactions to tune the wettability gradient, desired microfluidic operations such as injection, pumping, mixing or sorting might be realized and reconfigured on demand in future devices.<sup>21</sup>

Along with a wettability gradient, wedge-patterned surfaces have become a promising strategy for the directed transport of liquids.<sup>22</sup> The movement of the droplet is driven by the Laplace pressure gradient, which is controlled by the wedge angle. Recently, the concept was extended by Zheng and coworkers, who pursued a multi-gradient approach, which is also found in nature.<sup>23</sup> By mimicking the water-collecting strategies of desert beetles and spider silk, they prepared starshaped wettability patterns combining a wettability gradient and a Laplace pressure gradient to spontaneously move a water droplet on a high adhesion surface. Graphite plates were used as substrates, which were treated by anodic oxidation to accomplish the wettability gradient whilst the hydrophobic frame of the wedge was obtained by a paraffin wax coating. Thus, the fabrication of the multi-gradient surface is rather complex and is limited to inorganic materials.

Inspired by this study, we transferred the concept of multigradients to photopolymer surfaces by preparing photocurable thiol-yne formulations with photo-switchable wettability and solubility properties. The molecular architecture of the networks relies on the synthesis of o-nitrobenzyl alcohol derivatives with terminal alkyne groups, which are crosslinked across multi-functional thiols by a photo-induced thiol-yne reaction (see Fig. 1a). The curing of the resin formulation is initiated by visible light exposure using phenylbis(2,4,6-trimethylbenzoyl)phosphine oxide (BAPO) as photoinitiator whilst the subsequent cleavage of the chromophores proceeds in the UV-A spectral region. This

enables a spatially controlled modulation of material properties simply by light exposure. For sample preparation, thin films were cured by flood exposure with visible light (see Fig. 1b). In a subsequent step, wedge-shaped structures with a wettability gradient were inscribed by patterned and asymmetrical UV irradiation (see Fig. 1c). Due to the photo-induced formation of polar cleavage groups and oxidation products, a lengthwise wettability gradient is realized within the wedge (see Fig. 1d). Since the nonilluminated areas remain hydrophobic, both a Laplace pressure gradient and a wettability gradient are obtained during one process step. Thus, the photo-triggered approach benefits from a high versatility as wettability and Laplace pressure gradients can be easily and locally adjusted by varying the irradiation parameters and pattern designs.

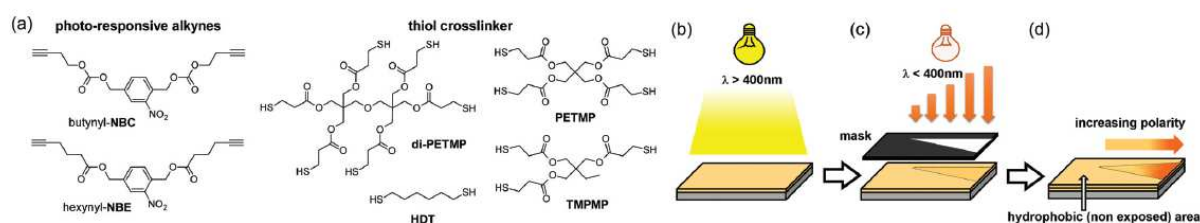


**Fig. 1** (a) Photo-responsive bi-functional alkynes and multi-functional thiols used for the preparation of thiol-ene networks with multi-gradient surface properties and schematic representation of the photo-induced formation of a Laplace pressure gradient and a wettability gradient on thiol-ene photopolymer surfaces. (b) Flood exposure with visible light to generate the photo-responsive thiol-ene network. (c) Patterned and asymmetrical UV exposure to realize (d) a wedge-shaped surface area with a lengthwise wettability gradient, which is surrounded by the hydrophobic (not exposed and thus, not-cleaved) thiol-ene network.

## Results and discussion

### Synthesis and curing of photo-responsive thiol-ene networks

Two *o*-NB alcohol derivatives bearing terminal alkyne groups were synthesized (see Fig. 2) for the preparation of photoswitchable thiol-ene networks. (2-Nitro-1,4-phenylene)bis(methylene) 1-hexynoate (hexynyl-NBE) was obtained by a Steglich esterification of (2-nitro-1,4-phenylene)dimethanol with 5-hexynoic acid. The one-step synthesis afforded the product in 70% of the theoretical yield.

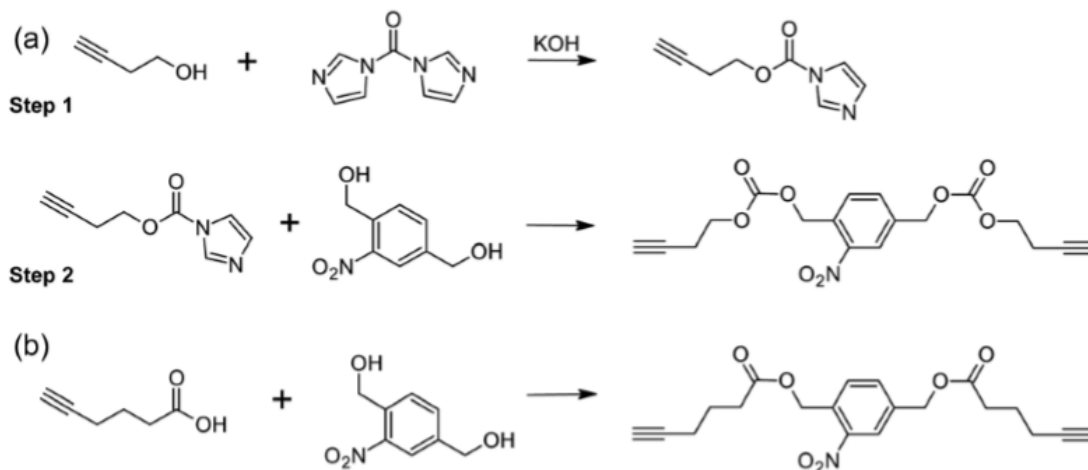


Fig. 2 Synthesis of (a) butynyl-NBC and (b) hexynyl-NBE.

In addition, di(but-3-yn-1-yl)[(2-nitro-1,4-phenylene)bis(methylene)]bis(carbonate) (butynyl-NBC) was achieved by a two-step reaction involving the formation of an imidazole carboxylic ester derivative by reaction of 3-butyn-1-ol with a slight excess of 1,1'-carbonyldiimidazole and catalytic amounts of KOH.<sup>24</sup> The formed intermediate was reacted with (2-nitro-1,4-phenylene)dimethanol to give butynyl-NBC in decent yields (76%). <sup>1</sup>H NMR, <sup>13</sup>C NMR and FT-IR spectra were in accordance with the proposed structures (see Fig. S1–S6 in ESI†).

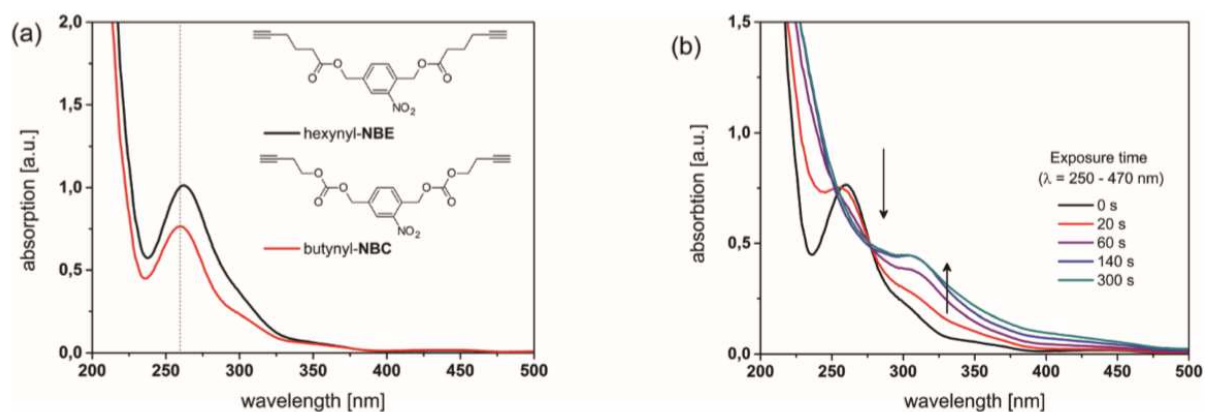


Fig. 3 (a) UV-vis absorption spectra of the photosensitive alkyne monomers ( $0.01 \text{ mg mL}^{-1}$  in acetonitrile). (b) Following the UV-vis absorbance of butynyl-NBC ( $0.01 \text{ mg mL}^{-1}$  in acetonitrile) upon UV exposure ( $269 \text{ mW cm}^{-2}$ ).

The absorption profile of both monomers in acetonitrile was determined by UV-vis spectroscopy (see Fig. 3 and Fig. S7 in ESI†). With respect to hexynyl-NBE the characteristic absorption maximum of the o-NBE group is observed at 262 nm, which

slightly shifts to shorter wavelengths (260 nm) if a carbonate group is introduced as linker (butynyl-NBC). Upon prolonged UV exposure, the absorption band of the photosensitive chromophore disappears in both monomers, whilst increasing absorption bands between 270 and 470 nm are observed. The results are in good agreement with the absorption spectra shown by Wirz and co-workers, who have studied the photocleavage reaction of 2-nitrobenzyl methyl ether. They reported that the arising absorption bands can be attributed to the formation of primary (e.g. o-nitrosobenzaldehyde) and secondary cleavage (e.g. azo-derivatives) products.<sup>25</sup> These characteristic changes in the UV-vis spectra were also observed in our previous work on o-NBE derivatives bearing terminal alkene groups.<sup>26</sup> From the results it can be concluded that the photolysis of the two newly synthesized alkyne monomers proceeds rapidly in solution.

Photopolymer networks were subsequently prepared by photo-induced curing of the photo-sensitive alkyne monomers with selected multi-functional thiols (see Fig. 1a). The radicalmediated thiol-yne reaction proceeds with two thiol groups adding consecutively to a single alkyne bond giving rise to the formation of various addition products as shown in Fig. 4a. Due to their step-growth mechanism, thiol-yne networks are well known for their homogeneous network characteristics, which correspond to low shrinkage stress and high toughness.<sup>27,28</sup>

The curing kinetics was determined by FT-IR spectroscopy following the depletion of the characteristic C-H absorption band of the terminal alkyne groups at 3100–3200  $\text{cm}^{-1}$  and the S-H absorption peak of the thiols at 2670  $\text{cm}^{-1}$  (see Fig. S8 in ESI†). In the first step, the reaction kinetics of the two alkyne monomers with 2 equiv. of thiols was studied as a function of the thiol functionality (3, 4 and 6). By comparing the reactivity of both alkynes, it is obvious that the radical-mediated addition of thiols to hexynyl-NBE is characterized by higher monomer conversions and faster reaction rates (see Fig. 4b and c). The superior curing performance of hexynyl-NBE is independent of the functionality of the thiol crosslinker and might be explained by the longer carbon spacer (3 methylene groups in hexynyl-NBE versus 2 in butynyl-NBC). A higher number of methylene groups may significantly alter the flexibility of the spacer with the terminal alkyne groups and thus, the reactivity of the monomer in the thiol-yne reaction.



The results further show that both reaction rate and final monomer conversion increase with decreasing functionality of the thiol (see Fig. 4b and c). This behaviour is also observed in radical-mediated thiol-ene reactions and can be attributed to diffusion limitations of the reactive monomers.<sup>29</sup> An increase in thiol functionality leads to a decrease in the monomer conversion at which the gel point occurs and thus, slowing down the photopolymerization kinetics. This is also in good agreement with the higher curing rates observed with hexynyl-NBE.

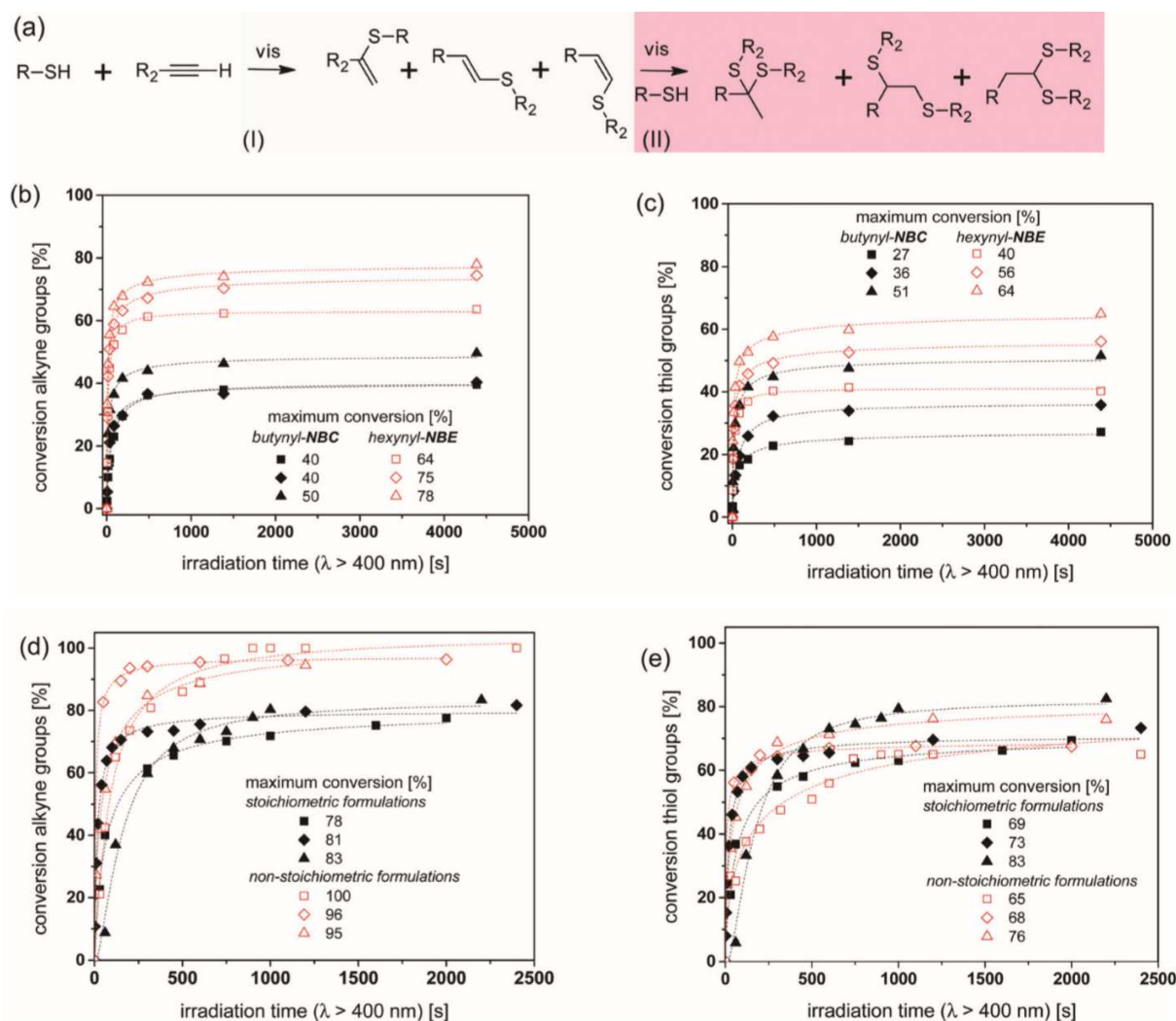


Fig. 4 (a) Schematic representation of possible addition products of the radical mediated thiol-alkyne reaction as obtained from ref. 27. (I) Radical-mediated hydrothiolation of an alkyne yielding a vinylthioether as intermediate product and (II) subsequent hydrothiolation of the vinylthioether leading to the formation of dithioether derivatives. Monitoring the normalized (b) alkyne ( $3100\text{--}3200\text{ cm}^{-1}$ ) and (c) thiol ( $2570\text{ cm}^{-1}$ ) conversion in thiol-yne resin formulations containing either butynyl-NBC (full symbols) or hexynyl-NBE (open symbols) and 2 equiv. of selected thiols by means of FT-IR spectroscopy: di-PETMP (squares), PETMP (diamonds) and TMPMP (triangles). Following the normalized (d) alkyne and (e) thiol conversion in thiol-yne formulations with hexynyl-NBE and a varying content of HDT by means of FT-IR spectroscopy. Thiol-yne formulations with 2 (full symbols) and 3 (open symbols) equiv. of selected thiols. The thiol component is varying and comprised a 1:1 molar ratio of TMPMP and HDT (squares), 1:2 molar ratio of TMPMP and HDT (diamonds) and 1:3 molar ratio of TMPMP and HDT (triangles). Irradiation was carried out with visible light ( $\lambda = 420\text{--}450\text{ nm}$ ,  $3.6\text{ mW cm}^{-2}$ ) under air. The lines are a guide for the eye.



Since diffusion control of the monomers plays an important role in the cure kinetics, a higher flexibility of the spacer may lead to a faster reaction.

Taken into account that the concentration of thiols is twice that of alkynes in the formulations, the FT-IR experiments reveal that the conversion of the monomers is not stoichiometric, since the alkyne conversion is significantly higher than the thiol one. This is particularly pronounced in thiol-yne formulations containing hexynyl-NBE as alkyne monomer. It is reported in literature, that intermediate vinyl sulfide species can undergo homopolymerization during the thiol-alkyne reaction, which would explain the higher alkyne conversion.<sup>30</sup> In the FT-IR spectra of the cured thiol-yne networks (see Fig. S8 in ESI<sup>†</sup>), vinyl sulfide peaks (between 1650 and 1700  $\text{cm}^{-1}$ ) were not observed. However, it has to be considered that the absorption bands may be considerably shifted compared to the expected range. In addition, vinyl sulfide absorption bands comprise a low intensity in FTIR spectroscopy and due to the possible overlap with other intense peaks the presence of vinyl sulfides cannot be clearly confirmed by the reported data.

Along with the monomer conversion, the FT-IR spectra further revealed that the normalized peak area of the two characteristic  $\text{NO}_2$  absorption bands at 1537  $\text{cm}^{-1}$  (asym. stretching) and 1348  $\text{cm}^{-1}$  (sym. stretching) does not change significantly during the photocuring process (see Fig. S9 in ESI<sup>†</sup>). This indicates that the photocleavable chromophore is not affected by the curing step, which is carried out with visible light at wavelengths between 420 and 450 nm. These results are also confirmed by UV-vis measurements, since the absorption profile of resin 3EQ-1H-1T did not change significantly during the photocuring reaction (see Fig. S10 in ESI<sup>†</sup>).

To increase the alkyne conversions in the thiol-yne networks, two strategies were pursued involving the addition of bi-functional thiols to overcome diffusion limitations and an increase of the thiol concentration from 2 to 3 thiols equiv. Fig. 4d and e detail the conversion of hexynyl-NBE with 2 equiv. thiols comprising different ratios of TMPMP (3 thiol groups) and HDT (2 thiol groups). Whilst the photopolymerization of hexynyl-NBE with TMPMP yields a final alkyne and thiol conversion of 78% and 64%, respectively, both monomer conversions can be successfully increased to 83% at a 1:3 molar ratio of TMPMP and HDT. The stoichiometric conversion of the monomers at a high level of the

bifunctional HDT suggests that the amount of homopolymerization can be reduced in the presence of highly mobile thiols. This effect seems to be even more pronounced if increasing at the same time the thiol concentration from 2 to 3 equivalents. All three resin formulations exhibited the 2 to 1, thiol-to-alkyne reactivity with an equimolar (with 3 equivalents of thiol groups an equimolar consumption equals a thiol conversion of approximately 66% that of alkynes) and nearly full conversion of the alkyne groups. Due to the significantly higher conversion, the further cleavage studies were carried out with resin formulations containing hexynyl-NBE as alkyne monomers together with TMPMP and HDT as thiol crosslinkers.

The glass transition temperature ( $T_g$ ) of these networks was studied in a subsequent step. Due to their flexible thioether bonds, the  $T_g$  of the described photo-responsive thiol-yne systems did not exceed  $-10\text{ }^\circ\text{C}$  (see Table 1). This is explained by the high content of bifunctional HDT, which lowers the crosslink density of the networks. This is also confirmed by the decrease in  $T_g$  (from  $-10$  to  $-16\text{ }^\circ\text{C}$ ) by rising the HDT concentration from a 1:1 to a 1:3 molar ratio of TMPMP:HDT. This effect is even more pronounced in networks containing 3 thiols equiv. Although the low  $T_g$  limits the applicability of the networks in structural applications, it is beneficial in the subsequent photocleavage, since previous work showed that highly mobile polymer networks are typically characterized by fast photocleavage rates.<sup>26,31,32</sup>

#### *Photo-switching the properties of photo-responsive thiol-yne networks*

The photocleavage of the photo-cured thiol-yne formulations was studied in spin-cast films upon irradiation with UV-light at wavelengths below 400 nm. The photo-induced cleavage of *o*-NB alcohol derivatives can be conveniently monitored by FT-IR spectroscopy (see Fig. 5a).<sup>33</sup> The nitro group is converted to nitroso moieties leading to a decrease of the two characteristic  $\text{NO}_2$  absorption bands at  $1537\text{ cm}^{-1}$  (asym. stretching) and  $1348\text{ cm}^{-1}$  (sym. stretching) upon UV exposure.

The depletion of the nitro signals is accompanied by a broadening of the C=O absorption band ( $1635\text{--}1802\text{ cm}^{-1}$ ), which is attributed to the formation of the characteristic cleavage products (e.g. carboxylic acids).

The kinetics of the cleavage reaction as a function of the thiol equivalency and the ratio between HDT and TMPMP was determined by following the depletion of the NO<sub>2</sub> absorption band at 1537 cm<sup>-1</sup> upon prolonged UV exposure (see Fig. 5b). The FT-IR studies reveal that the photocleavage proceeds rapidly with a final nitro group conversion ranging between 89 and 100%. Besides the conversion of the nitro groups, a decrease of the remaining thiol band at 2670 cm<sup>-1</sup> (see insert in Fig. 5a) is observed upon UV exposure. It should be noted that residual photoinitiator and thiol monomers were not extracted from the film prior to UV exposure. Thus, the decrease in the thiol peak is explained by a photo-induced disulfide formation, which is more pronounced in highly mobile thiol- $\pi$  networks that contain a high content of free thiol groups. The additional disulfide formation might be responsible for the lower cleavage rate of thiol- $\pi$  networks comprising a higher total thiol content and a higher HDT concentration, since the incident light initiates two different reactions. However, even in the presence of the disulfide formation, the photocleavage is highly efficient and is accomplished between 60 and 160 s.

Extraction experiments with various organic solvents were carried out to lower the amount of residual monomers and photoinitiator in the polymer networks. However, the organic solvents compromised on the film quality (formation of cracks and other defects) and led to a deformation of the surface (formation of wrinkles). Since a defined and high surface quality is crucial for the subsequent experiments on the directed transport of water droplets, no extraction procedures were applied.

**Table 1 Glass transition temperature ( $T_g$ ), advancing ( $\theta_{adv}$ ) and receding ( $\theta_{rec}$ ) water contact angle and hysteresis ( $\Delta\theta$ ) of thiol- $\pi$  formulations prior to and after UV exposure**

	Cured <sup>a</sup>				Cured and cleaved <sup>b</sup>		
	$T_g$ (°)	$\theta_{adv}$ (°)	$\theta_{rec}$ (°)	$\Delta\theta_{non-irr}$ (°)	$\theta_{adv}$ (°)	$\theta_{rec}$ (°)	$\Delta\theta_{irr}$ (°)
2EQ-1T-1H	-10	91 ± 1	36 ± 4	55	14 ± 5	12 ± 2	2
2EQ-1T-2H	-16	96 ± 4	42 ± 3	54	19 ± 3	19 ± 3	0
2EQ-1T-3H	-16	96 ± 2	30 ± 5	66	22 ± 3	8 ± 2	14
3EQ-1T-1H <sup>c</sup>	-12	93 ± 3	27 ± 10	66	13 ± 1	13 ± 2	0
3EQ-1T-2H	-20	94 ± 1	27 ± 5	67	24 ± 1	15 ± 3	9
3EQ-1T-3H	-26	89 ± 2	41 ± 9	48	21 ± 4	8 ± 3	13

<sup>a</sup> 4.1 J cm<sup>-2</sup>,  $\lambda > 400$  nm, air. <sup>b</sup> 538 J cm<sup>-2</sup>,  $\lambda < 400$  nm, air. <sup>c</sup> 807 J cm<sup>-2</sup>,  $\lambda < 400$  nm, air.

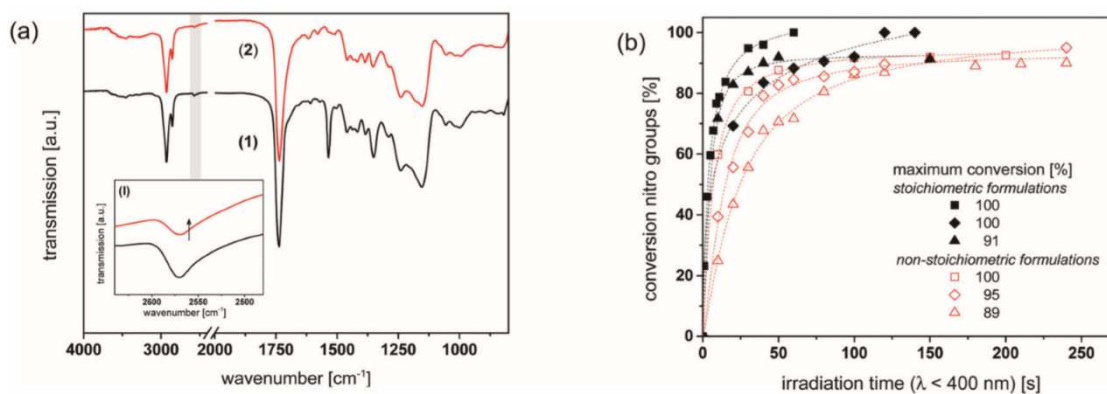


Fig. 5 (a) FT-IR spectra of cured 3EQ-1T-3H (see Table 3) (1) prior to and (2) after photo-induced cleavage of the o-NBE links ( $21.5 \text{ J cm}^{-2}$ ,  $\lambda < 400 \text{ nm}$ ,  $\text{N}_2$ ). (I) Absorption band related to SH groups magnified out of the FT-IR spectra. (b) Following the photoisomerization kinetics of the o-NBE links in photo-responsive thiol- $\pi$  networks by FT-IR spectroscopy upon prolonged UV exposure ( $269 \text{ mW cm}^{-2}$ ,  $\lambda < 400 \text{ nm}$ ,  $\text{N}_2$ ). Thiol- $\pi$  formulations with hexynyl-NBE and 2 (full symbols) and 3 (open symbols) equiv. of selected thiols. The thiol component is varying and comprised a 1:1 molar ratio of TMPMP and HDT (squares), 1:2 molar ratio of TMPMP and HDT (diamonds) and 1:3 molar ratio of TMPMP and HDT (triangles). The lines are a guide for the eye.

Several studies demonstrate the change of hydrophobic to hydrophilic surface characteristics by the photocleavage of o-NBE chromophores.<sup>34</sup> The majority of the concepts describe latent polymer brushes and polymer chains from which o-NBE groups are cleaved off by UV exposure.<sup>35</sup> In the current study, the photolysis of o-NBE links proceeded in a polymer network and the formation of polar groups was confirmed by contact angle measurements. Fig. 6a illustrates the static water contact angle of spin-cast thiol- $\pi$  formulations comprising hexynyl-NBE and 3 equiv. of thiols. The contact angle of the cured films is rather high and ranges between  $92$  and  $97^\circ$ . Subsequent UV exposure was carried out either under inert conditions or air. In  $\text{N}_2$  atmosphere, the water contact angle steadily decreases with increasing exposure dose and reaches a plateau ( $82$ – $85^\circ$ ) if the irradiation time exceeds  $60 \text{ s}$ . This behavior is independent on the type and content of the thiol crosslinker (see also Fig. S11a in ESI†) and was also observed in previous work on thiol-epoxy networks.<sup>32</sup> The increase in wettability is related to the formation of polar groups (mainly carboxylic acid groups) and a plateau is reached if the o-NBE groups on the surface of the polymer are fully cleaved. Moreover, the results suggest that the surface is not prone to photo-oxidation reactions under inert conditions since no further change of the contact angle is observed upon prolonged UV irradiation.

In air, the UV induced increase in surface wettability is more pronounced. In all investigated thiol- $\pi$  systems, the water contact angle did not exceed  $25^\circ$  for longer UV

irradiation times (see Fig. 6b and Fig. S11b in ESI+).

Previous work revealed that the enhanced wettability is mainly related to photo-oxidation involving an additional formation of carboxylic acid groups, which becomes the dominating reaction mechanism at higher exposure doses.<sup>32</sup> In the thiol–yne formulations under investigations a distinctive amount of free mercapto groups is present in the networks due to the incomplete conversion of the thiol crosslinker (see FT-IR kinetics in Fig. 4c and e).

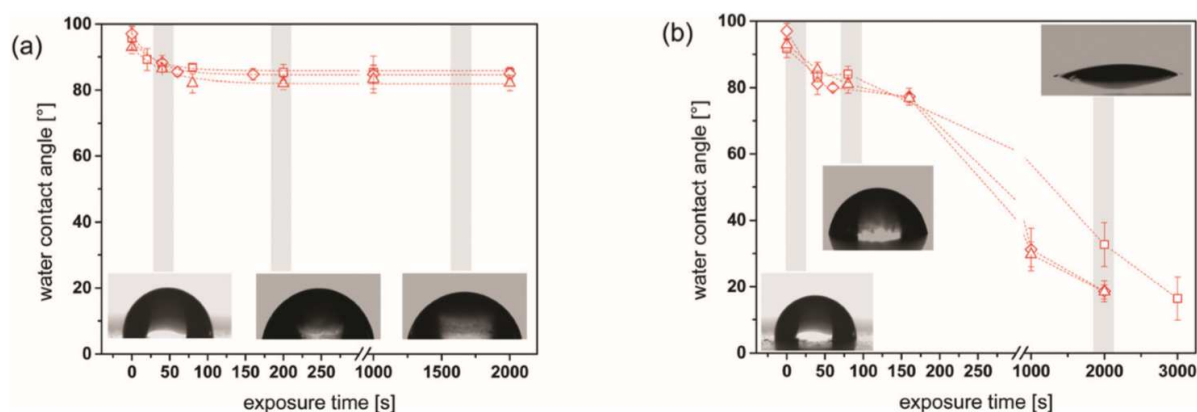


**Fig. 6** Static water contact angles of cured thiol–yne systems comprising hexynyl-NBE and 3 equiv. of selected thiols versus exposure time ( $269 \text{ mW cm}^{-2}$ ,  $\lambda < 400 \text{ nm}$ ). The thiol component is varying and comprised a 1:1 molar ratio of TMPMP and HDT (open squares), 1:2 molar ratio of TMPMP and HDT (open diamonds) and 1:3 molar ratio of TMPMP and HDT (open triangles). UV exposure was carried out either in (a) nitrogen or (b) air. Inserts depict the photographs of respective water droplet at the selected exposure dose highlighted in grey. The lines are a guide for the eye.

Griesser and co-workers reported that surface bound thiol groups are prone to UV induced oxidation reactions leading to the formation of sulfonic acids.<sup>36</sup> To study the UV-induced changes of the photopolymer surface, high-resolution XPS measurements of a cured thiol–yne formulation (2EQ-1T-2H) were performed prior to and after UV exposure. In Fig. 7a, the S 2p region of the XPS spectrum is depicted for the cured thiol–yne network. Two signals at 162 (S 2p3) and 164 eV (S 2p1) are observed, which are characteristic for mercapto groups.<sup>32</sup> Both signals decrease upon prolonged UV irradiation under air (2000 s), whilst two new bands arise at 168 and 169 eV, corresponding to the formation of sulfonic acid groups (see Fig. 7b).<sup>37</sup> Fig. 7c shows variations of the signal intensity in the S 2p region versus UV irradiation time (under air). The decrease of the mercapto groups is accompanied by a rise in the  $\text{SO}_3\text{H}$  signal with a similar rate. Upon 2000 s UV exposure more than 70% of the mercapto groups have been oxidized. In contrast, the amount of

oxidized mercapto groups does not exceed 25%, if the irradiation is carried out under inert conditions (see Fig. S12<sup>+</sup>), even at prolonged exposure time (2000 s).

With the combined processes of photocleavage and photooxidation the contact angle can be varied over a wide range (from 97–19°), which is crucial for creating high gradients in surface wettability on the surface.

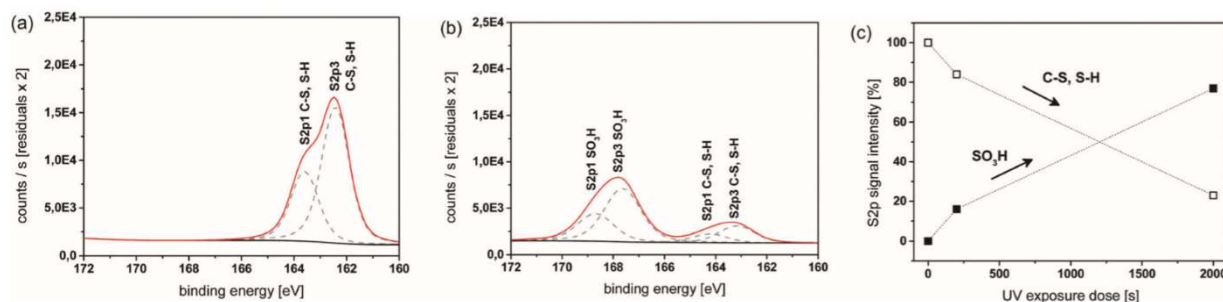


**Fig. 7** High-resolution XPS spectra of the S 2p region of a cured thiol–yne formulation (2EQ-1T-2H) (a) prior to and (b) after prolonged UV exposure (269 mW cm<sup>-2</sup>,  $\lambda < 400$  nm) under air. (c) Variations of the signal intensity in the S 2p region at 161–165 eV (open squares) and 166–170 eV (full squares) versus UV exposure time (air). The lines are a guide for the eye.

#### *Directed movement of water droplets on the surface of photo-responsive thiol–yne networks*

Previous work on the directed motility of liquids on surfaces with a gradient in wettability revealed that a low contact angle hysteresis is required to induce a movement of the droplet.<sup>7</sup> Ito and co-workers demonstrated a successful movement of a water droplet by asymmetric photodegradation of self-assembled monolayers if the hysteresis of the contact angle ( $\Delta\theta = \theta_{adv} - \theta_{rec}$ ) was below 10°.<sup>17</sup> For the thiol–yne systems under investigation, it was observed that both advancing and receding contact angle change upon UV exposure (see Table 1). In the UV irradiated state, the hysteresis is low and ranges between 0 and 13° but in the cured (not UV irradiated) state the thiol–yne networks suffer from a high hysteresis with values, which are far above 10°.

Thus, it was possible to inscribe a unidirectional wettability gradient on the surface, but due to the high hysteresis at the start of the non-exposed gradient, the droplets were only spreading longitudinally instead of moving (see Fig. 9a).

To overcome the initial restriction of the high hysteresis in the non-illuminated area, the wettability gradient was combined with a Laplace pressure gradient. In particular, a V-shaped pattern was inscribed by photolithography employing asymmetrical exposure to

UV-light. With this set-up, the motion of the water droplet is affected by four main forces (see Fig. 8).<sup>23</sup> The wettable gradient force ( $F_{wg}$ ) arises from the wettability gradient, due to the different contact angle at both ends of the droplet. Due to the wedge-shaped pattern a Laplace pressure force ( $F_L$ ) is formed length-wise, which facilitates the movement of the droplet from a less wettable to a higher wettable surface.

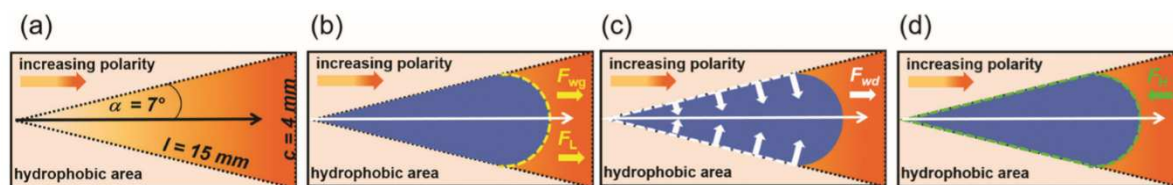


Fig. 8 Forces, which act on a water droplet on a (a) multi-gradient thiol-ylene surface comprising a Laplace pressure gradient (inscribed V-shaped pattern) and a wettability gradient (inscribed length-wise in the V-shaped pattern). Forces, which influence the movement of the water droplet, as derived from ref. 23. (b and c) Driving forces, which contribute to the movement, including wettability gradient force ( $F_{wg}$ ), Laplace pressure force ( $F_L$ ) and wettability different force ( $F_{wd}$ ). (d) The hysteresis force ( $F_H$ ), as resistance force, which prevents movement of the droplet.

Previous work revealed that the Laplace pressure is strongly influenced by the half wedge angle and Zheng and co-workers reported that it should range between 7 and 30° if a droplet volume of 2  $\mu\text{L}$  is applied.<sup>23</sup> In the current study, a half wedge angle of 7° has been chosen. By inscribing the wedge-shaped gradient on a film surface, which is rather hydrophobic, an additional force arises from the difference of wettability between inside and outside area of wedge-pattern. This force is called wettability different force ( $F_{wd}$ ) and together with the former two, represents the main driving forces for the droplet movement. In contrast, the hysteresis force ( $F_H$ ) is acting opposite to the moving direction and reduces the ability of the droplet for directed motility.

The multi-gradients were inscribed in the six investigated thiol-ylene systems and the maximum movement distance ( $L$ ) and the velocity of movement ( $v$ ) of the 2  $\mu\text{L}$  water droplet were determined. In formulations with a  $\Delta\theta_{\text{non-irr}}$  of 66° or above, spreading instead of movement of the droplet was again observed, even if  $\Delta\theta_{\text{irr}}$  was below 10°. The same behavior was obtained in the thiol-ylene system 3EQ-1T-3H, which comprises a lower  $\Delta\theta_{\text{non-irr}}$  but suffers from a  $\Delta\theta_{\text{irr}}$  above 10°. The results suggest that in these cases,  $F_L$  and  $F_{wd}$  are not able to overcome the hysteresis force ( $F_H$ ) and also increasing the half wedge angle from 7 to 10 and 20° in further experiments did not induce a movement of the droplet.

However, the combined gradients facilitated a unidirectional movement of a single 2  $\mu\text{L}$  water droplet, if  $\Delta\theta_{\text{non-irr}}$  as well as  $\Delta\theta_{\text{irr}}$  were below 60 and 10°, respectively. Both  $L$  and  $v$  increase with lower hysteresis of the irradiated and non-irradiated gradient areas within the wedge-pattern. In particular, for 2EQ-1T-1H, with a  $\Delta\theta_{\text{non-irr}}$  of 55° and  $\Delta\theta_{\text{irr}}$  of 2°, the movement distance amounted to 5 mm with a velocity of 0.85 mm s<sup>-1</sup> (see Fig. S13 in ESI†). Regarding 2EQ-1T-2H, comprising a slightly lower hysteresis in the non-irradiated (54°) and irradiated (0°) end of the wedge, the efficiency of the droplet movement significantly increased and the movement distance was doubled to 10 mm (see Fig. 9b). The larger distance was accompanied with a higher velocity that amounted to 1.25 mm s<sup>-1</sup> (a video of the droplet movement is provided in ESI†).

The concept enables the transport of the droplet, even on an inclined (20°) photopolymer surface as shown in Fig. 9c. The movement distance is lower but the water droplet can be successfully transported uphill over 5 mm.

Due to the moderate hydrophilicity of the thiol–yne surface prior to UV exposure, a retention of the water droplet at the surface is observed if the sample is turned upside down. Thus, the directed movement of the water droplet ( $L = 10$  mm) can be also realized if the sample is inverted (see Fig. 9d).

The results clearly showed that by combining gradients in wettability and Laplace pressure, directed movement of droplets on a photopolymer surface can be realized, even if the surface comprises a high initial hysteresis at one end of the V-shaped pattern. Due to the photo-responsive nature and versatility of the photo-switchable thiol–yne systems (curing as well as wettability performance are optically triggered), complex design patterns and gradients can be easily generated simply by light exposure. Going beyond 2D patterning, the developed concept has also the potential to be transferred to additively manufactured structures, since the network formation relies on photo-induced thiol–yne chemistry. This opens the path towards a controlled movement of individual or multiple droplets on surfaces with complex topology and tailored surface polarity.

However, it should be noted that the irreversible nature of both cleavage and oxidation reactions limits the applicability of the photo-responsive thiol–yne material in microfluidic devices. When it comes to digital microfluidic applications, a bi-directional manipulation



of discrete droplets by light is often desired, which requires a reversible switching of surface properties.

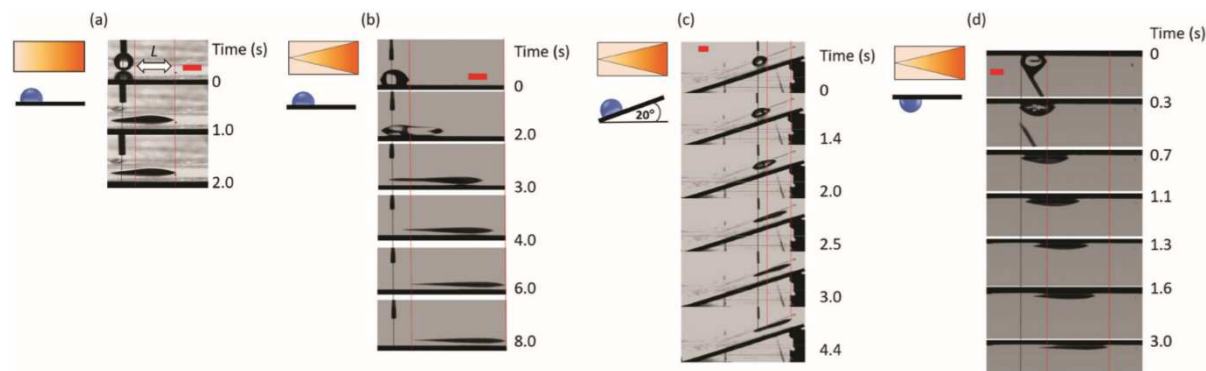


Fig. 9 Movement of a 2  $\mu\text{L}$  water droplet on the surface of 2EQ-1T-2H (see Table 3) with (a) a unidirectional gradient in wettability and (b) with a combined gradient of wettability and Laplace pressure. Movement of a 2  $\mu\text{L}$  water droplet on the surface of 2EQ-1T-2H with a combined gradient of wettability and Laplace pressure if the prepared surface is (c) tilted ( $20^\circ$ ) or (d) turned upside down. The scale bar is 2 mm.

## Experimental

### Materials and chemicals

The photoinitiator phenylbis (2,4,6-trimethylbenzoyl)-phosphine oxide (BAPO) was obtained from BASF (Germany). Dipentaerythritol hexa(3-mercaptopropionate) (di-PETMP), pentaerythritol tetra(3-mercaptopropionate) (PETMP) and trimethylolpropane tris(3-mercaptopropionate) (TMPMP) were provided by Bruno Bock Thiochemicals (Germany). (2-Nitro-1,4-phenylene)dimethanol was supplied by TCI (Belgium). 1,6-Hexanedithiol (HDT) and all other chemicals were from Sigma-Aldrich (United States) and were used without further purification.

### Synthesis

**Di(but-3-yn-1-yl)[(2-nitro-1,4-phenylene)bis(methylene)]bis (carbonate) (butynyl-NBC):** Step 1: 3-Butyn-1-ol (25.0 g, 0.36 mol) was added to a mixture of 1,1'-carbonyldiimidazole (CDI) (70.0 g, 0.43 mol) in 350 mL abs. toluene with a catalytic amount (10 mg) of KOH at  $60^\circ\text{C}$ . After 6 h, the reaction was quenched by the addition of water. It was extracted by dichloromethane three times and the combined organic layers were washed with water and NaCl solution. The combined organic layers were dried over  $\text{Na}_2\text{SO}_4$ . The solvent was evaporated under reduced pressure to yield 57.9 g (98%) of imidazole carboxylic ester derivative (see Fig. 2), without further purification, as a

colorless solid.

<sup>1</sup>H-NMR (δ, 400 MHz, 25 °C, CDCl<sub>3</sub>): 8.08 (s, 1H, Im-H), 7.40 (d, 1H, Im-H), 6.99 (d, 1H, Im-H), 4.92 (d, 2H, CH<sub>2</sub>-O), 2.61 (t, 1H, C=CH), 1.36 (t, 2H, CH<sub>2</sub>-CH<sub>2</sub>-O) ppm.

<sup>13</sup>C-NMR (δ, 400 MHz, 25 °C, CDCl<sub>3</sub>): 150.20 (1C, CH<sub>2</sub>-O-C=O); 136.81 (1C, Im-C); 130.84 (1C, Im-C); 117.66 (1C, Im-C); 81.49 (1C, C=CH); 69.70 (1C, C=CH); 60.27 (1C, CH<sub>2</sub>-O); 21.71 (C, CH<sub>2</sub>-CH<sub>2</sub>-O) ppm.

FT-IR (cm<sup>-1</sup>): 2970, 1739, 1369, 1286, 1217, 1015, 847, 764, 742, 649.

Step 2: The imidazole carboxylic ester derivative (5 g, 30 mmol, 2.2 equiv.) was dissolved in 50 mL toluene with a catalytic amount of KOH (0.9 mmol) and (2-nitro-1,4-phenylene)dimethanol (2.5 g, 13.6 mmol, 1 equiv.) was added to the stirred solution. After stirring the reaction mixture for 24 hours at 60 °C, the solvent was removed by rotary evaporation. The product mixture was dissolved in dichloromethane and extracted with water and saturated NaHCO<sub>3</sub> solution. The combined organic layers were dried over Na<sub>2</sub>SO<sub>4</sub>, filtered and the solvent was evaporated under reduced pressure. Chromatography on silica gel (cyclohexane:ethyl acetate 1:1) afforded butynyl-NBC as a white solid (76% of the theoretical yield).

<sup>1</sup>H-NMR (δ, 400 MHz, 25 °C, CDCl<sub>3</sub>): 8.16 (s, 1H, ph<sup>3</sup>), 7.66 (s, 2H, ph<sup>5,6</sup>), 5.58 (q, 2H, CH<sub>2</sub><sup>1b</sup>), 5.21 (q, 2H, CH<sub>2</sub><sup>1a</sup>), 4.25 (m, 4H, CH<sub>2</sub><sup>3a,3b</sup>), 2.59 (m, 4H, CH<sub>2</sub><sup>4a,4b</sup>), 2.01 (m, 2H, CH<sup>6a,6b</sup>) ppm.

<sup>13</sup>C-NMR (δ, 400 MHz, 25 °C, CDCl<sub>3</sub>): 154.49 (s, 1C, C=O<sup>2b</sup>), 154.36 (s, 1C, C=O<sup>2a</sup>), 147.07 (s, 1C, ph<sup>2</sup>), 136.75 (s, 1C, ph<sup>4</sup>), 133.2 (s, 1C, ph<sup>5</sup>), 131.93 (s, 1C, ph<sup>1</sup>), 128.86 (s, 1C, ph<sup>6</sup>), 124.51 (s, 1C, ph<sup>3</sup>), 79.24 (d, 2C, C<sup>5a,5b</sup>), 70.39 (d, 2 CH<sup>6a,6b</sup>), 65.89 (d, 4C, CH<sub>2</sub><sup>1a,3a,1b,3b</sup>), 18.97 (d, 2C, CH<sub>2</sub><sup>4a,4b</sup>).

FT-IR (cm<sup>-1</sup>): 3292, 1740, 1536, 1397, 1346, 1250, 976, 940, 829, 787, 649.

**(2-Nitro-1,4-phenylene)bis(methylene)1-hexynoate (hexynylNBE).** 6-Hexenoic acid (10.7 mL; 95 mmol) was added to a stirred solution of (2-nitro-1,4-phenylene)dimethanol (6.7 g; 36.6 mmol) in 40 mL dichloromethane. The reaction mixture was cooled to 0 °C and 4-(N,N-dimethylamino)pyridine (DMAP) (0.8 g; 6.5 mmol) was added. A solution of N,N'-dicyclohexylcarbodiimide (DCC) (20 g; 96.9 mmol) in 50 mL dichloromethane was placed drop-wise to the reaction mixture that was subsequently stirred at room

temperature for 2 h. The yellowish precipitate was collected by filtration and the solution was washed with water and NaHCO<sub>3</sub> solution. The combined organic layers were dried over Na<sub>2</sub>SO<sub>4</sub> and the solvent was removed by rotary evaporation. Chromatography on silica gel (cyclohexane:ethyl acetate 1:1) afforded 9.5 g of hexynylNBE (70% theoretical yield).

<sup>1</sup>H-NMR (δ, 400 MHz, 25 °C, CDCl<sub>3</sub>): 8.06 (s, 1H, ph<sup>3</sup>), 7.56 (s, 2H, ph<sup>5,6</sup>), 5.47 (d, 2H, CH<sub>2</sub><sup>1b</sup>), 5.15 (d, 2H, CH<sub>2</sub><sup>1a</sup>), 2.54 (m, 4H, CH<sub>2</sub><sup>5a,5b</sup>), 2.24 (m, 4H, CH<sub>2</sub><sup>3a,3b</sup>), 1.95 (m, 2H, CH<sup>7a,7b</sup>), 1.85 (m, 4H, CH<sub>2</sub><sup>4a,4b</sup>) ppm.

<sup>13</sup>C-NMR (δ, 400 MHz, 25 °C, CDCl<sub>3</sub>): 172.54 (s, 1C, C=O<sup>2b</sup>), 172.29 (s, 1C, C=O<sup>2a</sup>), 147.54 (s, 1C, ph<sup>2</sup>), 137.51 (s, 1C, ph<sup>4</sup>), 132.89 (s, 1C, ph<sup>5</sup>), 131.87 (s, 1C, ph<sup>1</sup>), 129.34 (s, 1C, ph<sup>6</sup>), 124.31 (s, 1C, ph<sup>3</sup>), 83.0 (d, 2C, C<sup>6a,6b</sup>), 69.35 (s, 2C, CH<sup>7a,7b</sup>), 64.34 (s, 1C, CH<sub>2</sub><sup>1a</sup>), 62.68 (s, 1C, CH<sub>2</sub><sup>1b</sup>), 32.62 (s, 2C, CH<sub>2</sub><sup>3a,3b</sup>), 23.39 (s, 4C, CH<sub>2</sub><sup>4a,5a,4b,5b</sup>) ppm.

FT-IR (cm<sup>-1</sup>): 3295, 2942, 1739, 1657, 1536, 1435, 1349, 1233, 1152, 1020, 940, 891, 819.

#### *Physico-chemical characterization of the photo-responsive alkyne monomers*

<sup>1</sup>H NMR and <sup>13</sup>C NMR spectra were taken with a Varian (United States) 400-NMR spectrometer operating at 399.66 MHz and 100.5 MHz, respectively. The spectra were referenced to Si(CH<sub>3</sub>)<sub>4</sub> and a relaxation delay of 10 s and 45° pulse were used for the acquisition of <sup>1</sup>H NMR spectra.

UV-vis spectra were recorded with a Varian (United States) Cary 50 UV-Vis spectrophotometer in absorbance mode. For irradiation experiments, butynyl-NBC and hexynyl-NBE were dissolved in acetonitrile (0.01 mg mL<sup>-1</sup>) and the solution was placed in a quartz cuvette. UV-vis spectra were taken prior to and after different UV exposures with a medium pressure Hg lamp (Omniculture S1000, Lumen Dynamics, Canada). The light intensity (power density P; in mW cm<sup>-2</sup>) in the sample plane was characterized with an integrating radiometer (Powerpuck II, EIT Instrument Markets, United States) and amounted to 269 mW cm<sup>-2</sup> (λ = 250–470 nm).

*Preparation of thiol–alkyne formulations*

Resin formulations were prepared by mixing the multi-functional thiols (see Fig. 1a) with either butynyl-NBC or hexynylNBE in specific molar ratios with 4 wt% BAPO as photoinitiator. The resin mixture was stirred at 50 °C for 50 min in order to dissolve BAPO and butynyl-NBC. The composition of the different thiol–alkyne resin formulations is summarized in Tables 2 and 3.

**Table 2 Composition of photocurable thiol–alkyne resin formulations comprising TMPMP, PETMP or di-PETMP as thiol crosslinker**

Sample	Hexynyl-NBE (mol%)	Butynyl-NBC (mol%)	Thiol crosslinker	Molar ratio alkyne/thiol groups
2EQ-1T	100	0	TMPMP	1 : 2
2EQ-1T	0	100	TMPMP	1 : 2
2EQ-1P	100	0	PETMP	1 : 2
2EQ-1P	0	100	PETMP	1 : 2
2EQ-1DP	100	0	di-PETMP	1 : 2
2EQ-1DP	0	100	di-PETMP	1 : 2

**Table 3 Composition of photocurable thiol–alkyne resin formulations comprising TMPMP and HDT as thiol crosslinker**

Sample	Hexynyl-NBE (mol%)	Molar ratio HDT : TMPMP	Molar ratio alkyne/thiol groups
2EQ-1T-1H	100	1 : 1	1 : 2
2EQ-1T-2H	100	1 : 2	1 : 2
2EQ-1T-3H	100	1 : 3	1 : 2
3EQ-1T-1H	100	1 : 1	1 : 3
3EQ-1T-2H	100	1 : 2	1 : 3
3EQ-1T-3H	100	1 : 3	1 : 3

*Characterization of the curing and cleavage kinetics*

The photocuring of the monomers and the photocleavage of the corresponding thiol–yne networks were monitored by FT-IR spectroscopy employing a Vertex 70 spectrometer (Bruker, United States). 16 scans were accumulated in transmission mode with a resolution of 4 cm<sup>-1</sup> and the absorption peak areas were calculated with OPUS software. For sample preparation, 1 μL of each resin formulation was placed between two CaF<sub>2</sub> discs. The thin films were illuminated with a light emitting diode (LED) lamp (zgood® wireless LED curing lamp). The light intensity amounted to 3.4 mW cm<sup>-2</sup> (λ = 420–450 nm). After the

curing, the polymer films were irradiated with the Omnicure S1000 lamp ( $269 \text{ mW cm}^{-2}$ ;  $\lambda = 250\text{--}470 \text{ nm}$ ) under nitrogen atmosphere and the cleavage reaction was monitored by taken FT-IR spectra after selected exposure times.

Differential scanning calorimetry (DSC) measurements were performed with a Mettler-Toledo DSC 821e instrument (United States) to characterize the thermal properties of hexynyl-NBE based resins crosslinked with TMPMP and HDT as thiol components. The cured samples were heated from  $-40$  to  $80 \text{ }^\circ\text{C}$  with a heating rate of  $30 \text{ K min}^{-1}$  in nitrogen atmosphere (nitrogen flow was  $20 \text{ mL min}^{-1}$ ). The glass transition temperature ( $T_g$ ) was obtained from the second heating run by taking the midpoint in heat capacity.

The XPS spectra of all the prepared samples were recorded using a Thermo Fisher Scientific Instrument equipped with a monochromatic Al K-Alpha X-ray source ( $1486.6 \text{ eV}$ ). High resolution scans were acquired with a pass energy of  $50 \text{ eV}$  and a step size of  $0.1 \text{ eV}$ . Survey scans were acquired with a pass energy of  $200 \text{ eV}$  and a step size of  $1.0 \text{ eV}$ . Photo electrons were collected using a take-off of  $90^\circ$  relative to the sample surface. Charge compensation was performed with an argon flood gun. All analyses were performed at  $20 \text{ }^\circ\text{C}$ .

#### *Characterization of surface polarity and wettability*

The photo-induced switching of the surface wettability was analyzed with static and dynamic contact angle measurements by using a drop shape analysis system, DSA 100, from Krüss, (Germany). Thin films were prepared by drop casting  $1.5 \text{ }\mu\text{L}$  resin formulation between a silicon wafer and a polytetrafluoroethylene foil. Irradiation was carried out with visible light (zgood® wireless LED curing lamp,  $3.4 \text{ mW cm}^{-2}$ ,  $420\text{--}450 \text{ nm}$ ) through the polymer foil in order to obtain a flat and homogeneous coating. The cured samples were UV irradiated with the Omnicure S1000 lamp ( $269 \text{ mW cm}^{-2}$ ;  $\lambda = 250\text{--}470 \text{ nm}$ ;  $\text{N}_2$  and air) to generate hydrophilic cleavage species. The surface tension of the irradiated sample was calculated by contact angle measurements ( $2 \text{ }\mu\text{L}$ ; water) few minutes (cooling down the surface temperature of the illuminated surface to room temperature) after the irradiation. To determine the dynamic contact angles the same software was used. The volume of the water droplet was  $5 \text{ }\mu\text{L}$  in order to facilitate the measurement. All of the

contact angles were determined by calculating the arithmetic average from ten different points on each sample, which have been UV irradiated with a selected exposure dose.

### *Preparation and characterization of polymer surfaces with wettability gradient and Laplace pressure gradient*

Photo-cured thiol–yne films on silicon wafers were prepared as described in the previous paragraph. In a subsequent step, wedge-shaped patterns ( $l = 15$  mm,  $c = 4$  mm,  $\alpha = 7^\circ$ ), were inscribed by photolithography using asymmetrical exposure with UV-light (see Fig. 8a). The sample surface except the wedge (dimensions mentioned above) was covered with aluminum foil and the light beam of the Omnicure S1000 lamp ( $269$  mW cm<sup>-2</sup>;  $\lambda = 250$ – $470$  nm; air) was focused on the end of the wedge. Due to the inhomogeneous intensity of the beam (2 cm distance between light source and the surface of the sample), a wettability gradient could be inscribed.

A 2  $\mu$ L water droplet was placed on the apex of the inscribed wedge (more hydrophobic area of the inscribed gradient) with the contact angle device (DSA 100, Krüss). For experiments on samples which were turned upside down, the water droplet was applied manually with a syringe. By using the high-speed digital camera system of the device, sequential photos were taken with a recording rate of 1.042 fps. The velocity of the movement was estimated by measuring the sliding distance between the starting point and the rear edge of the contact line of the droplet and the sample surface (see Fig. 9). The droplet movement behavior was recorded at least two times.

### *Conclusions*

Multi-gradients were inscribed in photopolymer networks by introducing irreversibly cleavable chromophores in photocurable thiol–yne networks. *o*-Nitrobenzyl alcohol derivatives with terminal alkyne groups were synthesized and cured across multifunctional thiols by the radical-mediated step-growth reaction. Curing of the photosensitive ester derivative (hexynylNBE) is reasonably efficient whilst its carbonate counterpart (butynyl-NBC) suffers from a low monomer conversion. Both systems are

diffusion controlled and curing rate as well as final monomer conversion increase with decreasing thiol functionality and rising total thiol content.

Patterned gradients in wettability were realized by subsequent asymmetrical UV irradiation of the visible light cured networks. The chromophores cleaved rapidly in the highly mobile thiol–yne networks ( $T_g$  ranges from  $-26$  to  $-10$  °C) as shown by FT-IR experiments. The formation of polar cleavage products led to an increase in surface polarity and wettability, which was confirmed by contact angle measurements. The light triggered modulation of surface wettability is governed by exposure dose and the atmosphere in which the UV illumination is carried out. Under inert atmosphere the change in the contact angle did not exceed  $20^\circ$  whilst the surface of the thiol–yne networks became nearly fully wettable if the UV irradiation was performed under air due to additional photo-oxidation of the surface.

The localized change in the surface polarity was exploited to generate a Laplace pressure gradient and a wettability gradient on the surface of the photopolymer network by inscribing wedge-shaped patterns (half wedge angle of  $7^\circ$ ) with photolithography and asymmetrical UV irradiation. Both gradients provide the driving force for the directed motility of a water droplet (volume  $2 \mu\text{L}$ ). Efficient movement of the water droplet over a distance of 10 mm was obtained if the contact angle hysteresis of the non-irradiated and irradiated surface area amounted to  $54$  and  $0^\circ$ , respectively. Under these conditions, directed movement of the water droplet is observed, even if the surface is inclined ( $20^\circ$ ) or turned upside down.

The developed material benefits from a high flexibility due to the light controlled tuning of Laplace pressure and wettability whilst the photocurable nature of the monomers offers the opportunity to transfer the concept to 2D and 3D printed structures. Thus, the photo-responsive photopolymer has great potential to realize complex movements of liquids, which is of great interest in pharmaceutical detection and microfluidic tools.

#### Conflicts of interest

There are no conflicts to declare.

*Acknowledgements*

This research work was performed at the Polymer Competence Center Leoben GmbH (PCCL, Austria) within the framework of the COMET-program of the Federal Ministry for Transport, Innovation and Technology and Federal Ministry for Economy, Family and Youth with contributions by the Chair of Chemistry of Polymeric Materials (Montanuniversitaet Leoben, Austria). The PCCL is funded by the Austrian Government and the State Governments of Styria, Upper and Lower Austria. D. Hennen and T. Griesser thank the Christian Doppler research association and the Austrian Ministry for Economy, Family and Youth (BMWFJ) for financial support.

*References*

- 1) K. Zhang, F. Wang and X. Zhao, *Comput. Mater. Sci.*, 2016, 124, 190–194.
- 2) M. Cao, K. Li, Z. Dong, C. Yu, S. Yang, C. Song, K. Liu and L. Jiang, *Adv. Funct. Mater.*, 2015, 25, 4114–4119.
- 3) H. Gau, *Science*, 1999, 283, 46–49.
- 4) H. G. Andrews, E. A. Eccles, W. C. E. Schofield and J. P. S. Badyal, *Langmuir*, 2011, 27, 3798–3802.
- 5) K. Liu, M. Cao, A. Fujishima and L. Jiang, *Chem. Rev.*, 2014, 114, 10044–10094.
- 6) Y.-J. Chen, Y. Nagamine and K. Yoshikawa, *Phys. Rev. E: Stat., Nonlinear, Soft Matter Phys.*, 2009, 80, 16303.
- 7) M. K. Chaudhury and G. M. Whitesides, *Science*, 1992, 256, 1539–1541.
- 8) (a) I. Paradisanos, C. Fotakis, S. H. Anastasiadis and E. Stratakis, *Appl. Phys. Lett.*, 2015, 107, 111603; (b) C. Lv, C. Chen, Y.-C. Chuang, F.-G. Tseng, Y. Yin, F. Grey and Q. Zheng, *Phys. Rev. Lett.*, 2014, 113, 26101.
- 9) I. E. Agranovski and R. D. Braddock, *AIChE J.*, 1998, 44, 2775–2783.
- 10) H. P. Greenspan, *J. Theor. Biol.*, 1978, 70, 125–134.
- 11) (a) P. C. Zielke, R. Shankar Subramanian, J. A. Szymczyk and J. B. McLaughlin, *Proc. Appl. Math. Mech.*, 2003, 2, 390–391; (b) S. C. Hernández, C. J. C. Bennett, C. E. Junkermeier, S. D. Tsoi, F. J. Bezares, R. Stine, J. T. Robinson, E. H. Lock, D. R. Boris, B. D. Pate, J. D. Caldwell, T. L. Reinecke, P. E. Sheehan and S. G. Walton, *ACS*



- Nano, 2013, 7, 4746–4755; (c) S. Feng, S. Wang, C. Liu, Y. Zheng and Y. Hou, Chem. Commun., 2015, 51, 6010–6013.
- 12) S. Daniel, S. Sircar, J. Gliem and M. K. Chaudhury, Langmuir, 2004, 20, 4085–4092.
- 13) S. Daniel and M. K. Chaudhury, Langmuir, 2002, 18, 3404–3407.
- 14) (a) T. Ueda-Yukoshi and T. Matsuda, Langmuir, 1995, 11, 4135–4140; (b) J. H. Lee, H. G. Kim, G. S. Khang, H. B. Lee and M. S. Jhon, J. Colloid Interface Sci., 1992, 151, 563–570; (c) S. Morgenthaler, C. Zink and N. D. Spencer, Soft Matter, 2008, 4, 419; (d) T. G. Ruardy, J. M. Schakenraad, H. C. van der Mei and H. J. Busscher, Surf. Sci. Rep., 1997, 29, 3–30; (e) I. Caelen, H. Gao and H. Sigrüst, Langmuir, 2002, 18, 2463–2467.
- 15) (a) T. Wu, K. Efimenko and J. Genzer, J. Am. Chem. Soc., 2002, 124, 9394–9395; (b) S. Daniel, M. K. Chaudhury and J. C. Chen, Science, 2001, 291, 633–636; (c) M. R. Tomlinson and J. Genzer, Langmuir, 2005, 21, 11552–11555; (d) O. Bliznyuk, J. R. T. Seddon, V. Veligura, E. S. Kooij, H. J. W. Zandvliet and B. Poelsema, ACS Appl. Mater. Interfaces, 2012, 4, 4141–4148.
- 16) S. Wang, Y. Song and L. Jiang, J. Photochem. Photobiol., C, 2007, 8, 18–29.
- 17) Y. Ito, M. Heydari, A. Hashimoto, T. Konno, A. Hirasawa, S. Hori, K. Kurita and A. Nakajima, Langmuir, 2007, 23, 1845–1850.
- 18) K. Ichimura, S.-K. Oh and M. Nakagawa, Science, 2000, 288, 1624–1626.
- 19) J. Berná, D. A. Leigh, M. Lubomska, S. M. Mendoza, E. M. Pérez, P. Rudolf, G. Teobaldi and F. Zerbetto, Nat. Mater., 2005, 4, 704–710.
- 20) D. Baigl, Lab Chip, 2012, 12, 3637–3653.
- 21) C. Monat, P. Domachuk, C. Grillet, M. Collins, B. J. Eggleton, M. Cronin-Golomb, S. Mutzenich, T. Mahmud, G. Rosengarten and A. Mitchell, Microfluid. Nanofluid., 2008, 4, 81–95.
- 22) M. H. Alheshibri, N. G. Rogers, A. D. Sommers and K. F. Eid, Appl. Phys. Lett., 2013, 102, 174103.
- 23) S. Deng, W. Shang, S. Feng, S. Zhu, Y. Xing, D. Li, Y. Hou and Y. Zheng, Sci. Rep., 2017, 7, 45687.

## PUBLICATION I

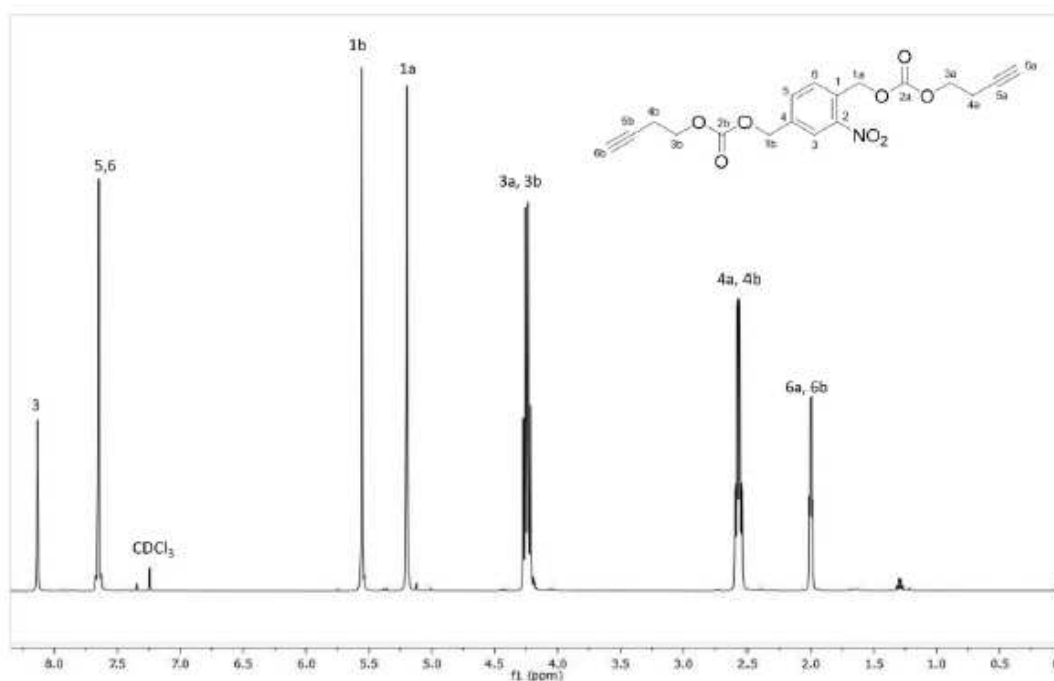
- 24) A. Oesterreicher, J. Wiener, M. Roth, A. Moser, R. Gmeiner, M. Edler, G. Pinter and T. Griesser, *Polym. Chem.*, 2016, 7, 5169–5180.
- 25) Y. V. Il'ichev, M. A. Schwörer and J. Wirz, *J. Am. Chem. Soc.*, 2004, 126, 4581–4595.
- 26) S. V. Radl, C. Schipfer, S. Kaiser, A. Moser, B. Kaynak, W. Kern and S. Schlögl, *Polym. Chem.*, 2017, 8, 1562–1572.
- 27) A. B. Lowe, *Polymer*, 2014, 55, 5517–5549.
- 28) A. Oesterreicher, C. Gorsche, S. Ayalur-Karunakaran, A. Moser, M. Edler, G. Pinter, S. Schlögl, R. Liska and T. Griesser, *Macromol. Rapid Commun.*, 2016, 37, 1701–1706.
- 29) S. K. Reddy, O. Okay and C. N. Bowman, *Macromolecules*, 2006, 39, 8832–8843.
- 30) A. B. Lowe, C. E. Hoyle and C. N. Bowman, *J. Mater. Chem.*, 2010, 20, 4745.
- 31) M. Giebler, S. V. Radl, M. Ast, S. Kaiser, T. Griesser, W. Kern and S. Schlögl, *J. Polym. Sci., Part A: Polym. Chem.*, 2018, 56, 2319–2329.
- 32) A. Romano, I. Roppolo, M. Giebler, K. Dietliker, Š. Možina, P. Šket, I. Mühlbacher, S. Schlögl and M. Sangermano, *RSC Adv.*, 2018, 8, 41904–41914.
- 33) A. P. Pelliccioli and J. Wirz, *Photochem. Photobiol. Sci.*, 2002, 1, 441–458.
- 34) N. Wagner and P. Theato, *Polymer*, 2014, 55, 3436–3453.
- 35) A. A. Brown, O. Azzaroni, L. M. Fidalgo and W. T. S. Huck, *Soft Matter*, 2009, 5, 2738.
- 36) F. H. Mostegel, R. E. Ducker, P. H. Rieger, O. El Zubir, S. Xia, S. V. Radl, M. Edler, M. L. Cartron, C. N. Hunter, G. J. Leggett and T. Griesser, *J. Mater. Chem. B*, 2015, 3, 4431–4438.
- 37) S. K. Bhatia, J. J. Hickman and F. S. Ligler, *J. Am. Chem. Soc.*, 1992, 114, 4432–4433.

## Supporting Information

## Supporting Information

**Directed motion of water droplets on multi-gradient photopolymer surfaces**Elisabeth Rossegger,<sup>a</sup> Daniel Hennen,<sup>b</sup> Thomas Griesser,<sup>b,c</sup> Ignazio Roppolo<sup>d</sup> and Sandra Schlögl<sup>a,\*</sup><sup>a</sup>Polymer Competence Center Leoben GmbH, Roseggerstrasse 12, A-8700 Leoben, Austria

e-mail: sandra.schloegl@pcccl.at

<sup>b</sup>Christian Doppler Laboratory for Functional and Polymer based Ink-Jet Inks, Otto Glöckel-Strasse 2, A-8700 Leoben, Austria<sup>c</sup>Institute of Chemistry of Polymeric Materials, Montanuniversitaet Leoben, Otto Glöckel-Strasse 2, A-8700 Leoben, Austria<sup>d</sup>Department of Applied Science and Technology, Politecnico di Torino, Corso Duca degli Abruzzi 24, 10129 Torino, ItalyFigure S1 – <sup>1</sup>H NMR spectrum of butynyl-NBC

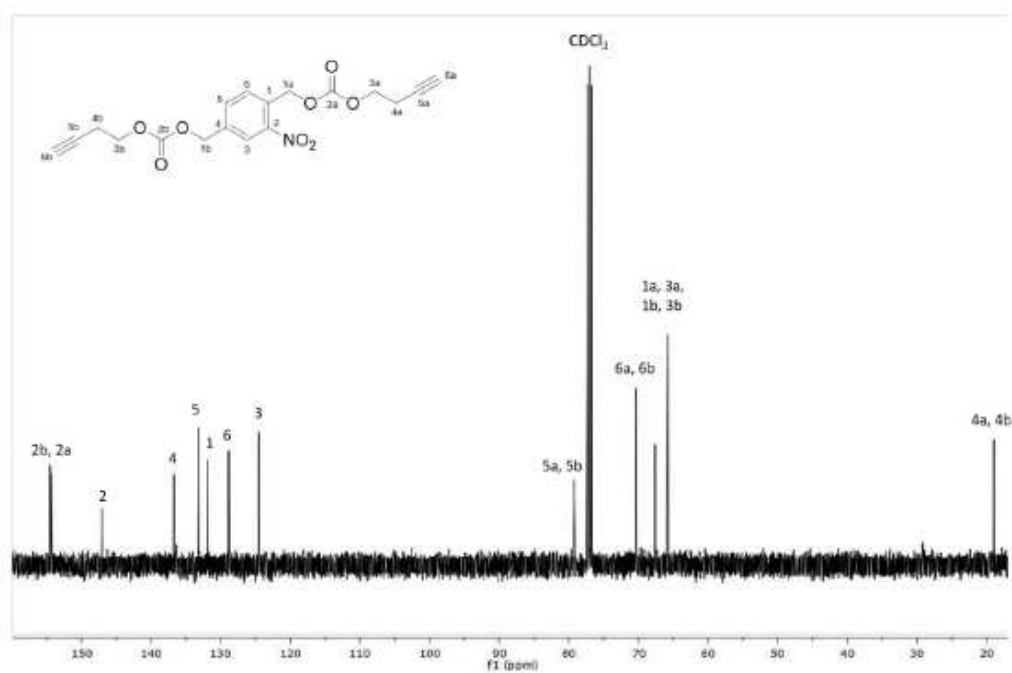
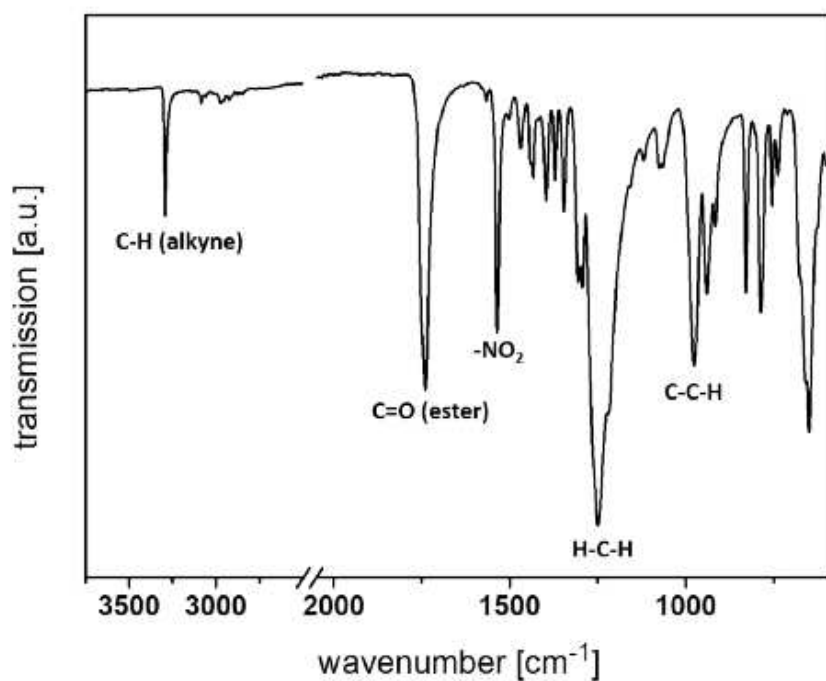
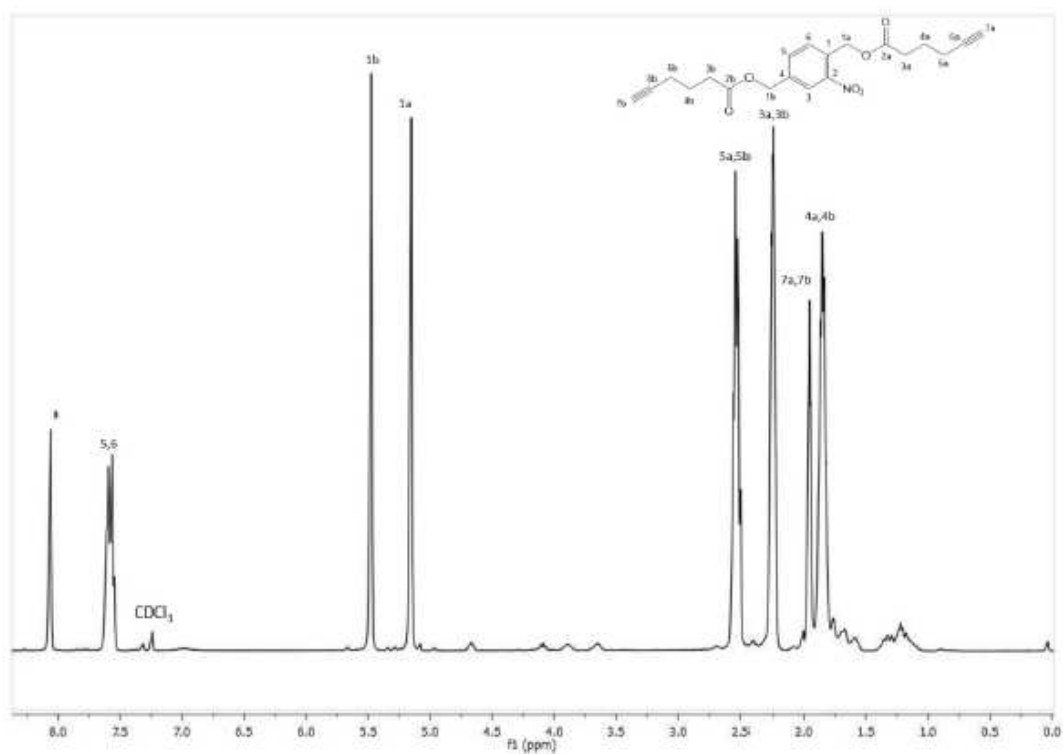
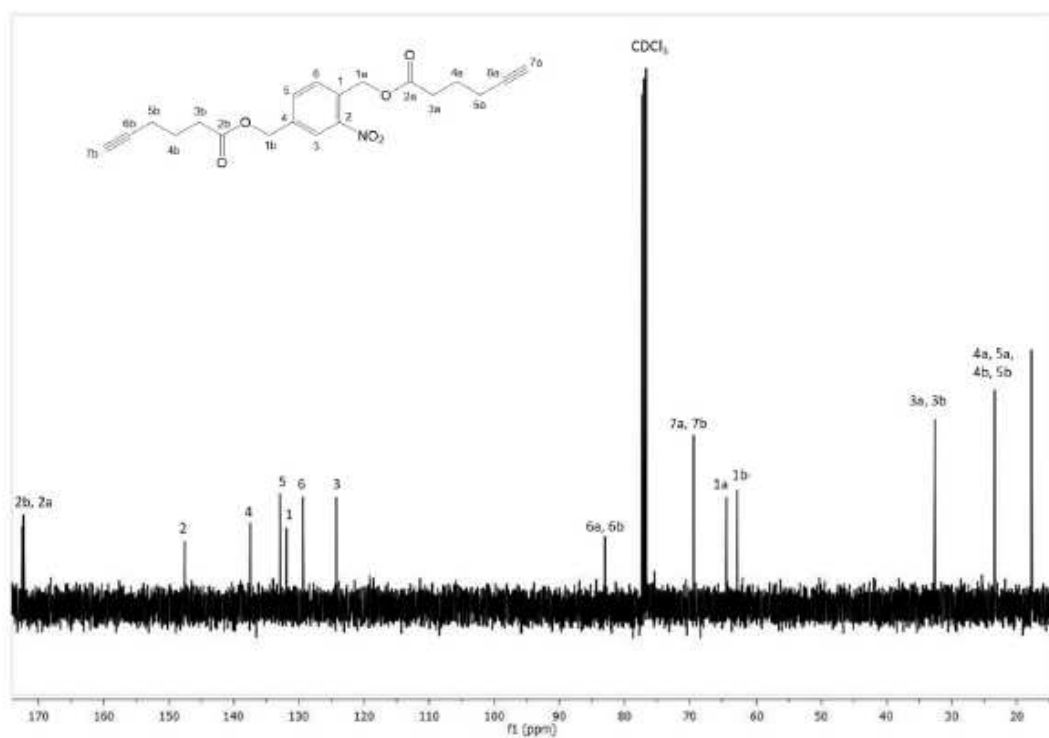
Figure S2 –  $^{13}\text{C}$  NMR spectrum of butynyl-NBC

Figure S3 – FT-IR spectrum of butynyl-NBC

Figure S4 –  $^1\text{H}$  NMR spectrum of hexynyl-NBEFigure S5 –  $^{13}\text{C}$  NMR spectrum of hexynyl-NBE

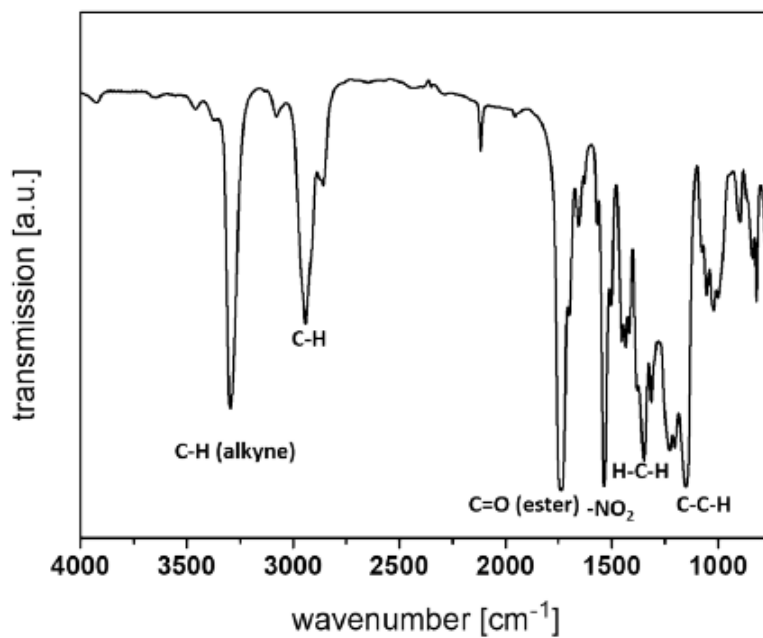
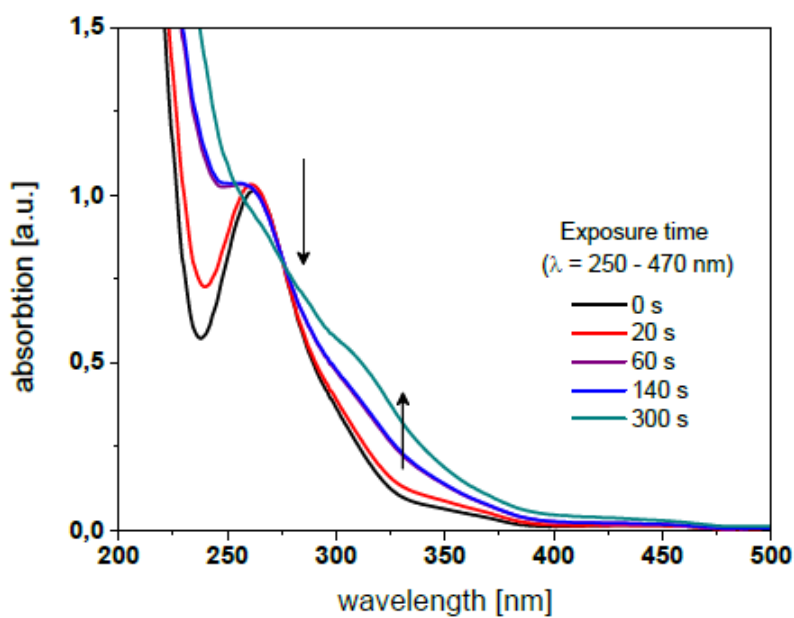
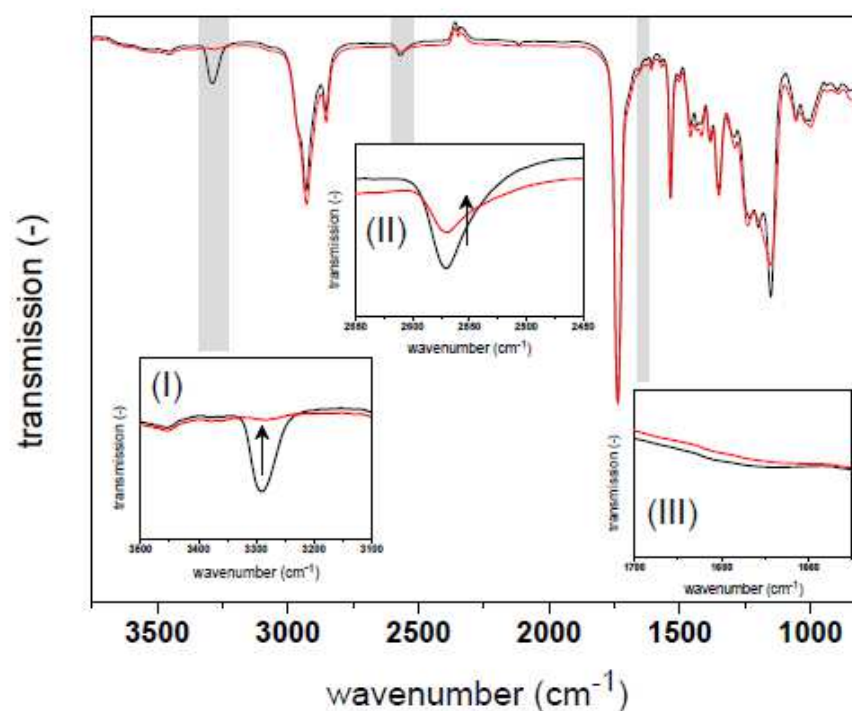
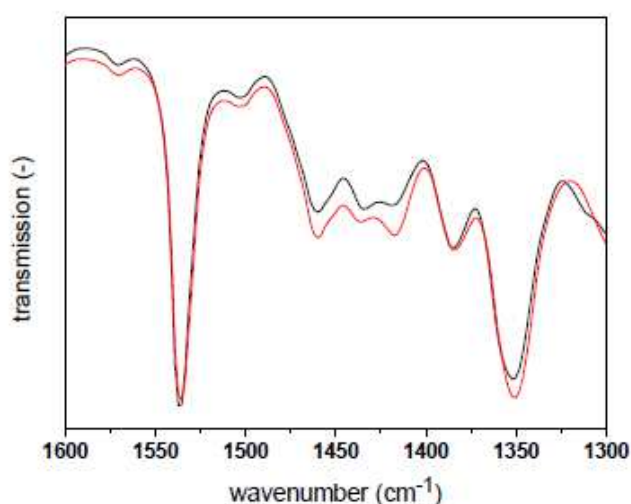


Figure S6 – FT-IR spectrum of hexynyl-NBE

Figure S7 – Following the UV-vis absorbance of hexynyl-NBE (0.01 mg/mL in acetonitrile) upon UV exposure (269 mW/cm<sup>2</sup>).



**Figure 58** – FT-IR spectra of resin 3EQ-1H-1T prior to (*black line*) and after photo-curing (*red line*). Inserts show the IR bands of the characteristic (I) alkyne, (II) thiol and (III) vinyl sulfide groups magnified out of the FT-IR spectra. Irradiation was carried out with visible light ( $\lambda = 420 - 450 \text{ nm}$ ,  $3.6 \text{ mW/cm}^2$ ) under air.



**Figure 59** – FT-IR spectra of resin 3EQ-1H-1T prior to (*black line*) and after photo-curing (*red line*). The characteristic  $\text{NO}_2$  absorption bands at  $1537 \text{ cm}^{-1}$  (asym. stretching) and  $1348 \text{ cm}^{-1}$  (sym. stretching) are magnified out of the FT-IR spectra. Irradiation was carried out with visible light ( $\lambda = 420 - 450 \text{ nm}$ ,  $3.6 \text{ mW/cm}^2$ ) under air.

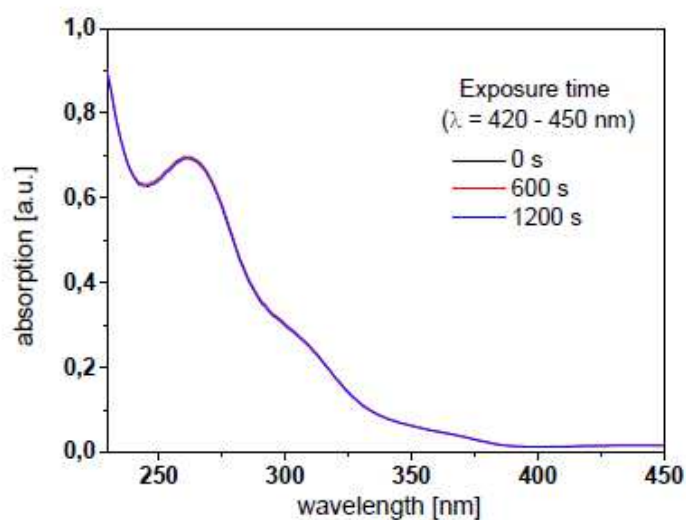


Figure S10 – UV-vis spectra of resin 3EQ-1H-1T prior to (*black line*) and after photo-curing for 600 (*red line*) and 1200 s (*blue line*). Irradiation was carried out with visible light ( $\lambda = 420 - 450$  nm,  $3.6$  mW/cm<sup>2</sup>) under air.

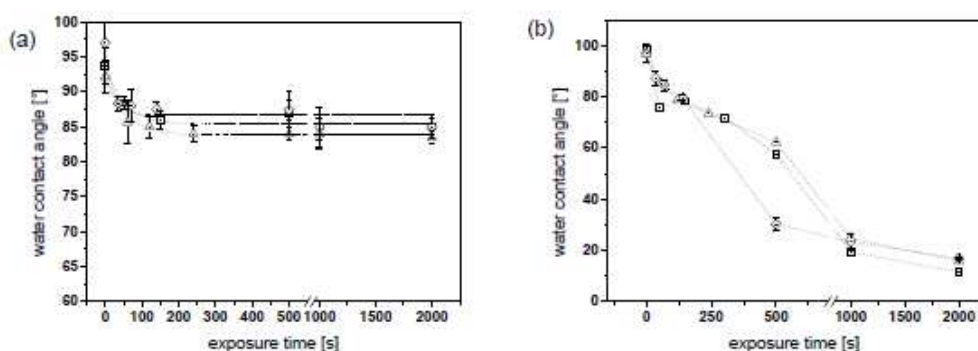


Figure S11 – Static water contact angles of cured thiol-yne systems comprising butynyl-NBC and 3 equiv. of selected thiols versus exposure time ( $269$  mW/cm<sup>2</sup>,  $\lambda < 400$  nm). The thiol component is varying and comprised a 1:1 molar ratio of TMPMP and HDT (*open squares*), 1:2 molar ratio of TMPMP and HDT (*open diamonds*) and 1:3 molar ratio of TMPMP and HDT (*open triangles*). UV exposure was carried out either in (a) nitrogen or (b) air. The lines are a guide for the eye.



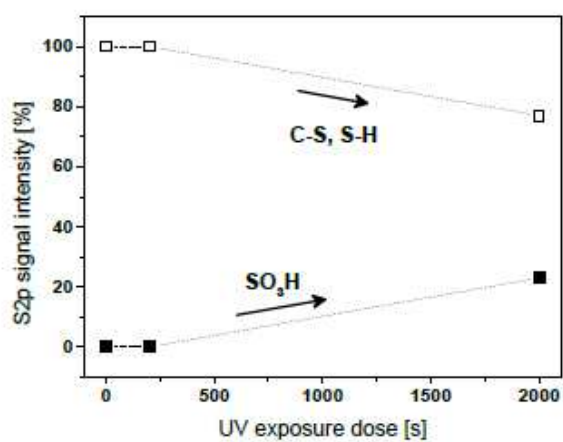


Figure S12 – Variations of the signal intensity in the S2p region at 161-165 eV (*open squares*) and 166-170 eV (*full squares*) versus UV exposure time. UV irradiation was carried out under nitrogen atmosphere. The lines are a guide for the eye.

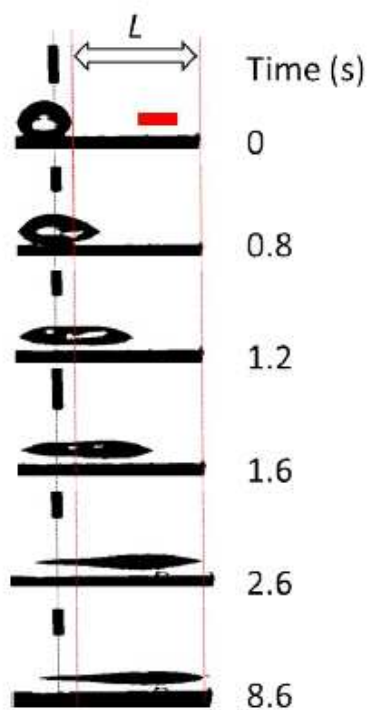


Figure S13 – Movement of a 2- $\mu$ L water droplet on the surface of 2EQ-1T-1H with a combined gradient of wettability and Laplace pressure. The scale bar is 2 mm.

**PUBLICATION II:**

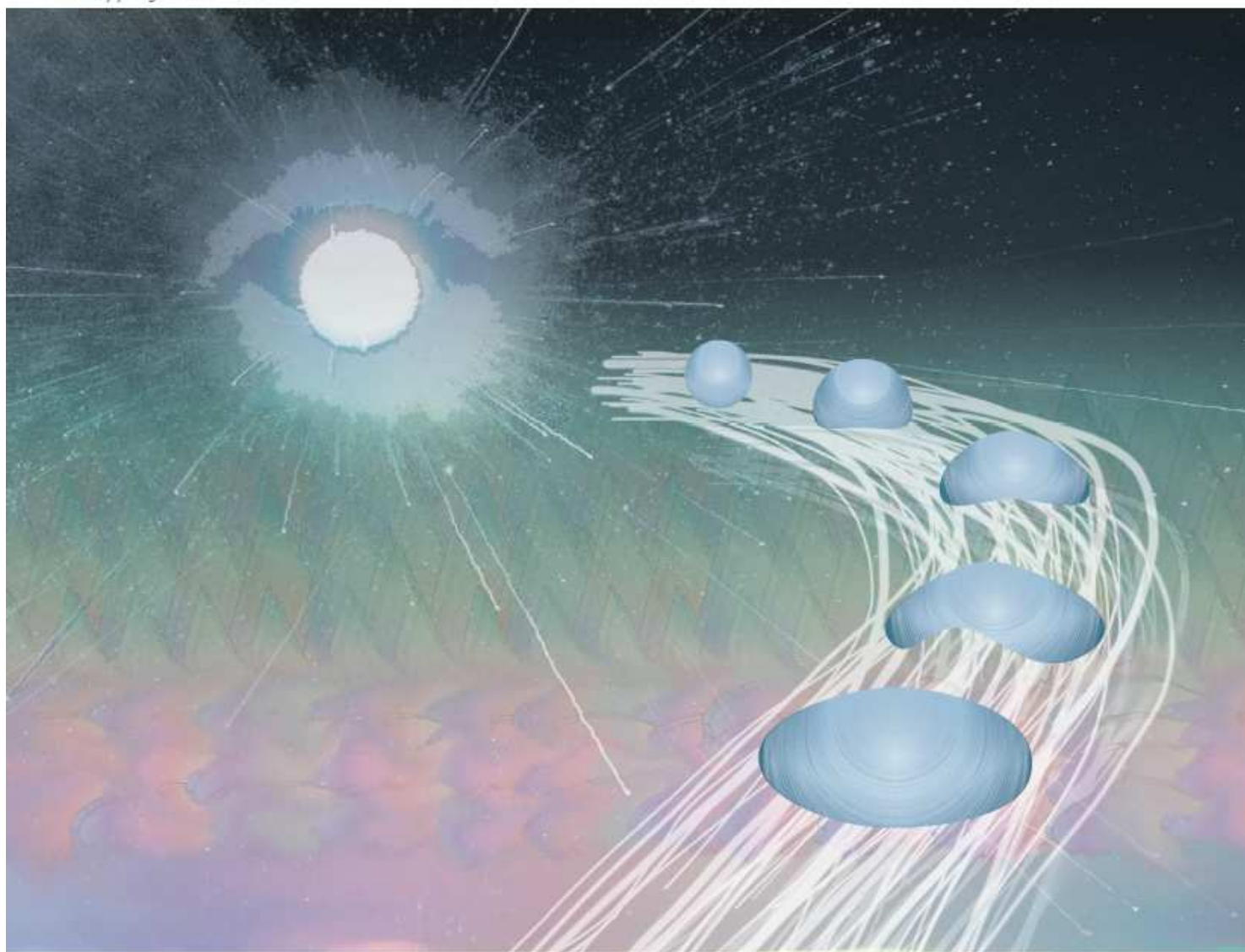
*Photo-switching of surface wettability on micropatterned photopolymers for fast transport of water droplets over a long distance*

Rossegger, Elisabeth; Nees, Dieter; Turisser, Simon; Radl, Simone; Griesser, Thomas;  
Schlögl, Sandra

*Polymer Chemistry*, 2020, 11, 3125-3135

# Polymer Chemistry

rsc.li/polymers



ISSN 1759-9962

**PAPER**

S. Schlögl *et al.*

Photo-switching of surface wettability on micropatterned photopolymers for fast transport of water droplets over a long-distance

*Abstract*

The present work addresses the directional movement of water droplets (2  $\mu\text{L}$  droplet) across a photopolymer surface over a distance of more than 20 mm. The long-distance movement of the droplet is achieved by inscribing multi-gradients onto the surface, which is realized by a photo-induced increase in wettability amplified by a change in surface texture. To create highly hydrophobic surface characteristics, photo-reactive resin formulations containing an o-nitrobenzyl alcohol derivative with terminal acrylate groups, a multi-functional thiol and a fluorinated methacrylate monomer are patterned by visible light-assisted nanoimprint lithography. The needle-like surface microstructures in combination with the fluorine groups of the methacrylate monomer enable the formation of photopolymers with static water contact angles in the range of  $140^\circ$ . Subsequent irradiation of the photopolymer with light in the UV-A spectral region leads to the localized formation of polar groups such as carboxylic acids (photolysis of the o-nitrobenzyl ester moieties) and sulfonic acids (photooxidation of free thiol groups). Along with the change in the chemical surface composition, prolonged UV exposure under air erodes the surface microstructures leading to fully wettable surfaces. The controlled photo-switching between highly hydrophobic ( $140^\circ$ ) and fully wettable ( $7^\circ$ ) photopolymer surfaces enables the introduction of wettability gradients by asymmetrical UV irradiation. Linear-shaped gradients rapidly drive a water droplet over a distance of 14 mm. By inscribing the wettability gradient in wedge-shaped patterns, a Laplace pressure gradient is additionally formed, which allows a directed movement of water droplets over a distance of 22 mm.

*Introduction*

Along with a change in the chemical surface composition of polymers, a well-established approach towards tuning material properties such as wettability,<sup>1</sup> adhesion<sup>2</sup> or friction<sup>3</sup> in a controlled manner is the introduction of structures on the polymer surface. Strongly inspired by nature, the shape of the patterns covers a wide range of sizes (from micro- to nanoscale) to mimic the surface of lotus leaves, desert beetles, butterfly wings or sharks.<sup>4</sup>

Common synthesis strategies to re-engineer these sophisticated structures are light-assisted direct writing processes,<sup>5</sup> interference lithography,<sup>6</sup> nanoimprint lithography (NIL),<sup>7</sup> mask stereolithography,<sup>8</sup> etching processes<sup>9</sup> or ink-jet printing.<sup>10</sup> By changing surface topologies, they enable the introduction of advanced functions into polymer materials. Prominent examples are “superhydrophobic” surfaces, which are extremely water repellent surfaces that are characterized by contact angles  $>150^\circ$  and sliding angles  $<5^\circ$ .<sup>11</sup> Typical fabrication routes include the patterning of hydrophobic materials such as polydimethylsiloxane (PDMS)<sup>12</sup> or the covalent attachment of fluorinated compounds onto patterned polymers during a post-modification process.<sup>13</sup> The salient features of superhydrophobic surfaces make them interesting candidates for technical applications such as self-cleaning,<sup>14</sup> antifingerprint<sup>15</sup> or anti-corrosion coatings<sup>16</sup> and water-repellant textiles.<sup>17</sup>

Advancing from “passive” nano/microstructures, several studies describe the stimuli-triggered switching of wettability. Recently, Jiang et al. prepared shape memory polymers with magnetically actuated microstructures that were able to reversibly switch between superhydrophobic and hydrophilic states and underwent a controlled change in color.<sup>18</sup> Among the various stimuli, light as an external trigger to change surface wettability of polymers has gained increased attention, since it benefits from temporal and spatial control and can be carried out under mild conditions.<sup>19</sup> Moreover, light-triggered reactions facilitate the formation of surfaces with gradients in wettability (by gradual light exposure), which is of particular interest for the directed motility of droplets.<sup>20</sup> By being able to transport liquids without the use of pumps or other external devices across a surface, the directed motion of liquids has gained increased attention for numerous future applications such as microfluidic devices,<sup>21</sup> fog-harvesting<sup>22</sup> and functional coatings (e.g. self-cleaning, anti-fog, anticorrosion).<sup>23</sup>

In terms of light-triggered reactions, the concepts towards the fabrication of surfaces with wettability gradients either rely on reversible or irreversible photoreactions. In particular, Ichimura and co-workers attached calix[4]resorcinarene derivatives with terminal azobenzene units at a surface.<sup>24</sup> In the cisstate of the azobenzene units, the surface was characterized by a significantly higher hydrophilicity than in the trans-state. A gradient in

surface free energy was realized by an asymmetrical irradiation, which allowed the directional motion of an oil droplet over the surface. In another study, Leigh et al. reported the transport of a liquid droplet by using rotaxane-based photoresponsive molecular shuttles.<sup>25</sup>

In terms of irreversible photoreactions, Ito and co-workers reported a switching between hydrophobic and hydrophilic surface properties by a controlled photodegradation of an alkylsilane self-assembled monolayer.<sup>26</sup>

Zheng et al. extended the concept of wettability gradients for the directed transport of liquids by additionally introducing a Laplace pressure gradient.<sup>27</sup> They anodically oxidized graphite plates to create a wettability gradient. In a subsequent step, they applied a hydrophobic paraffin wax with a V-shaped pattern to accomplish the Laplace pressure gradient. With this multi-gradient approach, Zheng and co-workers were able to spontaneously force a water droplet across a high adhesion surface.

In a recent study, we transferred the concept of multi-gradients for the directed motility of droplets to photopolymer surfaces.<sup>28</sup> In particular, we synthesized photo-curable thiol-yne formulations bearing UV sensitive o-nitrobenzyl ester links. Thin cured films were prepared by flood exposure with visible light followed by a photolithography step, in which wedged structures with a wettability gradient were inscribed by asymmetrical UV exposure. In the exposed areas, polar cleavage and oxidation groups were formed and a lengthwise wettability gradient was realized within the wedge. In contrast, the non-illuminated areas on the outer side of the wedge remained hydrophobic facilitating the formation of a Laplace pressure gradient. Although both wettability and Laplace pressure gradients can be easily and locally adjusted by varying the irradiation parameters and pattern designs, we were not able to drive the water droplets over a distance of longer than 10 mm.

As a new approach, we aim at the preparation of photopolymer surfaces that are comprised by a significantly higher gradient in wettability and Laplace pressure (Fig. 1). Since it is well known that microstructures strongly govern the wettability of polymer surfaces, we introduced needle-like micropatterns on the photopolymer surface by visible light-assisted NIL. However, the photocleavable thiol-yne system suffered from a high

surface tack and a low glass transition temperature, which posed a serious problem for the demolding of the micropatterns in the NIL process. Thus, the thiol–yne system was replaced with a binary thiol–acrylate photopolymer.

For this, an *o*-nitrobenzyl alcohol derivative with terminal acrylate groups (acrylate-NBE) was synthesized and cured upon visible light exposure in the presence of a multi-functional thiol, isobornyl acrylate and a fluorinated methacrylate (Fig. 1d).

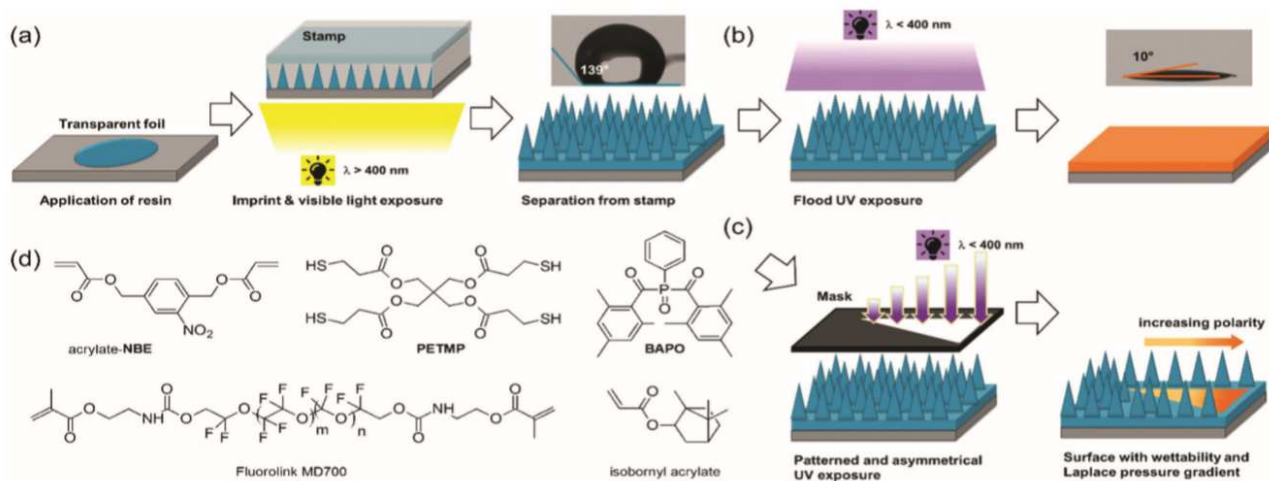


**Fig. 1** (a) Preparation of needle-like surface patterns by visible-light assisted NIL. (b) Changing the wettability of the highly hydrophobic surface by flood UV exposure involving a photolysis of the *o*-NBE groups, a photooxidation of the remaining thiol moieties and an erosion of the surface patterns. (c) Asymmetrical UV exposure to generate a wedge-shaped surface area with a lengthwise wettability gradient, which is surrounded by the hydrophobic micropatterned network. (d) Functional acrylates, fluorinated methacrylate, photoinitiator (BAPO) and multi-functional thiol (PETMP) used for the preparation of micropatterned acrylate and thiol–acrylate photopolymers with multi-gradient surface properties.

The needle-like surface structures combined with the fluorine moieties of the functional methacrylate yielded photopolymers with highly hydrophobic surface properties (water contact angle around  $140^\circ$ ). Wedge-shaped gradients in wettability were then obtained by asymmetrical UV irradiation of the micropatterned photopolymers (Fig. 1c). Prolonged UV exposure did not only lead to the formation of polar cleavage products but also to an erosion of the microstructures and hydrophilic photopolymer surfaces were obtained, which were highly wettable. Compared to photopolymers without microstructures, the amplification of the multi-gradients with appropriate surface textures enabled the transport of the droplets over a longer distance. In addition, the higher gradients in wettability further facilitated the directed movement of water droplets even in the absence of a Laplace pressure gradient, which enables more freedom in design when it comes to the fabrication of functional surfaces for controlled water transport.

*Results and discussion**Synthesis and characterization of photocleavable acrylate and thiol–acrylate networks for visible light assisted NIL*

Photocleavable thiol–yne formulations based on (2-nitro-1,4-phenylene) bis(methylene) 1-hexynoate and multi-functional thiols as crosslinker were successfully used for the directed movement of water droplets in our previous work.<sup>28</sup> The study clearly showed that both o-NBE chromophores and free thiol moieties are required to gradually switch the wettability of a photopolymer surface by asymmetric UV irradiation. However, those thiol–yne formulations were not applicable for inscribing microstructures by visible light assisted NIL. Due to the high surface tack of the formulations in their cured state, the micropatterns were destroyed during the demolding process. The same problem arose when photocleavable thiol–ene systems with o-NBE groups were employed.<sup>29</sup>

To overcome the high surface tack, the fabrication of photosensitive thiol–acrylate photopolymers with a higher glass transition temperature ( $T_g$ ) was aimed at. For this, an o-NBE derivative with terminal acrylate groups was synthesized and cured with a tetra-functional thiol (PETMP). Functional acrylate monomers were added to the formulation to increase the glass transition temperature (isobornyl acrylate) and the hydrophobicity (fluorinated methacrylate) of the cured networks (Fig. 1d). It should be noted that the content of the fluorinated methacrylate was limited to 1 wt%. Formulations with higher concentrations were not stable and separation of the phases was rapidly observed after the mixing process.

The radical-mediated thiol–acrylate reaction proceeds via a mixed-mode photopolymerization since alkenes with electron withdrawing groups comprise a lower reactivity in thiol–ene reactions than electron-rich ones.<sup>30</sup> Thus, the carbon-centered radicals – formed by the addition of thiyl radicals to the unsaturated carbon bonds – are not only participating in chain transfer reactions but also in propagation reactions.



Complex network structures are obtained with intertwined thiol-ene and homopolymerized acrylate segments.<sup>31</sup>

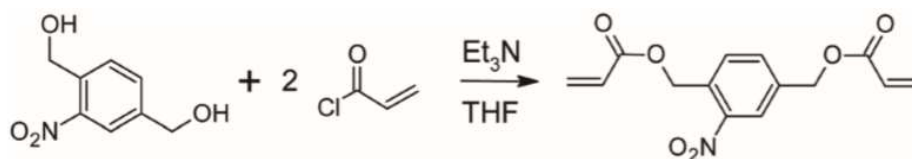


Fig. 2 Synthesis of acrylate-NBE.

Thiol-acrylate networks with varying amount of PETMP were prepared and the cure kinetics, cleavage behavior and wettability properties were compared to an acrylate network. The one-step synthesis of (2-nitro-1,4-phenylene) bis (methylene) diacrylate (acrylate-NBE) involved an esterification of (2-nitro-1,4-phenylene) dimethanol with acryloyl chloride (Fig. 2) and afforded the product in 82% of the theoretical yield. <sup>1</sup>H NMR, <sup>13</sup>C NMR and FT-IR spectra were in accordance with the proposed structure (Fig. S1–S3 in ESI†).

The absorption profile of acrylate-NBE in acetonitrile was determined by UV-vis spectroscopy (Fig. S4 in ESI†). The characteristic absorption maximum of the o-NBE groups is observed at 260 nm, which rapidly disappears upon UV exposure. The decrease of the absorption band is accompanied by the appearance of a broad absorption between 270 and 470 nm. As reported by Wirz and co-workers, those bands are related to primary (e.g. o-nitrosobenzaldehyde) and secondary (e.g. azo-derivatives) cleavage products of the o-NBE chromophore.<sup>32</sup> The results are in good agreement with our previous work on o-NBE derivatives bearing terminal epoxy, alkene and alkyne groups.<sup>28,29,33,44,45</sup>

Acrylate and thiol-acrylate photopolymers were prepared by visible light induced curing of the functional acrylates and the fluorinated methacrylate with the tetra-functional thiol PETMP in the presence of phenylbis (2,4,6-trimethylbenzoyl)phosphine oxide (BAPO) as long wavelength absorbing photoinitiator.

The curing kinetics was studied by FT-IR spectroscopy following the depletion of the characteristic CvC–H absorption band of the acrylate groups at 1616 and 1634 cm<sup>-1</sup> (Fig. S5 in ESI†). For sample preparation, the solid acrylate-NBE was dissolved in an equimolar content of isobornyl acrylate before adding the fluorinated methacrylate. The conversion of the acrylate groups was then determined as a function of the PETMP content (0–25

mol%). From the results, it can be obtained that both reaction rate and final monomer conversion are affected by the amount of thiol in the formulation (Fig. 3a). In particular, by increasing the PETMP content from 0 to 25 mol%, the final acrylate conversion increases from 72 to 84%. This behaviour is well known in literature and is related to diffusion limitations of the acrylate monomers. Bowman and Cramer reported that the thiol acts as chaintransfer agent for the chain-growth polymerization of the acrylate leading to a reduction of the kinetic chain length.<sup>34</sup> The shorter kinetic chain length facilitates a higher monomer conversion at which the gel point occurs and thus, accelerates the photopolymerization kinetics and increases the final monomer conversion. In addition, thiol–acrylate photopolymers are less prone to oxygen inhibition compared to acrylate systems.<sup>35</sup>

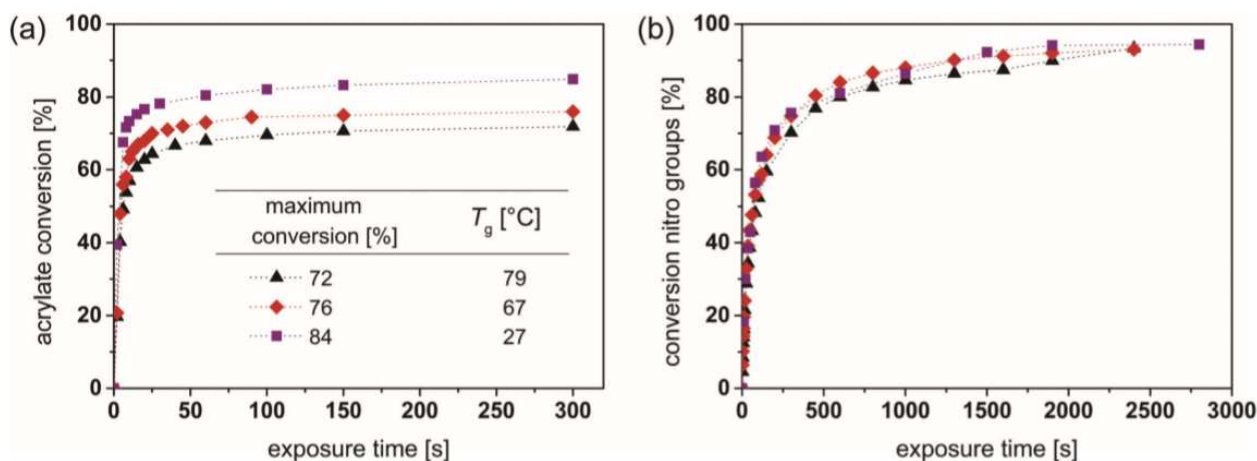


Fig. 3 (a) Monitoring the cure kinetics in acrylate and thiol–acrylate resin formulations by FT-IR spectroscopy. The normalized peak area of the IR absorption bands of the acrylate groups ( $1616$  and  $1634$   $\text{cm}^{-1}$ ) is plotted against exposure time. The PETMP content is varying and comprised 0 (triangles), 10 (diamonds) and 25 mol% (squares). Irradiation was carried out with visible light ( $\lambda = 420\text{--}450$  nm,  $3.2$   $\text{mW cm}^{-2}$ ) under air. The lines are a guide for the eye. (b) Monitoring the cleavage kinetics in acrylate and thiol–acrylate resin formulations by FT-IR spectroscopy. The normalized peak area of the IR absorption band of the nitro group ( $1537$   $\text{cm}^{-1}$ ) is plotted against exposure time. The PETMP content is varying and comprised 0 (triangles), 10 (diamonds) and 25 mol% (squares). Irradiation was carried out with UV light ( $269$   $\text{mW cm}^{-2}$ ,  $\lambda < 400$  nm) under air. The lines are a guide for the eye.

However, since the step-growth reaction between thiols and acrylates competes with the faster acrylate homopolymerization, the final conversion of the thiol groups is typically lower than the conversion of the acrylates.<sup>36</sup> In the current work, the conversion of the thiol groups amounts to 58% in thiol–acrylate networks comprising 25 mol% PETMP (Fig. S5b in ESI†). In formulations with 10 mol% PETMP, the IR signal of the mercapto groups (at

2575  $\text{cm}^{-1}$ ) was too weak for adequate quantification. The incomplete conversion of the thiol groups is crucial for an efficient switching of the wettability gradient since the free thiol groups are converted to sulfonic acid groups upon prolonged UV exposure.<sup>28</sup>

Along with the reaction kinetics, the thiol content further influences the  $T_g$ . The acrylate network comprised a relatively high  $T_g$  of 79 °C, which is mainly due to the presence of isobornyl groups in the network. The  $T_g$  decreases to 67 and 27 °C in thiol–acrylate networks containing 10 and 25 mol% PETMP, respectively. This behavior is related to flexible thioether links, whose number increases with rising thiol content.<sup>36</sup> In addition, non-reacted thiols can act as plasticizer in the network, which further leads to a decrease of the  $T_g$ .<sup>34</sup> However, compared to previously synthesized thiol–yne ( $T_g$  between –10 and –16 °C) and thiol–ene networks ( $T_g$  between –9 and –20 °C), the  $T_g$  was significantly higher, even in the presence of 25 mol% PETMP.

In the cured state, both acrylate and thiol–acrylate networks were characterized by a low surface tack, which made them ideal candidates for visible light assisted NIL.

For the NIL process, the liquid resin formulation was uniformly cast on a transparent polymer foil and an imprint stamp was pressed into the resin layer. Curing of the resin layer was accomplished via visible light exposure through the transparent foil acting as substrate (Fig. 1a). The surface of the cured resin replicated the inverted pattern of the master after demolding from the stamp.

In the present study, a needle-like surface pattern was imprinted to increase the hydrophobicity of the networks (in the non-cleaved state). The detached surface structures were characterized by SEM and AFM and an exemplary surface obtained with resin 25SH-AD (comprising 25 mol% PETMP) is shown in Fig. 4a and d, respectively. The micrographs clearly show that the thiol–acrylate formulations are suitable for the NIL process as the microstructure could be replicated on the sample's surface.

*Surface properties of photocleavable acrylate and thiol– acrylate networks as a function of surface patterns*

Both resin composition and imprinted microstructures have a distinctive influence on the wettability of the photopolymers. Not surprisingly, the static water contact angle of the acrylate network increases from 83 to 90° by the addition of the fluorinated methacrylate. However, a further increase of the static water contact angle to 96 and 108° is observed by adding 10 and 25 mol% PETMP, respectively, although the introduction of the polar thiol groups should lead to a decrease in the water contact angle (Table 1). This behavior can be explained by the differences in the diffusion limitation of the acrylate monomers in the presence of the thiol (changing from a chaingrowth mechanism to a mixed mode one), which facilitates the migration of the fluorinated methacrylate to the air surface. Vitale and co-workers reported the important role of cure kinetics of acrylic photopolymers on the migration of hydrophobic co-monomers in photocurable resin formulations.<sup>37</sup>

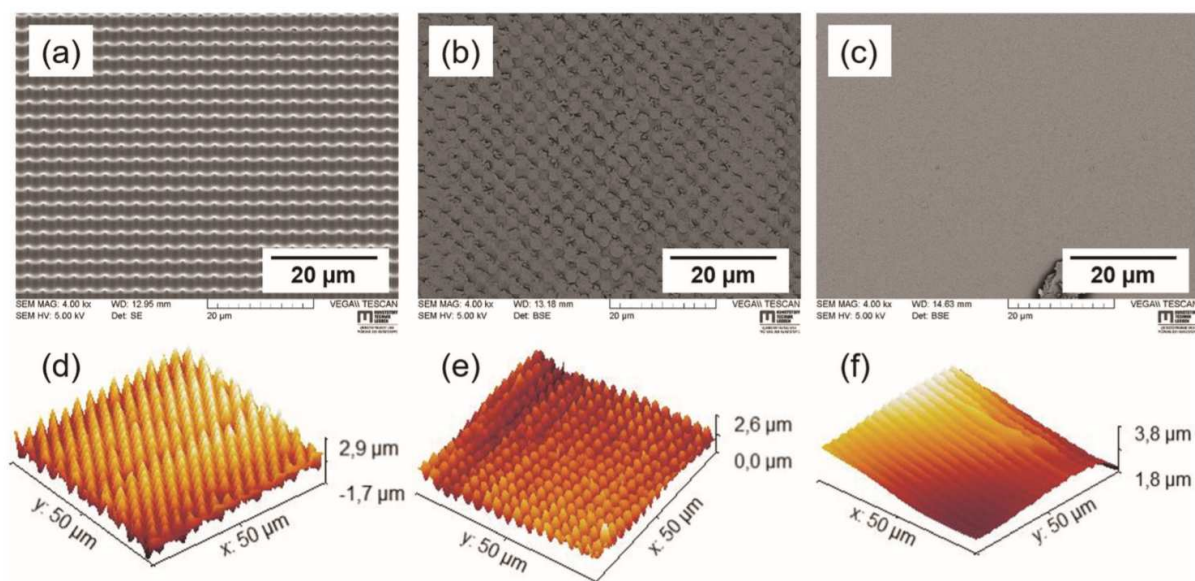


**Fig. 4** (a–c) SEM micrographs and (d–f) 50 μm × 50 μm AFM micrographs of the topography of needle-like micropatterns inscribed in resin 25SH-AD (comprising 25 mol% PETMP) by visible light assisted NIL. Surface structures of the photocured thiol–acrylate photopolymer after (a and d) 0, (b and e) 1000 and (c and f) 1500 s of UV exposure (269 mW cm<sup>-2</sup>) under air.

**Table 1** Static ( $\theta_{\text{stat}}$ ), advancing ( $\theta_{\text{adv}}$ ) and receding ( $\theta_{\text{rec}}$ ) water contact angle and hysteresis ( $\Delta\theta$ ) of photocured acrylate and thiol–acrylate formulations with either a non-patterned surface or a needle-like surface structure

PETMP (mol%)	Fluorinated methacrylate (wt%)	Non-patterned surface (not UV exposed)				Needle-like patterned surface (not UV exposed)			
		$\theta_{\text{stat}}$ (°)	$\theta_{\text{adv}}$ (°)	$\theta_{\text{rec}}$ (°)	$\Delta\theta_{\text{non-irr}}$ (°)	$\theta_{\text{stat}}$ (°)	$\theta_{\text{adv}}$ (°)	$\theta_{\text{rec}}$ (°)	$\Delta\theta_{\text{non-irr}}$ (°)
0	1	90 ± 0.3	89 ± 0.9	48 ± 7	41	140 ± 6	133 ± 2	57 ± 9	76
10	1	96 ± 1	93 ± 0.1	51 ± 3	42	140 ± 7	138 ± 1	64 ± 12	74
25	1	108 ± 1	98 ± 0.4	51 ± 0.3	47	139 ± 6	149 ± 0.1	146 ± 2	3

Depending on the cure parameters, they were able to tune the surface tension between 42 and 22 mN m<sup>-1</sup>.

By additionally imprinting the needle-like microstructures on the surface of the photopolymers, a further increase of the water contact angle is observed. Highly hydrophobic surfaces are obtained with static water contact angles in the range of 140°.

The influence of surface roughness on the static contact angle is well known and was first described by Wenzel, who established a linear relationship between the contact angle of a liquid ( $\theta$ ) on a smooth surface and on a rough surface ( $\theta_r$ ) with the same chemical composition (eqn (1)).<sup>38</sup>

$$\cos \theta_r = r \cos \theta \quad (1)$$

Wenzel introduced the roughness factor ( $r$ ), which is the ratio between the true area of the solid surface to the apparent area and he hypothesized that the depressions in the rough surface area of solid–liquid contact are completely filled with the liquid.

Exploiting this effect, Picraux et al. reported that an appropriate surface roughness amplifies the light-induced change in water contact angle of a photo-responsive silica surface.<sup>39</sup>

In the present work, the light triggered switching of the surface wettability relies on a UV induced change of chemical composition and topology. For non-patterned surfaces, the wettability is mainly controlled by photo-triggered changes of the chemical surface composition. UV irradiation induces a cleavage of the *o*-NBE groups and a photo-oxidation of free thiol groups yielding sulfonic acid groups.

In particular, the photolysis of the *o*-NBE groups was studied by FT-IR spectroscopy (Fig. S6 in ESI<sup>†</sup>). Upon irradiation with light in the UV-A spectral region, the nitro groups are converted to nitroso moieties leading to a decrease of the two characteristic NO<sub>2</sub> absorption bands at 1537 cm<sup>-1</sup> (asym. stretching) and 1348 cm<sup>-1</sup> (sym. stretching). In addition, a broadening of the C=O absorption band (1635–1802 cm<sup>-1</sup>) is observed, which is associated with the formation of primary cleavage products (e.g. carboxylic acids).

The kinetics of the cleavage reaction as a function of the thiol concentration was studied by following the depletion of the NO<sub>2</sub> absorption band at 1537 cm<sup>-1</sup> upon UV exposure (Fig. 3b). From the results, it can be obtained that the three networks have a comparable

cleavage kinetics with final conversions in the range of 93%.

The change of the surface composition clearly affects the wettability of the photosensitive networks as shown by static water contact angle measurements (Tables 1, 2 and Fig. 5a). In particular, for the acrylate network, the water contact angle decreases with increasing exposure dose and reaches 44° at an irradiation time of 2000 s. In thiol–acrylate networks, the decrease is more pronounced and for the network with 25 mol% PETMP, the surface becomes fully wettable upon prolonged UV exposure with a water contact angle below 10°. The higher wettability of thiol–acrylate networks can be explained by the additional photo-oxidation of free thiols present in the network.

It is interesting to note that in all three networks the contact angle slowly decreases upon exposure times up to 1000 s. However, at prolonged exposure (>1000 s), the decrease rate of the water contact angle is significantly accelerated and is particularly fast for the thiol–acrylate network with 25 mol% PETMP. These results are in good agreement with our previous work on thiol–yne systems and reveal that photo-oxidation of the free thiol groups becomes the dominating reaction mechanism at higher exposure times.<sup>28</sup> At lower exposure times (<1000 s), the change in the water contact angles can be mainly attributed to the photolysis of the *o*-NBE moieties.

This is confirmed by contact angle measurements (Fig. S7 in ESI†) on reference acrylate and thiol–acrylate networks containing no photo-responsive *o*-NBE groups. The results clearly show that the acrylate network is not prone to any photo-oxidation reactions since the contact angle stays nearly constant over an exposure time of 2000 s. In contrast, the water contact angle of the thiol–acrylate reference network significantly drops to lower values if the exposure dose exceeds 1000 s.

The switch from non-polar to highly wettable surfaces is also observed with micropatterned photopolymers comprising needle-like surface structures (Tables 1, 2 and Fig. 5b). However, the decrease rate of the water contact angle is different, since the wettability of the patterned surfaces is affected by both surface topology and surface chemistry.

Account has be taken into the fact that the change in the surface composition is accompanied by a shape change of the microstructures. As obtained from SEM and AFM

micrographs (Fig. 4b, c, e and f), the microstructures are degrading upon UV exposure. After demolding the micro-sized needles have a height of 2.4  $\mu\text{m}$  (topology profiles obtained from AFM micrographs are shown in Fig. S8 in ESI†). Upon UV exposure under air, the needles are gradually ablated and the height of the structures decreases to 0.9 and 0.2  $\mu\text{m}$  after 1000 and 1500 s of UV irradiation, respectively. The degradation of the surface might be related to a photo-ablation of the polymer under the irradiation conditions, which is facilitated by the cleavage of the network across the o-NBE groups.<sup>40</sup>

**Table 2** Static ( $\theta_{\text{stat}}$ ), advancing ( $\theta_{\text{adv}}$ ) and receding ( $\theta_{\text{rec}}$ ) water contact angle and hysteresis ( $\Delta\theta$ ) of photocleaved ( $269 \text{ mW cm}^{-2}$ , 2000 s,  $\lambda < 400 \text{ nm}$ ) acrylate/thiol–acrylate formulations with either a non-patterned surface or a needle-like surface structure

PETMP (mol%)	Fluorinated methacrylate (wt%)	Non-patterned surface (UV irradiated)				Needle-like patterned surface (UV irradiated)			
		$\theta_{\text{stat}}$ ( $^{\circ}$ )	$\theta_{\text{adv}}$ ( $^{\circ}$ )	$\theta_{\text{rec}}$ ( $^{\circ}$ )	$\Delta\theta_{\text{irr}}$ ( $^{\circ}$ )	$\theta_{\text{stat}}$ ( $^{\circ}$ )	$\theta_{\text{adv}}$ ( $^{\circ}$ )	$\theta_{\text{rec}}$ ( $^{\circ}$ )	$\Delta\theta_{\text{irr}}$ ( $^{\circ}$ )
0	1	$63 \pm 2$	$45 \pm 2$	$14 \pm 3$	31	$36 \pm 2$	$51 \pm 1$	$10 \pm 2$	41
10	1	$21 \pm 1$	$32 \pm 0.2$	$15 \pm 1$	17	$22 \pm 1$	$37 \pm 0.3$	$18 \pm 4$	19
25	1	$< 10$	$20 \pm 0.4$	$13 \pm 1$	7	$7 \pm 2$	$25 \pm 6$	$19 \pm 4$	6

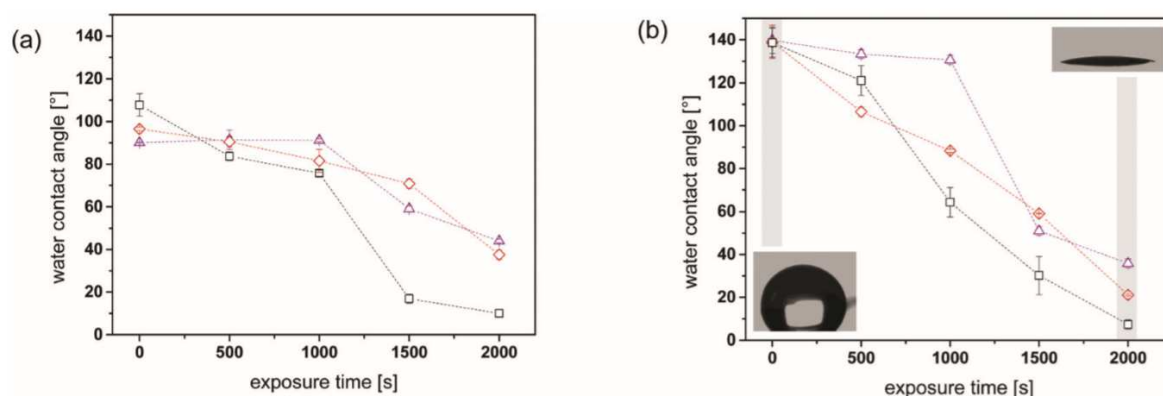


**Fig. 5** Static water contact angles of (a) non-patterned and (b) micropatterned acrylate and thiol–acrylate networks versus exposure time ( $269 \text{ mW cm}^{-2}$ ,  $\lambda < 400 \text{ nm}$ ). The PETMP content is varying and comprised 0 (triangles), 10 (diamonds) and 25 mol% (squares). UV exposure was carried out under air. Inserts depict the photographs of a respective water droplet at the selected exposure dose highlighted in grey. The lines are a guide for the eye

The results indicate that the change in wettability is amplified by the surface structure and covers a broader range. In particular, for the thiol–acrylate formulation with 25 mol% PETMP the contact angle decreases from 139 to  $7^{\circ}$  upon irradiation with UV-light. In addition, for thiol–acrylate networks the decrease rate of the water contact angle is faster at lower irradiation times compared to the non-patterned counterpart. In terms of surface



chemistry, patterned and nonpatterned surfaces should be characterized by a comparable rate of photo-oxidation (thiol groups) and photo-cleavage (o-NBE groups). Thus, the significant change in the contact angles at lower irradiation times (<1000 s) can be mainly attributed to structural changes of the surface topology during the photo-ablation process. In contrast, the water contact angle of the patterned acrylate network does not decrease significantly at exposure times up to 1000 s. We attribute this behavior to different photo-ablation rates of the networks, with the acrylate system being more stable under the irradiation conditions than the thiol-acrylate one.

#### *Directed movement of water droplets on patterned acrylate and thiol-acrylate networks*

A contact angle hysteresis ( $\Delta\theta = \theta_{\text{adv}} - \theta_{\text{rec}}$ ) below  $10^\circ$  is crucial for inducing a movement of a liquid on surfaces with a gradient in wettability.<sup>26,41</sup> Our previously studied thiol-yne systems suffered from a high hysteresis in the cured (not UV irradiated) state with values of more than  $60^\circ$ , which significantly decreased ( $0\text{--}14^\circ$ ) upon UV irradiation.<sup>28</sup> Although it was possible to inscribe a unidirectional wettability gradient on the surface, the high hysteresis at the start of the nonexposed gradient prevented a directed movement of the droplets. Instead of a movement, a longitudinal spreading was observed.

Contact angle hysteresis depends on several factors of a polymer surface including topology, chemical composition, swelling and molecular reorientation when the polymer surface is in contact with the test liquid.<sup>42,43</sup>

In terms of non-patterned thiol-acrylate polymers, the hysteresis is mainly influenced by the surface composition. In the non-illuminated state, the advancing contact angle increases with rising thiol content (Table 1). This effect is attributed to the higher number of  $\text{CF}_2$ -groups on the surface (due to the enhanced migration of the fluorinated methacrylate to the air surface), which is also reflected by the increase of the static water contact angle from  $96$  to  $108^\circ$ . In contrast, the receding contact angle is only slightly changing, which leads to an increase of the hysteresis with rising thiol content.

The high hysteresis values can be overcome by UV exposure of the photopolymer networks, which is related to a distinctive change of the chemical surface composition (Table 2). In our previous work on thiol-yne systems, the formation of polar species led to



highly wettable surfaces with low hysteresis values ( $\Delta\theta_{\text{irr}} = 0 - 14^\circ$ ).<sup>28</sup>

For the networks under investigation, low advancing and receding contact angles – and thus, a low hysteresis ( $\Delta\theta_{\text{irr}} = 7$  and  $17^\circ$ ) – could be only obtained with irradiated thiol–acrylate networks. The advancing contact angle is steadily decreasing with increasing thiol content, whilst the receding contact stays nearly constant. Thus, the acrylate network containing no thiol is characterized by a substantially higher hysteresis. The results suggest that the low hysteresis of the irradiated thiol–acrylate networks can be mainly attributed to the thiol content and the related photo-oxidation of the free thiol groups, which is more pronounced in the presence of a higher number of thiol moieties. The same trend is observed with patterned surfaces after prolonged UV exposure (2000 s). This is not surprising since the surfaces lose their microstructures by gradual photo-ablation and thus, surface wettability and hysteresis in the irradiated state of the eroded surfaces is mainly governed by chemical surface composition.

In contrast, in the non-illuminated state the wettability of the patterned surfaces is mainly influenced by the surface structure. Whilst the static contact angle data are comparable for all three networks under investigation, both receding and advancing contact angle are increasing with rising thiol content. Since we assume that thiol–acrylate networks with higher thiol content comprise a higher content of  $\text{CF}_2$  groups on the surface (migration of the fluorinated methacrylate monomer to the surface), the results suggest that dynamic contact angle data are more sensitive to changes of the chemical surface composition of the patterned samples.

In addition, it has to be considered that the imprinting of needle-like surface structures may change the wettability regime. Due to the shape of the surface structures, air can be trapped between the water droplet and the polymer surface. In this Cassie–Baxter regime, the liquid-repellency of a surface is improved, since the water droplet is in contact with both air and polymer.<sup>43</sup> Due to the combined effect of surface structure and higher content of  $\text{CF}_2$  groups on the surface, the receding angle of the thiol–acrylate network containing 25 mol% thiol increases from  $57$  to  $146^\circ$  leading to a remarkably low hysteresis value ( $\Delta\theta_{\text{non-irr}} = 3^\circ$ ).

In subsequent experiments, the directed movement of a 2  $\mu\text{L}$  water droplet was studied

on both smooth and patterned surfaces of cured resin 25SH-AD. In terms of non-patterned surfaces, a spontaneous movement of the droplets is observed with a moving distance of 9 mm, if a unidirectional wettability gradient is inscribed by asymmetric UV irradiation (Fig. 6a). The successful movement of the droplet compared to the previously investigated thiol-yne systems is mainly related to the lower hysteresis of the surface in the cured and non-irradiated state ( $\Delta\theta_{\text{non-irr}}$ ):  $66^\circ$  (thiol-yne) versus  $47^\circ$  (thiol-acrylate). As shown in previous work, the initial restriction of the high hysteresis can be overcome if an additional Laplace pressure gradient is inscribed. The hysteresis force acts opposite to the moving direction of the droplet and reduces the droplet's ability for directed motility. In contrast, the forces, which arise from the wettability gradient and the Laplace pressure, facilitate the movement of the droplet from a less wettable to a higher wettable surface. For the preparation of multi-gradient surfaces, a wedge-shaped pattern with a halfwedge angle of  $3.5$  and  $7^\circ$  was inscribed in the non-patterned resin 25SH-AD by photolithography with asymmetrical UV exposure. For sample preparation, the surface of the cured resin except the wedge was protected with aluminum foil and the light beam of the UV lamp was moved over the pattern with a defined velocity. The exposure time gradually increases lengthwise and reaches 2000 s at the end of the wedge. Under these conditions, the Laplace pressure force and the wettability force are able to move the  $2 \mu\text{L}$  water droplet over a larger distance (16 mm) if the half wedge angle amounted to  $7^\circ$  (Fig. 6c). At a half wedge angle of  $3.5^\circ$ , the moving distance is comparable to surfaces without Laplace pressure gradient (Fig. 6b). The results are in good agreement with the work of Zheng et al., who reported that the half-wedge should range between  $7$  and  $30^\circ$  for the transport of droplets with a volume of  $2 \mu\text{L}$ .<sup>27</sup>

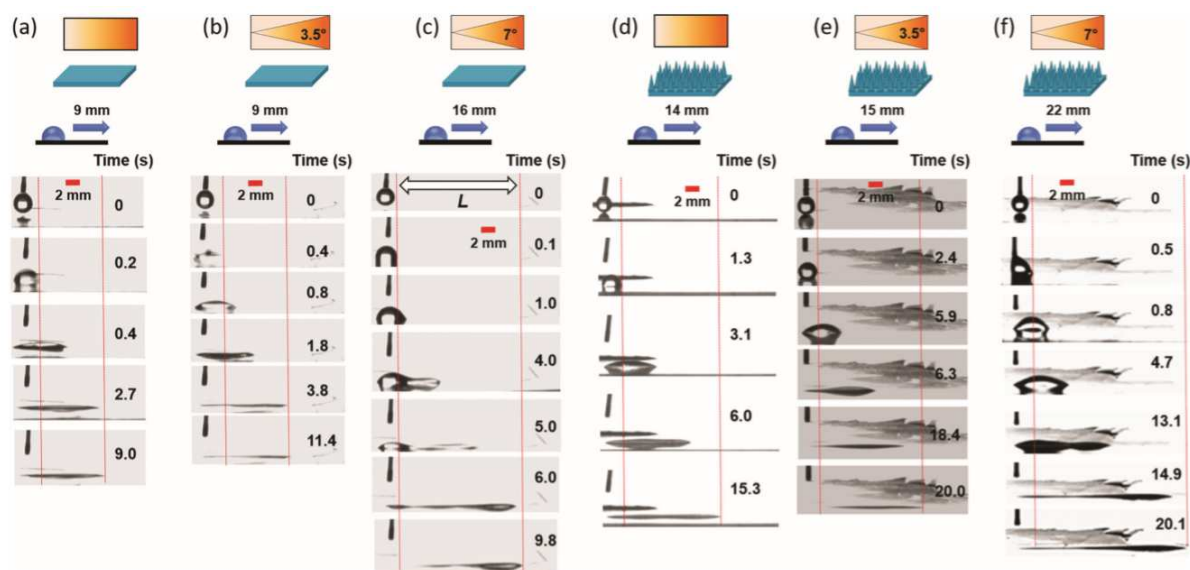


Fig. 6 Movement of a 2  $\mu\text{L}$  water droplet on the surface of photocured 25SH-AD (25 mol% PETMP): non-patterned surface with either (a) a unidirectional gradient in wettability and or (b and c) with a combined gradient of wettability and Laplace pressure; half wedge angle amounted to (b) 3.5 and (c) 7°. Patterned surface with either (d) a unidirectional gradient in wettability or (e and f) with a combined gradient of wettability and Laplace pressure; half wedge angle amounted to (e) 3.5 and (f) 7°. L in Fig. 6c denotes the movement distance.

Also on the multi-gradient 25SH-AD surface, the moving distance is higher compared to the previously investigated thiol–yne systems (16 versus 10 mm), which confirms the crucial role of the hysteresis force in the transport of droplets.

Based on these results, an enhanced performance for the water transport was expected with the patterned 25SH-AD resin, since the network comprises a low hysteresis in both non-irradiated ( $\Delta\theta_{\text{non-irr}} = 3^\circ$ ) and irradiated ( $\Delta\theta_{\text{irr}} = 6^\circ$ ) state. In addition, asymmetrical UV exposure leads to a higher wettability gradient since the water contact angle of patterned 25SH-AD decreases from 139 to 7° upon prolonged UV irradiation. The higher wettability force together with the lower hysteresis force enabled the unidirectional movement of a 2  $\mu\text{L}$  water droplet over a distance of 14 mm if only a wettability gradient was inscribed within the surface (Fig. 6d). This distance is in the range of non-patterned multi-gradient (Laplace pressure and wettability gradient) surfaces without structures (Fig. 6c).

Moreover, the moving distance could be nearly doubled (22 mm), if an additional Laplace pressure gradient (half wedge angle of 7°) was introduced (Fig. 6c). It should be considered that the UV induced changes in the surface topology might contribute to a higher Laplace pressure gradient leading to an enhanced moving distance of the water

droplet. For patterned surfaces, the surface topology significantly differs over the length of the wedge and between the inner and outer area of the wedge-pattern.

The non-exposed outside parts of the wedge comprise needle-like microstructures with a surface height of 2.4  $\mu\text{m}$ . However, the asymmetric UV exposure of the inside area of the wedge leads to a gradual photo-ablation of the microstructures. At the end of the wedge, the irradiation time amounts to 2000 s. Under these conditions, the microstructures are significantly eroded and their remaining height are expected to be below 0.2  $\mu\text{m}$  (Fig. 4f and Fig. S8c in ESI†). Since during sample preparation the irradiation time is gradually increased lengthwise to the wedge, it is assumed that the height of the microstructures steadily decreases from 2.4  $\mu\text{m}$  at the beginning of the wedge to <0.2  $\mu\text{m}$  at the end of the wedge.

Shorter moving distances were again obtained if the half wedge angle was reduced from 7 to 3.5°. However, even in the absence of a Laplace pressure gradient the moving distances are reasonably high giving rise to the versatility of the concept in terms of surface design. In particular, the low hysteresis and high wettability gradient enable the directed movement in the absence of a Laplace pressure gradient over a distance of 14 mm, whilst the combination of both gradients paves the way towards long-distance movement of water droplets (22 mm).

### *Conclusions*

Water droplets were directed moved over a long distance (22 mm) by inscribing multi-gradients in micropatterned thiolclick photopolymers. Thiol–acrylate formulations bearing photosensitive o-NBE groups were synthesized that benefit from a low surface tack and were applicable for visible light assisted NIL. By adding fluorinated additives and introducing needlelike microstructures (sharp cones with a height of 2.4  $\mu\text{m}$ ), photopolymers with highly hydrophobic surfaces characteristics (water contact angle of 140°) were realized. By subsequent UV exposure under air, the networks became nearly fully wettable (water contact angle of 7°), as shown by static contact angle measurements. The distinctive increase in wettability is caused by the change in the chemical surface composition, which includes the formation of carboxylic acid groups by the cleavage of

the o-NBE chromophore and the formation of sulfonic acid groups by photo-oxidation of the free thiols. Along with the formation of polar species, the UV irradiation induces an ablation of the microstructures and the height of the needles gradually decreases to 0.2  $\mu\text{m}$  over 1500 s of UV exposure. The high wettability gradient generated by asymmetric UV exposure in combination with the low hysteresis (both in the UV irradiated and non-irradiated areas of the sample) are the driving force for a successful transport of a water droplet over a distance of 14 mm. To improve the moving distance of the droplet, multigradients were inscribed on the patterned thiol-acrylate system 25SH-AD by using the localized change in the surface polarity. In particular, a Laplace pressure gradient and a wettability gradient were generated by inscribing wedge-shaped patterns (half wedge angle of 3.5 and 7°) with photolithography and asymmetrical UV irradiation. With a half wedge angle of 7°, long-distance movement of the water droplet over 22 mm was successfully achieved.

## *Experimental*

### *Materials and chemicals*

Pentaerythritol tetra(3-mercaptopropionate) (PETMP) was obtained from Bruno Bock Thiochemicals (Germany). (2-Nitro-1,4-phenylene) dimethanol was from TCI (Belgium). Fluorolink MD®700 was supplied by Solvay (Brussels). The photoinitiator phenylbis (2,4,6-trimethylbenzoyl)-phosphine oxide (BAPO) and all other chemicals were supplied by Sigma-Aldrich (United States) and were used without additional purification.

### *Synthesis*

**(2-Nitro-1,4-phenylene) bis (methylene) diacrylate.** Acryloyl chloride (6.7 mL; 82 mmol) was mixed with a solution of (2-nitro-1,4-phenylene) dimethanol (5 g; 27 mmol) in 50 mL dry THF. Triethylamine (7.7 mL, 55 mmol) was dissolved in 50 mL dry THF and added dropwise to the reaction mixture. The reaction mixture was stirred overnight at room temperature and the progress was monitored by TLC. After evaporation of the solvent, the crude oil was dissolved in dichloromethane and extracted with water and saturated  $\text{Na}_2\text{CO}_3$  solution. The combined organic layers were dried over  $\text{MgSO}_4$  and the solvent

was removed by rotary evaporation. Chromatography on silica gel (cyclohexane:ethyl acetate 2:1) resulted in 6.5 g white crystals of acrylate-NBE (82% theoretical yield)

$^1\text{H}$  NMR ( $\delta$ , 400 MHz, 25 °C,  $\text{CDCl}_3$ ):  $\delta$  = 8.14 (s, 1H), 7.61 (dd, 2H), 7.26 ( $\text{CDCl}_3$ ), 6.47 (q, 2H), 6.19 (m, 2H), 5.92 (m, 2H), 5.60 (s, 2H), 5.26 (s, 2H).

$^{13}\text{C}$  NMR ( $\delta$ , 400 MHz, 25 °C,  $\text{CDCl}_3$ ):  $\delta$  = 165.6 (1C), 165.39 (1C), 147.51 (1C), 137.40 (1C), 133.03 (1C), 132.01 (2C), 129.23 (1C), 127.67 (2C), 124.43 (2C), 64.46 (1C), 62.77 (1C). FT-IR ( $\text{cm}^{-1}$ ): 3059, 2988, 1734, 1630, 1617, 1536, 1409, 1348, 1298, 1268, 1181, 1057, 980, 896, 842  $\text{cm}^{-1}$ .

#### *Characterization of the photo-responsive acrylate monomer*

$^1\text{H}$  NMR and  $^{13}\text{C}$  NMR spectra were carried out with a Varian (United States) 400-NMR spectrometer operating at 399.66 MHz and 100.5 MHz, respectively. The spectra were referred to  $\text{Si}(\text{CH}_3)_4$  and a relaxation delay of 10 s and 45° pulse were utilized for the acquisition of  $^1\text{H}$  NMR spectra.

UV-vis absorbance spectra were recorded with a Varian (United States) Cary 50 UV-Vis spectrophotometer. For cleavage experiments, acrylate-NBE was dissolved in acetonitrile (0.01 mg  $\text{mL}^{-1}$ ) and the solution was transferred into a quartz cuvette. UV-vis spectra were taken prior to and after different UV exposures with a medium pressure Hg lamp (Omnicure S1000, Lumen Dynamics, Canada). The light intensity (power density  $P$ ; in  $\text{mW cm}^{-2}$ ) in the sample plane was determined with an integrating radiometer (Powerpuck II, EIT Instrument Markets, United States) and amounted to 269  $\text{mW cm}^{-2}$  ( $\lambda$  = 250–470 nm).

#### *Preparation of acrylate/thiol-acrylate formulations*

Resin formulations were produced by mixing acrylate-NBE and isobornyl acrylate in equimolar ratio (Fig. 1d) with 1 wt% of the fluorinated methacrylate (Fluorolink MD®700). The thiol content was varied between 0 and 25 mol% and 2.5 wt% of BAPO were used as photoinitiator. The resin components were stirred in an ultrasonic bath for 10 minutes at 30 °C to dissolve BAPO and acrylate-NBE. The acrylate and thiol-acrylate formulations are shown in Table 3.

**Table 3 Composition of the acrylate and thiol–acrylate formulations**

Sample	Acrylate-NBE (mol%)	Isobornyl acrylate (mol%)	PETMP (mol%)	Fluorinated methacrylate (wt%)
0SH-AD	50	50	0	1
10SH-AD	45	45	10	1
25SH-AD	37.5	37.5	25	1

### *Characterization of the curing and cleavage kinetics*

The curing kinetics of the monomers and the photocleavage of the formed networks were followed by FT-IR spectroscopy utilizing a Vertex 70 spectrometer (Bruker, United States). 16 scans were performed in transmission mode with a resolution of 4 cm<sup>-1</sup> and the absorption peak areas were determined with OPUS software. To prepare the samples, 1 μL of each resin was deposited between two CaF<sub>2</sub> discs. The thin films were irradiated with a light emitting diode (LED) lamp (zgood® wireless LED curing lamp). The light intensity amounted to 3.2 mW cm<sup>-2</sup> ( $\lambda = 420\text{--}450$  nm). Afterwards, the polymer films were illuminated with the Omnicure S1000 lamp (269 mW cm<sup>-2</sup>;  $\lambda = 250\text{--}470$  nm) and the cleavage kinetics was followed by taking FT-IR spectra after defined exposure times.

Differential scanning calorimetry (DSC) measurements were done with a Mettler-Toledo DSC 821e instrument (United States) to determine the thermal properties of the resins. The cured samples were heated from  $-10$  to  $100$  °C with a heating rate of  $20$  K min<sup>-1</sup> in nitrogen atmosphere (nitrogen flow was set to  $20$  mL min<sup>-1</sup>). The glass transition temperature ( $T_g$ ) was obtained by taking the midpoint in heat capacity.

### *Preparation and characterization of needle-like polymer surfaces*

The imprinting of the needle-like microstructure was performed using a polymer stamp, which in turn was copied from a nickel-master stamp purchased from Fraunhofer-Institut für Solare Energiesysteme ISE.

The nickel master carrying the needle structures was coated with a UV-curable prepolymer (urethane acrylate) containing a perfluorinated antiadhesive-additive. Then, the prepolymer film was covered with a  $125$  μm thick PET-film and cured for  $30$  s with an

UV-LED at  $\lambda = 365$  nm and  $100 \text{ mW cm}^{-2}$  through the PET-film. After demolding, a polymer-stamp with the inverse needle structure was obtained. In order to ensure complete conversion of the reactive acrylate groups at the surface of the polymer stamp, it was exposed three times for 60 s with the same UV-light source.

For the preparation of the micropatterned acrylate and thiol– acrylate photopolymers, a  $5 \mu\text{L}$  droplet of resin (Table 3) was placed on a transparent PET foil. The polymer stamp was pressed on the resin layer and curing was performed by irradiating (300 s) the resin through the PET foil with the zgood® LED lamp.

The structured surfaces were characterized by using a Nanosurf FlexAFM atomic force microscope (AFM). The system worked with a  $100 \times 100 \mu\text{m}^2$  x–y-scanner and a closed loop  $10 \mu\text{m}$  z-scanner. The topography measurements were taken in tapping mode using Tap190-G silicon cantilevers with a spring constant of  $48 \text{ N m}^{-1}$  and a probe tip radii  $<10$  nm. The pillar heights were determined by using the free software Gwyddion.

Scanning electron microscopy (SEM) images were taken with a scanning microscope Tescan Vega II (Tescan Orsay Holding, Brno) using a working voltage of 5 kV.

#### *Preparation of non-patterned polymer samples*

The non-patterned surfaces were prepared by placing  $5 \mu\text{L}$  droplets of the resin between a PET and a PP foil. Irradiation with visible light (zgood® wireless LED curing lamp,  $3.4 \text{ mW/cm}^2$ , 420–450 nm) was carried out through the PET foil. To generate hydrophilic cleavage and oxidation species, the cured samples were exposed to UV light (Omnicure S1000 lamp;  $269 \text{ mW cm}^{-2}$ ;  $\lambda = 250\text{--}470$  nm; air) for defined times.

#### *Characterization of surface polarity and wettability*

The light induced changes in surface wettability were characterized with static and dynamic contact angle measurements via a drop shape analysis system, DSA 100, from Krüss (Germany).

The contact angles of  $2 \mu\text{L}$  water droplets were measured a few minutes (cooling down the surface temperature to room temperature) after the irradiation. For determining the



dynamic contact angles the same software was used. 6  $\mu\text{L}$  water droplets were employed in order to facilitate the measurement. All of the contact angles were investigated by calculating the arithmetic average from five different points of each sample, which has been UV illuminated with a selected exposure dose.

*Preparation and characterization of polymer surfaces with wettability gradient and Laplace pressure gradient*

Either needle-like or non-patterned photo-cured films on PET foil were prepared as described in the previous paragraphs. In the next step, wedge-shaped patterns ( $l = 20 \text{ mm}$ ,  $c = 4/2 \text{ mm}$ ,  $\alpha = 7^\circ/3.5^\circ$ ) were inscribed by using asymmetrical exposure with UV-light (Fig. 1c). The sample surface except the wedge (dimensions mentioned above) was protected with aluminum foil and the light beam of the Omnicure S1000 lamp ( $269 \text{ mW cm}^{-2}$ ;  $\lambda = 250\text{--}470 \text{ nm}$ ; air) was moved over the pattern with increasing illumination time (2000 s) at the end of the wedge.

A 2  $\mu\text{L}$  water droplet was placed on the beginning of the inscribed pattern (more hydrophobic area of the inscribed gradient) with the contact angle device (DSA 100, Krüss). By utilizing the high-speed digital camera system of the device, sequential photos were taken with a recording rate of 1.042 fps. The movement distance was determined by measuring the sliding distance between the starting point and the end of the contact line of the droplet and the sample surface (see L in Fig. 6c).

Conflicts of interest

There are no conflicts to declare.

*Acknowledgements*

The research work was performed within the COMET-Module "Chemitecture" (project-no.: 21647048) at the Polymer Competence Center Leoben GmbH (PCCL, Austria) within the framework of the COMET-program of the Federal Ministry for Transport, Innovation

and Technology and the Federal Ministry for Digital and Economic Affairs with contributions by Joanneum Research GmbH and Montanuniversitaet Leoben. The PCCL is funded by the Austrian Government and the State Governments of Styria, Upper and Lower Austria. In addition, the authors thank Josef Spreitz (Aglycon Dr. Spreitz KG) for his support in the synthesis of acrylate-NBE and Rita Höller for carrying out FT-IR experiments.

### *References*

- 1) D. Zhang, Z. Cheng and Y. Liu, *Chemistry*, 2019, 25, 3979–3992.
- 2) E. P. Chan, E. J. Smith, R. C. Hayward and A. J. Crosby, *Adv. Mater.*, 2008, 20, 711–716.
- 3) J. Manhart, D. Lenko, I. Mühlbacher, A. Hausberger, R. Schaller, A. Holzner, W. Kern and S. Schlögl, *Eur. Polym. J.*, 2015, 66, 236–246.
- 4) F. A. Müller, C. Kunz and S. Gräf, *Materials*, 2016, 9, 476.
- 5) J. del Barrio and C. Sánchez-Somolinos, *Adv. Opt. Mater.*, 2019, 7, 1900598.
- 6) A. F. Lasagni, D. F. Acevedo, C. A. Barbero and F. Mücklich, *Adv. Eng. Mater.*, 2007, 9, 99–103.
- 7) M. Leitgeb, D. Nees, S. Ruttloff, U. Palfinger, J. Götz, R. Liska, M. R. Beleggratis and B. Stadlober, *ACS Nano*, 2016, 10, 4926–4941.
- 8) L. Li, X. Liu, S. Pal, S. Wang, C. K. Ober and E. P. Giannelis, *Chem. Soc. Rev.*, 2017, 46, 4855–4866.
- 9) E. Wohlfart, J. P. Fernández-Blázquez, E. Knoche, A. Bello, E. Pérez, E. Arzt and A. del Campo, *Macromolecules*, 2010, 43, 9908–9917.
- 10) C. W. Sele, T. von Werne, R. H. Friend and H. Sirringhaus, *Adv. Mater.*, 2005, 17, 997–1001.
- 11) (a) S. Wang, K. Liu, X. Yao and L. Jiang, *Chem. Rev.*, 2015, 115, 8230–8293; (b) P. Roach, N. J. Shirtcliffe and M. I. Newton, *Soft Matter*, 2008, 4, 224–240.
- 12) M. Jin, X. Feng, J. Xi, J. Zhai, K. Cho, L. Feng and L. Jiang, *Macromol. Rapid Commun.*, 2005, 26, 1805–1809.
- 13) E. T. de Givenchy, S. Amigoni, C. Martin, G. Andrada, L. Caillier, S. Géribaldi and F. Guittard, *Langmuir*, 2009, 25, 6448–6453.

- 14) B. Bhushan, *Philos. Trans. R. Soc., A*, 2009, 367, 1445–1486.
- 15) L. Y. L. Wu, S. K. Ngian, Z. Chen and D. T. T. Xuan, *Appl. Surf. Sci.*, 2011, 257, 2965–2969.
- 16) K. Liu and L. Jiang, *Nanoscale*, 2011, 3, 825–838.
- 17) J. Zimmermann, F. A. Reifler, G. Fortunato, L.-C. Gerhardt and S. Seeger, *Adv. Funct. Mater.*, 2008, 18, 3662–3669.
- 18) S. Jiang, Y. Hu, H. Wu, Y. Zhang, Y. Zhang, Y. Wang, Y. Zhang, W. Zhu, J. Li, D. Wu and J. Chu, *Adv. Mater.*, 2019, 31, e1807507.
- 19) S. Wang, Y. Song and L. Jiang, *J. Photochem. Photobiol., C*, 2007, 8, 18–29.
- 20) K. Zhang, F. Wang and X. Zhao, *Comput. Mater. Sci.*, 2016, 124, 190–194.
- 21) H. Gau, *Science*, 1999, 283, 46–49.
- 22) H. G. Andrews, E. A. Eccles, W. C. E. Schofield and J. P. S. Badyal, *Langmuir*, 2011, 27, 3798–3802.
- 23) K. Liu, M. Cao, A. Fujishima and L. Jiang, *Chem. Rev.*, 2014, 114, 10044–10094.
- 24) K. Ichimura, S.-K. Oh and M. Nakagawa, *Science*, 2000, 288, 1624–1626.
- 25) J. Berná, D. A. Leigh, M. Lubomska, S. M. Mendoza, E. M. Pérez, P. Rudolf, G. Teobaldi and F. Zerbetto, *Nat. Mater.*, 2005, 4, 704–710.
- 26) Y. Ito, M. Heydari, A. Hashimoto, T. Konno, A. Hirasawa, S. Hori, K. Kurita and A. Nakajima, *Langmuir*, 2007, 23, 1845–1850.
- 27) H. Bai, L. Wang, J. Ju, R. Sun, Y. Zheng and L. Jiang, *Adv. Mater.*, 2014, 26, 5025–5030.
- 28) E. Rossegger, D. Hennen, T. Griesser, I. Roppolo and S. Schlögl, *Polym. Chem.*, 2019, 10, 1882–1893.
- 29) S. V. Radl, C. Schipfer, S. Kaiser, A. Moser, B. Kaynak, W. Kern and S. Schlögl, *Polym. Chem.*, 2017, 8, 1562–1572.
- 30) C. E. Hoyle, T. Y. Lee and T. Roper, *J. Polym. Sci., Part A: Polym. Chem.*, 2004, 42, 5301–5338.
- 31) (a) A. F. Senyurt, H. Wei, C. E. Hoyle, S. G. Piland and T. E. Gould, *Macromolecules*, 2007, 40, 4901–4909; (b) T. Y. Lee, T. M. Roper, E. S. Jonsson, C. A. Guymon and C.

## PUBLICATION II

- E. Hoyle, *Macromolecules*, 2004, 37, 3606–3613; (c) S. K. Reddy, K. S. Anseth and C. N. Bowman, *Polymer*, 2005, 46, 4212–4222.
- 32) Y. V. Il'ichev, M. A. Schwörer and J. Wirz, *J. Am. Chem. Soc.*, 2004, 126, 4581–4595.
- 33) S. Radl, M. Kreimer, J. Manhart, T. Griesser, A. Moser, G. Pinter, G. Kalinka, W. Kern and S. Schlögl, *Polymer*, 2015, 69, 159–168.
- 34) N. B. Cramer and C. N. Bowman, *J. Polym. Sci., Part A: Polym. Chem.*, 2001, 39, 3311–3319.
- 35) A. K. O'Brien, N. B. Cramer and C. N. Bowman, *J. Polym. Sci., Part A: Polym. Chem.*, 2006, 44, 2007–2014.
- 36) S. K. Kim and C. A. Guymon, *Polymer*, 2012, 53, 1640–1650.
- 37) A. Vitale, S. Touzeau, F. Sun and R. Bongiovanni, *Macromolecules*, 2018, 51, 4023–4031.
- 38) R. N. Wenzel, *Ind. Eng. Chem.*, 1936, 28, 988–994.
- 39) R. Rosario, D. Gust, A. A. Garcia, M. Hayes, J. L. Taraci, T. Clement, J. W. Dailey and S. T. Picraux, *J. Phys. Chem. B*, 2004, 108, 12640–12642.
- 40) K. Sugita, *Prog. Org. Coat.*, 1997, 31, 87–95.
- 41) M. K. Chaudhury and G. M. Whitesides, *Science*, 1992, 256, 1539–1541.
- 42) (a) A. Y. Fadeev and T. J. McCarthy, *Langmuir*, 1999, 15, 3759–3766; (b) H. Chen, T. Tang and A. Amirfazli, *Colloids Surf., A*, 2012, 408, 17–21.
- 43) K. Grundke, K. Pöschel, A. Synytska, R. Frenzel, A. Drechsler, M. Nitschke, A. L. Cordeiro, P. Uhlmann and P. B. Welzel, *Adv. Colloid Interface Sci.*, 2015, 222, 350–376.
- 44) A. Romano, I. Roppolo, M. Giebler, K. Dietliker, Š. Možina, P. Šket, I. Mühlbacher, S. Schlögl and M. Sangermano, *RSC Adv.*, 2018, 8, 41904–41914.
- 45) S. Radl, I. Roppolo, K. Pölzl, M. Ast, J. Spreitz, T. Griesser, W. Kern, S. Schlögl and M. Sangermano, *Polymer*, 2017, 109, 349–357.

## Supporting Information

## Supporting Information

## Photo-switching of surface wettability on micropatterned photopolymers for fast transport of water droplets over a long-distance

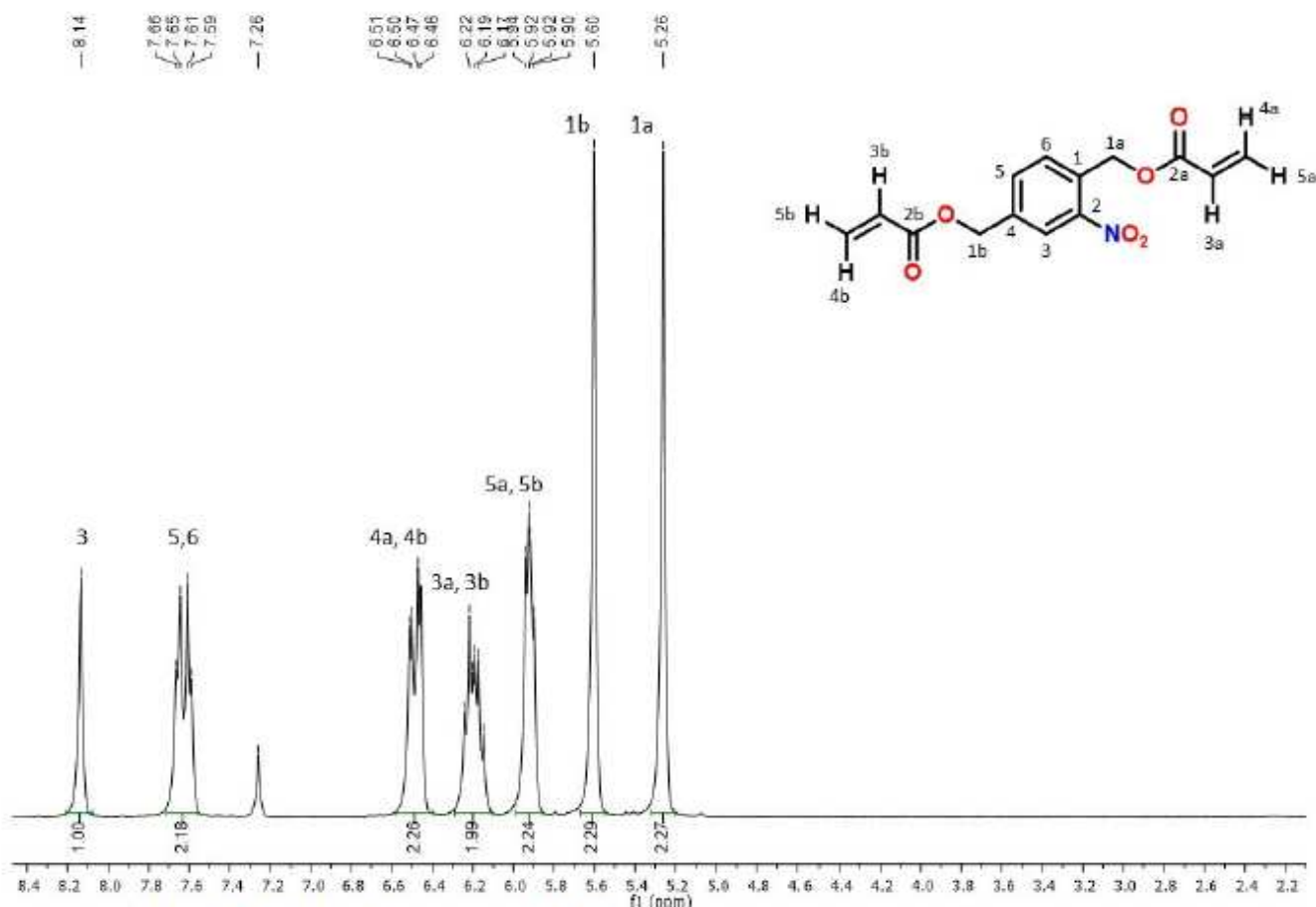
Elisabeth Rossegger,<sup>a</sup> Dieter Nees,<sup>b</sup> Simon Turisser,<sup>a</sup> Simone Radl,<sup>a</sup> Thomas Griesser,<sup>c</sup> and Sandra Schlögl<sup>a,\*</sup>

<sup>a</sup>Polymer Competence Center Leoben GmbH, Roseggerstrasse 12, A-8700 Leoben, Austria

e-mail: sandra.schloegl@pccl.at

<sup>b</sup>Joanneum Research GmbH, Franz-Pichler-Strasse 30, A-8160 Weiz, Austria

<sup>c</sup>Institute of Chemistry of Polymeric Materials, Montanuniversitaet Leoben, Otto Glöckel-Strasse 2, A-8700 Leoben, Austria



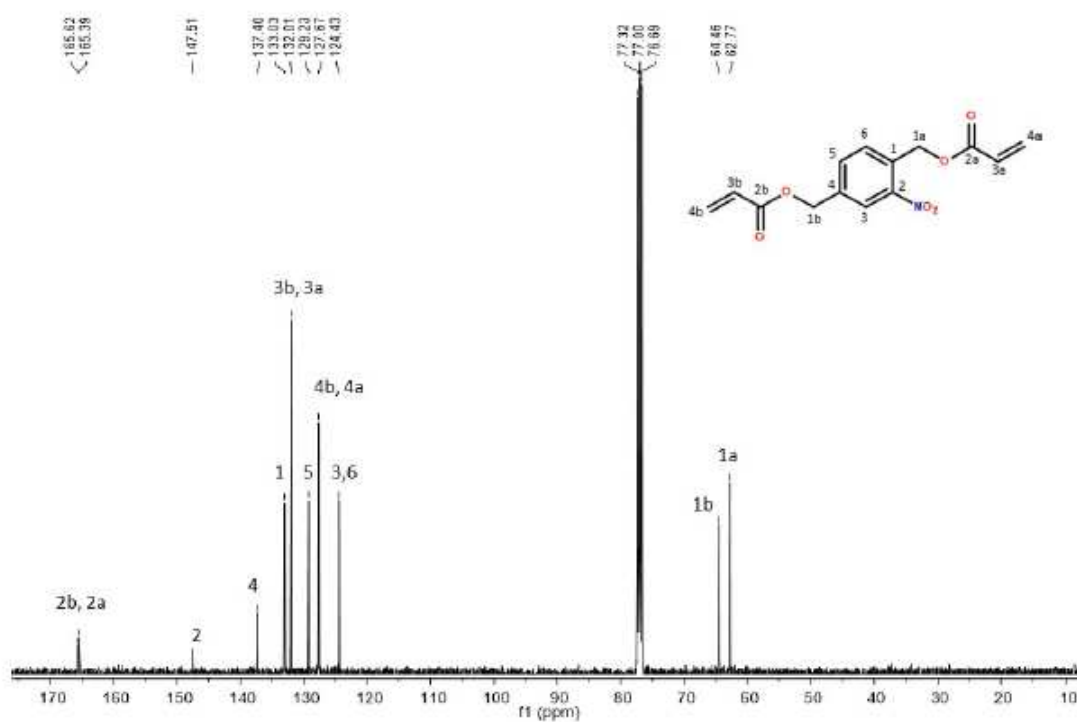


Figure S2 –  $^{13}\text{C}$  NMR spectrum of acrylate-NBE

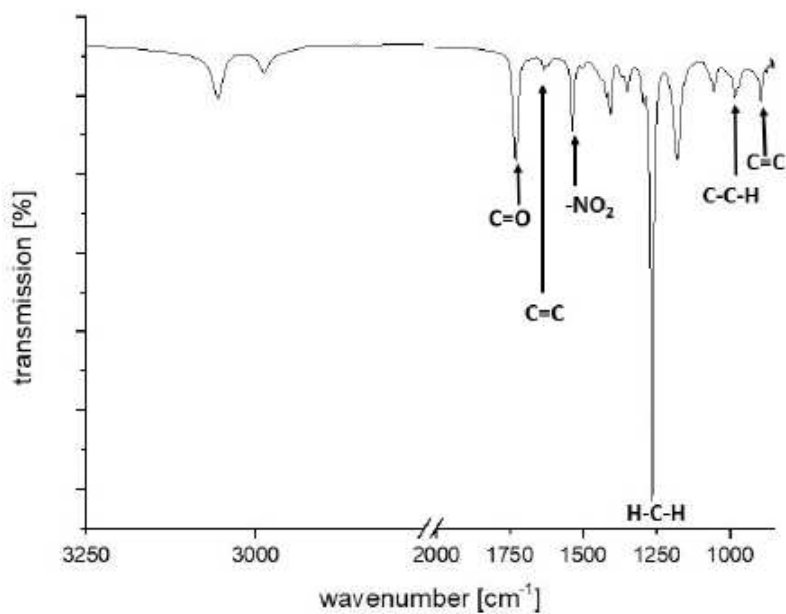


Figure S3 – FT-IR spectrum of acrylate-NBE

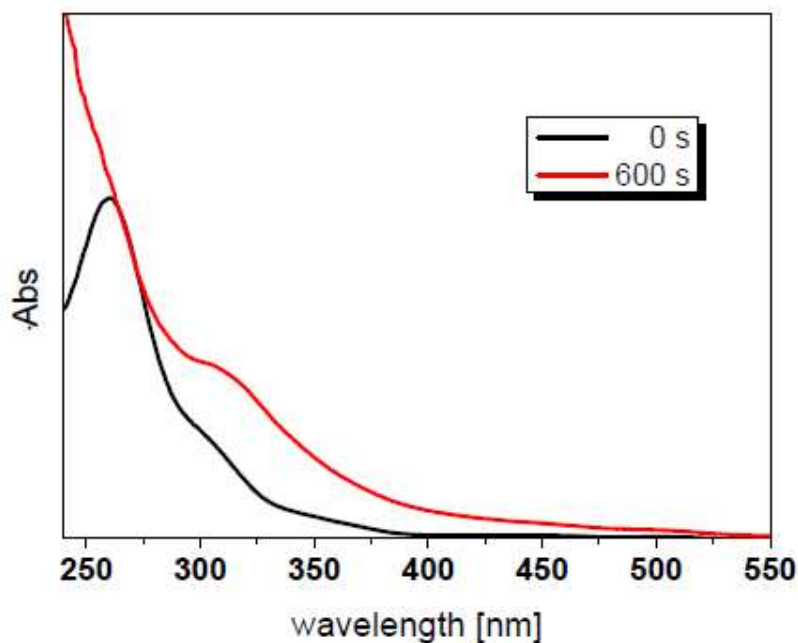


Figure S4 – Following the UV-vis absorbance of acrylate-NBE (10 mg/mL in acetonitrile) upon UV exposure (269 mW/cm<sup>2</sup>).

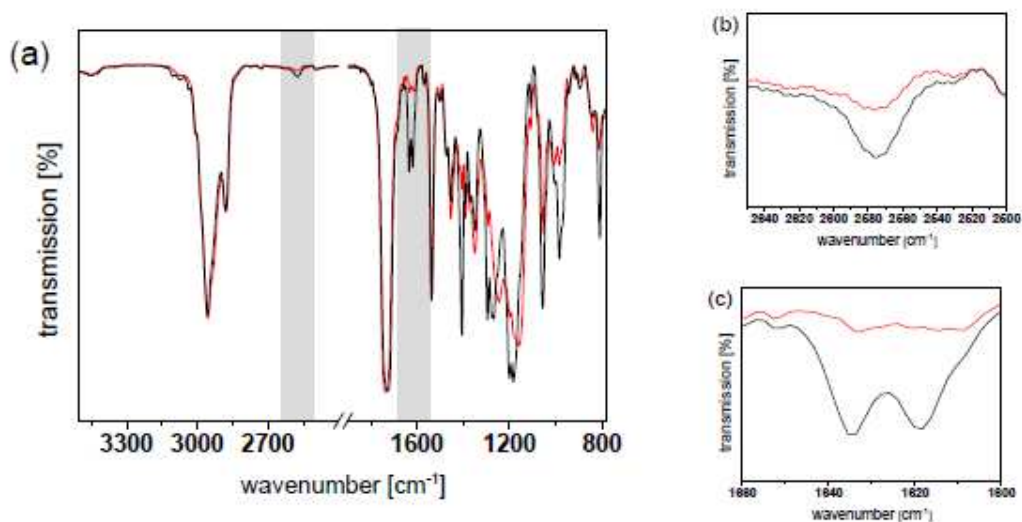


Figure S5 – (a) FT-IR spectra of resin 25SH-AD prior to (black line) and after photo-curing (red line). IR bands of the characteristic (b) thiol and (c) acrylate groups magnified out of the FT-IR spectra. Irradiation was carried out with visible light ( $\lambda = 420 - 450 \text{ nm}$ , 3.2 mW/cm<sup>2</sup>) under air.

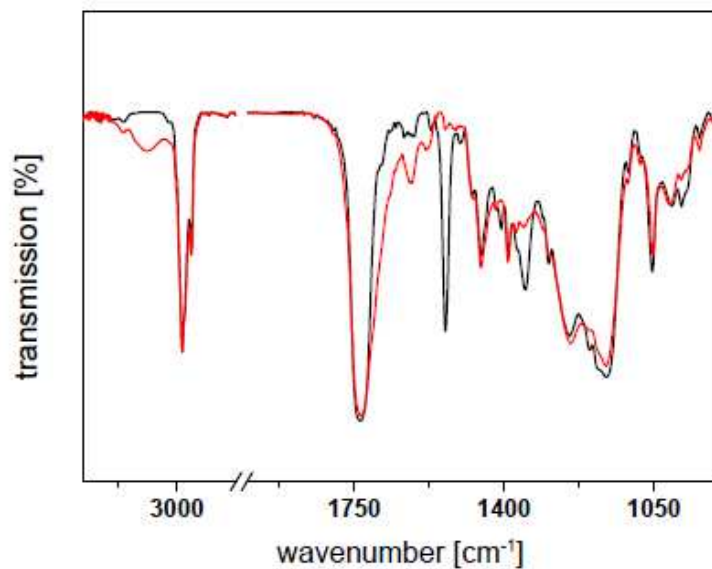


Figure S6 – (a) FT-IR spectra of photocured resin 25SH-AD prior to (*black line*) and after photocleavage (*red line*). Irradiation was carried out with UV light ( $\lambda = 250 - 470 \text{ nm}$ ,  $269 \text{ mW/cm}^2$ ) under air.

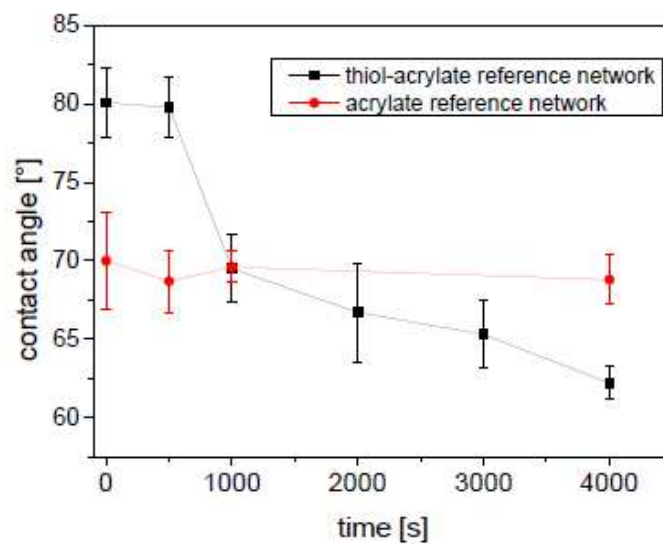
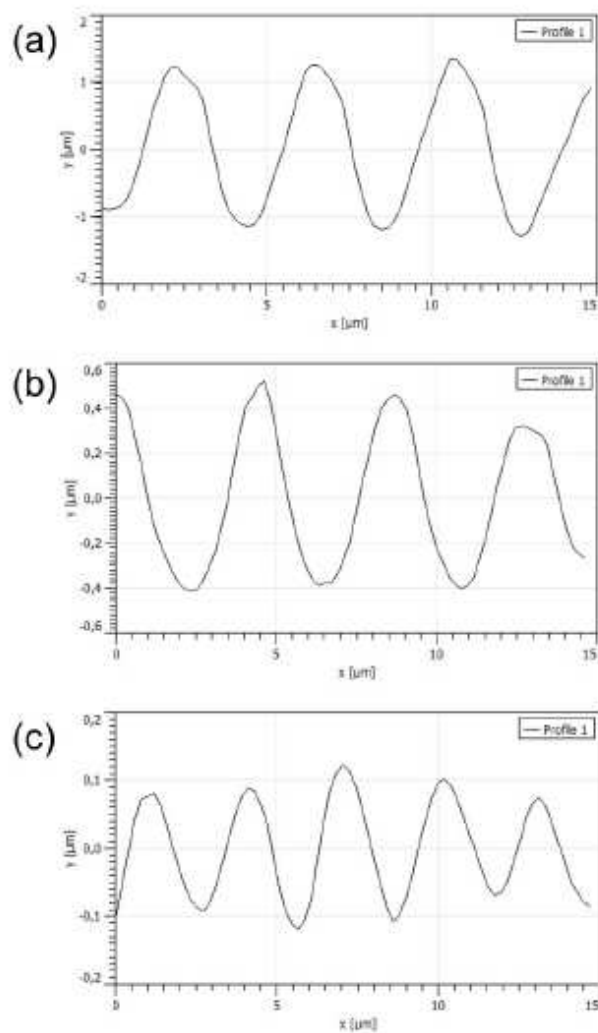


Figure S7 – Static water contact angles of cured acrylate and thiol-acrylate systems comprising no photo-sensitive *o*-NBE groups versus exposure time ( $269 \text{ mW/cm}^2$ ,  $\lambda < 400 \text{ nm}$ ). The thiol-acrylate formulation contained 75 mol% isobornyl acrylate, 25 mol% PETMP and 2.5 wt% BAPO. The acrylate formulation contained isobornyl acrylate and 2.5 wt% BAPO.





**Figure S8** – Topography profiles obtained from AFM micrographs of the needle-like micropatterns inscribed in resin 25SH-AD (comprising 25 mol% PETMP) by visible light assisted NIL after (a) 0, (b) 1000 and (c) 1500 s of UV exposure ( $269 \text{ mW/cm}^2$ ) under air.

**PUBLICATION III:**

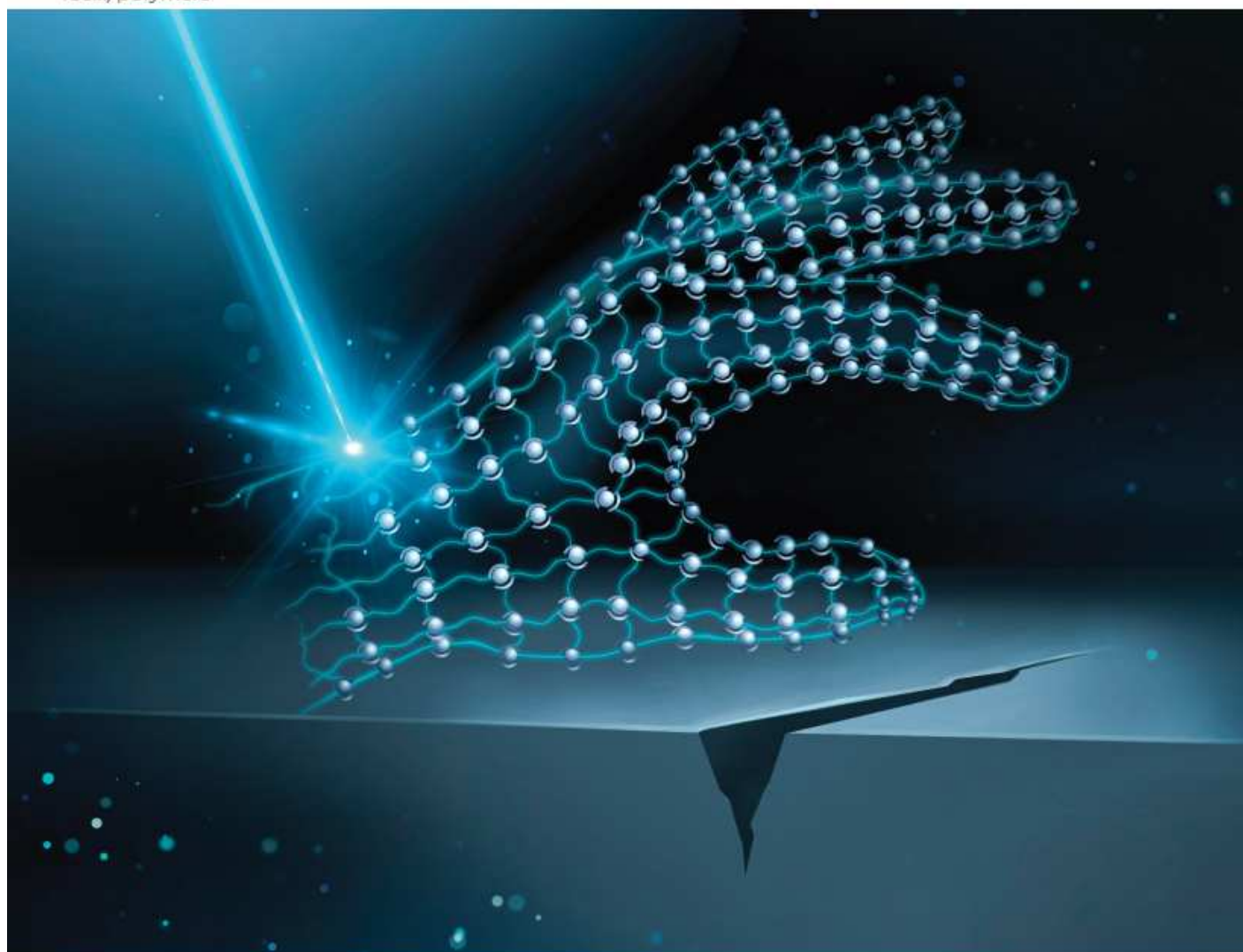
*Digital light processing 3D printing with thiol-acrylate  
vitrimers*

Rossegger, Elisabeth; Höller, Rita; Reisinger, David; Strasser, Jakob; Fleisch, Mathias;  
Griesser, Thomas; Schlögl, Sandra

*Polymer Chemistry*, 2021, 12, 639-644

# Polymer Chemistry

[rsc.li/polymers](https://rsc.li/polymers)



ISSN 1759-9962

### *Abstract*

Dynamic covalent bonds endow polymer networks with advanced functions such as self-healability, recyclability, malleability and shape memory. Currently, the most attractive dynamic networks are vitrimers, which rely on thermo-activated exchange reactions such as the catalyzed transesterification of hydroxyl ester moieties. However, the introduction of dynamic covalent bonds into 3D printable photopolymers is challenging, as commonly used transesterification catalysts are poorly soluble and compromise on cure rate and pot life of photocurable resins. Herein, a mono-functional methacrylate phosphate is presented as new transesterification catalyst, which overcomes these limitations and unlocks a new toolbox of photocurable vitrimers. Applied in thiol-acrylate vitrimer systems, the fast photopolymerization together with a high storage stability enables the successful additive manufacturing of precise 3D objects with features of 500  $\mu\text{m}$  using bottom-up digital light processing (DLP). Once photo-cured, the dynamic thiol-click networks are able to rapidly undergo thermo-activated rearrangements of their network topology as shown by stress relaxation experiments. The DLP printing of soft active structures with triple-shape memory and thermal mendability is demonstrated. Its versatility makes this unique class of material an ideal candidate for 3D printing of structural and fast acting functional devices in soft robotics, biomedicine and electronics.

### *Introduction*

With the advent of additive manufacturing techniques (AMTs), digitalization and personalization have found their way into material science. Virtual 3D models are conveniently translated into physical objects by digitally slicing computer-aided designs and building 3D objects layer-by-layer.<sup>1</sup> AMTs benefit from freedom in design and radically changed the way polymers are produced.<sup>2</sup>

Recently, soft active materials have been integrated within AMTs to precisely create polymer-based objects with additional/ improved functionality, since they are capable of undergoing large elastic deformation in response to environmental stimuli.<sup>3</sup> Currently, there are mainly two types of soft active materials being used: (i) hydrogels that swell

when solvent molecules diffuse into the polymer network and (ii) shape memory polymers (SMPs) that are capable of fixing temporary shapes and recovering to the permanent shape upon an external stimulus such as temperature,<sup>4</sup> magnetic fields,<sup>5</sup> and light.<sup>6</sup> Whilst hydrogels typically provide only a low modulus and also exhibit a slow response in a time scale of a few minutes, hours, and even days, 3D printing of SMPs is suitable for the manufacture of structural and fast acting devices.<sup>7</sup> Examples of customized functional devices are actuators for soft robotics,<sup>8</sup> self-evolving structures<sup>9</sup> piezoelectric and electronic devices.<sup>10</sup>

Another promising route to increase the functionality of additively manufactured objects is the 3D printing with thermosets comprising dynamic bonds, which are associative in nature. Associative covalent adaptable networks maintain their network connectivity at elevated temperature, since thermally induced bond breakage and reformation reactions occur simultaneously.<sup>11</sup> Above the topology freezing transition temperature ( $T_v$ ), the exchange reactions become significantly fast and induce a macroscopic flow of the polymer, which follows an Arrhenius trend analogous to silica-based glasses. Due to this unique behavior, Leibler and co-workers coined this class of networks vitrimers.<sup>12</sup> Whilst the chemistry of vitrimers has recently been expanded to numerous materials and exchange reactions, the most intensively studied ones are still epoxybased networks relying on reversible transesterification reactions.<sup>13</sup> In these systems, the addition of an appropriate catalyst is crucial to accelerate thermo-activated bond exchange reactions. Commonly used transesterification catalysts for vitrimeric networks are Brønsted acids, organo-metallic complexes and organic bases.<sup>14</sup> Based on the kinetics of the bond exchange reactions, the networks can be reprocessed, welded, reshaped and healed at temperatures well above the  $T_v$ .<sup>15</sup>

Shi and co-workers used thermo-activated transesterification to impart recycling properties in 3D printed parts.<sup>16</sup> However, the printed objects suffered from a rather low resolution and poor surface quality due to the applied filament extrusion printing technique. In contrast, Zhang et al. transferred the concept to photo-curable resins printable by digital light processing (DLP).<sup>17</sup> Compared to filament extrusion, DLP offers several advantages as it enables the fabrication of 3D objects with high resolution and

surface quality and comparably high throughput rates.<sup>18</sup> DLP is based on a layer-by-layer photopolymerization process, which is locally carried out in a vat containing a photocurable resin formulation (Fig. 1a).<sup>1</sup> During the printing process, each layer is illuminated all at once using a selectively masked light source comprising binary patterns presented by a digital micro-mirror device. Zhang and co-workers used a photo-curable resin formulation with hydroxyl-functional mono- and diacrylates, a Norrish Type I photoinitiator and  $\text{Zn}(\text{OAc})_2$  for catalyzing the bond exchange reactions, which rendered the network self-healable and reprocessable.<sup>17</sup> However, this approach lacks from a versatility in network design as  $\text{Zn}(\text{OAc})_2$  is insoluble in the majority of common acrylate monomers. Another well-known transesterification catalyst is triazabicyclodecene, which was applied by Bowman et al. for the preparation of covalent adaptable thiol-ene networks.<sup>19</sup> However, photocurable resins containing triazabicyclodecene are not applicable to manufacture 3D objects with an adequate speed, as triazabicyclodecene acts as radical scavenger and retards radically induced photopolymerization reactions. Herein, we unlock a new toolbox of functional monomers suitable for the DLP printing of vitrimers by introducing an oligomeric methacrylate phosphate as efficient transesterification catalyst. The catalyst is liquid, easily soluble in a wide range of acrylate monomers and covalently incorporated into the network across its methacrylate group. Another key property is its inertness in thiol-click formulations. Whilst acrylate-based photopolymers are well known for their heterogeneous network structure and inferior mechanical properties (e.g. low impact resistance), the addition of functional thiols, acting as chain transfer agents, shifts the gel point towards higher conversions and reduces shrinkage stress.<sup>20</sup> At higher thiol concentrations, the photopolymerization of acrylate monomers is dominated by a chain-growth mechanism (Fig. 1c) leading to improved mechanical properties and higher network homogeneity.<sup>21</sup> However, prominent transesterification catalysts such as  $\text{Zn}(\text{OAc})_2$ , triazabicyclodecene or triphenylphosphine promote thiol-Michael addition reactions, which compromise on the storage stability of the resins.<sup>22</sup> We observed fast gelation under dark conditions, which makes it impossible to print those formulations via DLP (Fig. S1, ESI†).

## Results and Discussion

To demonstrate the salient features of the new catalyst, a photocurable thiol-click formulation (resin-ER-1) was prepared, which consisted of mono- and bi-functional acrylate monomers with –OH groups (Fig. 1b). A high number of –OH groups is beneficial as they facilitate exchange reactions in the photopolymer network.<sup>23</sup> 25 mol% thiol was added as crosslinker together with 5 wt% catalyst and 2 wt% phenylbis(2,4,6-trimethylbenzoyl)phosphine oxide as photoinitiator.

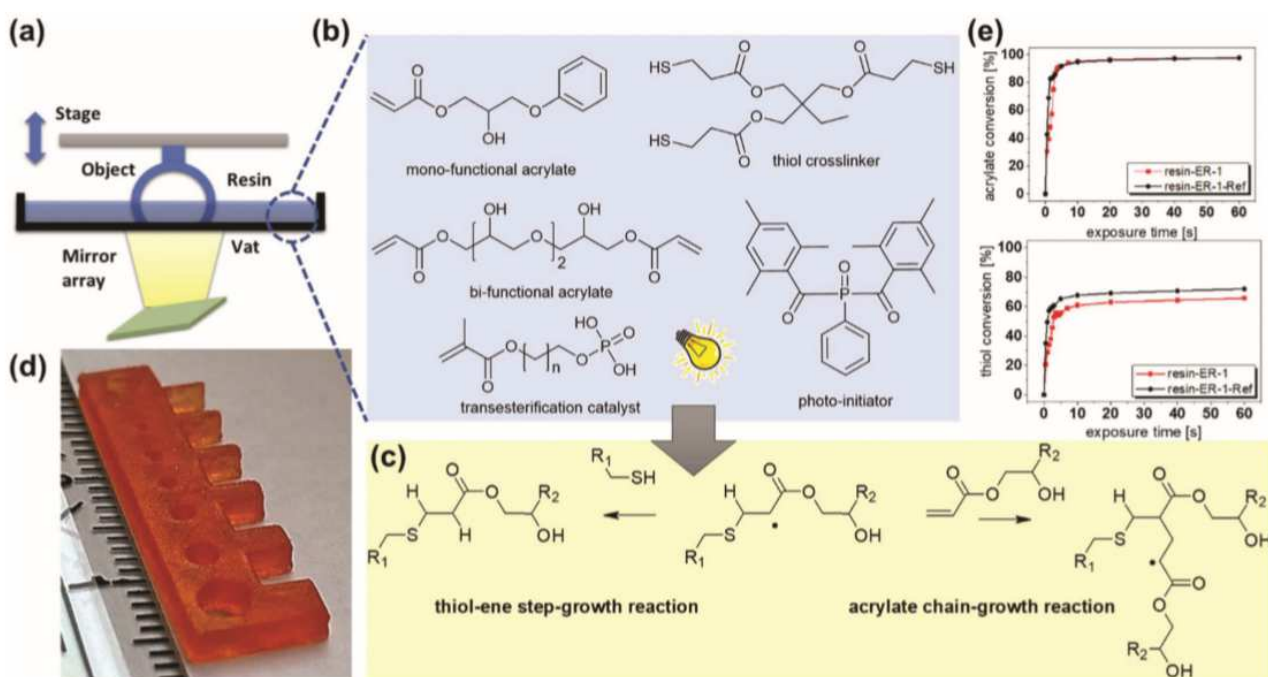


Fig. 1 (a) Schematic representation of DLP process. (b) Monomers and transesterification catalyst used for the preparation of covalent adaptable thiol-acrylate photopolymers. (c) Schematic representation of the photocuring reaction. (d) Photograph of a 3D printed test structure with a length of 2.6 cm. (e) Curing kinetics as obtained from FTIR data. The lines are a guide for the eye.

Rheological measurements revealed that the viscosity of resin-ER-1 amounted to 340 mPa s, directly after mixing, and it did not significantly change during a storage at room temperature for one week (415 mPa s). Along with a high storage stability, the formulation is characterized by a fast cure rate, which is crucial for the layer-by-layer build-up of 3D objects during DLP. The conversion of the acrylate and thiol groups was determined by FTIR spectroscopy, following the time-dependent depletion of the characteristic absorption bands of acrylate and thiol groups at 1635 and 2570  $\text{cm}^{-1}$ , respectively. FTIR spectra prior to and after UV exposure are shown in Fig. S2 (ESI<sup>†</sup>). The cure kinetics is

comparable to the non-catalysed reference system (resin-ER-1-Ref) and maximum conversion of thiol and acrylate groups is observed upon 10 s UV exposure (Fig. 1e). The fast photopolymerization enabled the DLP printing of 3D objects with high precision as demonstrated by printing a test structure with various substructures (Fig. 1d). All features with their thickness decreasing from 3 mm to 500  $\mu\text{m}$  were replicated successfully. Subsequently, discs with a diameter of 10 mm were printed for rheological experiments, to determine the stress relaxation of the network as a function of temperature (160–200  $^{\circ}\text{C}$ ). Under the applied conditions, thermal degradation was avoided, as thermogravimetric analysis revealed a thermal stability of cured resin-ER-1 well above 200  $^{\circ}\text{C}$  (Fig. S3, ESI†). Moreover, a high mobility of the chain segments was ensured as the network's  $T_g$  amounted to 0  $^{\circ}\text{C}$  (DSC curve is shown in Fig. S4a, ESI†). Fig. 2a provides the time-dependent evolution of the relaxation modulus at 180  $^{\circ}\text{C}$  for both non-catalyzed and catalyzed systems. Resin-ER-1-Ref showed a slight stress relaxation, which is explained by the thermal release of volumetric shrinkage stresses arising during network evolution.<sup>24</sup> In contrast, a very fast stress relaxation was observed for resin-ER-1, with 63% (1/e) of the initial stress being relaxed within 31.5 min. In contrast, lower crosslinked acrylate networks with  $\text{Zn}(\text{OAc})_2$  require a 4 times longer relaxation time (120 min) under the same conditions.<sup>17</sup> The stress relaxation is clearly temperature-dependent and indicates a rising bond exchange rate at increasing temperature.

Along with temperature, the stress relaxation kinetics of vitrimers is also governed by the amount of catalyst, with faster relaxation rates being observed at higher catalyst concentration.<sup>23</sup> In further experiments, we gradually increased the amount of the oligomeric methacrylate phosphate in the thiol–acrylate resin from 5 to 15 wt%. The results show that the higher catalyst content indeed accelerates the stress relaxation kinetics (Fig. 2d). Whilst at 5 wt%, the thiol–acrylate network requires 31.5 min to reach 63% relaxation of the initial stress, the relaxation time amounts to 11.3 and 7.5 min in the presence of 10 and 15 wt% of the catalyst, respectively.

Whilst mineral phosphates are widely used heterogeneous catalysts for transesterifications in solution,<sup>25</sup> the stress relaxation data clearly evidences that organic counterparts are able to efficiently catalyze transesterifications in solid polymer networks.



Mono and diester of the phosphoric acid contain free –OH groups and are strong Brønsted acids, which are able to catalyse both esterifications and transesterifications.<sup>26</sup> In acidcatalysed transesterifications, the oxygen of the carbonyl ester group is protonated, thereby leading to an increase of the electrophilicity of the adjoining carbon atom.<sup>27</sup>

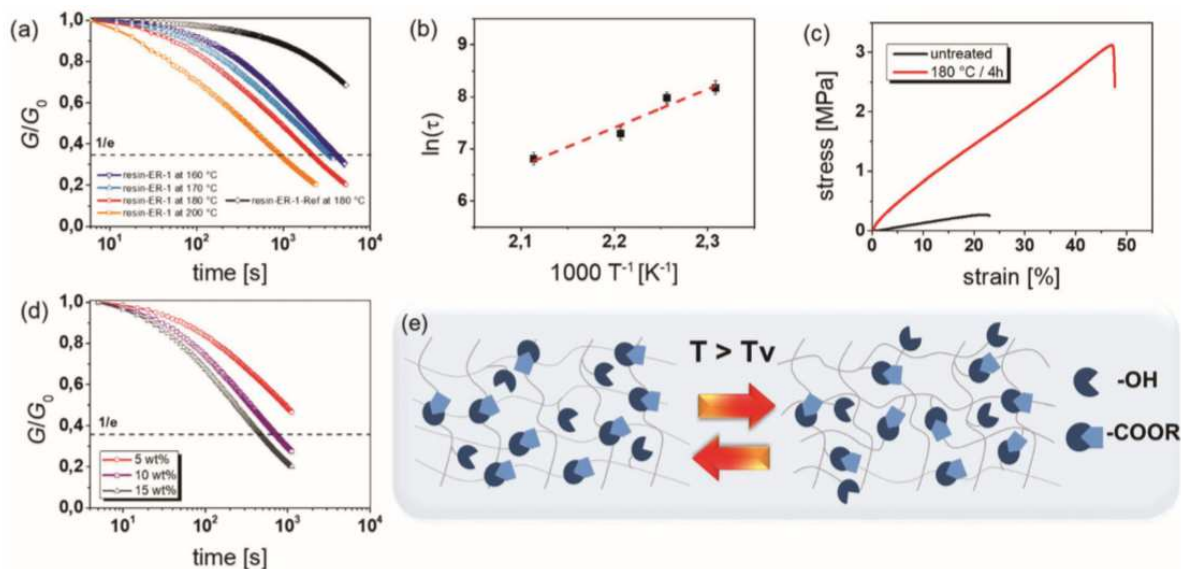


Fig. 2 (a) Normalised stress relaxation curves of resin-ER-1 versus temperature in comparison to the non-catalysed resin-ER-Ref. (b) Arrhenius plot of resin-ER-1 derived from measured relaxation times. (c) Stress-strain curves of DLP printed dumbbell specimens of resin-ER-1 prior to and after a thermal annealing at 180 °C for 4 h. (d) Normalised stress relaxation curves of thiol-acrylate vitrimers obtained at 180 °C as a function of the catalyst content. (e) Schematic representation of thermo-activated exchange reactions in covalent adaptable thiol-acrylate photopolymers.

Once protonated, the carbonyl group is more susceptible to a nucleophilic attack and forms a tetrahedral intermediate with an available –OH group in the network. A new ester bond is formed by subsequent proton transfer, departure of the leaving group and regeneration of the acidic catalyst ( $H^+$ ) by deprotonation.

Applying the Maxwell Model, the characteristic relaxation times ( $\tau^*$ ) were determined as the time required to relax to  $1/e$  of the initial stress at temperatures between 160 and 200 °C.<sup>28</sup> Fig. 2b demonstrates that the data satisfies the Arrhenius law, confirming the vitrimeric nature of the photopolymer. From the slope ( $m = -E_a/R$ ) of the straight line fitted to the data, an activation energy ( $E_a$ ) of 65.6 kJ mol<sup>-1</sup> was obtained. The  $T_v$  value was derived by extrapolation of the fitted data to a relaxation time of  $10^6$  s and amounted to 59 °C. Above  $T_v$ , the exchange reactions become macroscopically relevant and the network changes from an elastic solid to a viscoelastic liquid (Fig. 2e).<sup>12</sup> Along with topological

rearrangements, additional crosslink sites are formed by hydrogen bonding during prolonged treatment at 180 °C involving a decrease in –OH groups (FTIR spectra are shown in Fig. S5, ESI†) and a distinctive shift of the  $T_g$  from 0 to 20 °C (DSC curves are provided in Fig. S4, ESI†).<sup>29</sup> The reduced availability of functional groups slows down the stress relaxation kinetics (Fig. S6, ESI†). However, topological rearrangements and additional crosslink sites lead to a substantial improvement of the mechanical properties of printed test specimens. After a thermal treatment at 180 °C for 4 h, both strain and stress increase from 23 to 47% and from 0.26 to 3.1 N, respectively (Fig. 2c).

Whilst thermally annealed acrylic dynamic networks suffered from a brittle behavior with a strain about 8%,<sup>17</sup> resin-ER-1 benefits from an adequate stretchability, which is crucial for achieving large shape changes in 3D printed devices. Due to its dynamic bonds, resin-ER-1 features triple shape memory, as it is capable to undergo a controlled and active macroscopic deformation upon heating and programming the network above its two transition temperatures,  $T_g$  and  $T_v$ . As shown in Fig. 3a, the original/permanent shape of a printed and thermally annealed sample is changed by heating it above its highest thermal transition temperature, which is the  $T_v$  at 59 °C, and by applying an external force for deformation. The first temporary shape is fixed by cooling the sample to 40 °C, which is above the network's  $T_g$  and enables the programming of a second temporary shape, which is fixed by cooling the network to 0 °C. Subsequent heating of the sample facilitates a sequential recovery of the two shapes. A fast response time (40 s) is observed for the recovery of the second temporary shape, which is shown in video 1 (ESI†). The fast response time combined with the freedom in design makes these networks interesting candidates for the fabrication of customized active materials for soft actuator and soft robotics, as shown by the example of a grabber in Fig. 3b.

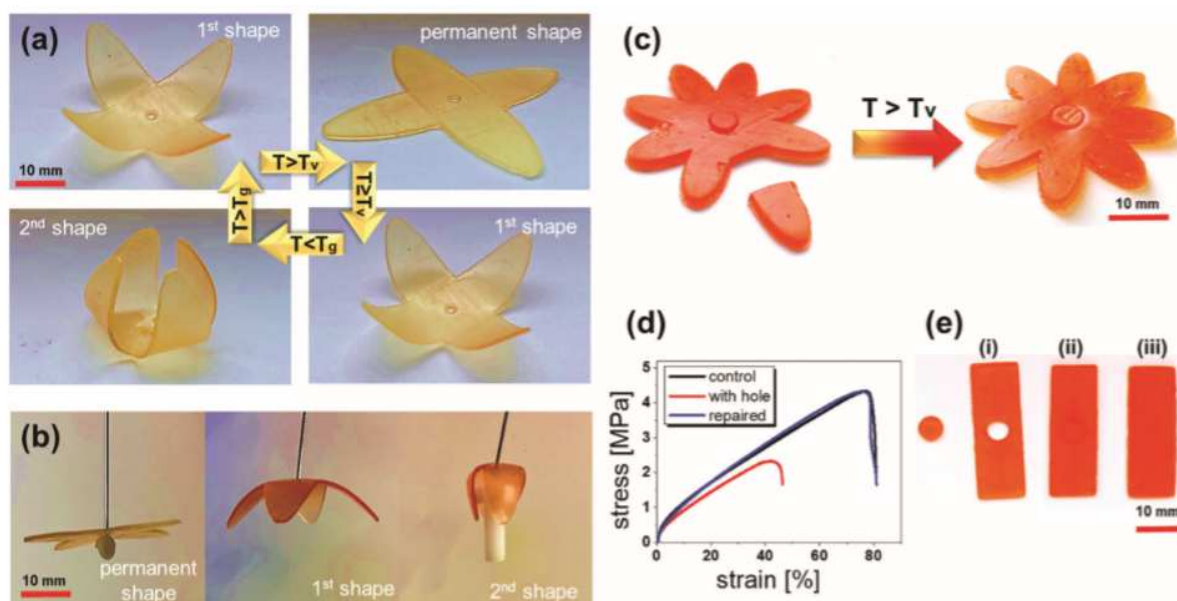


Fig. 3 (a) Photographs monitoring the triple-shape memory of DLP printed samples of resin-ER-1 using the  $T_v$  to fix the first temporary shape, and the  $T_g$  to fix the second temporary shape and sequential recovery of the shapes upon heating. (b) DLP printed gripper showing the potential of this new class of material for the customized production of structural and fast acting devices. (c) Thermally triggered healing of 3D printed test specimens at 180 °C for 4 h. (d) Stress–strain curves and photographs of DLP printed test specimens prior to and after a thermal mending at 180 °C for 4 h. (e) DLP printed test specimen for thermal mending experiments: (i) DLP printed test specimen with a circular-shaped hole in the centre and DLP printed circular shaped counterpart. (ii) Test specimen after fitting the circular-shaped counterpart in the hole and subsequent thermal treatment at 180 °C for 4 h. (iii) DLP printed control sample.

The dynamic nature of the bonds and the macroscopic reflow of the network above  $T_v$ , endows the soft active materials with additional functions such as intrinsic healability. Broken parts of 3D printed structures can be conveniently healed by a thermal treatment at 180 °C (Fig. 3c). The healing efficiency was determined by performing uniaxial tensile tests of 3D printed and thermally annealed dumbbell test specimen taking the ratio of the tensile strength prior to and after healing. The corresponding stress–strain curves are depicted in Fig. 3d. Since proper aligning of the thin broken test bars was challenging, we printed samples with a circular-shaped hole in the centre (Fig. 3e). For the repair step, the circularshaped counterpart was printed and fitted in the hole, followed by a thermal annealing at 180 °C for 4 h. After the repair, the boundaries between the two parts efficiently welded together and the original tensile strength (defect-free bar) could be fully recovered.

## *Conclusions*

Summing up, a new transesterification catalyst was introduced, which radically expands the toolbox of monomers suitable for the DLP printing of vitrimeric photopolymers. Compared to commonly used catalysts, the mono-functional methacrylate phosphate is superior in terms of solubility and stress relaxation. Moreover, it is covalently incorporated into the network and does not compromise on shelf life or cure kinetics of thiol-click photopolymers, which paves the way towards the DLP printing of complex soft active devices with triple-shape memory and additional functions such as selfhealability.

## *Experimental section*

### *Materials*

The catalyst (Miramer A99) was obtained from Miwon Specialty Chemical (Korea). All other chemicals were purchased from Sigma-Aldrich and used as received.

### *Preparation of resin-ER-1*

2-Hydroxy-2-phenoxypropyl acrylate (50 mol%) was mixed with glycerol 1,3-diglycerolate diacrylate (25 mol%) and 5 wt% Miramer A99. 0.05 wt% Sudan II was added and the formulation was ultra-sonicated until the photoabsorber was dissolved. 2 wt% phenylbis(2,4,6-trimethylbenzoyl)phosphine oxide and 25 mol% trimethylolpropane tri(3-mercaptopropionate) were added and dissolved by stirring the formulation at room temperature.

### *Characterization*

Light-induced curing of resin-ER-1 was monitored by FTIR spectroscopy utilizing a Vertex 70 spectrometer (Bruker, USA). 16 scans were cumulated in transmission mode from 4000 to 700  $\text{cm}^{-1}$  with a resolution of 4  $\text{cm}^{-1}$  and the absorption peak areas were calculated with OPUS software. 1.5  $\mu\text{L}$  of resin were drop-cast between two  $\text{CaF}_2$  discs and cured with a light emitting diode lamp (zgood® wireless LED curing lamp) comprising a power density of 3.3  $\text{mW cm}^{-2}$  ( $\lambda = 420\text{--}450 \text{ nm}$ ).

The viscosity of the resins was determined by using a modular compact rheometer MCR

102 from Anton Paar (Austria) with a CP60-0.5/TI cone (49.97 mm diameter and 1.982° opening angle). Each measurement was carried out with 1 mL resin at room temperature and a shear rate of 300 s<sup>-1</sup>. Thermal gravimetric analysis was performed with a Mettler Toledo (USA) TGA/DSC thermogravimetric analyzer. The measurements were carried out under oxygen atmosphere by heating the sample from 23 to 900 °C with a heating rate of 10 °C min<sup>-1</sup>. Differential scanning calorimetry measurements were carried out with a Mettler-Toledo DSC 821e instrument (USA). A temperature program from -20 to 150 °C with a heating rate of 20 K min<sup>-1</sup> was applied under nitrogen atmosphere. The T<sub>g</sub> was calculated from the second heating run by using the midpoint in heat capacity. Stress relaxation experiments at temperatures between 160 and 200 °C were carried out on an Anton Paar Physica MCR 501 rheometer (Austria) with parallel plate geometry. The samples were equilibrated to the selected measurement temperature and the specified constant normal force of 20 N for 20 min. Subsequently, 3% step strain was applied and the decreasing stress was recorded over time. For the Arrhenius plot, three measurements were taken for each data point. Tensile tests were performed on a ZwickRoell (Germany) Z1.0 static materials testing machine with a crosshead speed of 250 mm min<sup>-1</sup>. Dumbbell specimens with the dimensions of 2 × 12.5 × 75 mm were 3D printed.

#### *DLP 3D printing*

3D printing was performed on an Anycubic Photon S printer (China) with a LED 405 nm light source. Two bottom layers were exposed for 20 s, whereas the other layers were illuminated for 8 s. The layer height was set to 50 μm with a building speed of 6 mm s<sup>-1</sup> and a retracting speed of 1 mm s<sup>-1</sup>.

#### *Self-healing and shape memory experiments*

For self-healing experiments, the control sample (30 × 10 × 1.5 mm), the sample with a hole and the corresponding disc (d = 5 mm) were prepared via DLP 3D printing of resinER-1. To demonstrate the self-healing ability, the printed disc was fitted inside the hole and all samples were heated to 180 °C for 4 h. Shape memory experiments were carried out with 3D printed grippers (d = 50 mm), which were heated to 180 °C for 4 h. The first shape was fixed by heating the sample to 80 °C for 2 h. For the second shape, the sample was cooled down to 40 °C, re-shaped and cooled down with an ice bath below room temperature. By

heating to 80 °C, the first shape could be regained within 40 s. To restore the permanent shape, the sample was heated to 120 °C for 2 h.

#### Conflicts of interest

There are no conflicts to declare.

#### *Acknowledgements*

The research work was performed within the COMET-Module “Chemitecture” (project-no.: 21647048) at the Polymer Competence Center Leoben GmbH (PCCL, Austria) within the framework of the COMET-program of the Federal Ministry for Transport, Innovation and Technology and the Federal Ministry for Digital and Economic Affairs with contributions by Montanuniversitaet Leoben (Institute of Chemistry of Polymeric Materials). The PCCL is funded by the Austrian Government and the State Governments of Styria, Upper and Lower Austria.

#### *References*

- 1) S. C. Ligon, R. Liska, J. Stampfl, M. Gurr and R. Mülhaupt, *Chem. Rev.*, 2017, 117, 10212–10290.
- 2) M. Nadgorny and A. Ameli, *ACS Appl. Mater. Interfaces*, 2018, 10, 17489–17507.
- 3) (a) A. S. Gladman, E. A. Matsumoto, R. G. Nuzzo, L. Mahadevan and J. A. Lewis, *Nat. Mater.*, 2016, 15, 413–418; (b) Z. X. Khoo, J. E. M. Teoh, Y. Liu, C. K. Chua, S. Yang, J. An, K. F. Leong and W. Y. Yeong, *Virtual Phys. Prototyping*, 2015, 10, 103–122.
- 4) A. Lendlein and S. Kelch, *Angew. Chem., Int. Ed.*, 2002, 41, 2034.
- 5) A. M. Schmidt, *Macromol. Rapid Commun.*, 2006, 27, 1168–1172.
- 6) J. Ryu, M. D’Amato, X. Cui, K. N. Long, H. Jerry Qi and M. L. Dunn, *Appl. Phys. Lett.*, 2012, 100, 161908.

- 7) M. D. Hager, S. Bode, C. Weber and U. S. Schubert, *Prog. Polym. Sci.*, 2015, 49–50,3–33.
- 8) Y. Mao, K. Yu, M. S. Isakov, J. Wu, M. L. Dunn and H. Jerry Qi, *Sci. Rep.*, 2015, 5, 13616.
- 9) D. Raviv, W. Zhao, C. McKnelly, A. Papadopoulou, A. Kadambi, B. Shi, S. Hirsch, D. Dikovsky, M. Zyracki, C. Olguin, R. Raskar and S. Tibbits, *Sci. Rep.*, 2014, 4, 7422.
- 10) J. Lee, H.-C. Kim, J.-W. Choi and I. H. Lee, *Int. J. Precis. Eng. Manuf.-Green Tech.*, 2017, 4, 373–383.
- 11) C. J. Kloxin and C. N. Bowman, *Chem. Soc. Rev.*, 2013, 42, 7161–7173.
- 12) D. Montarnal, M. Capelot, F. Tournilhac and L. Leibler, *Science*, 2011, 334, 965–968.
- 13) J. M. Winne, L. Leibler and F. E. Du Prez, *Polym. Chem.*, 2019, 10, 6091–6108.
- 14) W. Alabiso and S. Schlögl, *Polymers*, 2020, 12, 1660.
- 15) (a) S. Kaiser, J. N. Jandl, P. Novak and S. Schlögl, *Soft Matter*, 2020, 16, 8577–8590; (b) S. Kaiser, S. Wurzer, G. Pilz, W. Kern and S. Schlögl, *Soft Matter*, 2019, 15, 6062–6072; (c) M. Giebler, C. Sperling, S. Kaiser, I. Duretek and S. Schlögl, *Polymers*, 2020, 12, 1148.
- 16) Q. Shi, K. Yu, X. Kuang, X. Mu, C. K. Dunn, M. L. Dunn, T. Wang and H. Jerry Qi, *Mater. Horiz.*, 2017, 4, 598–607.
- 17) B. Zhang, K. Kowsari, A. Serjouei, M. L. Dunn and Q. Ge, *Nat. Commun.*, 2018, 9, 1831
- 18) B. C. Gross, J. L. Erkal, S. Y. Lockwood, C. Chen and D. M. Spence, *Anal. Chem.*, 2014, 86, 3240–3253.
- 19) G. B. Lyon, L. M. Cox, J. T. Goodrich, A. D. Baranek, Y. Ding and C. N. Bowman, *Macromolecules*, 2016, 49, 8905–8913.
- 20) C. E. Hoyle and C. N. Bowman, *Angew. Chem., Int. Ed.*, 2010, 49, 1540–1573.
- 21) M. Sahin, S. Ayalur-Karunakaran, J. Manhart, M. Wolfahrt, W. Kern and S. Schlögl, *Adv. Eng. Mater.*, 2017, 19, 1600620.

### PUBLICATION III

- 22) (a) K. R. Rohit, S. M. Ujwaldev, K. K. Krishnan and G. Anilkumar, *Asian J. Org. Chem.*, 2018, 7, 85–102; (b) D. P. Nair, M. Podgórski, S. Chatani, T. Gong, W. Xi, C. R. Fenoli and C. N. Bowman, *Chem. Mater.*, 2013, 26, 724–744.
- 23) M. Hayashi and R. Yano, *Macromolecules*, 2019, 53, 182–189.
- 24) J. Chen, S. Jiang, Y. Gao and F. Sun, *J. Mater. Sci.*, 2018, 53, 16169–16181.
- 25) (a) F. Bazi, H. El Badaoui, S. Sokori, S. Tamani, M. Hamza, S. Boulaajaj and S. Sebti, *Synth. Commun.*, 2006, 36, 1585–1592; (b) K. Thinnakorn and J. Tscheikuna, *Appl. Catal., A*, 2014, 476, 26–33.
- 26) A. Streitwieser, C. H. Heathcock and E. M. Kosower, *Introduction to organic chemistry*, 4th edn, 1998.
- 27) (a) P. A. Alaba, Y. M. Sani and W. M. Ashri Wan Daud, *RSC Adv.*, 2016, 6, 78351–78368; (b) E. Lotero, Y. Liu, D. E. Lopez, K. Suwannakarn, D. A. Bruce and J. G. Goodwin, *Ind. Eng. Chem. Res.*, 2005, 44, 5353–5363.
- 28) M. Capelot, M. M. Unterlass, F. Tournilhac and L. Leibler, *ACS Macro Lett.*, 2012, 1, 789–792.
- 29) S. Wang, N. Teng, J. Dai, J. Liu, L. Cao, W. Zhao and X. Liu, *Polymer*, 2020, 210, 123004.



*Supporting Information***Supporting Information****Digital light processing 3D printing with thiol-acrylate vitrimers**

Elisabeth Rossegger,<sup>a</sup> Rita Höller,<sup>a</sup> David Reisinger,<sup>a</sup> Jakob Strasser,<sup>a</sup> Mathias Fleisch,<sup>a</sup> Thomas Griesser<sup>b</sup> and Sandra Schlögl<sup>a\*</sup>

<sup>a</sup>Polymer Competence Center Leoben GmbH, Roseggerstrasse 12, A-8700 Leoben, Austria

e-mail: [sandra.schloegl@pcccl.at](mailto:sandra.schloegl@pcccl.at)

<sup>b</sup>Institute of Chemistry of Polymeric Materials, Montanuniversitaet Leoben, Otto Glöckel-Strasse 2, A-8700 Leoben, Austria

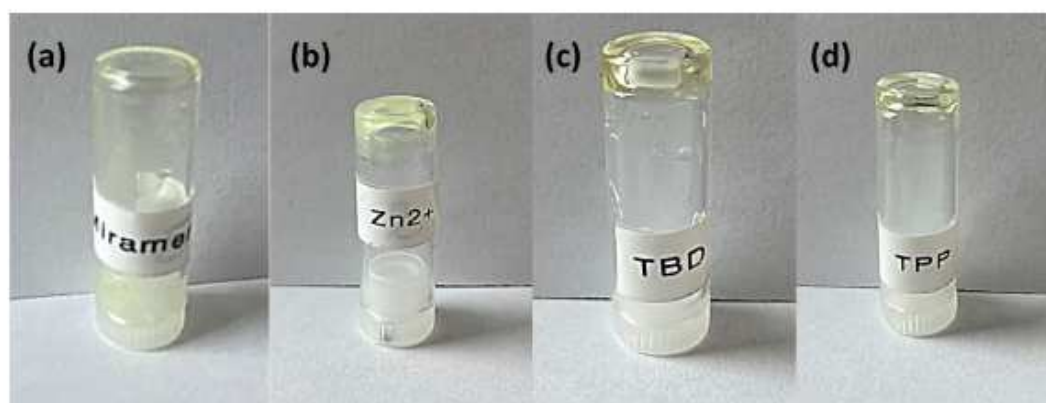


Figure S1 - Monitoring the premature gelation of a thiol-acrylate formulation containing 50% 2-hydroxy-2-phenoxypropyl acrylate, 25 mol% glycerol 1,3-dicycerolate diacrylate, 25 mol% trimethylolpropane tri(3-mercaptopropionate) and 2 wt% phenylbis(2,4,6-trimethylbenzoyl)phosphine oxide after adding a commonly used transesterification catalyst (5 mol% related to -OH groups) versus the behavior of ER-resin-1. Photographs show (a) ER-resin-1 and the thiol-acrylate resin directly after the addition of (b)  $\text{Zn}(\text{OAc})_2$ , (c) triazabicyclodecene and (d) triphenylphosphine.

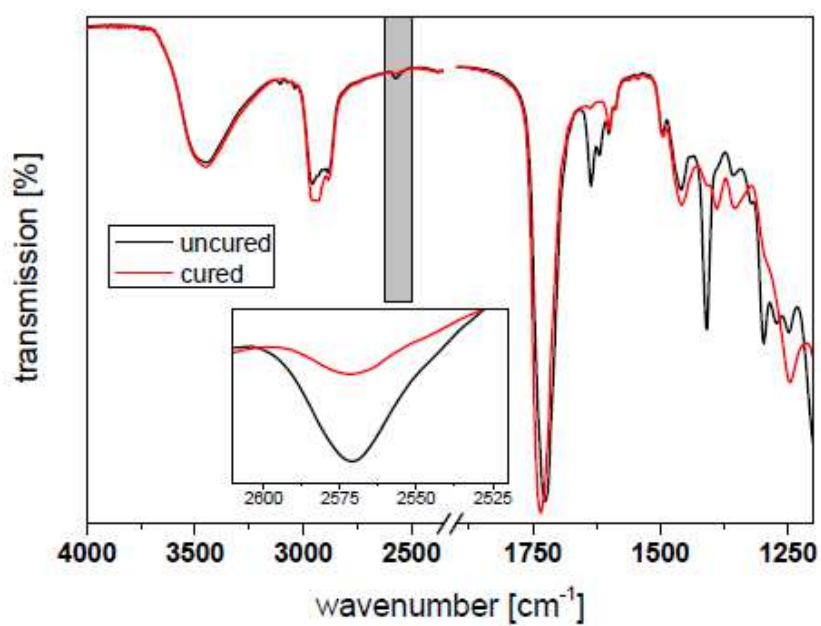


Figure S2 - FTIR spectra of resin-ER-1 prior to and after photocuring with a light emitting diode lamp (zgood<sup>®</sup> wireless LED curing lamp) comprising a power density of  $3.3 \text{ mW cm}^{-2}$  ( $\lambda = 420 - 450 \text{ nm}$ ).

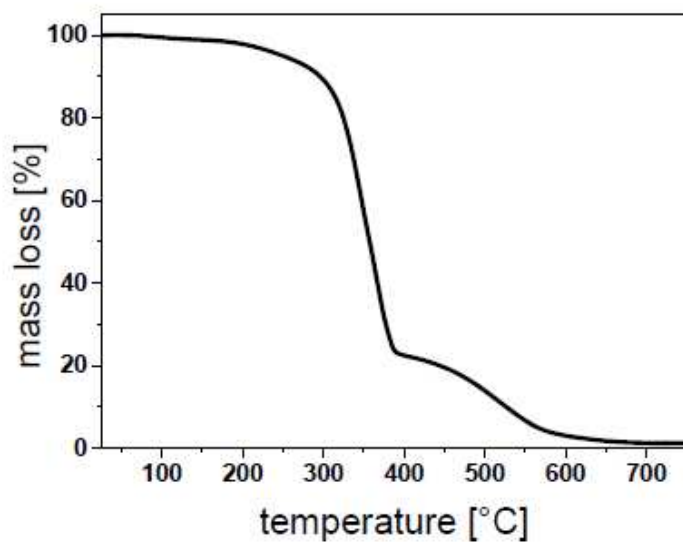


Figure S3 - TGA curve of cured resin-ER-1.

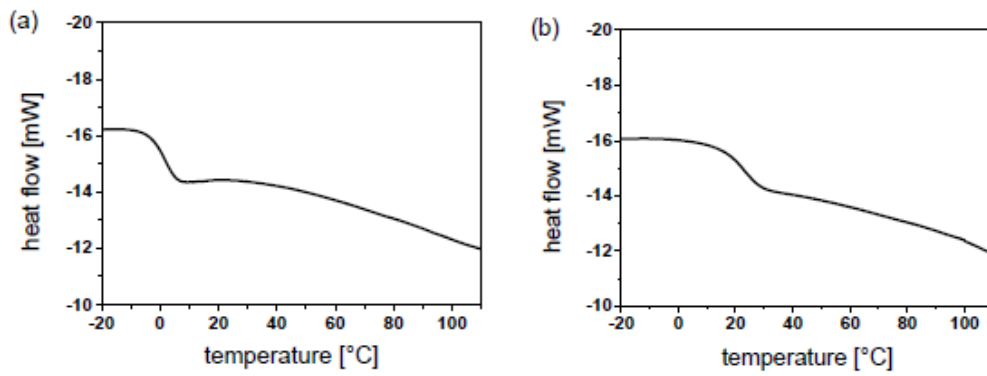


Figure S4 - DSC curves of DLP printed test specimen from catalyzed resin-ER-1 (a) prior to and (b) after thermal treatment at 180 °C for 4 h.

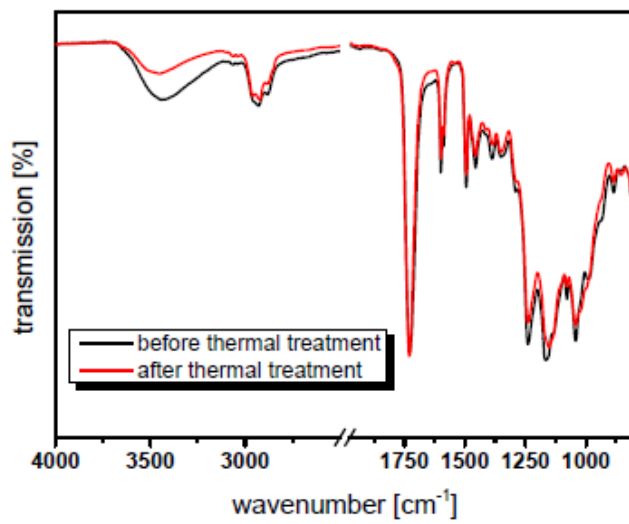


Figure S5 - FTIR spectra of cured resin-ER-1 prior to and after thermal treatment at 180 °C for 4 h.

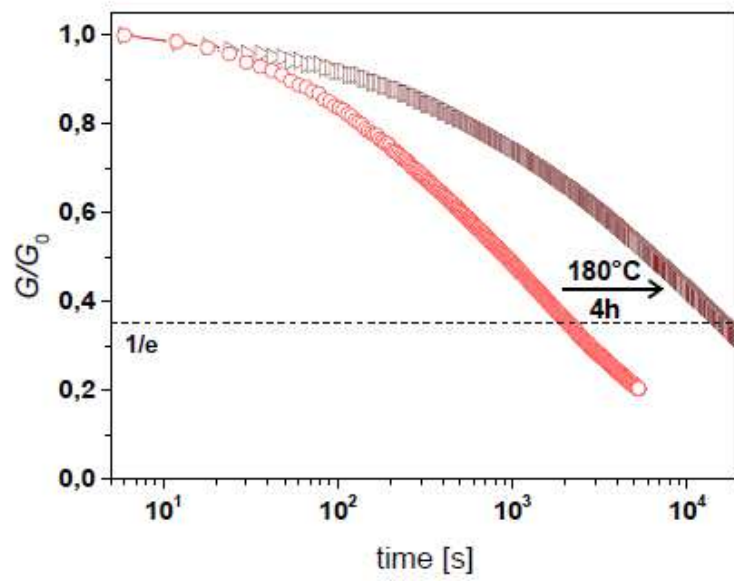


Figure S6 - Normalised stress relaxation curves of DLP printed test specimen from catalyzed resin-ER-1, prior to and after thermal treatment of the samples at  $180^\circ\text{C}$  for 4 h. The stress relaxation experiments were carried out at  $180^\circ\text{C}$ .

**PUBLICATION IV:**

*High resolution additive manufacturing with acrylate based vitrimers  
using organic phosphates as transesterification catalyst*

Rossegger, Elisabeth; Höller, Rita; Reisinger, David; Strasser, Jakob; Fleisch, Mathias;  
Griesser, Thomas; Wieser, Viktoria; Schlögl, Sandra

*Polymer*, 2021, 221, 123631

*Abstract*

The present study highlights the high resolution additive manufacturing of covalent adaptable acrylate photopolymers, which undergo catalyzed transesterification reactions at elevated temperature. A methacrylate phosphate is introduced as a new transesterification catalyst, which considerably extends the toolbox of acrylate monomers for 3D printing of vitrimers, as it is easily soluble in a wide range of acrylate monomers and does not affect cure kinetics or storage stability of the resins. By appropriate design of monomer composition and catalyst, a series of acrylate-based vitrimers was prepared, whose glass transition temperature was conveniently adjusted by the chemical structure and functionality of the acrylate monomers. Rheometer studies revealed that the stress relaxation rate slows down with increasing crosslink density and lower amount of –OH moieties. In contrast, increasing the catalyst concentration in the photopolymer network from 5 to 15 wt% significantly accelerated the relaxation rate, with 63% of the initial stress being relaxed within 102 min. Complex 3D objects with feature sizes below 50  $\mu\text{m}$  were manufactured by bottom-up digital light processing (DLP) and the dynamic nature of the covalent crosslinks endowed the printed structures with triple-shape memory and thermo-activated mendability. As shown by tensile tests, up to 99% of the initial strength could be recovered after the first healing step, showing the potential to improve functionality and lifetime of additively manufactured duromer networks. Moreover, the fast response time (60 s) of the shape recovery and the high resolution of the 3D printed structures pave the way towards a customized fabrication and miniaturization of soft robotic applications.

*Introduction*

Additive manufacturing technologies (AMTs) have become a popular field of research in the last years as they allow for the fabrication of complex and individually shaped architectures from different materials including metals,<sup>1</sup> ceramics<sup>2</sup> and polymers.<sup>3</sup> Going beyond materials produced by conventional processes such as injection molding or extrusion, AMT enables the design and the fabrication of complex structures with new

functionalities and/or improved performance.<sup>4,5</sup> One exciting approach towards 3D objects with additional functionality is the additive manufacturing of covalent adaptable networks (CANs), which undergo exchange reactions upon an external stimulus.<sup>6</sup> The dynamic nature of the bonds endows the polymer networks with unique properties such as recyclability, weldability, malleability and the ability for self-healing.<sup>7–9</sup> The majority of the reported studies use filament extrusion techniques to fabricate 3D objects from CANs. In particular, Voit and co-workers exploited thermo-reversible Diels-Alder chemistry to create a thermoset with dynamic furan–maleimide links, which was processable with a syringe extrusion technique.<sup>10</sup> Thermo-reversible Diels-Alder networks belong to the class of dissociative CANs, which undergo a temporary decrease in crosslink density due to thermally triggered bond cleavage reactions.<sup>11</sup> Reformation of the cleaved bonds occurs at lower temperatures due to their entropically favored state. The decrease in both crosslink density and viscosity leads to a loss of mechanical integrity and elicits a softening process, reminiscent of thermoplastic reprocessing.<sup>12</sup> Thus, the printed 3D objects could be conveniently melted and re-printed again at temperatures  $>90$  °C. Recently, Vanderborght and co-workers successfully fabricated furan–maleimide networks with fused filament fabrication (FFF) techniques and printed adaptive grippers for soft robotics, which were able to self-repair cuts and punctures.<sup>13</sup>

Along with dissociative CANs, research is also geared to the additive manufacturing with thermosets comprising dynamic bonds, which are associative in nature. Whilst the former suffers from a loss of network integrity during the exchange reactions, the latter maintains its network integrity due to a simultaneous breakage and reformation of bonds.<sup>14</sup> Leibler et al. transferred the concept of associative bond exchange to classic epoxy/acid or epoxy/anhydride thermosets by adding appropriate transesterification catalysts.<sup>15</sup> The rate of the transesterification reactions is affected by several parameters including type and amount of catalyst, availability of –OH and ester groups or network structure. Typically used transesterification catalysts for vitrimeric networks are Brønsted acids, organo-metallic complexes and organic bases.<sup>16</sup> Above the so-called topology freezing transition temperature ( $T_v$ ), the bond exchange reactions become significantly fast and result in a macroscopic flow of the polymer network. The thermally triggered gradual

decrease in viscosity follows an Arrhenius trend analogous to silica-based glasses. Thus, Leibler and co-workers coined this new class of CANs vitrimers.<sup>15</sup>

Shi et al. employed the concept of vitrimers to additively manufacture recyclable polymer parts.<sup>17</sup> They prepared an epoxy-based thermoset with hydroxyl ester moieties that undergo catalyzed transesterifications. By slightly pre-curing the formulation, they obtained a highly viscous ink, which was 3D printable with a syringe extrusion technique. Recycling was accomplished by dissolving the networks via solvent-assisted transesterification in the presence of ethylene glycol. Repeated printability of the solution could be shown without a significant loss of the mechanical performance of the printed parts.

Advancing from filament extrusion, Zhang et al. reported the 3D printing of vitrimers with digital light processing (DLP) technique.<sup>18</sup> DLP relies on a layer-by-layer polymerization of a photo-curable resin formulation, which is locally solidified in a vat.<sup>3</sup> It benefits from a high resolution and surface quality and comparably fast throughput rates.<sup>19</sup> Their network design relied on a photo-curable acrylate resin formulations, which contained hydroxyl-functional mono- and diacrylates, a Norrish Type I photoinitiator and an organic zinc salt for catalyzing the bond exchange reactions. During the printing process, the 3D objects were fabricated by the radical induced chain growth polymerization of the acrylates. Solid networks with hydroxyl ester moieties were formed, which underwent catalyzed transesterifications upon elevated temperature and rendered the networks self-healable and reprocessable. However, in this approach the network design is limited by the poor solubility of the zinc salt in the acrylic monomers. A high amount of 2-hydroxy-3-phenoxypropyl acrylate is required for adequately dissolving the catalyst, which only allows the preparation of photopolymers with low crosslink density.

Recently, we introduced a mono-functional methacrylic phosphate as new catalyst for thermo-activated transesterification in thiol-click photopolymers.<sup>20</sup> Compared to commonly used catalysts, it is liquid, easily soluble in a wide range of acrylate monomers, covalently incorporated into the network across its methacrylate group and does not compromise on cure kinetics of radically induced photopolymerization reactions. We



successfully 3D printed thiol-acrylate photopolymers with DLP and the functional test structures were able to undergo shape memory and intrinsically heal damages at elevated temperature.

Herein, we expand the concept towards DLP printable acrylate networks and highlight the versatility of this new catalyst, which enables the fabrication of a wide range of vitrimeric acrylate photopolymers. Due to its superior solubility properties, the catalyst can be applied in numerous acrylate monomers and we prepared a series of photopolymer networks with varying network structure, mobility and related mechanical properties. Structure-property relationships with the corresponding stress relaxation were established, giving evidence on the influence of network mobility, number of functional groups and catalyst content on the kinetics of the stress relaxation. The high photoreactivity of the functional resins was exploited to additively manufacture functional 3D objects with a feature size of 50  $\mu\text{m}$  by DLP printing. Due to the dynamic nature of the hydroxyl ester groups, the printed structures could be conveniently mended and underwent triple-shape memory at elevated temperature, demonstrating the improved functionality and the potential to enhance the lifetime of additively manufactured duromer networks.

### *Results and Discussion*

The design of covalent adaptable acrylate photopolymers combines the advantages of photo-triggered curing reactions, which enable a localized solidification of the material, with thermo-activated exchange reactions, to impart the network with advanced functions such as triple-shape memory and self-healability (Figure 1). The thermo-activated exchange reactions are based on catalyzed transesterifications of hydroxyl ester links, which are introduced in the photopolymer network by using acrylate monomers with free  $-\text{OH}$  groups. In particular, the bi-functional glycerol 1,3-diglycerolate diacrylate together with the mono-functional 2-hydroxy-3-phenoxypropyl acrylate (HPPA) were applied (Figure 1c) to provide a high number of  $-\text{OH}$  groups in the networks, which is important to facilitate efficient exchange reactions.<sup>21</sup>

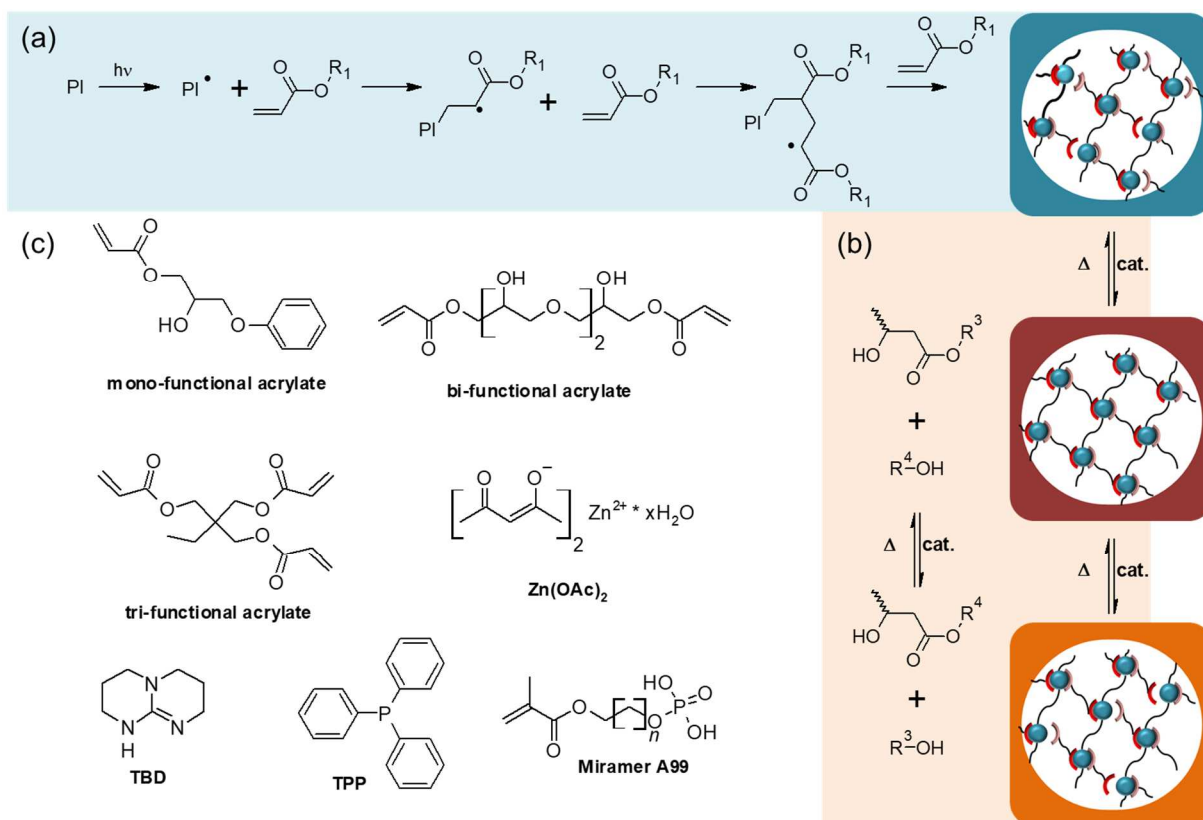


Figure 1. (a) Photo-curing and (b) thermally triggered exchange reactions of acrylate based vitrimers. (c) Monomers and catalysts used in the preparation of acrylate based vitrimers.

We used selected catalysts including triazabicyclodecene (TBD), triphenylphosphine (TPP) and zinc acetyl acetonate, which are well known for enhancing the bond exchange rate of transesterifications, thereby accelerating the stress relaxation of the networks at elevated temperature.<sup>16</sup> In addition, we employed an organic phosphate (Miramer A99) as alternative catalyst, whose catalytic efficiency towards transesterifications had been demonstrated in thiol-acrylate systems.<sup>20</sup> Whilst TBD, TPP and Miramer A99 are soluble in numerous acrylate formulations,  $Zn(acac)_2$  requires a high amount (at least 50 mol%) of the mono-functional acrylate HPPA and elevated temperature to be well dissolved in the formulation.

Thus, for a first screening of the role of the transesterification catalyst on photo-curing kinetics and stress relaxation properties of vitrimeric acrylate networks, an acrylate formulation was chosen, in which all catalysts could be properly dissolved. The resin formulations contained 90 mol% HPPA, 4.5 mol% of the bi-functional acrylate GDGDA acting as crosslinker and phenylbis(2,4,6-trimethylbenzoyl)phosphine oxide as typical

Norrish Type I photoinitiator (Table 1). The conversion of the acrylate groups was determined by FTIR spectroscopy, monitoring the related absorption band at  $1635\text{ cm}^{-1}$  as a function of the irradiation time. The results reveal that TPP and  $\text{Zn}(\text{acac})_2$  do not significantly change the cure kinetics compared to the reference system without catalyst (Figure 2a). In both systems, the final conversion of the acrylate groups amounted to 95% and was reached within 10 s irradiation. In contrast, the addition of Miramer A99 slightly accelerated the cure kinetics and led to higher final monomer conversions (98%). Miramer A99 contains mono-functional methacrylate groups, which are expected to reduce diffusion limitations in the radically induced chain-growth polymerization and thus, speed up the curing reaction. However, the picture completely changes if the acrylate formulation contains TBD as transesterification catalyst. TBD acts as radical scavenger and substantially retards the radically induced chain-growth reaction of the acrylate monomers. The time for reaching maximum monomer conversion shifts from 10 to 2000 s. Bowman et al. also observed a stabilizing effect of TBD in their work on dynamic thiol-ene systems.<sup>22</sup> Due to their sluggish photopolymerization rate, formulations with TBD are not applicable to manufacture 3D objects with an adequate speed in the DLP process.

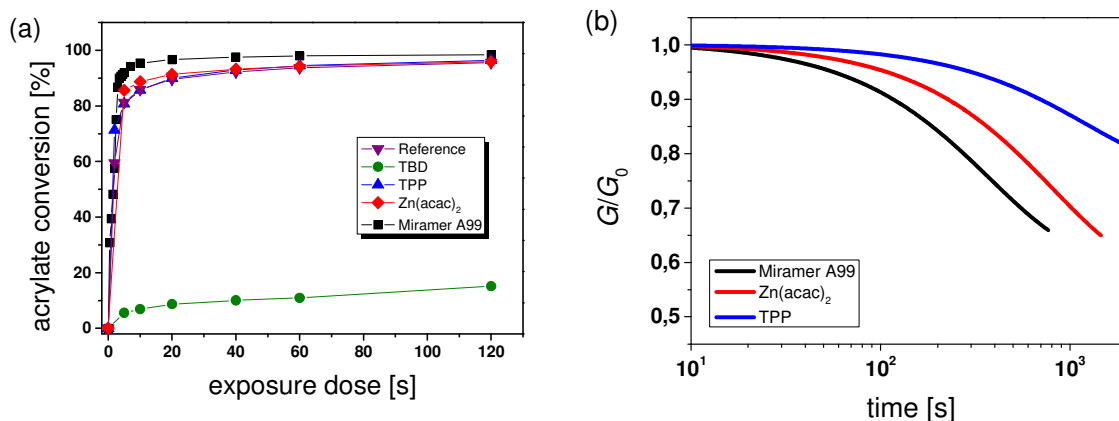


Figure 2. (a) Monitoring the cure kinetics of acrylate based vitrimers by FTIR spectroscopy as a function of the transesterification catalyst at 5 mol%. The normalized peak area of the IR absorption bands of the acrylate groups ( $1635\text{ cm}^{-1}$ ) is plotted against exposure time. Irradiation was carried out with visible light ( $\lambda = 420\text{--}450\text{ nm}$ ,  $3.2\text{ mW/cm}^2$ ) under air. The lines are a guide for the eye. (b) Normalized stress relaxation curves of catalyzed acrylate networks obtained at  $180\text{ }^\circ\text{C}$ .

Due to the limitations of TBD, further work mainly focused on formulations containing Miramer A99, TPP or  $\text{Zn}(\text{acac})_2$ , from which discs with a diameter of 10 mm were 3D

printed with DLP. The discs were used in rheological experiments to determine the stress relaxation of the acrylate networks at 180 °C and in Figure 2b, the evolution of the relaxation modulus at 180 °C as a function of time is shown. The relaxation rate increases in the following order: TPP > Zn(acac)<sub>2</sub> > Miramer A99. TPP catalyzes transesterifications via the lone electron pair of its phosphorous atom and its low reactivity is also so found in other vitrimer network such as epoxy-anhydride systems.<sup>23,24</sup> In contrast, Zn(acac)<sub>2</sub> significantly accelerates bond exchange reactions at elevated temperature, which makes it one of the most widely used catalysts for epoxy-acid and epoxy-anhydride vitrimers.<sup>15,25</sup> Zn(acac)<sub>2</sub> increases the electrophilicity of the ester carbonyl by polarization and brings the reactive species together through directional coordination bonds, shifting the alcohol/alkoxide equilibrium toward the more nucleophile alkoxide.<sup>26</sup>

However, the best performance was obtained with Miramer A99 as catalysts. Mono and diester of the phosphoric acid contain free –OH groups and are strong Brønsted acids,<sup>27</sup> and particularly mineral phosphates are well known transesterification catalysts in bio fuel production.<sup>28,29</sup> The results clearly show Miramer A99 as organic counterpart promotes rapid stress relaxation in acrylate photopolymers without affecting cure kinetics of the resin formulation. Moreover, due to its high solubility in numerous acrylate monomers, it radically expands the material platform for the preparation of 3D printable acrylate vitrimers.

To demonstrate the versatility of this new transesterification catalyst, we prepared a series of higher crosslinked HPPA/GDGDA photopolymer networks by adding a varying amount of trimethylolpropane triacrylate (TMPTA). The addition of the tri-functional acrylate significantly slows down the cure kinetics (Figure 3a) as the increase in acrylate functionality is associated with a decrease in the monomer conversion at which the gel point occurs.<sup>30</sup> Thus, the final monomer conversion decreases from 98% (resin RH-4 containing no TMPTA) to 76% (resin ER-6 with 10 mol% TMPTA). Along with cure kinetics, the addition of TMPTA also slows down the stress relaxation kinetics (Figure 3b), which is mainly explained by the lower number of –OH groups in the networks (part of the –OH functional acrylate monomers HPPA and GDGDA is replaced by TMPTA). In contrast, the network mobility is expected to play a minor role since the glass transition

temperature of the networks only slightly increases from 20 °C (resin RH-4) to 28 °C (resin ER-6).

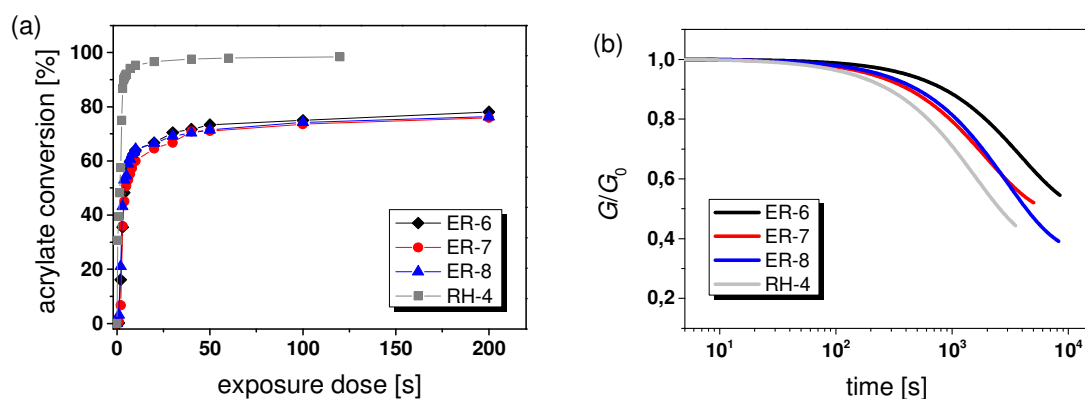


**Figure 3.** (a) Monitoring the cure kinetics of acrylate based vitrimers by FTIR spectroscopy as a function of the Miramer A99 content (5 – 15 wt%) in acrylate resins with 5 mol% TMPTA: resin ER-6, ER-7 and ER-8. The values are compared to resin RH-4, which contained 5 wt% Miramer A99 but no TMPTA. The normalized peak area of the IR absorption bands of the acrylate groups ( $1635\text{ cm}^{-1}$ ) is plotted against exposure time. Irradiation was carried out with visible light ( $\lambda = 420\text{-}450\text{ nm}$ ,  $3.2\text{ mW/cm}^2$ ) under air. The lines are a guide for the eye. (b) Corresponding normalized stress relaxation curves of the cured acrylate networks obtained at 180 °C.

However, the lower reactivity could be overcome by increasing the amount of Miramer A99 from 5 to 15 wt%. It is well known that the amount of catalyst influences the stress relaxation kinetics of vitrimers, leading to faster relaxations rates at higher concentration.<sup>23</sup> Whilst the cure kinetics is not affected by the higher Miramer A99 content, it significantly accelerated the stress relaxation. In particular in resin ER-8 containing 15 wt% Miramer A99, 63% ( $1/e$ ) of the initial stress is being relaxed within 102 min, whilst at 5 wt% the network requires 634 min to reach the same level of relaxation.

In further experiments, higher crosslinked networks were prepared by step-wise increasing the TMPTA content from 10 to 45 mol%, whilst keeping the HPPA and Miramer A99 concentration constant at 10 mol% and 15 wt%, respectively. As expected the higher content of the tri-functional acrylate leads to a reduction in final monomer conversion and cure rate (Figure 4a), whilst the higher crosslink density leads to an increase in the  $T_g$ . As TMPTA does not bear  $\text{-OH}$  groups in its structure, the number of hydroxyl moieties required for the catalyzed transesterification reaction decreases. The reduction in the number of available  $\text{-OH}$  groups is directly affecting the stress relaxation properties as

shown in Figure 4a. Fast stress relaxation is observed in resin ER-11 (molar ratio of OH:COOR groups = 1:1) with 63% of the stress being relaxed within 30 min.

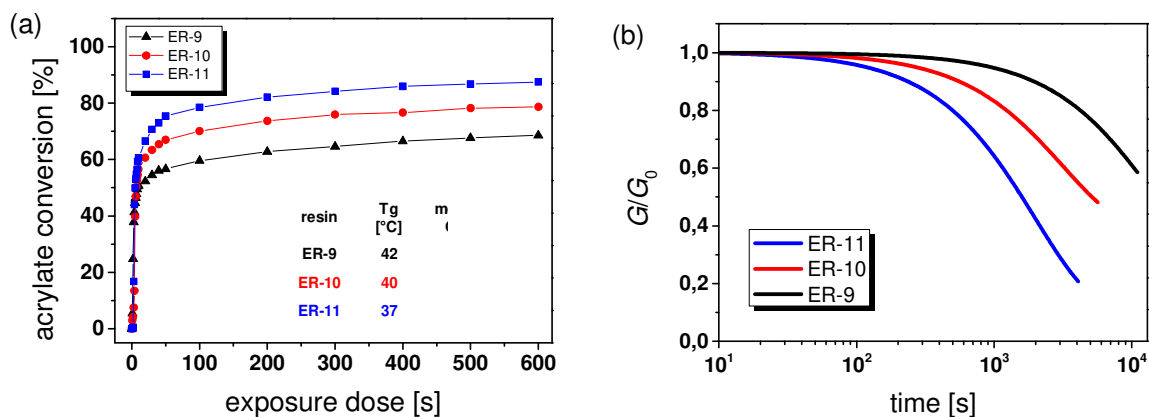
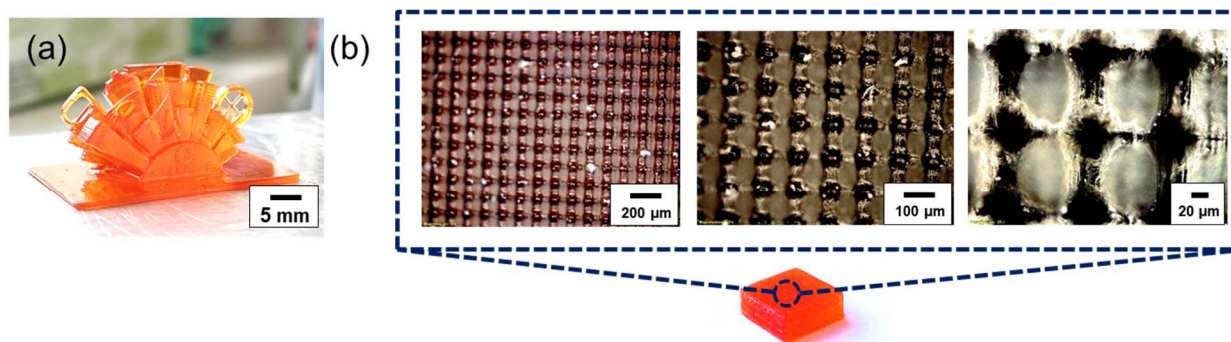


Figure 4. (a) Monitoring the cure kinetics of acrylate based vitrimers by FTIR spectroscopy as a function of the TMPTA content, whilst keeping the Miramer A99 concentration constant at 15 wt%. The normalized peak area of the IR absorption bands of the acrylate groups ( $1635\text{ cm}^{-1}$ ) is plotted against exposure time. Irradiation was carried out with visible light ( $\lambda = 420\text{-}450\text{ nm}$ ,  $3.2\text{ mW/cm}^2$ ) under air. The lines are a guide for the eye. (b) Corresponding normalized stress relaxation curves of the resins versus TMPTA content obtained at  $180\text{ °C}$ .

In contrast, changing the molar ratio from 1:1 to 2:3 (resin ER-9) results in a distinctive increase in the time (130 min) to relax  $1/e$  of the initial stress at  $180\text{ °C}$ . The results confirm that along with type and amount of catalyst, the number of free  $\text{-OH}$  groups is crucial for ensuring efficient stress relaxation in acrylate based vitrimers.

Due to its superior performance in cure kinetics and stress relaxation, resin ER-11 was applied for further printing studies. The low viscosity of resin ER-11 ( $830\text{ - }860\text{ mPa}\cdot\text{s}$  obtained at shear rates between  $0.1$  and  $300\text{ s}^{-1}$ ) together with the fast photopolymerization enabled the DLP printing of 3D objects with high precision (Figure 5a) and a test structure with substructures below  $50\text{ }\mu\text{m}$  was replicated successfully (Figure 5b).



**Figure 5.** (a) Photograph of a DLP printed test structure and (b) optical micrographs of DLP printed substructures on the surface of a test structure ( $l = 10$  mm,  $w = 10$  mm,  $h = 5$  mm).

Whilst the photo-induced formation of covalent bonds can be exploited for the additive manufacturing of complex and customized structures, the thermo-activated bonds endow vitrimeric acrylates with triple shape memory (Figure 6a). It has to be noted that the acrylate based vitrimer network has two transition temperatures, which can be used to program temporary shapes. The classic  $T_g$  and the topology freezing transition temperature ( $T_v$ ), at which the exchange reactions become macroscopically relevant and the network changes from an elastic solid to a viscoelastic liquid.<sup>15</sup> For the shape memory studies, the original/permanent shape was DLP 3D printed and heated at 180 °C, which is expected to be well above the  $T_v$  since distinctive stress relaxation was observed in the rheometer experiments. By applying an external force the 3D printed test specimen was deformed and the first temporary shape was fixed by cooling the sample to 60 °C, which is above the  $T_g$  of cured ER-11 (37 °C). At 60 °C, the second temporary shape was programmed, which was fixed by cooling the network to 23 °C. The two shapes could be sequentially recovered by heating the sample from 23 to 180 °C and particularly, the second temporary shape was characterized by a fast response time (60 s). Moreover, the exceptional solubility properties of Miramer A99 as new transesterification catalysts enable the employment of a wide range of acrylate monomers for the preparation of vitrimer networks. Thus, the  $T_g$  of the cured resins and the related switching temperature of the shape recovery can be adjusted over a broad range by appropriate network design.

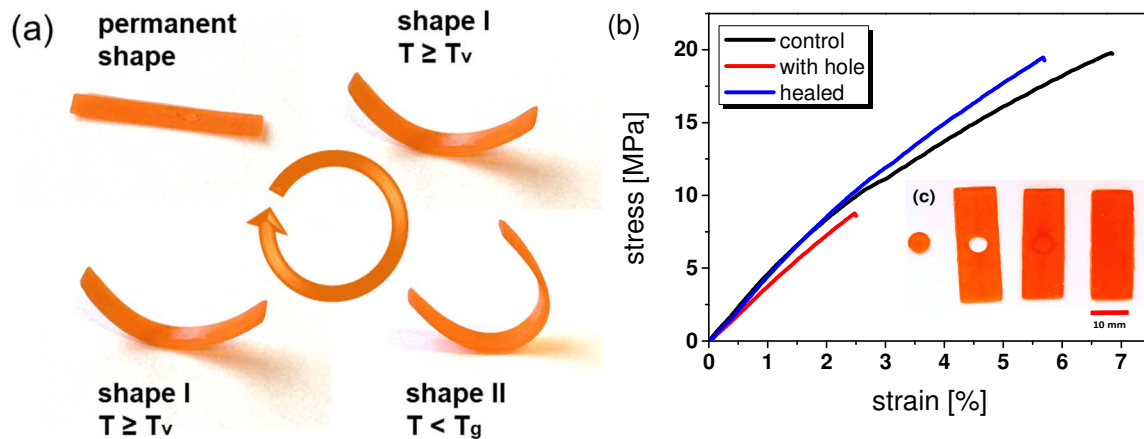


Figure 6. (a) Photographs showing the triple-shape memory of DLP printed samples of resin-ER-11 employing the  $T_v$  to fix the first temporary shape at 180 °C, and the  $T_g$  to fix the second temporary shape at 60 °C and sequential recovery of the shapes upon heating from 23 to 180 °C. (b) Stress-strain curves of resin ER-11 prior to and after a thermal mending at 180 °C for 4 h. (c) Inset shows photographs of 3D printed test specimens prior to and after healing at 180 °C for 4 h.

Along with the ability for reshaping, the thermo-activated macroscopic reflow of the network enables a thermally triggered healing of 3D printed structures. The healing efficiency was characterized via uniaxial tensile tests of 3D printed test specimen taking the ratio of the tensile strength prior to and after healing. The related stress-strain curves are shown in Figure 6b. It should be noted that a proper aligning of the thin broken test bars was challenging. Thus, samples with a circular-shaped hole in the centre and its circular-shaped counterpart were 3D printed. For the repair the counterpart was fitted in the hole, followed by a thermal healing at 180 °C for 4 h, in which the boundaries between the two parts were efficiently welded together. As obtained from tensile tests, the original tensile strength (defect-free bar) could be nearly fully recovered (99%), whilst the strain slightly decreased from 6.8 to 5.7%.



## *Experimental*

### *Materials*

Mirammer A99 serving as transesterification catalyst was purchased from Miwon Specialty Chemical (Korea). Trimethylolpropane triacrylate was supplied by TCI (Belgium). All other transesterification catalysts, acrylate monomers and chemicals were obtained from Sigma-Aldrich (USA) and were used without further purification.

### *Preparation of Resin Formulations*

For the preparation of vitrimeric photopolymers with  $\text{Zn}(\text{acac})_2$  as catalyst,  $\text{Zn}(\text{acac})_2$  was dissolved in 2-hydroxy-3-phenoxypropyl acrylate (HPPA) at 70 °C. After cooling the resin down to room temperature, the bi-functional acrylate glycerol 1,3-diglycerolate diacrylate (GDGDA), the photoinitiator phenylbis(2,4,6-trimethylbenzoyl)phosphine oxide (BAPO) and Sudan II were added and the formulation was stirred at room temperature until the components were dissolved. Sudan II was used as a photoabsorber to increase the resolution during the printing process.

For the vitrimeric acrylate formulation containing triphenylphosphine (TPP) as catalyst, TPP, Sudan II and BAPO were dissolved in acetone (1  $\mu\text{L}$  per 1 mg solid). The acetone solution was added to the premixed acrylates HPPA and GDGDA, and the formulation was stirred at room temperature until a homogenous mixture was obtained.

For 1,5,7-triazabicyclo(4.4.0)dec-5-ene (TBD) containing formulations, TBD, BAPO and Sudan II were dissolved in dichloromethane (1  $\mu\text{L}$  per 1 mg solid) and added to the premixed acrylates HPPA and GDGDA. The formulation was stirred at room temperature until a homogenous mixture was achieved.

Resin formulations with Miramer A99 as catalyst were prepared by dissolving BAPO and Sudan II in a mixture of the catalyst and the acrylates HPPA, GDGDA and trimethylolpropane triacrylate (TMPTA) at room temperature. The composition of the acrylic resin formulations is summarized in Table 1.

Table 1. Summarized composition of the vitrimeric acrylate formulations

resin	HPPA mol%	GDGDA mol%	TMPTA mol%	Zn(acac) <sub>2</sub> mol%	TPP mol%	TBD mol%	Mirammer A 99 wt%	BAPO wt%	Sudan II wt%
Reference	90.5	4.5	-	-	-	-	-	2	0.05
RH-1	90.5	4.5	-	5	-	-	-	2	0.05
RH-2	90.5	4.5	-	-	5	-	-	2	0.05
RH-3	90.5	4.5	-	-	-	5	-	2	0.05
RH-4	95.5	4.5	-	-	-	-	5	2	0.05
RH-5	95.5	4.5	-	-	-	-	-	2	0.05
ER-6	45	45	10	-	-	-	5	2	0.05
ER-7	45	45	10	-	-	-	10	2	0.05
ER-8	45	45	10	-	-	-	15	2	0.05
ER-9	10	45	45	-	-	-	15	2	0.05
ER-10	10	60	30	-	-	-	15	2	0.05
ER-11	10	67.5	22.5	-	-	-	15	2	0.05

### Characterization Methods

Photo-induced curing of the resins was followed by FTIR spectroscopy using a Vertex 70 spectrometer (Bruker, USA). 16 scans were accumulated in transmission mode from 3700 to 700  $\text{cm}^{-1}$  with a resolution of 4  $\text{cm}^{-1}$  and the absorption peak areas were calculated with OPUS software. 1.3  $\mu\text{L}$  of resin were drop-cast between two  $\text{CaF}_2$  discs and photo-cured with a light emitting diode lamp (zgood® wireless LED curing lamp) with a power density of 3.2  $\text{mW cm}^{-2}$  ( $\lambda = 420 - 450 \text{ nm}$ ).

The viscosity of the resin formulations was determined by using a modular compact rheometer MCR 102 from Anton Paar (Austria) with a CP60-0.5/TI cone (49.97 mm diameter and 1.982° opening angle). Each measurement was performed with 1 mL resin at room temperature and a shear rate ranging from 0.1 to 300  $\text{s}^{-1}$ .

Differential scanning calorimetry (DSC) measurements were carried out on a Perkin Elmer DSC 8000 under nitrogen atmosphere. A temperature program ranging from -20 to 100 °C with a heating rate of 20 °C/min was applied. The glass transition temperature ( $T_g$ ) was calculated from the second heating cycle with pyris software.

Optical microscopy was performed on an Olympus BX 51 (Japan) and images were taken using a Colour View IIIu digital camera (Soft Imaging System, Germany).

Stress relaxation experiments at 180 °C were operated on a moving die rheometer from Anton Paar (Austria). The samples were conditioned to the selected measurement temperature for 20 min. Subsequently, a 1% step strain was used and the decreasing stress was recorded over time.

### *3D Printing Experiments*

DLP 3D printing was performed on an Anycubic Photon Z printer (China) with a LED 405 nm light source. Two bottom layers were exposed for 100 s, whereas the other layers were illuminated for 10 s. The layer height was set to 50  $\mu\text{m}$  with a building speed of 1  $\text{mm s}^{-1}$  and a retracting speed of 1  $\text{mm s}^{-1}$ .

### *Self-healing and Re-Shaping Experiments*

For the self-healing experiments, the reference sample (30 x 10 x 1.5 mm), the sample with a hole and the corresponding disc ( $d = 5$  mm) were produced by DLP 3D printing. To demonstrate the self-healing capability, the printed disc was fitted inside the hole and all samples were heated to 180 °C for 4 h. Tensile tests were conducted on a ZwickRoell (Germany) Z1.0 static materials testing machine with a crosshead speed of 250  $\text{mm min}^{-1}$ .

Shape memory experiments were carried out with DLP 3D printed stripes (50 x 5 x 0.7 mm), which were heated to 180 °C for 4 h. The first shape was fixed by heating the sample to 180 °C for one hour. For the second shape, the sample was cooled down to 60 °C, re-shaped and cooled down to room temperature. By heating to 60 °C, the first shape could be regained within one minute. To restore the permanent shape, the sample was heated to 180 °C for 2 h.

### *Conclusions*

DLP 3D printable acrylate photopolymers were developed undergoing thermally triggered exchange reactions at elevated temperature. Miramer A99 was introduced as new transesterification catalyst, which is superior to traditionally applied organic zinc salts or amine bases when it comes to radically cured photopolymer networks. On the one hand, it does not compromise on the cure kinetics enabling a fast printing process. On the other hand, the catalyst enables an efficient stress relaxation of the networks at elevated temperature, which is crucial for the thermo-activated mending and reshaping of 3D printed parts. The low viscosity together with the fast cure rates made the acrylate formulations ideal candidates for the bottom-up DLP process and 3D objects with feature sizes below 50  $\mu\text{m}$  could be conveniently prepared. In addition, the new catalyst is soluble in a wide range of acrylate monomers and thus, radically expands the toolbox of monomers for DLP printing of vitrimer networks. A series of higher crosslinked networks were prepared by adding TMPTA in various amounts (from 10 to 45 mol%) and we were able to adjust the  $T_g$  between 20 and 42  $^{\circ}\text{C}$ . However, TMPTA compromises on the cure kinetics due to diffusion limitations and slows down the relaxation kinetics as it does not contain free  $-\text{OH}$  groups in its structure. The lower activity could be overcome by increasing the catalyst concentration from 5 to 15 wt%, evidencing the important role of catalyst and availability of free  $-\text{OH}$  groups in the transesterification kinetics of vitrimers. Employing 15 wt% Miramer A99 as transesterification catalyst, the exchange reactions are sufficiently high enabling to impart triple-shape memory and to thermally heal defects in DLP 3D printed structures. The unique features of the vitrimeric networks including a fast response time (60 s) of the shape recovery and the ability to be processed with high resolution additive manufacturing techniques make them promising candidates for the customized fabrication and miniaturization of soft robotic applications.

### *Funding Sources*

The research work was performed within the COMET-Module project “Chemitecture” (project-no.: 21647048) at the Polymer Competence Center Leoben GmbH (PCCL, Austria) within the framework of the COMET-program of the Federal Ministry for Transport, Innovation and Technology and the Federal Ministry for Digital and Economic Affairs

with contributions by Montanuniversitaet Leoben (Institute of Chemistry of Polymeric Materials). The PCCL is funded by the Austrian Government and the State Governments of Styria, Lower Austria and Upper Austria.

### *Abbreviations*

3D, three dimensional; -OH, -hydroxyl; -COOR, -ester; DLP, digital light processing; AMTs, additive manufacturing technologies; CANs, covalent adaptable networks; FFF, fused filament fabrication;  $T_v$ , topology freezing transition temperature;  $T_g$ , glass transition temperature; DSC, differential scanning calorimetry; LED, light emitting diode; FTIR, Fourier-transform infrared spectroscopy; TPP, triphenylphosphine; TBD, 1,5,7-triazabicyclo(4.4.0)dec-5-ene; TMPTA, trimethylolpropane triacrylate; BAPO, phenylbis(2,4,6-trimethylbenzoyl)phosphine oxide; GDGDA, glycerol 1,3-diglycerolate diacrylate; HPPA, 2-hydroxy-3-phenoxypropyl acrylate.

### *References*

- (1) Frazier, W. E. Metal Additive Manufacturing: A Review. *J. of Materi Eng and Perform* 2014, 23, 1917–1928.
- (2) Zanchetta, E.; Cattaldo, M.; Franchin, G.; Schwentenwein, M.; Homa, J.; Brusatin, G.; Colombo, P. Stereolithography of SiOC Ceramic Microcomponents. *Advanced materials* 2016, 28, 370–376.
- (3) Ligon, S. C.; Liska, R.; Stampfl, J.; Gurr, M.; Mülhaupt, R. Polymers for 3D Printing and Customized Additive Manufacturing. *Chemical reviews* 2017, 117, 10212–10290.
- (4) Gladman, A. S.; Matsumoto, E. A.; Nuzzo, R. G.; Mahadevan, L.; Lewis, J. A. Biomimetic 4D printing. *Nature materials* 2016, 15, 413–418.
- (5) Khoo, Z. X.; Teoh, J. E. M.; Liu, Y.; Chua, C. K.; Yang, S.; An, J.; Leong, K. F.; Yeong, W. Y. 3D printing of smart materials: A review on recent progresses in 4D printing. *Virtual and Physical Prototyping* 2015, 10, 103–122.

- (6) Kuang, X.; Roach, D. J.; Wu, J.; Hamel, C. M.; Ding, Z.; Wang, T.; Dunn, M. L.; Qi, H. J. *Advances in 4D Printing: Materials and Applications*. *Adv. Funct. Mater.* 2019, 29, 1805290.
- (7) Kaiser, S.; Jandl, J.; Novak, P.; Schlögl, S. Design and characterisation of vitrimer-like elastomeric composites from HXNBR rubber. *Soft Matter* 2020, 16, 8577–8590.
- (8) Giebler, M.; Sperling, C.; Kaiser, S.; Duretek, I.; Schlögl, S. Epoxy-Anhydride Vitrimers from Aminoglycidyl Resins with High Glass Transition Temperature and Efficient Stress Relaxation. *Polymers* 2020, 12, DOI: 10.3390/polym12051148.
- (9) van Zee, N. J.; Nicolaÿ, R. Vitrimers: Permanently crosslinked polymers with dynamic network topology. *Progress in Polymer Science* 2020, 104, 101233.
- (10) Yang, K.; Grant, J. C.; Lamey, P.; Joshi-Imre, A.; Lund, B. R.; Smaldone, R. A.; Voit, W. Diels-Alder Reversible Thermoset 3D Printing: Isotropic Thermoset Polymers via Fused Filament Fabrication. *Adv. Funct. Mater.* 2017, 27, 1700318.
- (11) Tasdelen, M. A. Diels–Alder “click” reactions: Recent applications in polymer and material science. *Polym. Chem.* 2011, 2, 2133.
- (12) Denissen, W.; Winne, J. M.; Du Prez, F. E. Vitrimers: Permanent organic networks with glass-like fluidity. *Chemical science* 2016, 7, 30–38.
- (13) Roels, E.; Terry, S.; Brancart, J.; Verhelle, R.; van Assche, G.; Vanderborght, B. Additive Manufacturing for Self-Healing Soft Robots. *Soft robotics* 2020, DOI: 10.1089/soro.2019.0081.
- (14) Kloxin, C. J.; Bowman, C. N. Covalent adaptable networks: Smart, reconfigurable and responsive network systems. *Chemical Society reviews* 2013, 42, 7161–7173.
- (15) Montarnal, D.; Capelot, M.; Tournilhac, F.; Leibler, L. Silica-like malleable materials from permanent organic networks. *Science (New York, N.Y.)* 2011, 334, 965–968.
- (16) Alabiso, W.; Schlögl, S. The Impact of Vitrimers on the Industry of the Future: Chemistry, Properties and Sustainable Forward-Looking Applications. *Polymers* 2020, 12, 1660.

- (17) Shi, Q.; Yu, K.; Kuang, X.; Mu, X.; Dunn, C. K.; Dunn, M. L.; Wang, T.; Jerry Qi, H. Recyclable 3D printing of vitrimer epoxy. *Mater. Horiz.* 2017, 4, 598–607.
- (18) Zhang, B.; Kowsari, K.; Serjouei, A.; Dunn, M. L.; Ge, Q. Reprocessable thermosets for sustainable three-dimensional printing. *Nature communications* 2018, 9, 1831.
- (19) Gross, B. C.; Erkal, J. L.; Lockwood, S. Y.; Chen, C.; Spence, D. M. Evaluation of 3D printing and its potential impact on biotechnology and the chemical sciences. *Analytical chemistry* 2014, 86, 3240–3253.
- (20) Rossegger, E.; Höller, R.; Reisinger, D.; Strasser, J.; Fleisch, M.; Griesser, T.; Schlögl, S. Unlocking a New Material Platform for 3D Printing of Soft Active Materials with Additional Functions. *Polym. Chem.*, 2020, under review.
- (21) Hayashi, M.; Yano, R. Fair Investigation of Cross-Link Density Effects on the Bond-Exchange Properties for Trans-Esterification-Based Vitrimers with Identical Concentrations of Reactive Groups. *Macromolecules* 2019, 53, 182–189.
- (22) Lyon, G. B.; Cox, L. M.; Goodrich, J. T.; Baranek, A. D.; Ding, Y.; Bowman, C. N. Remoldable Thiol–Ene Vitrimers for Photopatterning and Nanoimprint Lithography. *Macromolecules* 2016, 49, 8905–8913.
- (23) Capelot, M.; Unterlass, M. M.; Tournilhac, F.; Leibler, L. Catalytic Control of the Vitrimer Glass Transition. *ACS Macro Lett.* 2012, 1, 789–792.
- (24) Yadav, J. S.; Reddy, B.V.S.; Krishna, A. D.; Reddy, C. S.; Narsaiah, A. V. Triphenylphosphine: An efficient catalyst for transesterification of  $\beta$ -ketoesters. *Journal of Molecular Catalysis A: Chemical* 2007, 261, 93–97.
- (25) Kaiser, S.; Wurzer, S.; Pilz, G.; Kern, W.; Schlögl, S. Stress relaxation and thermally adaptable properties in vitrimer-like elastomers from HXNBR rubber with covalent bonds. *Soft Matter* 2019, 15, 6062–6072.
- (26) Demongeot, A.; Mougner, S. J.; Okada, S.; Soulié-Ziakovic, C.; Tournilhac, F. Coordination and catalysis of Zn<sup>2+</sup> in epoxy-based vitrimers. *Polym. Chem.* 2016, 7, 4486–4493.

## PUBLICATION IV

- (27) Streitwieser, A.; Heathcock, C. H.; Kosower, E. M. *Introduction to organic chemistry*, 4. ed., rev. print, 1998.
- (28) Bazi, F.; El Badaoui, H.; Sokori, S.; Tamani, S.; Hamza, M.; Boulaajaj, S.; Sebti, S. *Transesterification of Methylbenzoate with Alcohols Catalyzed by Natural Phosphate*. *Synthetic Communications* 2006, 36, 1585–1592.
- (29) Thinnakorn, K.; Tscheikuna, J. *Biodiesel production via transesterification of palm olein using sodium phosphate as a heterogeneous catalyst*. *Applied Catalysis A: General* 2014, 476, 26–33.
- (30) Andrzejewska, E. *Photopolymerization kinetics of multifunctional monomers*. *Progress in Polymer Science* 2001, 26, 605–665.



**PUBLICATION V:**

*Locally controlling dynamic exchange reactions in 3D printed thiol-acrylate vitrimers using dual-wavelength digital light processing*

Rossegger, Elisabeth; Moazzen, Khadijeh; Fleisch, Mathias; Schlögl, Sandra

*Nature communications*, 2021 under revision

### *Abstracts*

Vitrimers are covalent adaptable polymer networks, which are able to rearrange their topology in response to an external stimulus. Below the topological freezing temperature ( $T_v$ ) they behave like a classic thermoset, whilst above  $T_v$ , they become malleable, weldable and recyclable. However, vitrimers mainly rely on thermo-activated dynamic exchange reactions, which suffer from a lack in spatial control. Herein, we introduce triphenylsulfonium phosphate as a latent transesterification catalyst, which releases strong Brønsted acids upon UV exposure (365 nm). Once locally formed, the acids are able to efficiently catalyse thermo-activated transesterifications as confirmed by stress relaxation studies. The latent catalyst is introduced into visible light (405 nm) curable thiol-acrylate resins, whose fast curing kinetics enable the additive manufacturing of precise 3D objects. Due to the orthogonality between the curing reaction and the photo-activation of the catalyst, transesterifications can be selectively switched on in the photo-cured vitrimer simply by UV-light exposure. By using a dual-wavelength digital light processing 3D printer, operating at 405 and 365 nm, the catalyst is locally activated during the layer-by-layer build-up of the 3D structures. This enables the fabrication of soft active devices, which undergo locally controlled topology arrangements above the networks'  $T_v$ .

### *Introduction*

Covalent adaptable networks (CANs) contain dynamic bonds which break and reform either autonomously or upon an external stimulus. The bond exchange is based on interactions between repeating units, following either an associative (bond forming/breaking mechanism) or a dissociative (bond breaking/forming mechanism) pathway.<sup>1</sup> In associative bond exchange mechanisms, intermediate reactants are formed, which increase the crosslink density temporarily. However, as soon as the new crosslink is formed, the former bond is cleaved, which leads to a nearly constant crosslink density.<sup>2</sup>

In thermo-activated systems, the topological freezing transition temperature ( $T_v$ ) is crucial as it governs the kinetics of the exchange reactions and thus, influences the flow behavior of the associative CANs. Above  $T_v$ , the exchange reactions become macroscopically

relevant and a material flow is observed following an Arrhenius trend, comparable to silica-based glasses. Thus, the dynamic networks behave like re-shapeable, malleable and re-processable fluids.<sup>3</sup> Below  $T_v$ , the exchange reactions are slow and the network properties are comparable to a permanently crosslinked thermoset.<sup>1,2,4,5</sup> It should be noted that the  $T_v$  is influenced by numerous parameters involving crosslink density, exchange reaction kinetics (based on catalyst loading, favored chemical affinity between reactants and thermodynamic factors), monomer mobility or stiffness of the network.<sup>4</sup>

Leibler and co-workers coined associative CANs, whose viscosity follows the Arrhenius law above the  $T_v$ , vitrimers.<sup>6</sup> They prepared epoxy-acid and epoxy-anhydride networks, which were able to undergo thermo-activated transesterifications.<sup>7</sup> Based on the kinetics of the bond exchange reactions, the networks could be reprocessed, welded, reshaped and healed at temperatures well above the  $T_v$ .<sup>8</sup> Due to the high number of commercially available monomers and easy implementation in numerous application fields, vitrimers based on transesterification chemistry are still one of the most prominent classes of associative CANs reported in literature.<sup>5,9</sup> However, these dynamic networks require an appropriate transesterification catalyst, which accelerates the bond exchange reactions. Commonly used catalysts for transesterifications are Brønsted acids, organo-metallic complexes and organic bases.<sup>10</sup>

Current research is geared towards the processing of vitrimers with additive manufacturing techniques to obtain personalized 3D structures with improved functionality. In particular, Shi et al. developed thermosetting epoxy inks for direct ink writing at elevated temperatures. By dissolving the printed objects in ethylene glycol at elevated temperatures, the ink was recycled and used for further printing processes.<sup>11</sup>

Bowman et al. reported a recyclable thiol-ene photopolymer for photolithographic applications, which was able to undergo thiol-thioester exchange reactions.<sup>12</sup> Zhang and co-workers developed a photo-curable resin formulation with hydroxyl-functional mono- and diacrylates, a Norrish Type I photoinitiator and  $Zn(OAc)_2$  for catalyzing the transesterification reactions, which endowed the network with thermal mendability and reprocessability.<sup>13</sup> Inspired by this work, we recently expanded this concept towards 3D

printable thiol-acrylate vitrimers by introducing organic phosphates as alternative transesterification catalysts.<sup>14</sup>

Whilst these concepts enable a localized solidification of the material by photo-induced curing processes, the subsequent thermo-activation of the exchange reactions lacks from a spatial control. In previous work, a local control of the exchange reactions was realized by introducing nano-sized fillers with photothermal properties into epoxy-acid and epoxy-anhydride vitrimers.<sup>15</sup> The fillers efficiently convert light to heat and by employing NIR lasers as light source, localized healing, welding and shape memory was demonstrated.<sup>16</sup>

Herein, we follow a completely new approach to manufacture 3D objects that undergo spatially controlled topological rearrangements. By exploiting two orthogonal photoreactions, a thiol-acrylate system is cured by long-wavelength irradiation (405 nm), whilst in a subsequent step, the transesterification catalyst is activated upon short-wavelength irradiation (365 nm). With dual-wavelength digital light processing (DLP) 3D printing, operating at 405 and 365 nm, the catalyst is activated locally during the layer-by-layer build-up of the 3D structures (Figure 1b).

### *Results and Discussion*

For the network design, a photocurable thiol-acrylate formulation (resin-ER-1) is applied, whose vitrimeric properties and 3D processability have been demonstrated in a recent work.<sup>14</sup> The resin contains mono- and bi-functional acrylate monomers bearing functional –OH groups, which promote exchange reactions in the cured photopolymer network.<sup>17</sup> In addition, 25 mol% of a tri-functional thiol crosslinker and 2 wt% phenylbis(2,4,6-trimethylbenzoyl)phosphine oxide as long-wavelength absorbing photoinitiator are added to the formulation. However, the transesterification catalyst is replaced with an onium salt acting as latent transesterification catalyst (resin-ER-1-lat).

Onium salts have been introduced by Crivello in the late 1970s and are widely used to initiate cationic polymerization and curing of epoxides.<sup>18</sup> Upon UV exposure, onium salts undergo a cleavage reaction and, by subsequent reaction with solvents or monomers of the formulation, form strong Brønsted acids.<sup>19</sup> The acidic strength of the released acid

depends on the nucleophilicity of the counter-anion, with stronger acids being generated with lower nucleophilic counter-anions.<sup>19,20</sup> They are easily soluble in numerous monomers and provide a temperature stability up to 180 °C.<sup>21</sup> To ensure the orthogonality between the curing reaction and the activation of the catalyst, triphenylsulfonium phosphate was used as latent catalyst, which is transparent at 405 nm. In contrast to diaryliodonium salts, triphenylsulfonium salts have a low reduction potential and do not promote radical induced cationic polymerizations.<sup>22</sup> Consequently, the photolytically formed radicals from the curing reaction cannot be oxidized by triphenylsulfonium phosphate.

As shown in FT-IR experiments, following the time-dependent depletion of the characteristic absorption bands of acrylate and thiol groups at 1635 and 2570  $\text{cm}^{-1}$ , the cure kinetics is not affected by the addition of 10 wt% triphenylsulfonium phosphate (Figure S1 and S2, ESI). Maximum conversion of thiol and acrylate groups is obtained upon 60 s of light exposure at 405 nm.

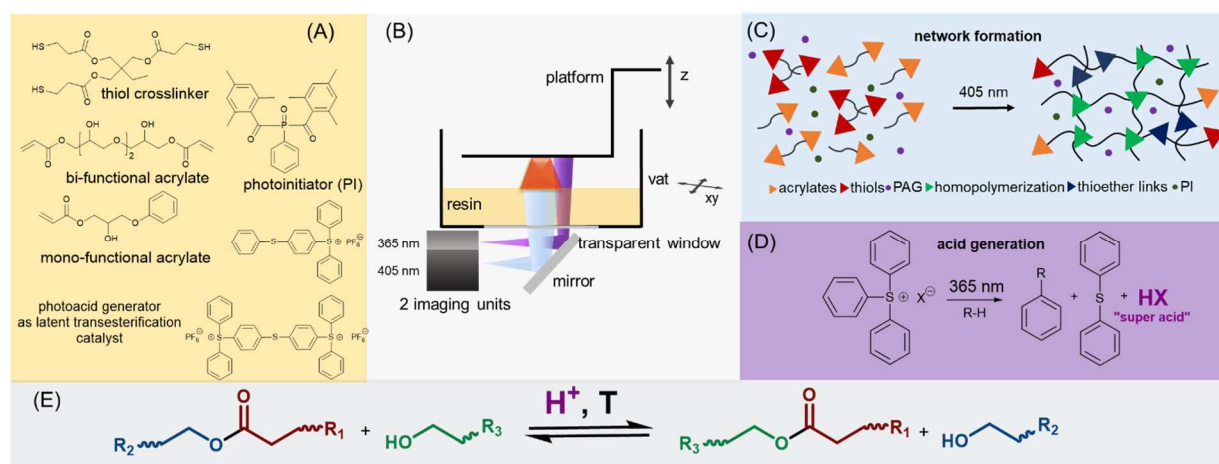


**Figure 1** – (a) Monomers and latent transesterification catalyst used for the preparation of the 3D printable thiol-acrylate vitrimer. (b) Schematic representation of the dual-wavelength DLP process. (c) Visible light curing of thiol-acrylate monomers and UV triggered activation of Brønsted acids acting as transesterification catalyst. (e) Transesterification process after photoacid generation at elevated temperatures.

Due to its fast cure speed and shelf life of at least 72 h, resin-ER-1-lat can be applied in 3D printing techniques relying on vat polymerization. In particular, digital light processing (DLP) was chosen, in which the 3D object is built-up via a layer-by-layer solidification of the photo-reactive resin formulation.

For rheological experiments, discs with a diameter of 10 mm were printed with a wavelength of 405 nm and the stress relaxation of the network (between 140 and 180 °C) was determined prior to and after UV exposure at 365 nm (Figure 2a). Under the applied conditions, the network is stable as confirmed by thermogravimetric analysis (Figure S3, ESI). In addition, the applied temperatures in the stress relaxation studies were well above the glass transition of the network, which amounted to 10.8 °C (DSC curve is shown in Figure S4, ESI).

After curing, resin-ER-1-lat exhibited a slight stress relaxation, which is comparable to a resin formulation containing no triphenylsulfonium phosphate (resin-ER-1-ref). Thus, the results suggest that the slight decrease in stress relaxation is not related to a premature release of acids (either photochemically induced or by thermal decomposition of the triphenylsulfonium salt) but can be attributed to a thermal release of volumetric shrinkage stresses arising during network evolution.<sup>23</sup>

Upon subsequent UV exposure, a rapid stress relaxation was observed for resin-ER-1-lat, with 63% of the initial stress being relaxed within 53.5 min. The results clearly show that the photochemically released Brønsted acids are able to efficiently catalyze thermo-activated transesterifications. It is well known that Brønsted acids are able to catalyze esterifications as well as transesterifications.<sup>24</sup> The reaction mechanism involves the protonation of the oxygen of the carbonyl ester group, which increases the electrophilicity of the adjoining carbon atom.<sup>25</sup> The protonated carbonyl group is more reactive towards a nucleophilic attack and it readily forms a tetrahedral intermediate with an available –OH group in the network. This is followed by a proton transfer and the departure of the leaving group. A new ester bond is formed whilst the acidic catalyst (H<sup>+</sup>) is regenerated.

The acid-catalysed transesterification is temperature-dependent, which is also in agreement with the stress-relaxation experiments. By increasing the temperature from 140 to 180 °C, a faster decrease of the stress relaxation is observed giving rise to a higher bond exchange rate at increasing temperature.

Besides temperature, the exchange rate is also increasing with higher catalyst concentration.<sup>26</sup> In terms of triphenylsulfonium phosphate acting as photolabile catalyst,

the number of released Brønsted acids can be increased either by extending the exposure time or by increasing the salt concentration in the formulation. Figure 2c shows the stress relaxation (at 180 °C) of UV activated resin-ER-1-lat as a function of the exposure dose, whilst keeping the catalyst content constant (10 wt%). A clear acceleration of the stress relaxation kinetics is observed at higher exposure dose, confirming a faster bond exchange rate due to the release of a higher number of Brønsted acids.

The same trend is observed, albeit at a higher extend, when increasing the amount of triphenylsulfonium phosphate from 5 to 15 wt% (Figure 2d). The results evidence that both catalyst content and exposure dose influence the stress relaxation kinetics of vitrimers containing triphenylsulfonium phosphate as photolabile catalyst.

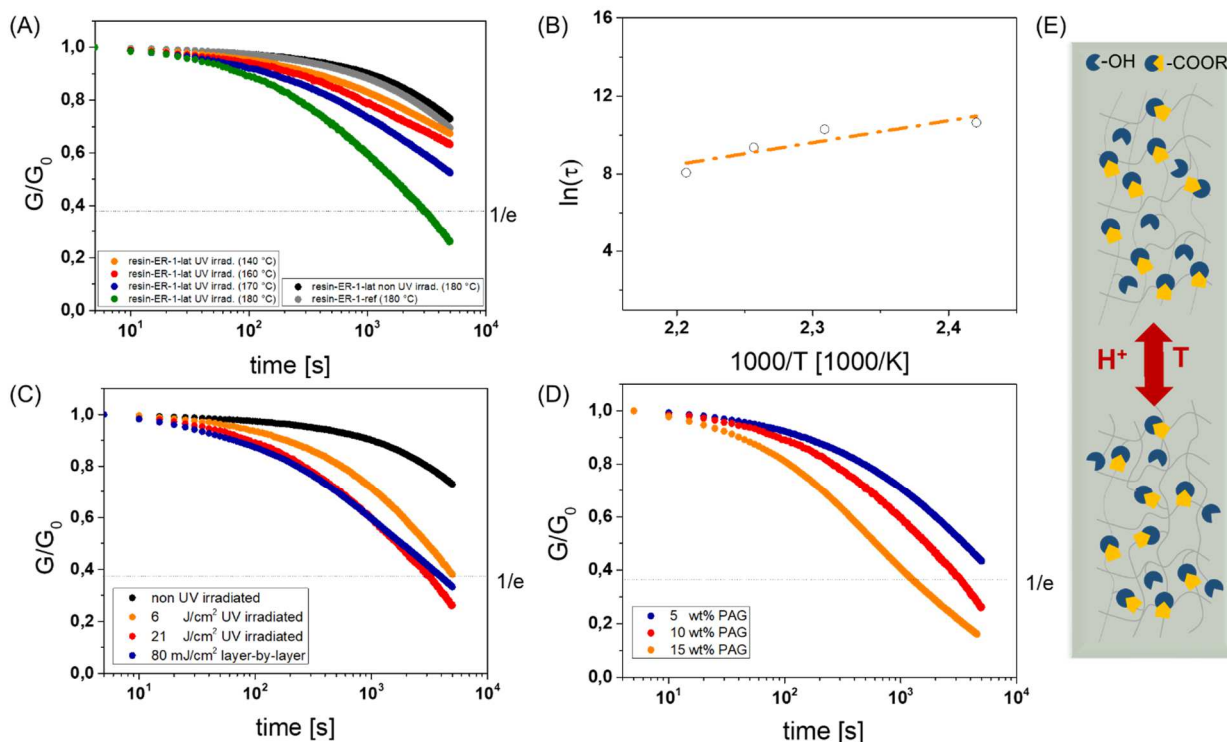


**Figure 2** – (a) Normalised stress relaxation curves of UV activated resin-ER-1-lat versus temperature in comparison to the non UV irradiated resin-ER-1-lat and the reference (resin-ER-1-ref) containing no triphenylsulfonium phosphate. (b) Arrhenius plot of UV activated resin-ER-1-lat derived from measured relaxation times. Normalised stress relaxation curves of UV activated resin-ER-1-lat obtained at 180 °C as a function of (c) the exposure dose and (d) the catalyst content. (e) Schematic representation of the transesterification reaction.

By using the Maxwell Model, the characteristic relaxation times ( $\tau^*$ ) were taken as the time required to relax to  $1/e$  of the initial stress at temperatures between 160 and 200 °C.<sup>26</sup> Figure 2b clearly shows that the stress relaxation data of UV activated resin-ER-1-lat satisfies the

Arrhenius law and confirm the vitrimeric nature of the irradiated resin-ER-1-lat. The activation energy ( $E_a$ ) was estimated from the slope ( $m=E_a/R$ ) of the straight line fitted to the data, and amounted to 93.7 kJ mol<sup>-1</sup>.

To demonstrate the network's ability to locally switch on the exchange reactions on demand, 3D objects were manufactured with dual-wavelength DLP 3D printing, operating at two different wavelengths (405 and 365 nm). During the printing process, resin-ER-1-lat is selectively crosslinked layer-by-layer upon visible light irradiation (405 nm). The set-up allows for an additional spatially controlled exposure at 365 nm of each layer after its solidification. Thus, the catalyst is selectively activated layer-by-layer and in a controlled lateral manner.

Test structures were printed, in which selected areas were additionally UV exposed layer-by-layer during the printing process as shown in Figure 3a and b. To confirm the localized activation of topological rearrangements in the 3D objects, selected reshaping experiments were carried out (Figure 3c and d).

In the first step, a rectangular shaped test specimen (shape I in Figure 3d) was placed in a U-shaped mold and heated at 120 °C for 240 min. One half of the test specimen was UV exposed at 365 nm during the printing and thus, contained the activated transesterification catalyst (Figure 3b). At 120 °C, the network is able to undergo topological rearrangements in the UV-irradiated part of the test specimen. A remolding of the exposed half of the samples takes place as the network changes from an elastic solid to a viscoelastic liquid, which has been shown in the stress relaxation curves (Figure 2a). The test specimen was then cooled to room temperature and removed from the mold. The freestanding sample was able to retain its U-shaped form at 10 °C (shape II in Figure 3d). By heating the sample to 100 °C for 10 min, the non-exposed half was able to move back to its original flat position, whilst the exposed half was locked and maintained its angle (shape III in Figure 3d). In the non-exposed area, the photopolymer network is able to recover its original shape since the elongated polymer chains return to their entropically more favorable initial state above the network's  $T_g$ .



In contrast, in the exposed area, transesterification reactions occurred due to the photo-released Brønsted acids and caused a rearrangement of the network topology to the U-shaped mold. Consequently, rising the temperature above the network's  $T_g$  did not lead to a shape recovery of the UV-exposed part.

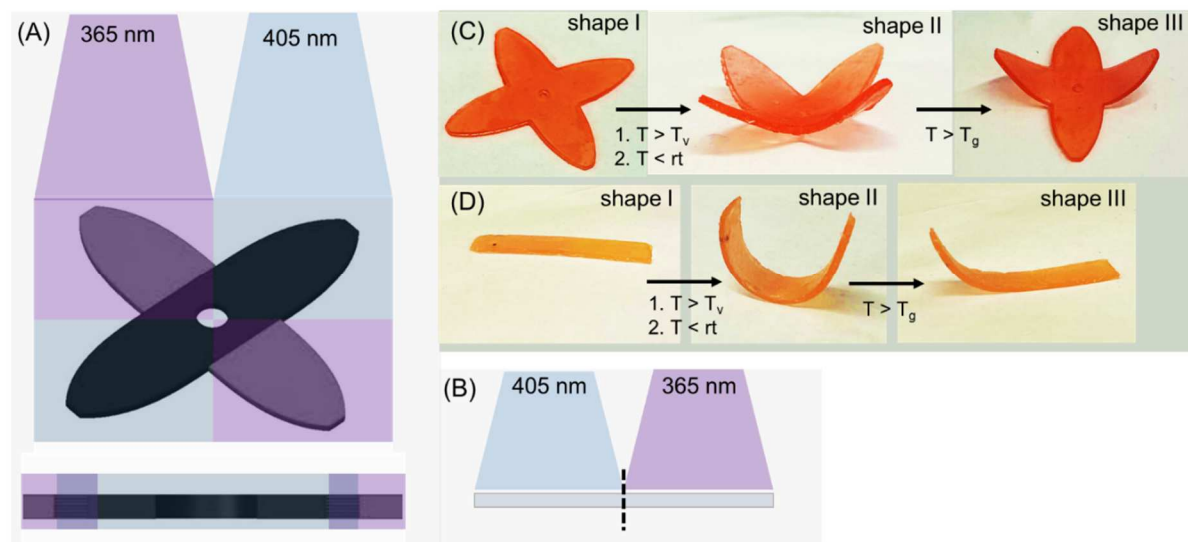


**Figure 3 – Illustrations monitoring the (a, b) printing set-up of the rectangular test structures and the grippers, and the programming and locally controlled reshaping of (c) grippers and (d) rectangular test structures obtained from resin-ER-1-lat. The test structures were fabricated by dual-wavelength DLP 3D-printing operating at 405 nm and 365 nm. During the layer-by-layer exposure at 405 nm the resin was solidified and selective areas of the test structures were additionally exposed at 365 nm to release Brønsted acids acting as transesterification catalyst.**

As additive manufacturing techniques benefit from a high freedom in design, the concept can be easily transferred to other 3D structures. In another experiment, a gripper was 3D printed, whose arms were selectively exposed at 365 nm (shape I in Figure 3c). After the programming step, a selective movement of the non-exposed arms is realized, whilst the exposed arms remain locked in their programmed positions due to the acid-catalyzed topological rearrangements (shape III in Figure 3c).

The results evidence that the use of triphenylsulfonium phosphate as photolabile transesterification catalyst enables a spatially resolved activation of topological rearrangements in vitrimers. By transferring the concept to 3D printable resin formulations, functional 3D structures are obtained, whose vitrimeric properties can be precisely controlled layer-by-layer by using a dual-wavelength DLP 3D printer.

## *Conclusions*

Summing up, a photolabile catalyst was employed for the local activation of topological rearrangements in thermo-activated vitrimers. Triphenylsulfonium phosphate was chosen as photolabile catalyst, as it benefits from a high temperature stability, is transparent in the visible light region and releases strong Brønsted acids upon UV exposure. By using the photolabile catalyst in a visible light curable thiol-acrylate vitrimer, selective curing of the photopolymer network at 405 nm was achieved without premature release of Brønsted acids. Subsequent UV exposure at 365 nm triggered the formation of Brønsted acids, which efficiently catalyzed transesterifications. Stress relaxation studies confirmed the vitrimeric properties of the photo-activated networks and revealed that the relaxation kinetics increase with rising temperature, exposure doses as well as catalyst content.

The photoreactive nature of the resin enabled the transfer of the concept towards 3D structures, which were fabricated with a dual-wavelength DLP printer, operating at 405 and 365 nm. Selective movement of the 3D structures was accomplished after a programming step above the network's  $T_v$ , due to the localized activation of the catalyst during the printing process. Thus, the use of photolabile catalysts in photo-reactive vitrimer systems is a versatile strategy to fabricate soft active devices, which are able to undergo locally programmable shape change.

## *Experimental section*

### *Materials*

Trimethylolpropane tri(3-mercaptopropionate) was obtained from Bruno Bock (Germany) and all other chemicals were purchased from Sigma-Aldrich and used as received.

### *Preparation of resin-ER-1-lat*

Sudan II (0.01 wt%), 2-hydroxy-2-phenoxypropyl acrylate (50 mol%) and glycerol 1,3-diclycerolate diacrylate (25 mol%) were mixed with 5-15 wt% triarylsulfonium hexafluorophosphate solution in an ultrasonic bath until the photoabsorber was dissolved.

2 wt% phenylbis(2,4,6-trimethylbenzoyl)phosphine oxide and 25 mol% trimethylolpropane tri(3-mercaptopropionate) were added and dissolved by stirring the formulation at 45 °C.

### *Characterization*

Light-induced curing of resin-ER-1 was followed by FTIR spectroscopy utilizing a Vertex 70 spectrometer (Bruker, USA). 16 scans were accumulated in transmission mode from 4000 to 700  $\text{cm}^{-1}$  with a resolution of 4  $\text{cm}^{-1}$  and the absorption peak areas were determined with OPUS software. 1  $\mu\text{L}$  of the resin was drop-cast between two  $\text{CaF}_2$  discs and cured with a light emitting diode lamp (zgood® wireless LED curing lamp) comprising a power density of 3.5  $\text{mW cm}^{-2}$  ( $\lambda = 420 - 450 \text{ nm}$ ).

Thermal gravimetric analysis was carried out with a Mettler Toledo (USA) TGA/DSC thermogravimetric analyzer. The measurements were performed under nitrogen atmosphere by heating the sample from 23 to 900 °C with a heating rate of 10 °C  $\text{min}^{-1}$ .

Differential scanning calorimetry measurements were carried out with a Perkin Elmer DSC 4000 instrument (USA). A temperature program from -30 to 100 °C with a heating rate of 10 K  $\text{min}^{-1}$  was applied under nitrogen atmosphere. The  $T_g$  was determined from the second heating run by taking the midpoint in heat capacity.

Stress relaxation experiments at temperatures between 140 and 180 °C were performed on a moving die rheometer from Anton Paar (Austria). The samples were balanced to the selected measurement temperature for 20 min. Subsequently, a 1% step strain was inserted and the decreasing stress was recorded over time.

### *DLP 3D printing*

A dual-wavelength DLP 3D-printer prototype (with 405 and 365 nm light sources) from way2production (Austria) was used for 3D printing experiments. To cure the network without activating the photolabile catalyst, one bottom layer was exposed for 10 s, whereas the other layers were illuminated for 7 s with the 405 nm light source. The activation of the PAG was achieved by irradiating the desired layers upon 10 s exposure with UV-A light (365 nm).

*Re-shaping experiments*

Re-shaping experiments were carried out with 3D printed grippers (d= 35 mm) and a 3D printed rectangular test specimen (l= 40mm, b= 5 mm, h= 1 mm), which were heated to 140 °C for 4 h, to fix the first shape. The second shape was programmed by heating the sample to 120 °C for 4 h in a mold. For fixing the second shape, the sample was cooled down to 0 °C. By heating up to 100 °C, the first shape was regained in the non-exposed areas.

*Conflicts of interest*

There are no conflicts to declare.

*Acknowledgements*

Part of the research work was performed within the COMET-Module “Chemitecture” (project-no.: 21647048) at the Polymer Competence Center Leoben GmbH (PCCL, Austria) within the framework of the COMET-program of the Federal Ministry for Transport, Innovation and Technology and the Federal Ministry for Digital and Economic Affairs with contributions by Montanuniversitaet Leoben (Institute of Chemistry of Polymeric Materials). The PCCL is funded by the Austrian Government and the State Governments of Styria, Upper and Lower Austria.

In addition, part of the research work was also performed with the “SMART” project. This project has received funding from the European Union’s Horizon 2020 research and innovation programme under the Marie Skłodowska-Curie grant agreement No 860108.

*References*

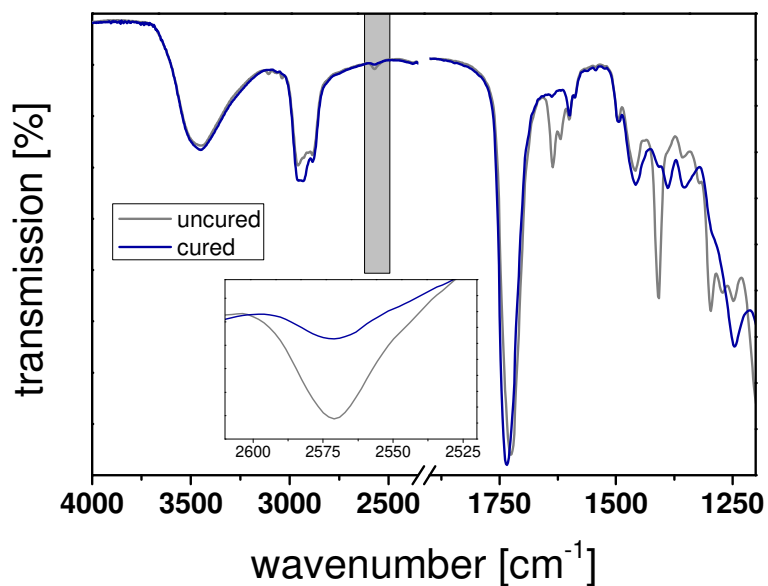
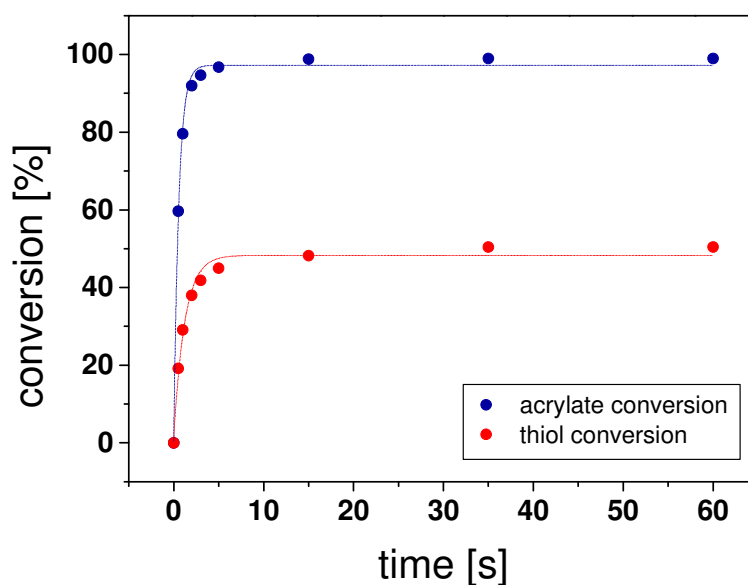
- 1 W. Zou, J. Dong, Y. Luo, Q. Zhao and T. Xie, *Advanced Materials*, 2017, 29, 1606100.
- 2 J. M. Winne, L. Leibler and F. E. Du Prez, *Polym. Chem.*, 2019, 10, 6091–6108.
- 3 L. Tuan, B. Zhao and J. Zhang, *Polymer*, 2020, 194, 122392.

PUBLICATION V

- 4 W. Denissen, J. M. Winne and F. E. Du Prez, *Chemical Science*, 2016, 7, 30–38.
- 5 W. Alabiso and S. Schlögl, *Polymers*, 2020, 12.
- 6 D. Montarnal, M. Capelot, F. Tournilhac and L. Leibler, *Science*, 2011, 334, 965–968.
- 7 M. Giebler, C. Sperling, S. Kaiser, I. Duretek and S. Schlögl, *Polymers*, 2020, 12.
- 8 a) S. Kaiser, J. N. Jandl, P. Novak and S. Schlögl, *Soft Matter*, 2020; b) S. Kaiser, S. Wurzer, G. Pilz, W. Kern and S. Schlögl, *Soft Matter*, 2019, 15, 6062–6072
- 9 M. Capelot, D. Montarnal, F. Tournilhac and L. Leibler, *Journal of the American Chemical Society*, 2012, 134, 7664–7667.
- 10 M. Guerre, C. Taplan, J. M. Winne and F. E. Du Prez, *Chemical Science*, 2020, 11, 4855–4870.
- 11 Q. Shi, K. Yu, X. Kuang, X. Mu, C. K. Dunn, M. L. Dunn, T. Wang and H. Jerry Qi, *Mater. Horiz.*, 2017, 4, 598–607.
- 12 C. Wang, T. M. Goldman, B. T. Worrell, M. K. McBride, M. D. Alim and C. N. Bowman, *Mater. Horiz.*, 2018, 5, 1042–1046.
- 13 B. Zhang, K. Kowsari, A. Serjouei, M. L. Dunn and Q. Ge, *Nature communications*, 2018, 9, 1831.
- 14 E. Rossegger, R. Höller, D. Reisinger, J. Strasser, M. Fleisch, T. Griesser and S. Schlögl, *Polym. Chem.*, 2021, 117, 10212.
- 15 a) Y. Yang, Z. Pei, X. Zhang, L. Tao, Y. Wei and Y. Ji, *Chem. Sci.*, 2014, 5, 3486–3492; b) Z. Wang, Z. Li, Y. Wei and Y. Ji, *Polymers*, 2018, 10, 65;
- 16 Z. Feng, J. Hu, H. Zuo, N. Ning, L. Zhang, B. Yu and M. Tian, *ACS Appl. Mater. Interfaces*, 2018, 11, 1469–1479.
- 17 M. Hayashi and R. Yano, *Macromolecules*, 2019, 53, 182–189.
- 18 a) J. V. Crivello, *Advances in Polymer Science*, 1984, 62, 3–48; b) J. V. Crivello, *Journal of Polymer Science: Part A: Polymer Chemistry*, 1999, 37, 4241–4254;

## PUBLICATION V

- 19 J. V. Crivello and J. H. W. Lam, *Journal of Polymer Science: Polymer Chemistry Edition*, 1979, 17, 977–999.
- 20 M. Sangermano, I. Roppolo and A. Chiappone, *Polymers*, 2018, 10, 1–8.
- 21 T. J. Spencer and P. A. Kohl, *Polymer Degradation and Stability*, 2011, 96, 686–702.
- 22 Y. Yağci and I. Reetz, *Progress in Polymer Science*, 1998, 23, 1485–1538.
- 23 J. Chen, S. Jiang, Y. Gao and F. Sun, *J Mater Sci*, 2018, 53, 16169–16181.
- 24 A. Streitwieser, C. H. Heathcock and E. M. Kosower, *Introduction to organic chemistry*, 4th edn., 1998.
- 25 a) E. Lotero, Y. Liu, D. E. Lopez, K. Suwannakarn, D. A. Bruce and J. G. Goodwin, *Ind. Eng. Chem. Res.*, 2005, 44, 5353–5363; b) P. A. Alaba, Y. M. Sani and W. M. Ashri Wan Daud, *RSC Adv.*, 2016, 6, 78351–78368;
- 26 M. Capelot, M. M. Unterlass, F. Tournilhac and L. Leibler, *ACS Macro Lett.*, 2012, 1, 789–792.

*Supporting Information***Locally controlling dynamic exchange reactions in 3D printed thiol-acrylate vitrimers using dual-wavelength digital light processing**Elisabeth Rossegger,<sup>a</sup> Khadijeh Moazzen,<sup>a</sup> Mathias Fleisch<sup>a</sup> and Sandra Schlögl<sup>\*a</sup>**Figure S1** - FTIR spectra of resin-ER-1-lat prior to and after photocuring at 405 nm (3.6 mW cm<sup>-2</sup>).**Figure S2** – Monitoring the conversion of acrylate and thiol groups in resin-ER-1-lat by FT-IR spectroscopy versus exposure time. Light exposure was carried out at 405 nm (3.6 mW cm<sup>-2</sup>). The lines are a guide for the eye.

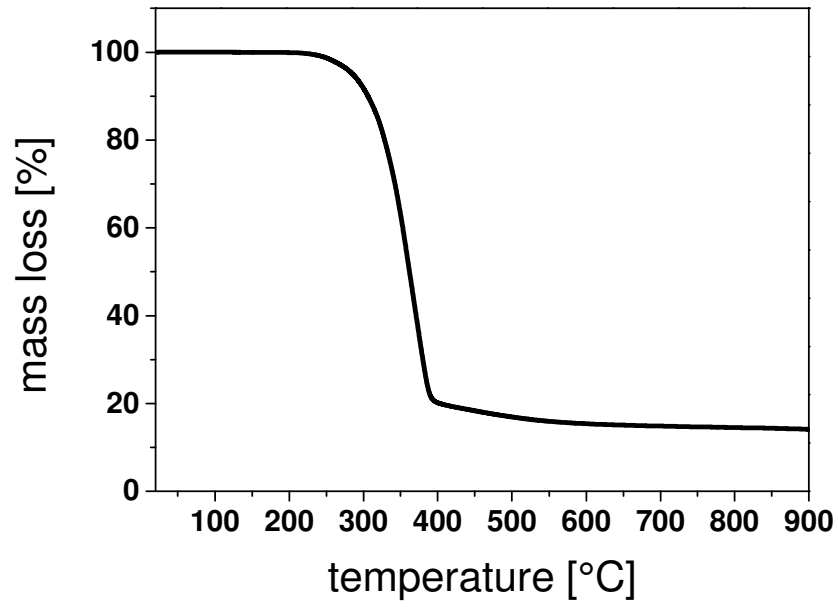


Figure S3 - TGA curve of cured resin-ER-1-lat.

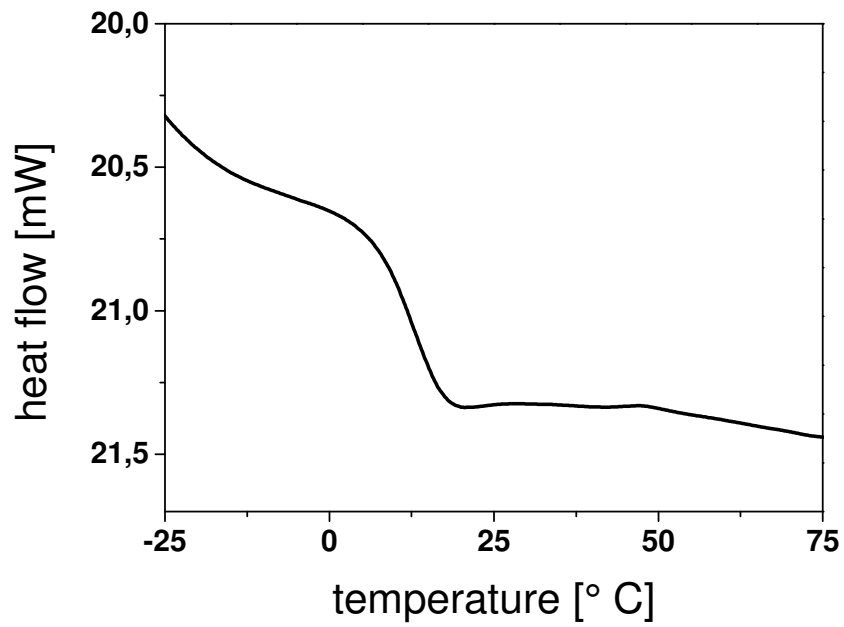


Figure S4 - DSC curve of cured resin-ER-1-lat.



## APPENDIX

## CURRICULUM VITAE

PERSONAL DATA

---

Name Dipl.-Ing. Elisabeth Rossegger

Date of birth 28.03.1994

Place of birth Graz

EDUCATION

---

10/2017-03/2021 PhD Studies at Montanuniversität Leoben  
PhD Thesis (PCCL): Synthesis and Characterization of Functional  
Photopolymers for Advanced Applications

11/2015-08/2017 Master Studies at the Technical University of Graz  
Master degree in Technical Chemistry with distinction  
Master thesis (PCCL): Crosslinked Poly (2-oxazoline)-Based  
Micelles as Drug Depots

10/2012-11/2015 Bachelor Studies at the Technical University/University of Graz  
Bachelor degree in Chemistry  
Bachelor thesis: Synthesis and Analysis of Sterylglycosides

09/2004-06/2012 AHS Bruck an der Mur  
School leaving examination with distinction

## APPENDIX

### PROFESSIONAL EXPERIENCE

---

- 05/2019-06/2019      Research stay at the Politecnico di Torino (Italy) in the group of Prof. Marco Sangermano
- Since 10/2017        Researcher at the Polymer Competence Center Leoben GmbH
- 08/2016-09/2016    Internship at ALLNEX Austria (Graz) in the field Synthesis and Characterization of water-based resins
- 08/2015-09/2015    Internship at BOREALIS-Polyolefine (Linz) in the field Research and Development of Polypropylene
- 08/2014-09/2014    Internship at BOREALIS-Polyolefine (Linz) in the field Research and Development of Polypropylene
- 07/2014              Internship at the University of Graz in the field of Biocatalysis
- 09/2012              Internship at ISOVOLTAIC AG (Lebring) in the field Research and Development

### AWARDS

---

- 02/2021              Best Paper of the Month in Polymer Chemistry: Digital light processing 3D printing with thiol-acrylate vitrimers

## APPENDIX

### EXTRA-CURRICULAR ACTIVITIES

---

- 08/2016 – 05/2019 Volleyball-player in the 2<sup>nd</sup> league of Austria
- 08/2014 – 05/2016 Volleyball-player in the 2<sup>nd</sup> league of Austria
- 08/2012 – 05/2014 Volleyball-player in the 1<sup>st</sup> league of Austria
- 09/2010 – 05/2018 Volleyball-trainer for girls in the age of 10 – 15 years
- 2008 - 2017 Tutor for the following subjects: mathematic, chemistry and physics

### HOBBIES

---

(Beach)Volleyball, running, hiking, cycling, playing tennis, cooking and reading

## ***LIST OF PUBLICATIONS***

### PAPERS

---

Reisinger, D.; Kaiser, S.; **Rossegger, E.**; Alabiso, W.; Rieger, B.; Schlögl, S. Introduction of photolabile bases for locally controlling dynamic exchange reactions in thiol-epoxy vitrimers. *Angewandte Chemie Int. Ed.*, **2021 submitted**

## APPENDIX

Moazzen, K.; **Rossegger, E.**; Alabiso, W.; Schlögl, S. Role of organic phosphates and phosphonates in catalyzing dynamic exchange reactions in thiol-click vitrimers. *Macromolecular Rapid Communications*, **2021 submitted**

Truszkiewicz, E.; Thalhamer, A.; Rossegger, M.; Vetter, M.; Meier, G.; **Rossegger, E.**; Fuchs, P.; Schlögl, S.; Berer, M. Mechanical behavior of 3D-printed polymeric metamaterials for lightweight applications. *Additive Manufacturing*, **2021 submitted**

**Rossegger, E.**; Moazzen, K.; Fleisch, M.; Schlögl, S. Locally controlling dynamic exchange reactions in 3D printed thiol-acrylate vitrimers using dual-wavelength digital light processing. *Nature communications*, **2021 submitted**

**Rossegger, E.**; Höller, R.; Reisinger, D.; Fleisch, M.; Strasser, J.; Wieser, V.; Griesser, T.; Schlögl, S. High resolution additive manufacturing with acrylate based vitrimers using organic phosphates as transesterification catalyst. *Polymer*, **2021 accepted**

Cazin, I.; **Rossegger, E.**; Guedes de la Cruz, G.; Griesser, T.; Schlögl, S. Recent Advances in Functional Polymers Containing Coumarin Chromophores. *Polymers*, **2021**, *13*, 56. <https://doi.org/10.3390/polym13010056>

**Rossegger, E.**; Höller, R.; Reisinger, D.; Strasser, J.; Fleisch, M.; Griesser, T.; Schlögl, S. Digital light processing 3D printing with thiol-acrylate vitrimers. *Polym. Chem.*, **2021**. <https://doi.org/10.1039/D0PY01520B>.

Romano, A.; Roppolo, I.; **Rossegger, E.**; Schlögl, S.; Sangermano, M. Recent Trends in Applying Ortho-Nitrobenzyl Esters for the Design of Photo-Responsive Polymer Networks. *Materials*, **2020**, *13*, 2777

Romano, A.; Angelini, A.; **Rossegger, E.**; Palmara, G.; Castellino, M.; Frascella, F.; Chiappone, A.; Chiadò, A.; Sangermano, M.; Schlögl, S.; Roppolo, I. Laser-Triggered Writing and Biofunctionalization of Thiol-Ene Network. *Macromol. Rapid Commun.* **2020**, 2000084

## APPENDIX

**Rossegger, E.;** Nees, D.; Turisser, S.; Radl, S.; Griesser, T.; Schlögl, S. Photo-switching of surface wettability on micropatterned photopolymers for fast transport of water droplets over a long-distance. *Polym. Chem.*, **2020**, *11*, 3125-3135. <https://doi.org/10.1039/D0PY00263A>.

**Rossegger, E.;** Hennen, D.; Griesser, T.; Roppolo, I.; Schlögl, S. Directed motion of water droplets on multi-gradient photopolymer surfaces. *Polym. Chem.*, **2019**, *10*, 1882-1893. <https://doi.org/10.1039/C9PY00123A>.

Taudt, C.; Nelsen, B.; **Rossegger, E.;** Schlögl, S.; Koch, E.; Hartmann, P. Spatially Resolved Cross-Linking Characterization by Imaging Low-Coherence Interferometry. *Sensors*, **2019**, *19*, 1152.

**Rossegger, E.;** Pirolt, F.; Hoepfener, S.; Schubert, U. S.; Glatter, O.; Wiesbrock, F. Crosslinkable/functionalizable poly(2-oxazoline)-based micelles. *European Polymer Journal*, **2019**, *121*, 109305

Gloger, D.; **Rossegger, E.;** Gahleitner, M.; Wagner, C. Plastic drawing response in the biaxially oriented polypropylene (BOPP) process: polymer structure and film casting effects, *Journal of Polymer Engineering*, **2019**, *40(9)*, 743-752

## CONFERENCES

---

### *Oral presentations:*

Photo-induced motion of water on tailored polymer surfaces. **Rossegger, E.;** Hennen, D.; Roppolo, I.; Griesser, T. & Schlögl, S., ACS Spring Meeting Orlando (USA) 2019

Additive manufacturing of tailored lightweight mechanical metamaterials for industrial applications. Truskiewicz, E., Vetter, M., Rossegger, M., Berer, M., **Rossegger, E.;** Schlögl, S., Fuchs, P., First European Conference on Structural Integrity of Additively Manufactured Materials (ESIAM19), Trondheim (NOR) 2019

## APPENDIX

### *Poster presentations:*

Directed Motion of Water Droplets on Multi-Gradient Photopolymer Surfaces **Rossegger, E.**; Hennen, D.; Roppolo, I.; Griesser, T. & Schlögl, S., Photopolymerization Fundamentals Monterey (USA) 2019

Photo-responsive thiol-ene networks for the design of surface with polarity gradient. **Rossegger, E.**; Radl, S. V.; Kern, W. & Schlögl, S., European Symposium of Photopolyme Science (ESPS) Mulhouse (FR) 2018